

Theory of odd frequency pairing as a probe of topological superconductivity and Majorana fermions

Eslam Ahmed

A thesis submitted in partial fulfillment of the requirements
for the degree of Doctor of Philosophy (Ph.D.) in Engineering

Supervisor:

Professor Yukio Tanaka



NAGOYA UNIVERSITY

Graduate School of Engineering
Department of Applied Physics

Theory of odd frequency pairing as a probe of topological superconductivity and Majorana fermions

Eslam Ahmed

June 30, 2025

Abstract

The pursuit of Majorana bound states (MBSs) in superconductor-semiconductor hybrids is crucial for topological quantum computation, yet their unambiguous identification remains challenging as trivial Andreev bound states (ABSs) can mimic their zero-energy signatures. This thesis presents a theoretical and numerical investigation into distinguishing MBSs from ABSs based on odd-frequency pairing signatures, focusing on the frequency dependence, disorder effects, and the impact of Floquet driving.

First, we analyze the emergent superconducting pairing correlations in static superconductor-semiconductor junctions based on Rashba nanowire model. We establish that while both ABSs and MBSs can show similar characteristics including large odd-frequency pairing amplitudes near zero frequency, only true zero-energy MBSs in long superconducting segments induce a unique divergent low-frequency profile ($\sim 1/\omega_n$) in the odd-frequency pairing amplitude stemming from the self-conjugate nature of MBSs. This is in clear contrast with the linear frequency dependence for trivial ABSs and offers a robust identification criterion.

Next, we investigate the influence of disorder by studying the anomalous proximity effect in clean normal metal/disordered normal metal/superconductor (CN/DN/S) junctions. We find that zero-energy peaks (ZEPs) in the local density of states (LDOS) associated with trivial ABSs are fragile against scalar disorder. Conversely, ZEPs from MBSs remain robust, particularly in long superconducting segments, providing a key indicator for topological MBSs in realistic disordered environments. This robustness is primarily attributed to odd-frequency spin-triplet pairs.

Finally, we extend our study to driven (Floquet) topological superconductors. We show that Floquet engineering can generate multiple Majorana modes, including zero-energy modes (MZMs) and π -energy

modes (MPMs), each having distinct signatures on odd-frequency pairing. MZMs yield a $\sim 1/\omega$ divergence, while MPMs lead to a $\sim 1/(\omega - \pi\hbar/T)$ divergence (where T is the drive period). A spectral bulk-boundary correspondence is established, linking boundary odd-frequency pairing to bulk topological invariants in these driven chiral systems, underscoring its utility as a topological probe.

Keywords: Topological Superconductivity, Majorana Fermions, Odd-Frequency Pairing, Andreev Bound States, Anomalous Proximity Effect, Disorder Effects, Floquet Engineering, Floquet Systems, Quantum Transport, Condensed Matter Physics.

Acknowledgments

This thesis would not have been possible without the support, guidance, and encouragement of many individuals to whom I am profoundly grateful. The journey through a PhD is long and arduous, and I was fortunate to have an incredible network of mentors, colleagues, friends, and family by my side.

First and foremost, I would like to express my deepest gratitude to my supervisor, **Professor Tanaka Yukio**. His invaluable guidance, immense patience, and profound wisdom have been the cornerstones of my doctoral studies. He provided me with the intellectual freedom to explore my own ideas while always being there to steer me back on course with insightful advice. His mentorship has not only shaped this thesis but has fundamentally shaped me as a researcher.

My research journey took a decisive turn thanks to the invaluable contributions of **Dr. Jorge Cayao**. He introduced me to the fascinating field of Floquet engineering and the intricate physics of trivial helical Andreev bound states. It was his suggestion to explore odd-frequency pairing as a distinguishing probe and his insight in reviving a dormant project that directly led to the core results presented in this thesis. I am also deeply indebted to **Dr. Shun Tamura**, whose mentorship during my Master's and early PhD years was foundational. He patiently taught me the intricacies of topological superconductivity and the numerical techniques that became the bedrock of my research.

I am grateful for the fruitful discussions with **Dr. Satoshi Ikegaya**. His timely reminders to focus on universality and to seek general principles beyond the specifics of a single model were crucial in shaping the direction and impact of my work.

This research was generously supported by a PhD scholarship from **Nagoya University** and a scholarship from the **Mitsubishi Foundation**. I am sincerely thankful for their financial support, which made this doctoral work possible.

The PhD journey is as much about the community as it is about the research. I am incredibly fortunate to have a friend like **Ziad Ahmed**. Despite our research fields being vastly different, he generously offered his expertise to help me debug and refactor my code, significantly enhancing its performance. His willingness to run my simulations on his university's high-performance cluster was an act of

immense kindness and a testament to his friendship. A special note of thanks goes to my dear friend and colleague, **Dhruv Walia**. Our countless hours discussing physics were a constant source of inspiration and learning. More than a colleague, he was a true brother to me in Japan, always there to help me navigate challenges. Although he has returned to India, I cherish our time together and hope our paths cross again soon.

My journey would have been immeasurably more difficult without the unwavering support of my friend of over a decade, **Ahmed Gado**. During challenging times, he was a pillar of support, even assisting me financially. I am particularly grateful for his incredible generosity in gifting me a new laptop when my old one failed. This thesis, and all the calculations within it, were brought to life on that machine.

To my beloved partner, **Runqi Li**, I offer my deepest love and gratitude. You have been the joy of my life throughout this entire process. Your unwavering support, your ability to make me smile every day, and your steadfast belief in me have been my anchor. You made me look forward to a brighter future beyond the horizon of this thesis, and for that, I am eternally grateful.

Finally, I owe everything to my family. To my wonderful parents, my mom and dad, who worked tirelessly every day to ensure I had the best possible life. Despite our humble beginnings, your love and sacrifice meant I never felt any disadvantage. Your unwavering support, especially during the pandemic when my scholarship was lost, was a lifeline. You endured hardship so that I could pursue my dream, and I will never forget it. To my dear brothers, who are not so little anymore—it pains me that distance and circumstances, particularly the COVID-19 travel ban and my financial situation, have kept us apart for so long. The boy who was starting elementary school when I left is now a young man in high school. I hope to see you all very soon. Your daily calls and constant encouragement were a reminder of the home and love waiting for me.

Many other friends and colleagues have supported me on this journey, and while I cannot name everyone, please know that your kindness has not gone unnoticed. I am grateful to you all.

All praise and thanks are due to Allah, the Most Gracious, the Most Merciful, for granting me the strength and opportunity to complete this work.

Contents

Acknowledgments	iii
1 Introduction	1
2 Theoretical Background	5
2.1 Fundamentals of Superconductivity	5
2.1.1 BCS Theory of Superconductivity	5
2.1.2 Bogoliubov-de Gennes Formalism	9
2.2 Topological Phases of Matter and Topological Superconductivity . .	12
2.2.1 Classification of Topological insulators and Topological Superconductors	13
2.2.2 Chiral Symmetric Superconductivity in one Dimension	17
2.3 Majorana Zero Modes and Topological Superconductivity	22
2.3.1 Majorana Fermions	22
2.3.2 Majorana Zero Modes in Topological Superconductors	24
2.3.3 Majorana Zero Modes in Superconducting Heterostructures .	28
2.4 experimental detection of Majorana bound states and pitfalls	32
2.5 Odd-Frequency Superconductivity and Majorana Zero Modes	37
2.5.1 Symmetry classification of superconductivity	37
2.5.2 Nambu Green's function method	39
2.5.3 Generation of odd-frequency pairing in heterostructures	41
2.5.4 Odd-frequency pairing and Majorana zero modes	42
2.6 anomalous proximity effect	46
2.6.1 Proximity Effect in Dirty Metal/Superconductor Junctions .	46
2.6.2 Anomalous Proximity Effect from Chiral Symmetry	48
2.7 Floquet Theory	50
2.7.1 Floquet theory in quantum mechanics	51
2.7.2 Rotating Frame Method	54
2.7.3 Extended Hilbert Space Formalism	56
2.7.4 Topological Floquet superconductors	58
2.8 Conclusion	61

3 Odd-Frequency Pairing in Static Superconductor-Semiconductor Junctions	62
3.1 Model and methods	63
3.1.1 System Hamiltonian	64
3.1.2 Calculation of Superconducting Pair Amplitudes	65
3.2 Different phases of the NS junction	67
3.3 Junctions Hosting Only Trivial Zero-Energy ABSs	69
3.3.1 Low-energy Spectrum and the Nature of Trivial Zero-Energy Andreev Bound States	69
3.3.2 Emergent Superconducting Correlations from Trivial ABSs	71
3.4 Junctions Hosting Both Trivial ABSs and MBSs	75
3.4.1 Low-energy Spectrum: from helical ABSs to MBSs	76
3.4.2 Emergent Superconducting Correlations from Trivial ABSs and MBSs	79
3.4.3 Accumulated Pair Amplitudes and their Zeeman Dependence	83
3.4.4 Experimental Signatures of Odd-Frequency Pairing	85
3.5 Effect of Zeeman Field Orientation on the Helical and Topological Regimes	87
3.6 Conclusions	91
4 Anomalous Proximity Effect in Semiconductor-Superconductor Junctions	93
4.1 Model and Methods	94
4.1.1 System Hamiltonian	94
4.1.2 Calculation of LDOS and Pair Correlations	96
4.2 Low-Energy Spectrum and Zero-Energy States in CN/DN/S Junctions	99
4.2.1 Low-Energy Spectrum in CN/DN/S Junctions with Short S Regions	99
4.2.2 Dependence on S Region Length	102
4.3 LDOS and Pair Correlations in CN/DN/S Junctions	104
4.3.1 No Anomalous Proximity Effect in CN/DN/S Junctions with Short S Regions	105
4.3.2 Anomalous Proximity Effect for Long S Regions	108
4.4 Conclusion	112
5 Odd frequency pairing in Floquet Topological Superconductors	115
5.1 Model	116
5.2 Floquet Majorana edge modes: Topological invariants and quasienergy spectrum	120
5.2.1 Bulk dispersion relation and multiple Fermi points	120
5.2.2 Topological Invariants	122

5.2.3	Open-boundary quasienergy spectrum	124
5.3	Odd-frequency superconducting pairing at stroboscopic times	126
5.3.1	Accumulated odd-frequency pairing at the edges	127
5.3.2	Characterization of topology by the odd-frequency pairing amplitude	132
5.3.3	Robustness Against Scalar Disorder	135
5.4	Concluding Remarks	136
5.5	Appendices of Chapter 5	137
5.5.1	Derivation of Bulk Quasienergy	137
5.5.2	Floquet Bulk-Boundary Correspondence and Odd-Frequency Pairing	138
5.5.3	Relation Between Effective and True Green's Functions	140
6	Conclusion and Outlook	142
6.1	Conclusion	142
6.2	Outlook	143

This thesis is based on two published papers and one preprint:

1. Ahmed, E., Tamura, S., Tanaka, Y., & Cayao, J. (2025). Odd-frequency pairing due to Majorana and trivial Andreev bound states. *Physical Review B*, 111(22), 224508.[[1](#)]
2. Ahmed, E., Tanaka, Y., & Cayao, J. (2025). Anomalous proximity effect under Andreev and Majorana bound states. *arXiv preprint arXiv:2505.03726*.[[2](#)]
3. Ahmed, E., Tamura, S., Tanaka, Y., & Cayao, J. (2025). Odd-frequency superconducting pairing due to multiple Majorana edge modes in driven topological superconductors. *Physical Review B*, 111(2), 024507.[[3](#)]

Chapter 1

Introduction

The hunt for different phases of matter has been a central theme in condensed matter physics for decades. For decades, the central framework for understanding these phases has been the Landau paradigm, which explains phase transitions in terms of symmetry breaking and the emergence of a non-zero local order parameter. This framework has successfully explained a wide range of phenomena, from the transition from liquid to solid in classical systems to the superconducting phase transition in quantum systems. However, despite its success, the Landau paradigm failed to explain the exotic conductance quantization observed in the integer quantum Hall effect (IQHE) and the fractional quantum Hall effect (FQHE) back in the 1980s [4]. The discovery of these phenomena led to the realization that there is a new class of phases of matter which cannot be characterized by a local order parameter. Instead, it became clear that these phases are necessarily characterized by a nonlocal order parameter. This realization has led to the development of a new framework for understanding phases of matter based on the concept of topological order [5–7].

The discovery of topological order has taken the field of condensed matter physics by storm. Soon after, a myriad of new phases of matter were discovered, including topological insulators and superconductors, crystalline topological insulators and superconductors, Weyl semimetals, Dirac semimetals, Floquet topological insulators, quantum spin liquids, and many more [6, 8–14]. These new phases of matter have been shown to exhibit a wide range of exotic properties, such as robust edge states, fractionalization of quantum numbers, and non-abelian statistics.

One of the most exciting developments in this field has been the discovery of Majorana zero modes (MZMs) in 2000 [15]. MZMs are exotic quasiparticles that are their own antiparticles and have been predicted to exist in different systems, such as topological superconductors, $\nu = 5/2$ fractional quantum Hall states, and quantum spin liquids. A remarkable property of MZMs is that they are non-

abelian anyons, which means that they can be used to perform topological quantum computation. This has led to a surge of interest in the search for MZMs in various systems. Perhaps the most promising candidate for realizing MZMs is in semiconductor-superconductor hybrid structures, where MZMs are expected to emerge at the ends of one-dimensional nanowires in the presence of strong spin-orbit coupling and a Zeeman field [16–18]. During the last decade, there has been a flurry of experimental activity aimed at detecting MZMs in nanowire devices, with the earliest experimental reports appearing in 2012 [19, 20]. In these experiments, the presence of MZMs was inferred from the observation of quantized zero-bias peaks in the differential conductance of the nanowire devices. However, soon after, the interpretation of these zero-bias peaks as evidence for MZMs has been challenged by the discovery of quantized zero-bias peaks in completely topologically trivial systems [21–28]. The main culprit behind these trivial zero-bias peaks was revealed to be Andreev bound states (ABSs), which are bound states that form at the interface between a superconductor and a normal metal. When ABSs are fine-tuned to have zero energy, a resonant Andreev reflection process can occur, leading to a zero-bias peak in the differential conductance of the system. Previously, it was thought that zero-energy ABSs required fine-tuning of the system parameters; however, it has been shown that zero-energy ABSs can appear as robust zero-energy states over a wide range of system parameters [29]. This has led to the realization that zero-bias peaks in the differential conductance of nanowire devices are necessary but not sufficient conditions for the presence of MZMs. Therefore, the need for more robust MZM signatures has become apparent. This has led to a renewed interest in the search for MZMs and the development of new techniques to distinguish them from other types of zero-bias peaks.

In this thesis, we present a new approach to distinguish MZMs from ABSs based on the concept of odd-frequency pairing [30–34]. Odd-frequency pairing is a type of superconducting pairing that is characterized by the fact that the pairing function is odd in time. This means that Cooper pairs can be formed between electrons that are separated in time rather than in space or spin. Studies of odd-frequency pairing have shown that it is connected to many exotic phenomena in condensed matter physics, such as attractive Meissner effect [35], spin-triplet superconductivity [31], and enhanced quantized zero-bias conductance peaks even in the presence of strong disorder, the so-called anomalous proximity effect [36–45]. Perhaps the most intriguing aspect of odd-frequency pairing is its strong connection to topology and MZMs [31, 32, 46–48]. On the one hand, it has been shown that the presence of MZMs at the edge of a topological superconductor leads to a divergent odd-frequency pairing amplitude at the edge of the system [31]. On the other hand, it was shown that the local odd-frequency pairing accumulated at the edge is proportional to an extended topological invariant divided by frequency [46–

[48]. Thus, we can interpret a robust divergent odd-frequency pairing amplitude at the edge of a topological superconductor as a signature of the MZMs. In contrast, ABSs are not expected to lead to a divergent odd-frequency pairing amplitude; instead, they lead to a linear frequency dependence of the odd-frequency pairing amplitude. Thus, we can use the odd-frequency pairing amplitude as a tool to distinguish MZMs from ABSs in nanowire devices.

Although the connection between odd-frequency pairing and MZMs has been established in the literature, no systematic study of the odd-frequency pairing amplitude in nanowire devices has been conducted. In particular, most studies work in the thermodynamic limit, where the system is considered infinite in size. However, in real experiments, the system is finite, and the presence of boundaries can lead to a finite-size effect that can affect the odd-frequency pairing amplitude. Moreover, the presence of disorder, confinement, and temporal modulations of the system can also affect the odd-frequency pairing amplitude. In this thesis, we present a systematic study of the odd-frequency pairing amplitude in nanowire devices with MZMs and ABSs under various conditions.

The remainder of this thesis is organized as follows. In Chapter 2, we present a quick overview of the theoretical background needed to understand the rest of this thesis. We begin with a brief introduction to superconductivity and the BCS theory, followed by a discussion of topological superconductors and MZMs. We then introduce the concept of odd-frequency pairing and its connection to the MZMs. We also introduce the anomalous proximity effect and its connection to the MZMs. We conclude this chapter with a brief overview of Floquet theory, which will be used in Chapter 5 to study the odd-frequency pairing amplitude in periodically driven topological superconductors.

In Chapter 3, we present a systematic study of the odd-frequency pairing amplitude in nanowire devices with MZMs. We consider normal metal/superconductor (NS) junctions which can host either MZMs or ABSs at the NS interface. We show that ABSs lead to a linear frequency dependence of the odd-frequency pairing amplitude, regardless of the length of the S segment. In junctions with short S segments, we find that MZMs give rise to a similar linear frequency dependence of the odd-frequency pairing amplitude. However, in junctions with long S segments, we find that MZMs lead to a divergent odd-frequency pairing amplitude at the edge of the S segment. This divergence is a signature of MZMs and can be used to distinguish them from the ABSs. We also present a detailed analysis of the role of the Zeeman field alignment with respect to the spin-orbit coupling in the nanowire and its effect on the odd-frequency pairing amplitude. We find that the odd-frequency pairing amplitude is maximized when the Zeeman field is orthogonal to spin-orbit coupling.

In Chapter 4, we extend our study to nanowire devices with disordered N

segments. In this chapter, we focus on the anomalous proximity effect and pairing correlations in the presence of disorder with ABSs or MZMs at the NS interface. We show that, in the clean limit, both MZMs and ABSs lead to a divergent odd-frequency pairing amplitude in N and a zero-energy peak (ZEP) in the local density of states (LDOS) in N. However, in the presence of disorder, we find that the trivial phase with ABSs is characterized by a strong suppression of the ZEP in the LDOS and a completely suppressed odd-frequency pairing amplitude in N, independent of the disorder strength and length of the disordered N segment. The topological phase with MZMs shows similar fragility to disorder if the S segment is short. We attribute this fragility to the fact that disorder increases the overlap between the MZMs at the edges of the S segment, which leads to finite energy splitting and a suppression of the odd-frequency pairing amplitude and ZEP in the LDOS across the entire junction. However, if the S segment is long, we find that the odd-frequency pairing amplitude and ZEP in the LDOS are robust against disorder and show a divergent behavior in N, even in the presence of strong disorder. This is a clear and strong signature of the MZMs.

In Chapter 5, we study the odd-frequency pairing amplitude in periodically driven topological superconductors. We show that periodic driving leads to a rich phase diagram with different phases characterized by multiple MZMs and also a new type of Majorana known as a Majorana π mode (MPM). We demonstrate that the odd-frequency pairing amplitude is sensitive to the presence of both MZMs and MPMs. In particular, we find that the accumulated odd-frequency pairing amplitude at the edge of the system is proportional to the number of MZMs and MPMs in the system and diverges as $\sim 1/\omega$ in the presence of MZMs and $\sim 1/(\omega - \pi)$ in the presence of MPMs. Interestingly, we show that this is a general feature of odd-frequency pairing in periodically driven chiral symmetric superconductors. We established a generalized bulk-edge correspondence for odd-frequency pairing in periodically driven chiral symmetric superconductors, which relates the accumulated odd-frequency pairing amplitude at the edge of the system to a topological invariant in the bulk, extending the so-called spectral bulk-edge correspondence to the time-dependent case.

Finally, in Chapter 6, we summarize our main results and discuss future research directions in this field.

Chapter 2

Theoretical Background

Ever since Kamerlingh Onnes's discovery of superconductivity in 1911 [49], superconductivity has become one of the largest subfields in condensed matter physics. Superconductivity is a very rich subject, touching almost all aspects of modern physics, from color superconductivity at the surface of neutron stars [50] to the Higgs mechanism in high-energy physics [51] to the behavior of atoms and electrons close to absolute zero temperature. [52] Due to this vast history, we will not be able to cover most of the pivotal developments in the field. Instead, in this chapter, we will only focus on reviewing the essential theoretical background needed to understand the subsequent chapters. We begin this chapter by reviewing the BCS theory and BdG equation in the context of conventional s-wave superconductors. We then review the basics of topological phases of matter and topological superconductivity, introduce Majorana bound states, and discuss their basic properties and experimental signatures. We then introduce Andreev bound states, which can mimic Majorana bound states signatures. We follow this with a quick overview of the interesting subject of odd-frequency Cooper pairing, which is the main focus of this thesis. We explain the connection between odd-frequency pairing and Majorana bound states. We also introduce the anomalous proximity effect. Finally, we conclude this chapter by reviewing Floquet theory and time-driven systems.

2.1 Fundamentals of Superconductivity

2.1.1 BCS Theory of Superconductivity

After the discovery of superconductivity in 1911, it took the physics community nearly half a century to develop a microscopic theory of superconductivity. In 1957, John Bardeen, Leon Cooper and J. Robert Schrieffer developed a microscopic description for superconductivity which is now known as BCS theory of

superconductivity.[53] The basic premise of BCS theory is that two electrons can form a bound state known as Cooper pair due to the existence of an attractive force between them. At first sight, this explanation sounds counterintuitive because electrons repel each other due to electrostatic repulsion. However, an effective attractive force can be formed between electrons as a result of their environment. BCS theory proposes that lattice vibrations can lead to an effective attractive force between electrons. As an electron moves through the lattice, it attracts nearby positive ions. As a result, the ions positions are distorted and a positive concentration of charge is created. If a second electron passes near the distorted area, it will experience an attractive force. The net result is an effective attractive force between the two electrons.[53–55]

The interaction between two electrons in a Cooper pair is a short-lived one. Generally speaking, Cooper pairs break and form all the time in a superconductor, which implies that all electrons in the superconductor interact with each other, forming a network of interacting electrons. If an electron collides with an atom, the network of interacting electrons will be forced to collide as well due to the collective nature of the electrons. This implies that collision in a superconductor is energetically too costly and hence, disfavored. Thus, electrons are energetically favored to not collide, and electric current can flow without resistance.

Now, let us discuss the mathematical description of BCS theory. First, let us consider the Hamiltonian of electrons in a metal (free electron gas):

$$H_0 = \sum_{p,\sigma} \epsilon(p) c_{p,\sigma}^\dagger c_{p,\sigma} \quad (2.1)$$

where $\epsilon(p) = \frac{p^2}{2m} - \mu$. Here, μ is the chemical potential, m is the electron mass, and $c_{p,\sigma}^{(\dagger)}$ is the annihilation(creation) operator that destroys (creates) an electron with momentum p and spin σ .

The lattice-electron interaction mentioned earlier produces an effective attractive electron-electron interaction. We model this attractive interaction between electrons using an interaction term of the following form:

$$V = \sum_{p,p'} V_{p,p'} c_{p,\uparrow}^\dagger c_{-p,\downarrow}^\dagger c_{-p',\downarrow} c_{p',\uparrow} \quad (2.2)$$

This interaction term describes the annihilation and creation of Cooper pairs (two electrons with opposite spins and momenta). $V_{p,p'}$ is the interaction strength, which can have an arbitrary dependence on momentum. However, the functional form is usually restricted by the symmetries and energy scale of the system. For example, for energies within $\hbar\omega_D$ of the Fermi surface (where ω_D is the Debye frequency), the interaction become isotropic ($V_{p,p'} = V_0$) which is the case for s-wave superconductors.[54] However, $V_{p,p'}$ can be a complicated function of momentum

in unconventional superconductors. By adding the terms, we obtain the following Hamiltonian:

$$\begin{aligned} H &= H_0 + V \\ &= \sum_{p,\sigma} \epsilon(p) c_{p,\sigma}^\dagger c_{p,\sigma} + \sum_{p,p'} V_{p,p'} c_{p,\uparrow}^\dagger c_{-p,\downarrow}^\dagger c_{-p',\downarrow} c_{p',\uparrow} \end{aligned} \quad (2.3)$$

To deal with this quadratic term, we perform the following mean-field approximation:

$$\langle c_{p,\uparrow}^\dagger c_{-p,\downarrow}^\dagger c_{-p',\downarrow} c_{p',\uparrow} \rangle \approx \langle c_{p,\uparrow}^\dagger c_{-p,\downarrow}^\dagger \rangle c_{-p',\downarrow} c_{p',\uparrow} + c_{p,\uparrow}^\dagger c_{-p,\downarrow}^\dagger \langle c_{-p',\downarrow} c_{p',\uparrow} \rangle - \langle c_{p,\uparrow}^\dagger c_{-p,\downarrow}^\dagger \rangle \langle c_{-p',\downarrow} c_{p',\uparrow} \rangle \quad (2.4)$$

Next, we define the pair potential Δ_p also known as the superconducting gap function defined as follows:

$$\Delta_p = - \sum_{p'} V_{p,p'} \langle c_{-p',\downarrow} c_{p',\uparrow} \rangle \quad (2.5)$$

Using Eq. 2.5, we can rewrite the interaction term in the Hamiltonian and obtain the following mean field Hamiltonian:

$$H_{MF} \approx \sum_{p,\sigma} \epsilon(p) c_{p,\sigma}^\dagger c_{p,\sigma} - \sum_p \left(\Delta_p c_{p,\uparrow}^\dagger c_{-p,\downarrow}^\dagger + \Delta_p^* c_{-p,\downarrow} c_{p,\uparrow} \right) + E_{const} \quad (2.6)$$

The last term is a constant energy shift and can therefore be ignored. We now arrive at a mean-field Hamiltonian H_{MF} which is quadratic in the fermionic operators and can be diagonalized easily using the so-called Bogoliubov transformation [56]. The transformation is defined by introducing new fermionic operators $\gamma_{p,\uparrow}$ and $\gamma_{-p,\downarrow}$ known as Bogoliubons, which are linear combinations of the original fermionic operators $c_{p,\uparrow}$ and $c_{-p,\downarrow}$:

$$\begin{aligned} \gamma_{p,\uparrow} &= u_p c_{p,\uparrow} - v_p c_{-p,\downarrow}^\dagger \\ \gamma_{-p,\downarrow} &= u_p c_{-p,\downarrow} + v_p c_{p,\uparrow}^\dagger \end{aligned} \quad (2.7)$$

Here, u_p and v_p are complex-valued Bogoliubov coefficients that satisfy the normalization condition $|u_p|^2 + |v_p|^2 = 1$. Under appropriate choices of u_p and v_p , the Bogoliubov transformation diagonalizes the mean-field Hamiltonian. The resulting Hamiltonian is given by:

$$H_{MF} = \sum_p E_p \left(\gamma_{p,\uparrow}^\dagger \gamma_{p,\uparrow} + \gamma_{-p,\downarrow}^\dagger \gamma_{-p,\downarrow} \right) \quad (2.8)$$

where $E_p = \sqrt{\epsilon(p)^2 + |\Delta_p|^2}$ is the quasiparticle energy. Note that there should also be a constant energy shift, but we have dropped it because it does not affect the main physics. It turns out that the Bogoliubov coefficients that diagonalize the Hamiltonian are given by:

$$\begin{aligned} u_p &= \sqrt{\frac{1}{2} \left(1 + \frac{\epsilon(p)}{E_p} \right)} \\ v_p &= \sqrt{\frac{1}{2} \left(1 - \frac{\epsilon(p)}{E_p} \right)} \end{aligned} \quad (2.9)$$

Having diagonalized the Hamiltonian, we can now write down the ground state of the system. The ground state is defined as the state annihilated by all the Bogoliubov operators $\gamma_{p,\sigma}$. This state is known as the BCS ground state, and it can be constructed from the vacuum state of the free electron gas $|0\rangle$ as follows:

$$|\text{BCS}\rangle = \prod_p \gamma_{p,\uparrow} \gamma_{-p,\downarrow} |0\rangle \quad (2.10)$$

We can clearly see that the BCS ground state is annihilated by all the Bogoliubov operators because $\gamma_{p,\sigma} \gamma_{p,\sigma} = 0$ owing to Fermi-Dirac statistics. If we substitute the Bogoliubov transformation in Eq. 2.7 into the BCS ground state, we can rewrite it in terms of the original fermionic operators $c_{p,\sigma}$:

$$|\text{BCS}\rangle = \prod_p \left(u_p + v_p c_{-p,\downarrow}^\dagger c_{p,\uparrow}^\dagger \right) |0\rangle \quad (2.11)$$

Looking at Eq. 2.11, we can see that the BCS ground state is a linear combination of states with even number of electrons. This is not surprising, since it is energetically favorable for electrons to form Cooper pairs; hence, the ground state of a superconductor is expected to be a superposition of states with only Cooper pairs. Furthermore, the pairing term in the Hamiltonian breaks the fermion number conservation symmetry because the pairing term is not invariant under the $U(1)$ transformation $c_{p,\sigma} \rightarrow e^{i\phi} c_{p,\sigma}$ where ϕ is a constant phase. On the other hand, the BCS Hamiltonian is invariant under the fermion parity transformation $c_{p,\sigma} \rightarrow (-1)^{\hat{N}} c_{p,\sigma}$ where \hat{N} is the total number of electrons. This implies that the BCS ground state is a superposition of states with an even number of electrons. Excited states can be easily constructed from the BCS ground state by the repeated application of the Bogoliubov operators $\gamma_{p,\sigma}$.

We conclude this section by discussing the self-consistency condition for the gap function Δ_p . We can obtain the self-consistency condition by substituting the Bogoliubov transformation from Eq. 2.7 into the gap function defined in Eq. 2.5.

After some algebra and using the fact that the Bogoliubov operators follow Fermi-Dirac statistics, we arrive at the following self-consistency condition:

$$\Delta_p = - \sum_{p'} V_{p,p'} \frac{\Delta_{p'}}{2E_{p'}} \tanh\left(\frac{E_{p'}}{2k_B T}\right) \quad (2.12)$$

which can be solved self-consistently to obtain the gap function Δ_p .

2.1.2 Bogoliubov-de Gennes Formalism

BCS theory has been widely successful in predicting many properties of conventional superconductors including phase diagrams, specific heat, critical temperature and critical field, etc. Despite its success, however, it fails to capture the physics of unconventional superconductors with p-wave or d-wave pairing, inhomogeneous systems like junctions and systems with superconducting vortices, and systems that break time-reversal symmetry which happens if the interaction term has spin dependence or an external magnetic field is applied, etc.

In order to resolve these issues, Bogoliubov and de Gennes came up with a simple formalism that allows us to generalize the BCS Hamiltonian seamlessly to more complicated situations. [57] The main innovation introduced by Bogoliubov and de Gennes is to write the Hamiltonian in a basis that puts particles and holes on equal footing. This introduces a redundancy since such a basis is overcomplete. Despite that, this trick leads to a much simpler and more elegant way to treat arbitrary superconducting systems.

To understand the Bogoliubov-de Gennes (BdG) formalism and how it generalizes BCS theory, let us start by rewriting the BCS Hamiltonian in a more general form. Instead of working in momentum space, we work in real space to account for any spatial inhomogeneity. Furthermore, we now assume that the gap function Δ can be any arbitrary complex-valued function of both spatial coordinates and spin (i.e. $\Delta \equiv \Delta_{\sigma\sigma'}(r, r')$). The generalized BCS mean field Hamiltonian can then be written as:

$$H = \sum_{r,r'} \sum_{\sigma,\sigma'} c_{r,\sigma}^\dagger H_{r\sigma,r'\sigma'}^0 c_{r',\sigma'} + \frac{1}{2} \sum_{r,r'} \sum_{\sigma,\sigma'} c_{r,\sigma}^\dagger \Delta_{\sigma\sigma'}(r, r') c_{r',\sigma'}^\dagger + \text{h.c.} \quad (2.13)$$

where $c_{r,\sigma}^{(\dagger)}$ is the annihilation(creation) operator that destroys(creates) an electron with spin σ at position r . The first term $H_{r\sigma,r'\sigma'}^0$ is the normal part of the Hamiltonian which contains the kinetic energy, chemical potential, and any external potential or interaction present in the system. The second term is the pairing term. Note that the gap function is antisymmetric under the exchange of its two arguments (i.e. $\Delta_{\sigma\sigma'}(r, r') = -\Delta_{\sigma'\sigma}(r', r)$) which follows from its definition in

Eq. 2.5 and we have $c_{r,\sigma}^\dagger c_{r',\sigma'}^\dagger = c_{r',\sigma'}^\dagger c_{r,\sigma}^\dagger$ due to the fermionic anticommutation relations. This means that we count each pair twice in our Hamiltonian, once for each ordering of the creation operators $c_{r,\sigma}^\dagger$ and $c_{r',\sigma'}^\dagger$ and hence, we need to divide the pairing term by 2 to avoid double counting.

The central trick of the BdG formalism is to utilize the fermionic anticommutation relations to express products of creation and annihilation operators in the following way:

$$c_{r,\sigma}^\dagger c_{r',\sigma'}^\dagger = \frac{1}{2} c_{r,\sigma}^\dagger c_{r',\sigma'}^\dagger - \frac{1}{2} c_{r',\sigma'}^\dagger c_{r,\sigma}^\dagger \quad (2.14a)$$

$$c_{r,\sigma}^\dagger c_{r',\sigma'} = \frac{1}{2} c_{r,\sigma}^\dagger c_{r',\sigma'} + \frac{1}{2} (\delta_{r,r'} \delta_{\sigma,\sigma'} - c_{r',\sigma'} c_{r,\sigma}^\dagger) \quad (2.14b)$$

substituting these relations into Eq. 2.13 leads to the following Hamiltonian:

$$\begin{aligned} H = & \frac{1}{2} \sum_{r,r'} \sum_{\sigma,\sigma'} c_{r,\sigma}^\dagger H_{r\sigma,r'\sigma'}^0 c_{r',\sigma'} - \frac{1}{2} \sum_{r,r'} \sum_{\sigma,\sigma'} c_{r',\sigma'} H_{r\sigma,r'\sigma'}^0 c_{r,\sigma}^\dagger + \frac{1}{2} \text{Tr}\{H^0\} \\ & + \frac{1}{2} \sum_{r,r'} \sum_{\sigma,\sigma'} \Delta_{\sigma\sigma'}(r, r') c_{r,\sigma}^\dagger c_{r',\sigma'}^\dagger + \frac{1}{2} \sum_{r,r'} \sum_{\sigma,\sigma'} \Delta_{\sigma'\sigma}(r', r) c_{r,\sigma} c_{r',\sigma'} \end{aligned} \quad (2.15)$$

At first glance, we gain nothing by doing this expansion. However, this expansion puts the Hamiltonian in a form where particles and holes are treated on equal footing. This allows us to think of particles and holes as internal degrees of freedom of a single fermionic operator called Nambu spinor.[58] The Nambu spinor is defined as follows:

$$\Psi_r^\dagger = (c_{r,\uparrow}^\dagger, c_{r,\downarrow}^\dagger, c_{r,\uparrow}, c_{r,\downarrow}) \quad (2.16)$$

where the first two components are the particle creation operators and the last two components are the hole annihilation operators. The Nambu spinor allows us to rewrite the Hamiltonian in a more compact form:

$$H = \frac{1}{2} \sum_{r,r'} \Psi_r^\dagger H_{BdG}(r, r') \Psi_{r'} + \frac{1}{2} \text{Tr}\{H^0\} \quad (2.17)$$

where the BdG Hamiltonian $H_{BdG}(r, r')$ is defined as:

$$H_{BdG}(r, r') = \begin{pmatrix} \hat{H}_0(r, r') & \hat{\Delta}(r, r') \\ \hat{\Delta}^\dagger(r', r) & -\hat{H}_0^T(r', r) \end{pmatrix} \quad (2.18)$$

Here, the $\hat{\cdot}$ notation is used to denote 2×2 matrix operators acting on the spin indices. Explicitly, blocks of the BdG Hamiltonian are defined as follows:

$$\hat{H}_0(r, r') = \begin{pmatrix} H_{r\uparrow,r'\uparrow}^0 & H_{r\uparrow,r'\downarrow}^0 \\ H_{r\downarrow,r'\uparrow}^0 & H_{r\downarrow,r'\downarrow}^0 \end{pmatrix} \quad (2.19a)$$

$$\hat{\Delta}(r, r') = \begin{pmatrix} \Delta_{\uparrow\uparrow}(r, r') & \Delta_{\uparrow\downarrow}(r, r') \\ \Delta_{\downarrow\uparrow}(r, r') & \Delta_{\downarrow\downarrow}(r, r') \end{pmatrix} \quad (2.19b)$$

The BdG Hamiltonian is a 4×4 matrix operator acting on the Nambu spinor Ψ_r . We note that the BdG Hamiltonian makes the particle-hole symmetry of the system manifest. This is because the hole-hole and hole-particle blocks of the BdG Hamiltonian are related to the particle-particle and particle-hole blocks by particle-hole symmetry transformation. For example, consider a uniform spin-singlet s-wave superconductors where the gap function is given by $\Delta_{\uparrow\downarrow}(r, r') = -\Delta_{\downarrow\uparrow}(r', r) = \Delta_0$ and $\Delta_{\uparrow\uparrow}(r, r') = \Delta_{\downarrow\downarrow}(r, r') = 0$ and let us assume that the normal part of the Hamiltonian is spin-independent (i.e. $H_{r\sigma, r'\sigma'}^0 = H_{r, r'}^0 \delta_{\sigma, \sigma'}$). In this case, the BdG Hamiltonian takes the following form:

$$H_{BdG}(r, r') = \begin{pmatrix} H_{r, r'}^0 & 0 & 0 & \Delta_0 \\ 0 & H_{r, r'}^0 & -\Delta_0 & 0 \\ 0 & -\Delta_0^* & -H_{r, r'}^0 & 0 \\ \Delta_0^* & 0 & 0 & -H_{r, r'}^0 \end{pmatrix} \quad (2.20)$$

We can define the particle-hole symmetry operator in this case in terms of Pauli matrices in particle-hole and spin spaces as follows:

$$\mathcal{C} = i\tau_y \otimes \sigma_0 \mathcal{K} \quad (2.21)$$

where τ_y is the Pauli matrix in particle-hole space and σ_0 is the identity matrix in spin space and \mathcal{K} is the complex conjugation operator. We can now check that the BdG Hamiltonian satisfies the particle-hole symmetry condition [6]:

$$H_{BdG} = -\mathcal{C} H_{BdG} \mathcal{C}^{-1} \quad (2.22)$$

with $\mathcal{C}^2 = -1$. If instead we have a spin-triplet p-wave superconductor, the particle-hole symmetry operator will be $\mathcal{C} = \tau_x \otimes \sigma_0 \mathcal{K}$ and it will square to +1 (i.e. $\mathcal{C}^2 = +1$).

Eq. (2.22) implies that the spectrum of the BdG Hamiltonian is symmetric around zero. In other words, if E is an eigenvalue of the BdG Hamiltonian H_{BdG} with associated eigenstate $|\psi_E\rangle$, then there exists another eigenstate $|\psi_{-E}\rangle$ with eigenvalue $-E$ satisfying $|\psi_{-E}\rangle = \mathcal{C} |\psi_E\rangle$. This is easy to see by directly applying the BdG Hamiltonian to the eigenstate $|\psi_{-E}\rangle$:

$$H_{BdG} |\psi_{-E}\rangle = -\mathcal{C} H_{BdG} \mathcal{C}^{-1} \mathcal{C} |\psi_E\rangle = -\mathcal{C} H_{BdG} |\psi_E\rangle = -E \mathcal{C} |\psi_E\rangle = -E |\psi_{-E}\rangle \quad (2.23)$$

When dealing with superconductors, we often ignore the constant energy shift term in Eq. 2.17 since the main physics is captured by the BdG Hamiltonian H_{BdG} .

Thus, solving the generalized BCS Hamiltonian in Eq. 2.13 is equivalent to solving the eigenvalue problem of the BdG Hamiltonian in Eq. 2.17:

$$H_{BdG}(r, r')\Psi_{r'} = E\Psi_r \quad (2.24)$$

This gives rise to a set of four coupled differential equations which couples the particle and hole degrees of freedom. In homogeneous conventional systems, Eq. 2.24 can be easily solved by applying a Fourier transform to write the BdG Hamiltonian in momentum space. We follow this by diagonalizing the BdG Hamiltonian in momentum space using the Bogoliubov transformation. The resulting eigenstates and eigenvalues agree with the BCS theory results which we obtained in the previous section. The power of the BdG formalism shines when dealing with inhomogeneous systems like superconducting junctions, vortices, and systems with spin-orbit coupling or in systems with unconventional pairing symmetries like p-wave or d-wave superconductors. In these cases, we can apply the extensive machinery of the theory of linear differential equations and numerical techniques to solve the BdG eigenvalue problem.

2.2 Topological Phases of Matter and Topological Superconductivity

Since the invention of Landau's theory of phase transitions and the development of the theory of critical phenomena, it was widely believed that the governing principle of phase transitions is the symmetry of the system. However, in the 1980s, the discovery of the integer quantum Hall effect [4] and the development of the theory of topological phases of matter by Thouless, Haldane, and Kosterlitz [5, 59] have shattered this belief. We now know that there exist phases of matter -topological phases of matter- that are not characterized by their symmetries and local order parameters but rather by their global topological properties and a global order parameter. In these phases, the system exhibits long-range order and non-local correlations that are robust against local perturbations and disorder. The topological properties of these phases are captured by topological invariants of the bulk Hamiltonian. These invariants are insensitive to local perturbations and disorder as long as the system remains gaped which is guaranteed by discrete symmetries of the system. Moreover, as a result of the bulk-boundary correspondence, these topological invariants are directly related to the existence of robust edge states at the boundary and interfaces of the system.

The subject of topological phases of matter is a vast and rich subject which has undergone a tremendous development in the past few decades. In this section, we will only review the essential concepts and definitions needed to understand the subsequent chapters.

2.2.1 Classification of Topological insulators and Topological Superconductors

After the discovery of the topological origin of the quantum Hall effect, it wasn't still clear whether topology is a unique property of the quantum Hall effect or it is a more general property of condensed matter systems. In 2005, Kane and Mele [60] and Bernevig et al. [61] have shown that topology is a more general property of condensed matter systems. In the last two decades, a large number of topological phases of matter have been discovered including topological insulators, quantum spin Hall insulators, topological superconductors, crystalline topological insulators, Weyl semimetals, and many more. Soon, it became clear that these topological phases of matter can be classified into ten distinct classes based on the discrete symmetries of the system and dimensionality [6]. Before we discuss the classification of topological phases of matter, let us first define the discrete symmetries that are relevant to this classification, mainly time-reversal symmetry (TRS), particle-hole symmetry (PHS), and chiral or sublattice symmetry (CS).

Time-Reversal Symmetry

Time-reversal symmetry transformation is a discrete symmetry transformation which reverse the arrow of time. Classically, this is done by reversing the direction of all velocities and generalized momenta. In quantum mechanics, this is translated into an operator \mathcal{T} which satisfies the following properties:

- \mathcal{T} is anti-unitary: $\mathcal{T}(a|\psi_1\rangle + b|\psi_2\rangle) = a^*\mathcal{T}|\psi_1\rangle + b^*\mathcal{T}|\psi_2\rangle$ where a and b are complex numbers and $|\psi_1\rangle$ and $|\psi_2\rangle$ are arbitrary quantum states.
- $\mathcal{T}^2 = \pm 1$.
- \mathcal{T} is local: \mathcal{T} acts on the wavefunction as $\mathcal{T}|\psi(x)\rangle = U|\psi^*(x)\rangle$ where U is a unitary operator and $|\psi^*(x)\rangle$ is the complex conjugate of the wavefunction $|\psi(x)\rangle$.

The first and third properties imply that the time-reversal operator \mathcal{T} can be expressed as a product of a unitary operator U which acts only on the internal degrees of freedom of the system (e.g. spin) and a complex conjugation operator \mathcal{K} :

$$\mathcal{T} = U\mathcal{K} \quad (2.25)$$

The second property is very important since it determines the behavior of the system. Before we discuss the implications of the second property, let us first define time-reversal symmetric systems. We say that a system is time-reversal symmetric if the Hamiltonian is invariant under the time-reversal transformation:

$$\mathcal{T}HT^{-1} = H \quad (2.26)$$

This implies that the Hamiltonian commutes with the time-reversal operator \mathcal{T} :

$$[H, \mathcal{T}] = 0 \quad (2.27)$$

Note that it is possible to define time-reversal symmetry in the momentum space as well. First, let's see how the time-reversal operator acts on the momentum eigenstates. Recall that the momentum eigenket is defined as $|p\rangle = \int_{-\infty}^{\infty} e^{ipx} |x\rangle dx$ where $|x\rangle$ is the position eigenket. It follows that due to the anti-unitary nature of the time-reversal operator, the time-reversal operator acts on the momentum eigenstates as follows:

$$\mathcal{T}|p\rangle = \int_{-\infty}^{\infty} e^{-ipx} \mathcal{T}|x\rangle dx = |-p\rangle \quad (2.28)$$

where we have used the fact that $\mathcal{T}|x\rangle = |x^*\rangle = |x\rangle$ since the position eigenstates are real. Thus, the time-reversal operator maps momentum eigenstates to their negative momentum eigenstates. This implies that time-reversal symmetry in the momentum space is defined as follows:

$$\mathcal{T}H(p)\mathcal{T}^{-1} = H(-p) \quad (2.29)$$

where $H(p)$ is the Hamiltonian in the momentum space. Now let us return to the second property of the time-reversal operator. It turns out that the second property of the time-reversal operator has very important implications for the spectrum of the system. If $\mathcal{T}^2 = 1$, which is the case for spinless systems, time-reversal symmetry implies that the eigenstates of the Hamiltonian can always be chosen to be real. The second case $\mathcal{T}^2 = -1$ is more interesting and it is satisfied by systems with spin-1/2 particles. In this case, time-reversal symmetry insures that the spectrum of the Hamiltonian is 2-fold degenerate. This is because if $|\psi\rangle$ is an eigenstate of the Hamiltonian with eigenvalue E , then $\mathcal{T}|\psi\rangle$ is also an eigenstate of the Hamiltonian with the same eigenvalue E . To see this, let us apply the Hamiltonian to the time-reversed state:

$$H\mathcal{T}|\psi\rangle = \mathcal{T}H|\psi\rangle = \mathcal{T}E|\psi\rangle = E\mathcal{T}|\psi\rangle \quad (2.30)$$

Next, we can show that the time-reversed state $\mathcal{T}|\psi\rangle$ is orthogonal to the original state $|\psi\rangle$. We can show that by contradiction. Assume that $\mathcal{T}|\psi\rangle$ is not orthogonal to $|\psi\rangle$, then we can write it as $\mathcal{T}|\psi\rangle = e^{i\phi}|\psi\rangle$ for some real phase ϕ . Now, let us apply the time-reversal operator to both sides. applying the time-reversal operator to the left-hand side gives us $\mathcal{T}^2|\psi\rangle = -|\psi\rangle$ since $\mathcal{T}^2 = -1$ for spin-1/2 systems. On the other hand, applying the time-reversal operator to the right-hand side gives us $e^{-i\phi}\mathcal{T}|\psi\rangle = e^{-i\phi}e^{i\phi}|\psi\rangle = |\psi\rangle$. This leads to a contradiction since we have $|\psi\rangle = -|\psi\rangle$ which implies that $|\psi\rangle = 0$. Thus, we conclude that if E is an eigenvalue of the Hamiltonian, then it must have a 2-fold degenerate eigenstate $|\psi\rangle$ and $\mathcal{T}|\psi\rangle$. This is known as Kramers theorem.

Particle-Hole Symmetry

We have already encountered particle-hole symmetry in Sec. 2.1.2 when we discussed the BdG Hamiltonian. We briefly review the definition of particle-hole symmetry here. Particle-hole symmetry is a discrete symmetry transformation that interchanges particles and holes. If we use the Nambu spinor defined in Eq. 2.16, we can define the particle-hole symmetry operator \mathcal{C} as the operator that interchanges the particle and hole degrees of freedom of the Nambu spinor:

$$\mathcal{C} \begin{pmatrix} c_{r,\uparrow} \\ c_{r,\downarrow} \\ c_{r,\uparrow}^\dagger \\ c_{r,\downarrow}^\dagger \end{pmatrix} \mathcal{C}^{-1} = U \begin{pmatrix} c_{r,\uparrow}^\dagger \\ c_{r,\downarrow}^\dagger \\ c_{r,\uparrow} \\ c_{r,\downarrow} \end{pmatrix} \quad (2.31)$$

It follows that the particle-hole symmetry operator \mathcal{C} is anti-unitary and can be expressed as follows:

$$\mathcal{C} = U\mathcal{K} \quad (2.32)$$

where U is a unitary operator that acts on the internal degrees of freedom of the system (e.g. spin) and \mathcal{K} is the complex conjugation operator. The particle-hole symmetry operator is often given by $\mathcal{C} = i\tau_y \otimes \sigma_0 \mathcal{K}$ or $\mathcal{C} = \tau_x \otimes \sigma_0 \mathcal{K}$ where τ_y and τ_x are the Pauli matrices in particle-hole space and σ_0 is the identity matrix in spin space. In general, the particle-hole symmetry operator can square to either the identity operator or minus the identity operator, i.e. $\mathcal{C}^2 = \pm 1$. Finally, we say that a system is particle-hole symmetric if the Hamiltonian satisfies:

$$\mathcal{C}H\mathcal{C}^{-1} = -H \quad (2.33)$$

or equivalently in momentum space:

$$\mathcal{C}H(p)\mathcal{C}^{-1} = -H(-p) \quad (2.34)$$

As we have seen in Sec. 2.1.2, the BdG Hamiltonian automatically satisfies the particle-hole symmetry condition. Particle-hole symmetry makes the spectrum of the Hamiltonian symmetric around zero as we have discussed in Sec. 2.1.2.

Chiral or Sublattice Symmetry

The final important discrete symmetry that we will discuss is chiral or sublattice symmetry. Unlike time-reversal and particle-hole symmetries, chiral symmetry is not an anti-unitary symmetry. Instead, it is described by a unitary operator Γ . Due to the CPT theorem, chiral operator is not independent and it can be derived

from the combination of time-reversal and particle-hole operators. It is defined as follows:

$$\Gamma = \mathcal{T}\mathcal{C} \quad (2.35)$$

It is easy to see that the chiral operator satisfies the following properties:

- $\Gamma^2 = 1$.
- Γ is unitary: $\Gamma^\dagger = \Gamma^{-1}$.
- Γ is Hermitian: $\Gamma^\dagger = \Gamma$.

We say that a system has chiral symmetry if the Hamiltonian anticommutes with the chiral operator Γ :

$$\{\Gamma, H\} = 0 \quad (2.36)$$

or equivalently in momentum space:

$$\{\Gamma, H(p)\} = 0 \quad (2.37)$$

Chiral symmetry has a similar effect on the spectrum of the Hamiltonian as particle-hole symmetry. If a system is chiral symmetric, then the spectrum of the Hamiltonian is symmetric around zero. This is because if E is an eigenvalue of the Hamiltonian with associated eigenstate $|\psi_E\rangle$, then there exists another eigenstate $|\psi_{-E}\rangle$ with eigenvalue $-E$ satisfying $|\psi_{-E}\rangle = \Gamma |\psi_E\rangle$. As we will see later, chiral symmetry plays a central role in this thesis since it is a necessary condition for the existence of Majorana zero modes in topological superconductors and the anomalous proximity effect in dirty metal/superconductor junctions which we will discuss in detail.

Having defined the discrete symmetries that are relevant to the classification of topological phases of matter, we can now discuss the classification itself. We saw that for both time-reversal and particle-hole symmetries, the system can either be not invariant under the symmetry which we denote by 0, or it can be invariant under the symmetry with the symmetry operator squaring to ± 1 . This gives us three possible cases for each symmetry. In addition, we can have chiral symmetry which is either present or absent which gives us two more cases. A system can have any combination of these symmetries or none at all. Naive counting gives us $3 \times 3 \times 2 = 18$ cases. However, since the chiral symmetry is not present when the system has only time-reversal symmetry or only particle-hole symmetry, we need to remove these cases. This gives us a total of 10 distinct classes of topological phases of matter which are summarized in Table 2.1. These classes are known as the ten-fold Altland-Zirnbauer classification scheme. This classification scheme was developed independent of the theory of topological phases of matter. However, it turned out that topological phases of matter can be classified according to this

Class	Time-Reversal Symmetry	Particle-Hole Symmetry	Chiral Symmetry
A	0	0	0
AI	+1	0	0
AII	-1	0	0
AIII	0	0	+1
BDI	+1	+1	+1
C	0	-1	0
CI	+1	-1	+1
CII	-1	-1	+1
D	0	+1	0
DIII	-1	+1	+1

Table 2.1: The ten distinct classes of topological phases of matter based on the presence or absence of time-reversal, particle-hole, and chiral symmetries. The symbols +1, -1, and 0 denote the presence of the symmetry with the symmetry operator squaring to +1, the presence of the symmetry with the symmetry operator squaring to -1, and the absence of the symmetry, respectively.

scheme. Kitaev, Ryu, and others have shown that the classification of topological insulators and topological superconductors depends on the symmetry class of the system as well as its dimensionality [6]. Thus, the so-called periodic table of topological insulators and superconductors was born. We show the periodic table in Table 2.2. The periodic table shows the topological invariants of the ten classes of topological insulators and superconductors in different dimensions. A \mathbb{Z} entry in the periodic table indicates that the system has a topological invariant that can take any integer value. A \mathbb{Z}_2 entry indicates that the topological invariant can take only two values, 0 or 1. Similarly, a $2\mathbb{Z}$ entry indicates that the topological invariant can take any even integer value. Finally, a blank entry indicates that the system does not have a topological invariant in that dimension.

2.2.2 Chiral Symmetric Superconductivity in one Dimension

In this subsection, we review the basic properties of chiral superconductors and their topological invariants. As we have seen earlier, symmetry plays an important role in determining the topological classification of physical systems. Of particular interest to us is the chiral symmetry and chiral superconductors. Superconductors have particle-hole symmetry by definition and hence, in order to have chiral symmetric superconductors, we require that time-reversal symmetry to be preserved. This restricts the symmetry classes of chiral superconductors to either BDI, CI,

class	d=0	1	2	3
A	\mathbb{Z}		\mathbb{Z}	
AI	\mathbb{Z}			
AII	$2\mathbb{Z}$		\mathbb{Z}_2	\mathbb{Z}_2
AIII		\mathbb{Z}		\mathbb{Z}
BDI	\mathbb{Z}_2	\mathbb{Z}		
C			$2\mathbb{Z}$	
CI				$2\mathbb{Z}$
CII		$2\mathbb{Z}$		\mathbb{Z}_2
D	\mathbb{Z}_2	\mathbb{Z}_2	\mathbb{Z}	
DIII		\mathbb{Z}_2	\mathbb{Z}_2	\mathbb{Z}

Table 2.2: The periodic table of topological insulators and superconductors. The entries in the table indicate the topological invariants of the ten classes of topological insulators and superconductors in different dimensions.

CII, or DIII classes. Note that the time-reversal operator need not correspond to the physical time-reversal operator. Thus, even if the physical time-reversal symmetry is broken, in some situations, we can find an anti-unitary operator \mathcal{T}' which commutes with the Hamiltonian and squares to ± 1 . We call \mathcal{T}' an effective time-reversal operator. In that case, we can still classify the system as a chiral superconductor with chiral symmetry operator $\Gamma = \mathcal{T}'\mathcal{C}$. This situation is often encountered when doing dimensional reduction from 2d systems to 1d systems. In this case, the effective time-reversal operator often turns out to be a simple complex conjugation operator.

We are interested in characterizing the implications of chiral symmetry on the energy spectrum, edge states, topological invariants, and the bulk-boundary correspondence of chiral superconductors in one dimension. For this purpose, only the chiral symmetry is sufficient and thus the following discussion applies also to topological insulators in class AIII. We only require that the Hamiltonian of the system is gaped and has chiral symmetry 2.36.

We begin our discussion by focusing on the system's bulk. To this end, we work in momentum space and consider a $2N \times 2N$ chiral symmetric Hamiltonian $H(p)$ with chiral symmetry operator Γ . Here N represents the number of internal degrees of freedom of the system (e.g. spin, valley, band, particle-hole, etc.). Since the chiral operator anti-commutes with the Hamiltonian, we see that if $|\psi_{E(p)}\rangle$ is an eigenstate of the Hamiltonian with eigenvalue $E(p)$, then $|\psi_{-E(p)}\rangle = \Gamma |\psi_{E(p)}\rangle$ is also an eigenstate of the Hamiltonian with eigenvalue $-E(p)$:

$$H(p)\Gamma |\psi_E\rangle = -\Gamma H(p) |\psi_E\rangle = -E\Gamma |\psi_E\rangle \quad (2.38)$$

Similarly, if $|\gamma\rangle$ is an eigenstate of the chiral operator Γ with eigenvalue γ , then

$|-\gamma\rangle = H(p)|\gamma\rangle$ is also an eigenstate of the chiral operator with eigenvalue $-\gamma$:

$$\Gamma H(p)|\gamma\rangle = -H(p)\Gamma|\gamma\rangle = -\gamma H(p)|\gamma\rangle \quad (2.39)$$

Since the chiral operator is Hermitian and squares to the identity operator, it follows that the eigenvalues of the chiral operator Γ are either $+1$ or -1 . Furthermore, the chiral operator Γ has to be traceless:

$$\text{Tr}_p(\Gamma) \propto \int_{-\pi}^{\pi} \langle \psi_{E(p)} | \Gamma | \psi_{E(p)} \rangle dp = \sum_{E(p)=0} \langle \psi_{E(p)} | \Gamma | \psi_{E(p)} \rangle = 0 \quad (2.40)$$

where in the last step, we used our assumption that the bulk Hamiltonian is gapped and hence, we don't have any zero energy states in the bulk. This implies that the number of eigenstates with eigenvalue $+1$ is equal to the number of eigenstates with eigenvalue -1 . Thus, in the chiral basis, we can define the chiral operator as follows:

$$\Gamma = \begin{pmatrix} \mathbb{1}_N & 0 \\ 0 & -\mathbb{1}_N \end{pmatrix} \quad (2.41)$$

where $\mathbb{1}_N$ is the $N \times N$ identity matrix. In this basis, Eq. 2.39 implies that the Hamiltonian takes an off-diagonal form:

$$H(p) = \begin{pmatrix} 0 & q(p) \\ q^\dagger(p) & 0 \end{pmatrix} \quad (2.42)$$

where $q(p)$ is a $N \times N$ complex-valued matrix. Since the Hamiltonian is gaped, it follows that $\det\{H(p)\} = \det\{q(p)\}\det\{q^\dagger(p)\} = |\det\{q(p)\}|^2 \neq 0$ for all p . This implies that the matrix $q(p)$ has to be non-singular and invertible for all p .

Topological Invariant: Winding number

The block off-diagonal form of the Hamiltonian in Eq. 2.42 allows us to define a topological invariant known as the winding number. We can think of $q(p)$ as a map from the first Brillouin zone $\mathbb{T}^1 = [-\pi, \pi]$ to the space of $N \times N$ complex-valued invertible matrices $\text{GL}(N, \mathbb{C})$. Its determinant $\det\{q(p)\} > 0$ is a complex-valued function that maps the first Brillouin zone to the complex plane. Due to the periodicity of the first Brillouin zone, the complex phase of the determinant will wind around the origin of the complex plane as we go around the first Brillouin zone. We can count the number of full windings as follows: We can ask how many times the function $f(p)$ winds around the origin of the complex plane as we go around the first Brillouin zone. This is known as the winding number and it is defined as follows:

$$W = \frac{1}{2\pi i} \int_{-\pi}^{\pi} \frac{d}{dp} \log(\det\{q(p)\}) dp = \frac{1}{2\pi i} \int_{-\pi}^{\pi} \text{Tr} \left\{ q^{-1}(p) \frac{dq(p)}{dp} \right\} dp \quad (2.43)$$

W is fittingly called the winding number. We know from complex analysis that the winding number is independent of the magnitude of the determinant and only depends on the winding of the determinant, we can see that it is an invariant under deformation of the Hamiltonian as long as the Hamiltonian remains gaped so that the determinant of $q(p)$ never crosses zero. Furthermore, since $\det\{q(p)\}$ is a single-valued function and the integration is done on a torus $\mathbb{T}^1 = [-\pi, \pi]$, the winding number can only take integer values. Thus, the winding number serves as a topological invariant of the system. We note that Eq. 2.43 can be rewritten in terms of the Hamiltonian $H(p)$ and the chiral operator Γ as follows:

$$W = \frac{1}{2\pi i} \int_{-\pi}^{\pi} \text{Tr} \left\{ \Gamma H^{-1}(p) \frac{dH(p)}{dp} \right\} dp \quad (2.44)$$

This form of the winding number is useful when we want to compute the winding number numerically.

Edge States and Bulk-Boundary Correspondence

Having introduced the topological invariant for bulk systems, we now focus on what happens when an edge is introduced to the system. We consider a chiral symmetric semi-infinite system extending in the positive x direction and let us assume that the boundary exists at $x = 0$. Away from the boundary, the system can be thought of as a bulk system since the space translation symmetry is weakly broken. Thus, we can define a winding number W . Now, let us consider the case when the system is topologically non-trivial with $W \neq 0$. Since the vacuum at $x < 0$ is a trivial insulator with $W = 0$, we see that $x = 0$ acts as a domain wall separating two topologically distinct phases.

It is interesting to understand what happens at the boundary from a topology perspective. For that, we define a winding number for the semi-infinite system. Strictly speaking, we cannot define a winding number for the semi-infinite system since momentum is not a good quantum number. Nevertheless, using Wigner transformation¹, we can express the Hamiltonian in the semi-infinite system as a function of the position x and momentum p as $H(x, p)$. We can define position-dependent winding number from $H(x, p)$ as follows:

$$W(x) = \frac{1}{2\pi i} \int_{-\pi}^{\pi} \frac{d}{dp} \log(\det\{q(x, p)\}) dp \quad (2.45)$$

where $q(x, p)$ is the off-diagonal block of the Hamiltonian $H(x, p)$ in the chiral basis. In the limit $x \rightarrow \infty$, we are well inside the bulk of the system and $W(x)$

¹Wigner transformation is a mathematical technique used in system with broken translational symmetry. It is used to define a phase space representation of the Hamiltonian in terms of position and momentum as follows: $H(x, p) = \int_{-\infty}^{\infty} e^{ipr} \langle x + r/2 | H | x - r/2 \rangle dr$.

approaches the bulk winding number W . On the other hand, for $x \rightarrow -\infty$, we are inside the vacuum and $W(x) = 0$. Thus, the winding number has to change value at the boundary $x = 0$. However, note that the winding number is a topological invariant and thus its value cannot change unless $\det\{q(x, p)\}$ crosses zero. This can only happen if the Hamiltonian $H(x, p)$ has a zero energy state at the boundary. Thus, we have shown that the existence of a nonzero winding number in the bulk necessarily implies the existence of a zero energy state at the boundary. This is known as the bulk-boundary correspondence.

We note that these boundary zero modes are necessarily chiral. By that, we mean that they are eigenstates of the chiral operator Γ . Chiral symmetry restricts the boundary zero modes on the same edge to have the same chirality. We can define a new topological invariant for the semi-infinite system known as the index of the Hamiltonian. The index counts the difference between the number of zero energy states with positive chirality N_+ and the number of zero energy states with negative chirality N_- . We can define the index in terms of the trace of the chiral operator Γ as follows:

$$\begin{aligned} I = \text{Tr}\{\Gamma\} &= \sum_{E_n=0} \langle n|\Gamma|n\rangle + \sum_{E_n \neq 0} \langle n|\Gamma|n\rangle \\ &= \sum_{E_n=0} \langle n|\Gamma|n\rangle = N_+ - N_- \end{aligned} \quad (2.46)$$

The index is clearly an integer and is independent of the details of the Hamiltonian as long as the Hamiltonian is gaped and has chiral symmetry. Since zero modes at the same boundary must share the same chirality, the total number of zero modes at the boundary must be equal to the absolute value of the index. Finally, using the index theorem, we can show that the winding number is equal to the index. Thus, $|W|$ is the number of zero modes at the boundary.

$$|W| = |I| = |N_+ - N_-| \quad (2.47)$$

This is known as the index theorem in mathematics and as the bulk-boundary correspondence in condensed matter physics. We note that for finite system with open boundaries on both ends, it is generally not possible to find zero-energy bound state solution that satisfies both boundary conditions. Thus, the edge modes will not be exactly at zero energy for finite systems. However, in the thermodynamic limit, the edge modes will approach zero energy. Physically, we can think of this finite size effect as follows: the edge modes decay exponentially away from the edge. If the system is shorter than twice the localization length of the edge modes, then the edge modes will have significant overlap and thus, they will hybridize and shift away from zero energy. However, in the thermodynamic limit, the edge modes will be well separated and thus, they will not hybridize and will remain at zero energy.

2.3 Majorana Zero Modes and Topological Superconductivity

Having explained the theory of superconductivity and topological phases of matter, we are now well equipped to understand the central object of this thesis, namely, Majorana fermions. Majorana fermions were initially developed in 1900s by Ettore Majorana as a real valued solution Dirac equation in the context of high energy physics [62]. Initially, Majorana fermions gained a lot of attention in the high energy physics community especially since they served as a candidate description for massless neutrinos due to their charge neutrality. However, after the discovery of neutrino masses, it became clear that they must be treated as regular fermions and the theory of Majorana fermions have started to lose attention in high energy physics. Interestingly, with the discovery of graphene and topological phases of matter, it became apparent that if though Majorana fermions are not fundamental particles of nature, they can still appear as quasiparticle excitations in certain condensed matter systems. In this section, we review the basic properties of Majorana fermions as well as candidate models realizing Majorana fermions based on chiral symmetric superconductors.

2.3.1 Majorana Fermions

As we have pointed out, Majorana fermions in condensed matter appear as quasi-particle excitations of the underlying many body system. They can also be understood as a different equivalent real representation of the fermionic creation and annihilation operators. To see that let us consider an arbitrary set of electron operators c_i^\dagger and c_i for $i \in \mathbb{Z}$ which satisfy the fermionic anticommutation relations:

$$\{c_i, c_j^\dagger\} = \delta_{ij}, \quad \{c_i, c_j\} = \{c_i^\dagger, c_j^\dagger\} = 0 \quad (2.48)$$

In terms of these operators, we can define a different set of Hermitian operators as follows:

$$\gamma_{2i} = c_i + c_i^\dagger, \quad \gamma_{2i-1} = i(c_i - c_i^\dagger) \quad (2.49)$$

The set of these Hermitian operators γ_{2i} and γ_{2i-1} are known as Majorana operators and they give the Majorana representation of fermionic systems. From the fermionic anti commutation relations in Eq. 2.48 and the definition of Majorana operators in Eq. 2.49, it is straightforward to see that Majorana operators satisfy the following algebra:

$$\{\gamma_i, \gamma_j\} = 2\delta_{ij}, \quad \gamma_i^\dagger = \gamma_i, \quad \gamma_i^2 = 1 \quad \forall i, j \in \mathbb{Z} \quad (2.50)$$

This is known as Clifford's algebra and it is the defining property of Majorana fermions. In fact, we take the definition of Majorana fermions to be any fermionic

operator satisfying Clifford's algebra regardless of whether or not it takes the simple form in Eq. 2.49.

Perhaps the most striking property of Majorana fermions is their Hermiticity and self-conjugation. Hermiticity implies that Majorana fermions are their own antiparticles while self-conjugation implies that the act of creating a Majorana fermion is equivalent to annihilating a Majorana fermion. These two properties are what makes Majorana fermions fundamentally different from regular fermions. In fact, these two properties give rise to the so-called non-abelian nature of Majorana fermions. This non-abelian nature implies that a Majorana system must have doubly-degenerate energy levels. Furthermore, under the exchange of two Majorana fermions, the wavefunction of the system rotates in the degenerate energy subspace by a unitary transformation U . Thus, if we have two Majorana fermions γ_1 and γ_2 , then exchanging them changes the wavefunction of the system as follows:

$$\Psi_{1,2} \rightarrow \Psi_{2,1} = U_{1,2}\Psi_{1,2}, \quad U_{1,2}U_{1,2}^\dagger = 1 \quad (2.51)$$

This non-abelian nature becomes particularly important when we consider systems with $2N$ Majorana fermions for $N > 1$. In this case, we see that the order of exchange of Majorana fermions matters since the unitary transformation $U_{i,j}$ is a matrix operator and thus $U_{i,j}U_{k,l} \neq U_{k,l}U_{i,j}$ in general. Kitaev and others have shown that this non-abelian nature of Majorana fermions can be used to perform topological quantum computation [15, 63]. In this thesis, we will not discuss the details of topological quantum computation; however, we refer the reader to the excellent review by Nayak et al. [12] for a more thorough introduction to this subject.

Having discussed the basic properties of Majorana fermions, we now look at physical realizations of Majorana fermions in condensed matter systems. Majorana fermions can appear in a wide range of condensed matter systems including quantum spin liquids, fractional quantum Hall states with $\nu = 5/2$, topological superconductors, superconducting heterostructures, and many more. However, the most prominent and well-studied realization of Majorana fermions is in topological superconductors. Majorana fermions in topological superconductors can come in four different flavors: Chiral Majorana 1d edge mode, Helical Majorana 1d edge mode, Helical Majorana 2d surface mode, and zero-energy 0d Majorana bound states. The first type appears in 2d time-reversal breaking superconductors (D class) and is characterized by a single Majorana mode propagating along the edge of the superconductor. The second type appears in 2d time-reversal invariant superconductors (DIII class) and is characterized by a pair of counter-propagating Majorana modes along the edge of the superconductor. The third type appears in 3d time-reversal invariant superconductors (DIII class) and is characterized by a helical surface state. The fourth type appears as a bound state at the end of

a 1d topological superconductor or at the core of a vortex in a 2d topological superconductor. Alternatively, it can also appear as corner or hinge modes in 2d and 3d higher-order topological superconductors, respectively. In this thesis, we will focus on the fourth type of Majorana fermions, namely, zero-energy Majorana bound states (MBSs) as it appears in topological superconductors and superconducting heterostructures. In the next section, we will construct a simple model of a topological superconductor and show how to obtain Majorana bound states in this model.

2.3.2 Majorana Zero Modes in Topological Superconductors

In this section, we construct a simple model of a 1d topological superconductor and show how MBSs emerge in this model. Instead of stating the Hamiltonian directly, let us try to motivate the Hamiltonian from first principles. Consider the case of a system with two Majorana fermions γ_1 and γ_{2N} for some integer $N \geq 1$. The naming convention will become clear later. To understand the Hilbert space of this system, let us first define a fermionic operator c as a linear combination of the Majorana fermions:

$$c = \frac{1}{2}(\gamma_1 + i\gamma_{2N}) \quad (2.52)$$

In terms of this fermionic operator, we can define two states in our Hilbert space, the vacuum state $|0\rangle$ and the single particle state $|1\rangle$ satisfying:

$$c|0\rangle = 0, \quad c^\dagger|0\rangle = |1\rangle, \quad c|1\rangle = |0\rangle, \quad c^\dagger|1\rangle = 0 \quad (2.53)$$

These two states form a two-dimensional Hilbert space. Assuming that $|1\rangle$ has energy different from the vacuum state $|0\rangle$ given by ϵ and setting the vacuum state energy to zero, it follows that we can write the Hamiltonian of the system as follows:

$$H_2 = \epsilon|1\rangle\langle 1| = \epsilon c^\dagger c = \frac{\epsilon}{2}(1 + i\gamma_1\gamma_{2N}) = \frac{i\epsilon}{2}\gamma_1\gamma_{2N} \quad (2.54)$$

where we have dropped the constant energy shift in the last step. This is the most general form of the Hamiltonian of a system with two Majorana fermions.² Our goal is to find the condition under which the system has Majorana zero mode. This is equivalent to finding the condition under which the Hamiltonian in Eq. 2.54 commutes with either one of the Majorana operators γ_1 or γ_{2N} . It turns out that this is only possible if the energy ϵ is zero. It follows that the Hamiltonian reduces to $H = 0$ and thus Majorana zero modes operators don't appear in the Hamiltonian.

²Note that in general, the Hamiltonian can also contain terms that couple the states $|0\rangle$ and $|1\rangle$ which are proportional to $|0\rangle\langle 1| + |1\rangle\langle 0|$; however, we can always redefine a new set of Majorana fermions such that the Hamiltonian takes the form in Eq. 2.54.

Since γ_1 and γ_{2N} are not coupled to each other, we call them unpaired Majorana fermions. Unfortunately, any arbitrarily weak perturbation to the Hamiltonian in Eq. 2.54 will couple the two Majorana fermions γ_1 and γ_{2N} and thus destroy the Majorana zero modes. We can avoid this by increasing the distance between the two Majorana fermions γ_1 and γ_{2N} . We do this by introducing new Majorana fermions $\gamma_2, \dots, \gamma_{2N-1}$ in between γ_1 and γ_{2N} . Here, we assume that the new Majorana fermions $\gamma_2, \dots, \gamma_{2N-1}$ are paired with each other while γ_1 and γ_{2N} remain unpaired. In this case, we can write the Hamiltonian of the system as follows:

$$H_{2N} = \frac{i\epsilon}{2}\gamma_1\gamma_{2N} + \sum_{i=2}^{2N-1} \frac{i\epsilon_i}{2}\gamma_i\gamma_{i+1} \quad (2.55)$$

where ϵ_i is the coupling strength between the Majorana fermions γ_i and γ_{i+1} . The Hamiltonian in Eq. 2.55 describes a system with $2N$ Majorana fermions. The first and last Majorana fermions γ_1 and γ_{2N} are paired with each other with coupling strength ϵ . Since there is a large distance between the first and last Majorana fermions, we can assume that the coupling strength ϵ is very small. In fact, we can take the limit $\epsilon \rightarrow 0$ to obtain a system with two unpaired Majorana fermions γ_1 and γ_{2N} . For simplicity, we will assume that the coupling strength ϵ_i between the Majorana fermions γ_i and γ_{i+1} for $i = 2, \dots, 2N - 1$ is the same and equal to $2w$ and take the limit $\epsilon \rightarrow 0$. In this case, we can rewrite the Hamiltonian in Eq. 2.55 as follows:

$$H_{unpaired} = iw \sum_{i=2}^{2N-1} \gamma_i\gamma_{i+1} \quad (2.56)$$

The above Hamiltonian doesn't contain any terms containing the first and last Majorana operators and thus, it commutes with both of them. It is also possible to consider a different scenario where the pairing between Majorana fermions is shifted by one Majorana fermion, i.e. γ_1 is paired with γ_2 , γ_3 is paired with γ_4 , and so on. In this case, we can write the Hamiltonian as follows:

$$H_{paired} = i\frac{\mu}{2} \sum_{i=1}^{2N-1} \gamma_i\gamma_{i+1} \quad (2.57)$$

where we have introduced a new parameter μ to denote the coupling strength in this scenario. It is now clear that the system doesn't commute with γ_i for all $i = 1, 2, \dots, 2N$. In fact, we can show that it is impossible to have Majorana zero modes in this case. This is because the Hamiltonian in Eq. 2.57 is an insulator with a unique ground state and an energy gap μ between the ground state and the first excited state. We can see this by rewriting the Hamiltonian in Eq. 2.57

in terms of fermionic operators c_i and c_i^\dagger using Eq. 2.49 as follows:

$$H = i\frac{\mu}{2} \sum_{i=1}^{2N-1} \gamma_i \gamma_{i+1} = \frac{\mu}{2} \sum_{i=1}^N \left(2c_i^\dagger c_i - 1 \right) = \mu \sum_{i=1}^N c_i^\dagger c_i \quad (2.58)$$

where we have dropped the unimportant constant energy shift in the last step. From the above expression, it is clear that the system has unique ground state $|0\rangle$ which is annihilated by all the fermionic operators c_i . A quasiparticle excitation can be created by acting on the ground state with a fermionic operator c_i^\dagger which creates a single particle state $|1_i\rangle$ with energy μ . Thus, there exists a unique ground state and an energy gap μ between the ground state and the first excited state. This is in contrast to the case of unpaired Majorana fermions where the system has two degenerate ground states $|0\rangle$ and $|1\rangle$ defined in Eq. 2.53 with zero energy.

Having introduced these two scenarios, a natural question arises: if the Hamiltonian contains both terms in Eq. 2.56 and Eq. 2.57, can we still have Majorana zero modes? The answer is yes. Let us consider the following Hamiltonian:

$$H = iw \sum_{i=2}^{2N-1} \gamma_i \gamma_{i+1} + i\frac{\mu}{2} \sum_{i=1}^{2N-1} \gamma_i \gamma_{i+1} \quad (2.59)$$

In this case, we can rewrite the Hamiltonian in terms of fermionic operators as follows:

$$H = \mu \sum_{i=1}^N \left(2c_i^\dagger c_i - 1 \right) + w \sum_{i=1}^{N-1} \left(c_i^\dagger c_{i+1} + c_i^\dagger c_{i+1}^\dagger + \text{h.c.} \right) \quad (2.60)$$

where we have dropped the unimportant constant energy shift in the last step. Let us examine this Hamiltonian in more detail. The first term corresponds to onsite interaction term with chemical potential μ . The second term corresponds to the hopping term which couples the fermionic operators c_i and c_{i+1} with hoping strength w . finally, the third term is a p-wave pairing term which pairs fermions on sites i and $i + 1$ with pairing gap function w . This is the Hamiltonian of a 1d p-wave superconductor. Note that since the second and last terms of the Hamiltonian in Eq. 2.60 don't couple the first and last Majorana operators γ_1 and γ_{2N} , it is possible to deform the Hamiltonian in Eq. 2.60 without closing the gap. We consider a deformation such that the pairing gap function becomes Δ . The resulting Hamiltonian is given by:

$$H = \mu \sum_{i=1}^N \left(2c_i^\dagger c_i - 1 \right) + \sum_{i=1}^{N-1} \left(wc_i^\dagger c_{i+1} + \Delta c_i^\dagger c_{i+1}^\dagger + \text{h.c.} \right) \quad (2.61)$$

This is known as the Kitaev model. It is the simplest model of a 1d topological superconductor. In the limit $\mu \rightarrow 0$ and $\Delta \rightarrow w$, the Kitaev model reduces to the Hamiltonian in Eq. 2.56 which has two unpaired Majorana fermions γ_1 and γ_{2N} . Meanwhile, in the limit $\Delta \rightarrow 0$ and $w \rightarrow 0$, the Kitaev model reduces to the Hamiltonian in Eq. 2.57 which has no Majorana zero modes. In the intermediate regime, when all system parameters are finite, we can still have that are exponentially close to zero energy provided that $|\mu| < 2|w|$. In this regime, two Majorana modes Γ_1^0 and Γ_{2N}^0 appear at the ends of the system, satisfying the following condition:

$$[H, \Gamma_i^0] \propto e^{-\frac{N}{\xi}}, \quad i = 1, 2N \quad (2.62)$$

where ξ is the coherence length of the system. Note that in the thermodynamic limit ($N \rightarrow \infty$), the Majorana zero modes Γ_1^0 and Γ_{2N}^0 become exact zero modes and the many-body ground state of the system is two-fold degenerate and satisfy the same condition as in Eq. 2.53 with c now defined as $c = \frac{1}{2}(\Gamma_1^0 + i\Gamma_{2N}^0)$.

Note that the Majorana zero modes Γ_1^0 and Γ_{2N}^0 are protected by the topological nature of the Kitaev model. This is because in the topological phase when they emerge, they appear at the opposite ends of the system and are unpaired. Assume that we apply a local perturbation to the system. In order to lift the degeneracy, we need to couple the two Majorana zero modes. Since the system has an energy gap, the zero modes cannot couple with the rest of the system. Thus, the only way to break the degeneracy is to couple the two Majorana zero modes Γ_1^0 and Γ_{2N}^0 with each other. Such coupling is suppressed exponentially with the system size N . Thus, the Majorana zero modes are robust against local perturbations and are protected by particle-hole symmetry.

When working with topological superconductors such as the Kitaev chain, it is often convenient to work with Bogoliubov-de Gennes (BdG) formalism. The Kitaev chain in the BdG formalism is given by:

$$H = \frac{1}{2} \sum_i^N \psi_i^\dagger (\mu \tau_z) \psi_i + \frac{1}{2} \sum_i^{N-1} \left(\psi_i^\dagger (w \tau_z + i \Delta \tau_y) \psi_{i+1} + \text{h.c.} \right) \quad (2.63)$$

where $\psi_i = (c_i, c_i^\dagger)^T$ is the Nambu spinor, and, $\tau_i (i = x, y, z)$ are Pauli matrices in the particle-hole space. In momentum space, we have:

$$H = \frac{1}{2} \sum_p \psi_p^\dagger H(p) \psi_p \quad (2.64)$$

with

$$H(p) = (\mu + 2w \cos(p)) \tau_z + 2\Delta \sin(p) \tau_y \quad (2.65)$$

The momentum space Hamiltonian $H(p)$ is a 2×2 matrix in the Nambu space and can be easily diagonalized to obtain the energy spectrum of the system. The eigenvalues of the Hamiltonian are given by:

$$E(p) = \pm \sqrt{(2w \cos(p) + \mu)^2 + 4\Delta^2 \sin^2(p)} \quad (2.66)$$

The spectrum is always gapped except at the topological phase transition point $\mu = 2w$ and $\mu = -2w$ where the gap closes for $p = \pi$ and $p = 0$, respectively. We note that the Kitaev chain Hamiltonian $H(p)$ has chiral symmetry given by $\Gamma = \tau_x$. Following the discussion in Sec. 2.2.2, it is possible to define a topological invariant for the bulk Hamiltonian $H(p)$ which counts the number of Majorana zero modes in the system. We have:

$$W = \frac{-1}{4\pi i} \int_{-\pi}^{\pi} dp \operatorname{Tr}\{\Gamma H^{-1}(p) \partial_p H(p)\} \quad (2.67)$$

The winding number can take values 0, 1, or -1 depending on the values of μ and w . The winding number is non-zero only in the topological phase when $|\mu| < 2|w|$. The bulk-boundary correspondence states that this winding number is equal to the number of Majorana zero modes at the ends of the system. We can count the number of Majorana zero modes from the semi-infinite limit of the real-space Kitaev chain Hamiltonian as follows:

$$\begin{aligned} \# \text{ of MZM} &= |Tr\Gamma| = \left| \sum_{E_n=0} \langle n|\Gamma|n\rangle + \sum_{E_n \neq 0} \langle n|\Gamma|n\rangle \right| \\ &= \left| \sum_{E_n=0} \langle n|\Gamma|n\rangle \right| = |N_+ - N_-| \end{aligned} \quad (2.68)$$

where N_+ and N_- are the number of Majorana zero modes with positive and negative chirality, respectively. In the trivial phase, we have $N_+ = N_- = 0$ and thus the number of Majorana zero modes is zero. In the topological phase, either $N_+ = 1$ and $N_- = 0$ or $N_+ = 0$ and $N_- = 1$. Thus, the number of Majorana zero modes is one in the topological phase. The Bulk-boundary correspondence is then given by:

$$|W| = |N_+ - N_-| = \# \text{ of MZM} \quad (2.69)$$

2.3.3 Majorana Zero Modes in Superconducting Heterostructures

We have seen that starting from simple assumptions about the pairing of Majorana fermions, we can construct a simple model of a 1d topological superconductor that hosts Majorana zero modes at its ends. However, such a model is unrealistic

and hard to find in nature. Instead of searching for a material that naturally hosts Majorana fermions, it is more practical to design a heterostructure that mimics the behavior of the Kitaev chain. The most prominent proposal for such a heterostructure is the nanowire model [16–18, 32, 64–67]. Before we discuss the nanowire model, let us motivate each component of the model.

First, let us remind the reader that the main motivation for studying Majorana bound states is their potential application in topological quantum computation. In order to achieve this, we need a platform that is easy to control and manipulate. The most promising platform for this purpose is semiconductor nanowires. They are easy to fabricate and control in experiment. Since semiconductors have low carrier density, it is convenient to define the chemical potential such that it is measured from the bottom of the band:

$$\mu \implies \mu - 2w \quad (2.70)$$

This changes the topological criterion in our Kitaev model such that the topologically non-trivial regime happens when $0 < \mu < 4w$. Note that realistically, the chemical potential will never reach the value $\mu = 4w$ due to low carrier density so it is sufficient to have positive chemical potential to obtain a topological superconductor.

Next, we add superconductivity to the nanowire. This can be achieved by placing the wire in contact with a superconductor. For now, let us assume that the pairing symmetry of the superconductor is p -wave and assume that the induced pairing gap couples electrons with the same spin inside the wire. Note that the induced pairing gap is not necessarily equal to the pairing gap in the superconductor. In fact, it is often much smaller than the pairing gap in the superconductor. Realistically, the induced pairing gap function is much smaller than the kinetic energy of the electrons in the wire. Since we have $\mu \ll w$ and $\Delta \ll w$, we can linearize the Hamiltonian (2.65) for the two spin species in the nanowire as follows:

$$H = \left(\frac{k^2}{2m} - \mu \right) \tau_z \sigma_0 + \Delta k \tau_y \sigma_0 \quad (2.71)$$

where k is the momentum of the electrons in the wire, m is the effective mass of the electrons, σ_0 is the identity matrix in the spin space. Since for each spin species, the Hamiltonian is of the form of the Kitaev model, we see that the system can host two Majorana zero modes at each end of the wire with each Majorana having fixed spin. This doubly degenerate Majorana zero mode structure is in fact a manifestation of Kramer's degeneracy in spinful time-reversal symmetric systems. Note that, however, having even number of Majorana modes on the same edge is not desirable for two reasons. First, any magnetic perturbation to the system will couple the two spinful Majorana modes and thus, remove them from zero

energy. Second, having two Majoranas on the same edge is the same as having one fermion mode fine-tuned to zero energy and hence, we cannot utilize the non-abelian nature of Majorana fermions for topological quantum computation. As we can see, it is crucial that we break the Kramer's degeneracy in order to obtain a single unpaired Majorana zero mode at each edge. The simplest way to do that is by adding magnetic field B to the system.

$$H = \left(\frac{k^2}{2m} - \mu - B\sigma_z \right) \tau_z + \Delta k \tau_y \quad (2.72)$$

We see that the magnetic field serves as a spin-dependent chemical potential. If $|B| > \mu$, we see that one spin species will be trivial since its effective chemical potential is negative while the other spin species will be topological. Thus, we have only one Majorana zero mode at each edge of the wire.

Thus, we showed that for spinful p-wave superconductors, we can recover the Kitaev model by only applying an external magnetic field. Unfortunately, it is very hard to find a material that naturally hosts p-wave superconductivity. Thus, we have to use s-wave pairing in the Hamiltonian:

$$H = \left(\frac{k^2}{2m} - \mu - B\sigma_z \right) \tau_z + \Delta \tau_y \sigma_y \quad (2.73)$$

We now ask if we still retain the topological properties of the Kitaev model. To do that, let's see if we can identify the different topological phases in the Hamiltonian. We know that at $B = 0$, the system is trivial since the Hamiltonian reduces to the conventional s-wave superconductor. The phase can only change if the spectrum of the Hamiltonian closes and reopens at some B . We can find the critical magnetic field B_c where the spectrum closes by computing the Eigenvalues of the Hamiltonian and setting them to zero.

$$E(k) = \pm B \pm \sqrt{\left(\frac{k^2}{2m} - \mu \right)^2 + \Delta^2} \implies B_c^2 = \left(\frac{k^2}{2m} - \mu \right)^2 + \Delta^2 \quad (2.74)$$

This equation implies that for any $B \geq \sqrt{\mu^2 + \Delta^2}$, we can find two momenta $\pm k(B)$ such that the spectrum closes and the system is degenerate. In other words, the system becomes gapless for $B \geq \sqrt{\mu^2 + \Delta^2}$ and we cannot define a topological invariant nor do we have protected zero energy states. In order to make the system topological, we need to open a gap. This is achievable by adding the last and final ingredient to the model, namely, spin-orbit coupling (SOC). Before that, let us understand why SOC is necessary to lift the degeneracy and open a gap. For $B = 0$, the Hamiltonian is invariant under spin-rotation symmetry. Applying finite B along, say, the z -direction reduces the spin-rotation symmetry

to only rotations around the z axis and thus, spin along z is still conserved. As it turned out, the two gap closing points $\pm k(B)$ have opposite spin and thus, they cannot couple to each other. In order to couple them, we need to add a term that allow coupling between two spin species at different momenta. This is exactly what SOC does. In the presence of SOC, the Hamiltonian becomes:

$$H = \left(\frac{k^2}{2m} - \mu - B\sigma_z + \frac{\alpha}{2}k\sigma_y \right) \tau_z + \Delta\tau_y\sigma_y \quad (2.75)$$

where α is the strength of the SOC. The SOC term couples the two gap closing points for any $B > \sqrt{\mu^2 + \Delta^2}$ and thus, it opens a gap. Note that the gap closing at $k = 0$ for $B = \sqrt{\mu^2 + \Delta^2}$ is not lifted by the SOC term.

To summarize, we used a semiconductor nanowire which gives us flexibility in controlling the chemical potential. We proximated the nanowire to a superconductor so that we can induce superconductivity in the wire. The induced superconductivity enforces particle-hole symmetry which is needed to protect the Majorana zero modes. We then applied a magnetic field to break the Kramers degeneracy and obtain a single Majorana zero mode at each edge of the wire. Finally, we added SOC to break spin rotation symmetry and couple the two gap closing points at finite magnetic field. The resulting Hamiltonian is given by Eq. 2.75 and is known as the Rashba nanowire model. It was originally proposed by Lutchyn, et al [18] and Oreg, et al [17] in 2010 and has been extensively studied since then.

Having finally derived the Rashba nanowire model, we can now focus on characterizing its topological properties. As mentioned earlier, the Hamiltonian (2.75) has a gap closing point at $k = 0$ when the magnetic field is equal to the critical magnetic field $B_c = \sqrt{\mu^2 + \Delta^2}$. We also showed that for any $B \neq B_c$, the bulk Hamiltonian is always gaped. Thus, it is possible to define a bulk topological invariant. To do this, identify the topological class of the Hamiltonian and we need to descritize the Hamiltonian such that we can define the Brillouin zone.

The Rashba model is a BdG Hamiltonian and thus, it has a particle-hole symmetry \mathcal{C} . Since the Hamiltonian doesn't contain any term proportional to τ_x , it follows that the particle-hole symmetry operator is given by $\mathcal{C} = \tau_x\mathcal{K}$ which squares to the identity. Note that the magnetic field breaks time-reversal symmetry. However, since the Hamiltonian is real for $\alpha = 0$ and SOC term is purely imaginary and odd function of momentum, it follows that the Hamiltonian has effective time-reversal symmetry $\mathcal{T}' = \mathcal{K}$. Thus, the Rashba model is a chiral superconductor with chiral symmetry $\Gamma = \tau_x$. It is in the BDI class and is characterized by a winding number topological invariant defined in Eq. (2.44).

Next, we need to descritize the Hamiltonian such that we can define the Brillouin zone. This achieved by introducing a lattice constant a and applying the

following substitution:

$$p \rightarrow \sin(pa)/a, \quad p^2 \rightarrow \frac{2}{a^2}(1 - \cos(pa)) \quad \text{with} \quad -\pi/a < p < \pi/a \quad (2.76)$$

This gives us the following descritized Hamiltonian:

$$H = \left(-2w \cos(pa) 2w - \mu - B\sigma_z + \frac{\alpha}{2a} \sin(pa) \sigma_y \right) \tau_z + \Delta \tau_y \sigma_y \quad (2.77)$$

where $w = \frac{1}{2ma^2}$ is the hopping strength. We can now compute the winding number. Unfortunately, we are not aware of a method to analytically compute the winding number, however, it is easy to compute it numerically. We finally have

$$W = \frac{-1}{4\pi i} \int_{-\pi/a}^{\pi/a} dp \operatorname{Tr}\{\Gamma H^{-1}(p) \partial_p H(p)\} = \begin{cases} 0 & \text{if } B < \sqrt{\mu^2 + \Delta^2} \\ 1 & \text{if } B > \sqrt{\mu^2 + \Delta^2} \end{cases} \quad (2.78)$$

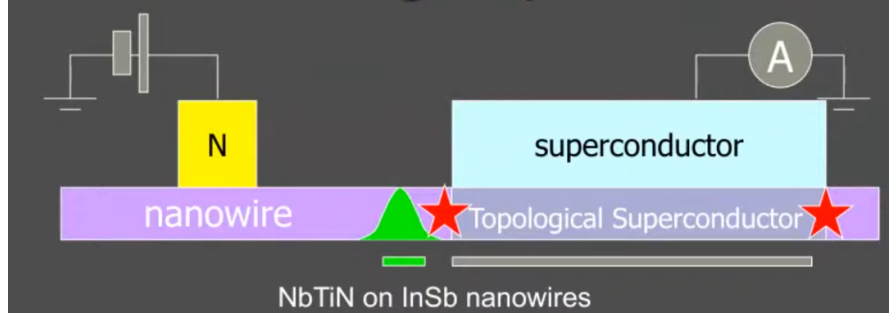


Figure 2.1: Schematic representation of the conductance experiment to detect Majorana bound states in semiconductor nanowires.

2.4 experimental detection of Majorana bound states and pitfalls

Following the theoretical proposal of the Rashba nanowire model by Lutchyn, et al and Oreg, et al, an intense theoretical and experimental effort was devoted to the detection of Majorana bound states in semiconductor nanowires. Different experimental setups were proposed to detect Majorana bound states in semiconductor-superconductor heterostructures including Josephson junctions, phase interferometry, and conductance experiments among others.

The simplest and most widely used experimental setup is the conductance experiment. In this setup, a nanowire with strong Rashba spin-orbit coupling is

placed in partial proximity to a conventional s-wave superconductor. The proximate region will develop a superconducting gap while the unproximate region will remain metallic, thus, realizing a Normal metal/Superconductor (NS) junction. The NS junction is then connected to two metallic leads which are used to measure the conductance of the system. Moreover, gates can also be attached to control the chemical potential. Conductance is measured by applying an external magnetic field and a voltage bias V between the two leads and measuring the current I flowing through the system. A schematic representation of the conductance experiment is given in Fig. 2.1.

By applying an external magnetic field to the system, the system can be tuned to the topological phase where Majorana bound states appear at the ends of the wire. Since a strong magnetic field will destroy superconductivity in the attached superconductor, weak magnetic fields are favorable for the stability of the experiment. Fortunately, the material used for the nanowire can be chosen to have a large g-factor so that weak magnetic fields are sufficient to induce topological transition. Furthermore, it is beneficial to have a large bulk energy gap to enhance topological protection of the Majorana bound states. In order to account for these requirements, researchers have focused on semiconductor nanowires such as InSb and InAs which have large g-factor and strong spin-orbit coupling. Let us now

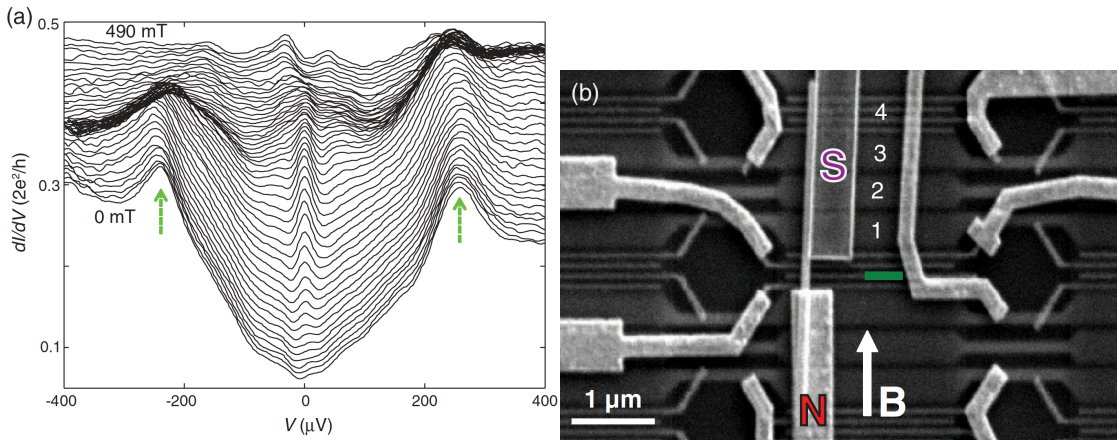


Figure 2.2: (a) Conductance as a function of bias voltage V . Conductance at different magnetic fields B is shifted vertically for clarity. (b) Scanning electron microscope image of the device. Adapted from Mourik et al. [19].

focus on what happens inside the NS junction. the superconductor region has an energy gap Δ below which no excitations can be created. Thus, an incoming electron with energy $E < \Delta$ cannot enter the superconductor region and is reflected back to the normal region as a hole, a process known as Andreev reflection with probability A . Thus result in a current of two units of charge $2e$. Conductance is

then given by scattering theory as $G = \frac{2e^2}{h} A$, where e is the electron charge and h is Planck's constant. The factor of 2 accounts for the charge of the electron and the hole. In the trivial phase, no in-gap states are present and thus, conductance

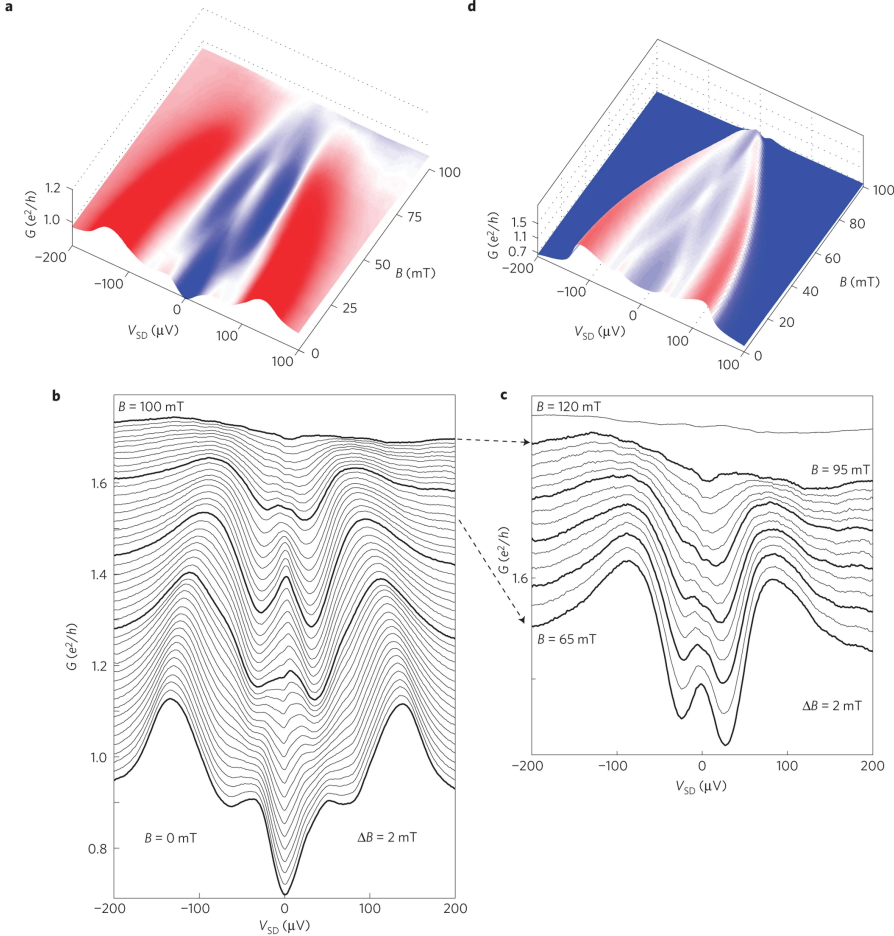


Figure 2.3: (a) Conductance as a function of bias voltage V and magnetic field B . (b,c) line cuts of the conductance at different magnetic fields. (d) theoretical prediction of conductance as a function of bias voltage and magnetic field. Adapted from Das et al. [20].

is suppressed for bias voltages $V < \Delta$ with sharp enhancement at $V = \Delta$. In the topological phase, however, the Majorana bound states appear at zero energy and thus, they contribute to the conductance. In fact, in the absence of bias voltage, resonant Andreev reflection through a zero-energy Majorana state is predicted to lead to a peak in conductance precisely at $G = \frac{2e^2}{h}$. This quantized zero bias conductance peak (ZBCP) was observed in multiple experiments as early as 2012 starting with the influential work by Mourik et al. [19], and by Das et al.[20],

among others. These initial findings generated tremendous excitement, as they seemed to provide strong evidence for Majoranas.

Fig. 2.2 shows the conductance as a function of bias voltage V and applied magnetic field B in the experiment by Mourik et al. [19]. The zero-bias conductance peak is observed between $B = 100$ mT and $B = 400$ mT. Interestingly, the peak is not quantized to the theoretical value of $G = \frac{2e^2}{h}$ but rather, it is around $0.05\frac{2e^2}{h}$. This was later attributed to the presence of disorder in the system and to multiple subbands.

Similar results were obtained by Das et al. [20] as shown in Fig. 2.3. The ZBCP is now observed between $B = 30$ mT and $B = 70$ mT. Despite the ap-

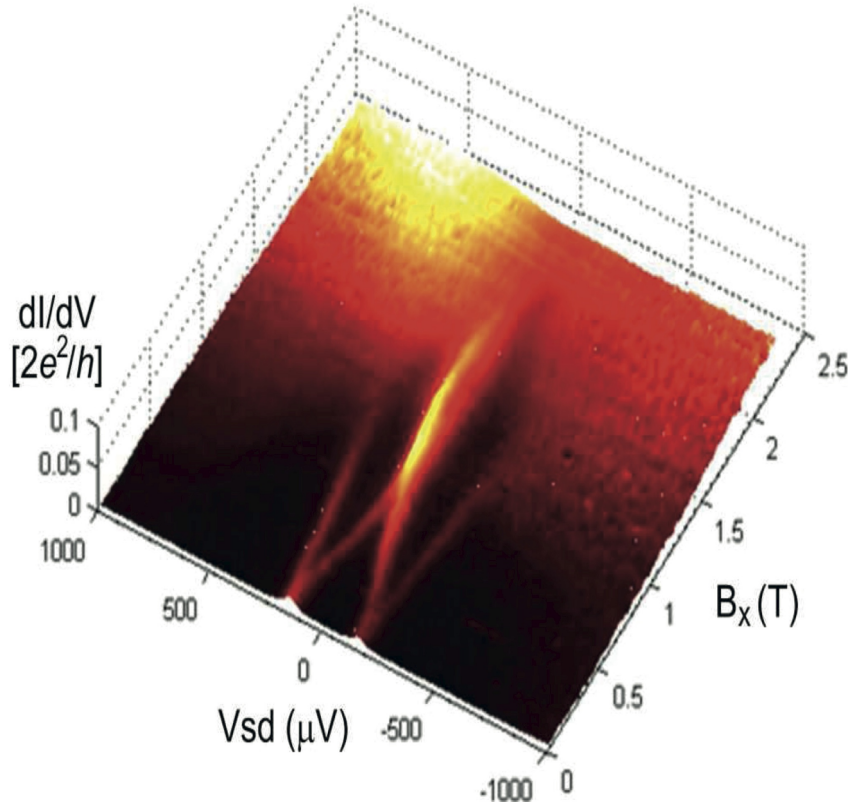


Figure 2.4: Conductance as a function of bias voltage V and magnetic field B in a trivial system without Majorana bound states. Adapted from Lee et al. [68].

parent successes of these experiments, it is important to note that the ZBCP is not a definitive proof of Majorana bound states. In fact, two years after the first experimental observation of ZBCP, an experiment by Lee et al [68] showed that

the ZBCP can be observed in a trivial system without Majorana bound states. In this experiment, the authors considered a situation where a quantum dot forms between the normal metal and the superconductor. Superconductivity is induced in the quantum dot by the proximity effect. At zero or low magnetic fields, the ground state in the quantum dot is the even parity singlet state $|0\rangle + |\uparrow\downarrow\rangle$, where $|0\rangle$ is the empty state and $|\uparrow\downarrow\rangle$ is the doubly occupied state. As magnetic field increases, the ground state changes to the odd parity doublet state $|\uparrow\rangle, |\downarrow\rangle$, where $|\uparrow\rangle$ and $|\downarrow\rangle$ are the singly occupied states. This transition induces an Andreev bound state at zero energy which leads to a ZBCP in the conductance. The ZBCP observed in this experiment is shown in Fig. 2.4. Comparing the ZBCP in this experiment with the one in Fig. 2.3, we see that the ZBCP in the trivial system is very similar to the one in the topological system.

Further studies have shown that the ZBCP can be observed in a variety of topologically trivial systems without Majorana bound states due to the presence of zero-energy or near zero-energy Andreev bound states [21–27]. There are multiple mechanisms that can lead to the formation of Andreev bound states. As we have seen earlier, the presence of a quantum dot coupled to a superconductor can host Andreev bound states which can be fine-tuned to zero energy. Another example is disorder. A strong elastic scattering can lead to Anderson localization which can trap electrons at zero energy and lead to the formation of Andreev bound states. Of particular interest to us is Andreev bound states appearing due to confinement in normal region.

As explored in detail in Chapter 3 of this thesis, even in clean semiconductor-superconductor junctions, the combined effects of Rashba spin-orbit coupling, an external Zeeman field, and spatial confinement can lead to the formation of robust zero-energy ABSs. These can emerge in parameter regimes that are topologically trivial for the bulk superconductor as zero-energy or near zero-energy states displaying similar oscillations around zero energy to that of Majorana bound states. Moreover, they closely resemble many properties of true MBSs such as the presence of ZBCP, oscillations of the ZBCP with magnetic field, and many zero-energy signatures. Thus, they pose a significant identification challenge. In chapter 3 and 4, we will develop odd-frequency pairing and anomalous proximity effect as basic diagnostic tools to differentiate between trivial Andreev bound states and Majorana bound states.

2.5 Odd-Frequency Superconductivity and Majorana Zero Modes

We have seen in the last section that Andreev bound states mimic many of the Majorana signatures. One particular reason for that is most experiments focus on the zero-energy signatures and only local probes are considered. It is important that we consider other properties of Majorana bound states that can help us distinguish them from Andreev bound states. One such property is odd-frequency pairing. In this section, we review the basics of symmetry classifications of Cooper pairs. We follow this by establishing the deep connection between the emergent odd-frequency pairing, Majorana fermions, and topology. We end this section by exploring anomalous proximity effect, a direct consequence of odd-frequency pairing, from the view point of topology.

2.5.1 Symmetry classification of superconductivity

In superconductors, Cooper pairs form as a bound state between two electrons. The symmetry classification of Cooper pairing is of vital interest to the research on superconductivity. The symmetry of Cooper pairing imposes non-trivial relationship between the internal degrees of freedom of the two electrons within a Cooper pair. For example, in conventional superconductors, a spin singlet Cooper pairing of electrons necessarily have even-parity wavefunction. On the other hand, a spin-triplet pairing leads to an odd-parity wavefunction. However, this behavior assumes that the pairing forms between electrons located at the same time. If we allow Cooper pairing between electrons at different time coordinates to form, an enlarged symmetry classification emerges. [31, 34]

For the bulk majority of the research on superconductivity, authors assumed that Cooper pairing form between electrons with the same time coordinates, thus, the symmetry under the exchange of the two time coordinates is necessarily even. However, in 1974, Berezinskii realized that if we allow Cooper pairs to form between electrons with non-zero relative time coordinate t , an odd-time Cooper pair amplitude can form. [30]

Let us investigate a full characterization of the possible symmetry classes for Cooper pairing. For that purpose, we consider an arbitrary electronic system. The wavefunction of a Cooper pair is proportional to the electron-electron correlation function:

$$F_{\sigma_1, \sigma_2; \eta_1, \eta_2}(t_1, x_1; t_2, x_2) = \langle \mathcal{T} c_{\sigma_1, \eta_1}^\dagger(t_1, x_1) c_{\sigma_2, \eta_2}^\dagger(t_2, x_2) \rangle \quad (2.79)$$

Here, $c_{\sigma,\eta}^\dagger(t, x)$ is the creation operator of an electron at position x , time t , spin σ , and has other internal degrees of freedom summarized in η . In the context of BdG formalism, the electron-electron correlation function can be obtained from the Green's function of the BdG Hamiltonian by taking the off-diagonal (anomalous) components in Nambu space. Hence, in practice, we often refer to this anomalous Green's function when discussing Cooper pairs. Furthermore, the anomalous Green's function provides us with information about the strength of Cooper pairing between two electrons and their pairing properties. Thus, we can study the symmetry classification of Cooper pairing by studying the anomalous Green's function.

For any fermionic system, Fermi statistics implies that the correlation function 2.79 must satisfy the total anti-symmetry criterion given below.

$$F_{\sigma_2,\sigma_1;\eta_2,\eta_1}(t_2, x_2; t_1, x_1) = -F_{\sigma_1,\sigma_2;\eta_1,\eta_2}(t_1, x_1; t_2, x_2) \quad (2.80)$$

We can break down the anti-symmetry criterion into the combined action of four discrete transformation. spin permutation \mathcal{S} , position permutation \mathcal{P} , time permutation \mathcal{T} , and orbital index permutation \mathcal{O} . The action of each transformation is summarized below:

$$F_{\sigma_1,\sigma_2;\eta_1,\eta_2}(t_1, x_1; t_2, x_2) \xrightarrow[\mathcal{P}]{\text{position permutation}} F_{\sigma_1,\sigma_2;\eta_1,\eta_2}(t_1, x_2; t_2, x_1) \quad (2.81a)$$

$$F_{\sigma_1,\sigma_2;\eta_1,\eta_2}(t_1, x_1; t_2, x_2) \xrightarrow[\mathcal{T}]{\text{time permutation}} F_{\sigma_1,\sigma_2;\eta_1,\eta_2}(t_2, x_1; t_1, x_2) \quad (2.81b)$$

$$F_{\sigma_1,\sigma_2;\eta_1,\eta_2}(t_1, x_1; t_2, x_2) \xrightarrow[\mathcal{S}]{\text{spin permutation}} F_{\sigma_2,\sigma_1;\eta_1,\eta_2}(t_1, x_1; t_2, x_2) \quad (2.81c)$$

$$F_{\sigma_1,\sigma_2;\eta_1,\eta_2}(t_1, x_1; t_2, x_2) \xrightarrow[\mathcal{O}]{\text{orbital index permutation}} F_{\sigma_1,\sigma_2;\eta_2,\eta_1}(t_1, x_1; t_2, x_2) \quad (2.81d)$$

Equation 2.80 implies that the combined action of these four transformations should satisfy

$$\mathcal{S}\mathcal{P}\mathcal{O}\mathcal{T} = -1 \quad (2.82)$$

We note that the Cooper pair correlation can be even or odd under each of the four transformations separately as long as the combined action of the four transformations satisfies equation 2.82. Thus, we can construct a symmetry classification of Cooper pairing based on its behavior under these transformations separately. The symmetry classes are summarized in the table below

	\mathcal{P} $(x_1, x_2) \rightarrow (x_2, x_1)$	\mathcal{T} $(t_1, t_2) \rightarrow (t_2, t_1)$	\mathcal{S} $(\sigma_1, \sigma_2) \rightarrow (\sigma_2, \sigma_1)$	\mathcal{O} $(\eta_1, \eta_2) \rightarrow (\eta_2, \eta_1)$
1	Even	Even	Singlet	Even
2	Even	Even	Triplet	Odd
3	Odd	Even	Singlet	Odd
4	Odd	Even	Triplet	Even
5	Even	Odd	Triplet	Even
6	Even	Odd	Singlet	Odd
7	Odd	Odd	Triplet	Odd
8	Odd	Odd	Singlet	Even

Table 2.3: All possible pairing symmetries in multi-orbital superconductors allowed by Fermi statistics

2.5.2 Nambu Green's function method

We now review how we can obtain $F_{\sigma_1, \sigma_2; \eta_1, \eta_2}(t_1, x_1; t_2, x_2)$ in practice. Consider a BdG Hamiltonian H . In its most general form, the Hamiltonian is a matrix with spatial, spin, and orbital degrees of Freedom. $H = \sum \Psi_{i, \sigma, \eta}^\dagger H_{i, \sigma, \eta; j, \sigma', \eta'} \Psi_{j, \sigma', \eta'}$ where $\Psi_{i, \sigma, \eta}^\dagger = (c_{i, \sigma, \eta}^\dagger, c_{i, \sigma, \eta})$ is Nambu spinor. We can now define the Nambu Green's function $\mathcal{G}_{\sigma, \sigma'; \eta, \eta'}(t, x; t', x')$ as follows:

$$\sum (i\partial_t - H_{x, \sigma, \eta; x', \sigma', \eta'}) \mathcal{G}_{\sigma, \sigma'; \eta, \eta'}(t, x; t', x') = i\delta(t - t')\delta(x - x')\delta_{\sigma\sigma'}\delta_{\eta\eta'} \quad (2.83)$$

Depending on the boundary condition for the time coordinates, one can obtain the retarded, advanced, or Matsubara Green's function. It is convenient to solve the above equation in frequency domain. We can see that the Nambu Green's function in the frequency domain is

$$\mathcal{G}_{\sigma, \sigma'; \eta, \eta'}(z; x, x') = (z - H)_{x, \sigma, \eta; x', \sigma', \eta'}^{-1} \quad (2.84)$$

where $z = \omega + \epsilon, \omega - \epsilon, i\omega$ for the retarded, advanced, and Matsubara Green's function respectively, ω is the frequency, and ϵ indicates a positive infinitesimal number.

The Nambu Green's function is a 2×2 block matrix in particle-hole space. Thus, it can be further decomposed in terms of the normal particle-particle and anomalous particle-hole components as follows:

$$\mathcal{G}_{\sigma, \sigma'; \eta, \eta'}(z; x, x') = \begin{pmatrix} G_{\sigma, \sigma'; \eta, \eta'}(z; x, x') & F_{\sigma, \sigma'; \eta, \eta'}(z; x, x') \\ \bar{F}_{\sigma, \sigma'; \eta, \eta'}(z; x, x') & \bar{G}_{\sigma, \sigma'; \eta, \eta'}(z; x, x') \end{pmatrix} \quad (2.85)$$

where $G_{\sigma, \sigma'; \eta, \eta'}(z; x, x')$ is the normal Green's function and $F_{\sigma, \sigma'; \eta, \eta'}(z; x, x')$ is the anomalous Green's function. $\bar{G}_{\sigma, \sigma'; \eta, \eta'}(z; x, x')$ and $\bar{F}_{\sigma, \sigma'; \eta, \eta'}(z; x, x')$ are their

particle-hole conjugates. The anomalous component $F_{\sigma,\sigma';\eta,\eta'}(z; x, x')$ defines the Cooper pair amplitude between two electrons with spin σ and σ' , orbital index η and η' , at position x and x' and frequency z . Throughout this thesis, we will refer to the anomalous Green's function as pair amplitude, pair correlation, and anomalous Green's function interchangeably.

Note that the anomalous Green's function can be further decomposed into a summation of different symmetry classes. For the sake of simplicity, let's assume that the system has only one orbital degree of freedom. Then, we can drop the orbital index. Writing the anomalous Green's function as a matrix in spin space, we have:

$$F_{\sigma,\sigma'}(z; x, x') = \begin{pmatrix} F_{\uparrow\uparrow}(z; x, x') & F_{\uparrow\downarrow}(z; x, x') \\ F_{\downarrow\uparrow}(z; x, x') & F_{\downarrow\downarrow}(z; x, x') \end{pmatrix} = \left(d_s(z; x, x') + \vec{d}(z; x, x') \cdot \vec{\sigma} \right) (i\sigma_y) \quad (2.86)$$

where σ_i are the Pauli matrices, $d_s(z; x, x')$ is the singlet component, and $\vec{d}(z; x, x') = (d_x(z; x, x'), d_y(z; x, x'), d_z(z; x, x'))^T$ is the triplet component. The singlet and triplet components are defined as follows:

$$d_s(z; x, x') = \frac{1}{2} (F_{\uparrow\downarrow}(z; x, x') - F_{\downarrow\uparrow}(z; x, x')) \quad (2.87)$$

$$d_x(z; x, x') = \frac{1}{2} (F_{\downarrow\downarrow}(z; x, x') - F_{\uparrow\uparrow}(z; x, x')) \quad (2.88)$$

$$d_y(z; x, x') = \frac{i}{2} (F_{\downarrow\downarrow}(z; x, x') + F_{\uparrow\uparrow}(z; x, x')) \quad (2.89)$$

$$d_z(z; x, x') = \frac{1}{2} (F_{\uparrow\downarrow}(z; x, x') + F_{\downarrow\uparrow}(z; x, x')) \quad (2.90)$$

If we further decompose the anomalous Green's function in terms of the frequency coordinates into even and odd frequency components, the resulting components will have to be either odd or even under the exchange or the spatial coordinates due to the anti-symmetry criterion 2.80. Thus, we can obtain the components corresponding to the different symmetry classes as follows:

- **Even-frequency spin-Singlet Even-parity (ESE):** ESE class has only one component given by:

$$F_{\text{ESE}}(z; x, x') = d_s^E(z; x, x') = \frac{1}{2} (d_s(z; x, x') + d_s(-z; x, x')) \quad (2.91)$$

- **Even-frequency spin-Triplet Odd-parity (ETO):** ETO class has three components corresponding to the three components of the triplet vector

$\vec{d}(z; x, x')$:

$$F_{\text{ETO},x}(z; x, x') = d_x^E(z; x, x') = \frac{1}{2} (d_x(z; x, x') + d_x(-z; x, x')) \quad (2.92)$$

$$F_{\text{ETO},y}(z; x, x') = d_y^E(z; x, x') = \frac{1}{2} (d_y(z; x, x') + d_y(-z; x, x')) \quad (2.93)$$

$$F_{\text{ETO},z}(z; x, x') = d_z^E(z; x, x') = \frac{1}{2} (d_z(z; x, x') + d_z(-z; x, x')) \quad (2.94)$$

- **Odd-frequency spin-Singlet Odd-parity (OSO):** OSO class has only one component given by:

$$F_{\text{OSO}}(z; x, x') = d_s^O(z; x, x') = \frac{1}{2} (d_s(z; x, x') - d_s(-z; x, x')) \quad (2.95)$$

- **Odd-frequency spin-Triplet Even-parity (OTE):** OTE class has three components corresponding to the three components of the triplet vector $\vec{d}(z; x, x')$:

$$F_{\text{OTE},x}(z; x, x') = d_x^O(z; x, x') = \frac{1}{2} (d_x(z; x, x') - d_x(-z; x, x')) \quad (2.96)$$

$$F_{\text{OTE},y}(z; x, x') = d_y^O(z; x, x') = \frac{1}{2} (d_y(z; x, x') - d_y(-z; x, x')) \quad (2.97)$$

$$F_{\text{OTE},z}(z; x, x') = d_z^O(z; x, x') = \frac{1}{2} (d_z(z; x, x') - d_z(-z; x, x')) \quad (2.98)$$

Note that each class can be further decomposed based on the exact spatial symmetry of the system. For example, Even parity classes can have *s*-wave or *d*-wave symmetry, while odd parity classes can have *p*-wave or *f*-wave symmetry. However, in this thesis, we will not focus on the spatial symmetry of the pair amplitude and we will only consider the time symmetry of the pair amplitude.

2.5.3 Generation of odd-frequency pairing in heterostructures

So far, odd-frequency pairing has never been confirmed in bulk. In fact, it was shown that odd-frequency pairing is energetically unstable and thus, unfavorable as the ground state of a bulk superconductivity. However, it is possible to generate odd-frequency pairing if one or more of the bulk symmetries are broken. [31, 34]

Examples:

1. space translation symmetry: In superconducting junctions, parity is not a good quantum number since space translation symmetry is broken. This implies that the anomalous Green's function has even-parity and odd-parity components. For a long chain, space translation is almost a symmetry in the bulk; however, as we get close to the boundary, the effect of spatial translation symmetry breaking is strongest. Thus, we expect that the parity near the boundary/surface of the material is different from that in the bulk. For example, if we start with an even-frequency spin-triplet odd-parity pair potential in the bulk, an odd-frequency spin-triplet even-parity pair amplitude is induced on the interface of superconducting junctions. [69, 70]
2. spin rotation symmetry : In superconductor/ferromagnet junctions, spin rotation symmetry is broken and the anomalous Green's function has spin-triplet and spin-singlet components mixing together, thus, an odd-frequency pairing can be generated. [71, 72]

2.5.4 Odd-frequency pairing and Majorana zero modes

Now that we understand the basics of symmetry classification of Cooper pairs and how odd-frequency pairing can be generated, we can now explore the connection between odd-frequency pairing and Majorana zero modes. A central theme of this thesis is that huge enhancement odd-frequency pairing is a strong signature of Majorana zero modes. Understanding why this is the case is crucial to understanding the rest of this thesis.

Generally speaking, odd-frequency pairing can appear in a variety of systems including topologically trivial systems. In fact, it was shown that trivial Andreev bound states can produce very large odd-frequency pairing amplitudes [73]. However, as we will see shortly, odd-frequency pairing in topological superconductors is fundamentally different from that in trivial systems. There are two key differences between odd-frequency pairing in topological superconductors and in trivial systems. First, odd-frequency pairing in topological superconductors is a direct consequence of Majorana self-conjugation and has a divergent low frequency profile $F_{\text{odd}} \propto \frac{1}{\omega}$, while odd-frequency pairing in trivial systems is strictly linear in frequency $F_{\text{odd}} \propto \omega$. To understand this, let us consider a simple case with a single Majorana operator γ which corresponds to a Majorana mode with zero energy. By definition, this operator satisfies $\gamma = \gamma^\dagger$ (self-conjugation) and $\gamma^2 = 1$. Then, the normal (g) and anomalous (f) Green's function associated with this Majorana operator are given by

$$g(\omega_n) = \langle \gamma^\dagger \gamma \rangle = \langle \gamma \gamma \rangle = f(\omega_n) = \frac{1}{i\omega_n}, \quad (2.99)$$

where ω_n is the Matsubara frequency. This immediately implies that the anomalous propagator is an *odd* function of the frequency ω_n because

$$f(\omega_n) = -f(-\omega_n). \quad (2.100)$$

implying that Majorana zero modes are the simplest states exhibiting pure odd-frequency superconducting pairing [32, 74]. Note that since unpaired Majorana zero modes in spinful systems are necessarily spin-polarized, the associated odd-frequency pairing is spin-triplet. In contrast, in topologically trivial systems, the anomalous Green's function is strictly linear in frequency $F_{\text{odd}} \propto \omega$ close to zero frequency, potentially having large but not divergent odd-frequency pairing amplitudes. This qualitative difference in the low-frequency profile of odd-frequency pairing is a central hypothesis explored in this thesis, mainly in Chapter 3.

The second and perhaps the most important difference is that odd-frequency pairing in chiral symmetric superconductors are related to a generalized topological invariant via the so-called spectral bulk-boundary correspondence (SBBC) [46–48]. To see that, let us consider an arbitrary semi-infinite chiral symmetric superconductor described by a BdG Hamiltonian H with chiral symmetry Γ such that $\Gamma H \Gamma = -H$. Let us define a complex-valued function $F(z)$ using the Nambu Green's function as follows:

$$F(z) = \text{Tr}\{\Gamma \mathcal{G}(z)\} = \text{Tr}\left\{\Gamma \frac{1}{z - H}\right\} \quad (2.101)$$

where z is a complex frequency, $\mathcal{G}(z)$ is the Nambu Green's function, Γ is a chiral operator, and the trace is taken over both the spatial coordinates and internal degrees of freedom. In practice, the spatial summation starts from the boundary of the superconductor and terminates inside the bulk. It is straightforward to show that $F(z)$ is an odd function of z due to the chiral symmetry of the Hamiltonian.

$$\begin{aligned} F(z) &= \text{Tr}\left\{\Gamma \frac{1}{z - H}\right\} = \text{Tr}\left\{\Gamma \frac{1}{z - H} \Gamma^2\right\} = \text{Tr}\left\{\frac{1}{z - \Gamma H \Gamma} \Gamma\right\} \\ &= \text{Tr}\left\{\frac{1}{z + H} \Gamma\right\} = -\text{Tr}\left\{\Gamma \frac{1}{-z - H}\right\} = -F(-z) \end{aligned} \quad (2.102)$$

Furthermore, $F(z)$ can be expressed as a summation of local odd-frequency pairing amplitudes. To see that, let's think about the form of the chiral operator Γ . In superconductors, the chiral operator is necessarily a Pauli matrix in particle-hole space. This is straightforward to see since the chiral operator in superconductors is a product of the particle-hole operator and time-reversal operator. The particle-hole operator must contain a Pauli matrix in particle-hole space, while the time-reversal operator doesn't usually act on the particle-hole space. Thus, without loss

of generality, we can assume that $\Gamma = \tau_x \sigma_i$, where τ_i and σ_i are the Pauli matrices in particle-hole and spin spaces respectively with $i = 0, x, y, z$. Then, we can write the trace as follows

$$\begin{aligned}
F(z) &= \text{Tr}\{\tau_x \sigma_i \mathcal{G}(z)\} = \sum_x \text{Tr}\left\{\tau_x \sigma_i \begin{pmatrix} G_{\sigma,\sigma'}(z; x, x) & F_{\sigma,\sigma'}(z; x, x) \\ \bar{F}_{\sigma,\sigma'}(z; x, x) & \bar{G}_{\sigma,\sigma'}(z; x, x) \end{pmatrix}\right\} \\
&= \sum_x (\text{Tr}\{\sigma_i (F_{\sigma,\sigma'}(z; x, x) + \bar{F}_{\sigma,\sigma'}(z; x, x))\}) \\
&= \sum_x (\text{Tr}\{\sigma_i (F_{\sigma,\sigma'}(z; x, x) - F_{\sigma,\sigma'}(-z; x, x))\}) \\
&= \sum_x \left(\text{Tr}\left\{\sigma_i \vec{d}^O(z; x, x) \cdot \vec{\sigma}(i\sigma_y)\right\} \right) \\
&= \begin{cases} 4i \sum_x \vec{d}_y^O(z; x, x) & \text{if } \sigma_i = \sigma_0 \equiv \mathbb{1} \\ -4 \sum_x \vec{d}_z^O(z; x, x) & \text{if } \sigma_i = \sigma_x \\ 0 & \text{if } \sigma_i = \sigma_y \\ 4 \sum_x \vec{d}_x^O(z; x, x) & \text{if } \sigma_i = \sigma_z \end{cases} \tag{2.103}
\end{aligned}$$

where we used the fact that $\bar{F}_{\sigma,\sigma'}(z; x, x) = -F_{\sigma,\sigma'}(z; x, x)$ due to particle-hole symmetry and that $\text{Tr}\{\sigma_i \sigma_j\} = 2\delta_{ij}$ for $i, j = x, y, z$. Note that we dropped the local singlet component since it is even under the exchange of the time coordinates and thus, does not contribute to the trace. We see that under very general assumptions, $F(z)$ is a summation that only involves OTE components of the anomalous Green's function. Thus, we interpret $F(z)$ as the accumulation of local odd-frequency pairing amplitudes near the boundary of the superconductor. Note that this accumulated odd-frequency pairing amplitude $F(z)$ is actually a generalization of the topological index. Indeed if we consider the limit $z \rightarrow 0$, we obtain the topological index I as follows:

$$\begin{aligned}
\lim_{z \rightarrow 0} zF(z) &= \lim_{z \rightarrow 0} z \text{Tr}\{\Gamma \mathcal{G}(z)\} \\
&= \lim_{z \rightarrow 0} \sum_{E_n=0} \langle n | \Gamma \frac{z}{z - H} | n \rangle + \lim_{z \rightarrow 0} \sum_{E_n \neq 0} \langle n | \Gamma \frac{z}{z - H} | n \rangle \\
&= \sum_{E_n=0} \langle n | \Gamma | n \rangle = N_+ - N_- = I \tag{2.104}
\end{aligned}$$

where N_+ and N_- are the number of zero-energy states with positive and negative chirality respectively. The above equation is exactly the definition of the topological index we saw in Eq. (2.46). Thus, we see that the accumulated odd-frequency pairing $F(z)$ has a pole at $z = 0$ whose residue is equal to the topological index I . Interestingly, $F(z)$ cannot have any other poles in the complex plane due to the

chiral symmetry of the Hamiltonian. This implies that the odd-frequency pairing amplitude $F(z)$ is a meromorphic function with a single pole at $z = 0$.

Now, let us consider the bulk of the superconductor. Away from the boundary, the system is approximately translation invariant and thus, we can consider periodic boundary conditions. Let $h(k)$ be the bulk Hamiltonian in momentum space and let the bulk Green's function be $g(k, z) = (z - h(k))^{-1}$. Then, we can define a generalization of the winding number Eq. (2.44) as follows:

$$W(z) = \frac{i}{4\pi} \int_{-\pi}^{\pi} dk \text{Tr}\{\Gamma g(z, k) \partial_k g^{-1}(z, k)\} = \frac{i}{4\pi} \int_{-\pi}^{\pi} dk \text{Tr}\{\Gamma g(z, k) \partial_k h(k)\} \quad (2.105)$$

It is straightforward to show that the extended winding number $W(z)$ reduces to the winding number of Eq. (2.44) in the limit $z \rightarrow 0$. Note that unlike the winding number W , the extended winding number $W(z)$ is not a topological invariant since it depends on the complex frequency z . Furthermore, for any given z different from zero, the extended winding number $W(z)$ is not quantized and can take any real value. However, it is still a useful quantity to study the topological properties of the system. In particular relevance to this thesis, it was shown that the extended winding number $W(z)$ is related to the accumulated odd-frequency pairing amplitude $F(z)$ via the so-called spectral bulk-boundary correspondence (SBBC) [46–48]. Mainly, we have the following relationship:

$$F(z) = \frac{W(z)}{z} \quad (2.106)$$

This relationship implies that the accumulated odd-frequency pairing amplitude $F(z)$ is in fact topological and is protected by chiral symmetry. In particular, near zero frequency, the accumulated odd-frequency pairing amplitude $F(z)$ has the following form:

$$F(z) = \frac{I}{z} + \chi z + \mathcal{O}(z^3) \quad (2.107)$$

where I is the topological index defined in Eq. (2.46) and χ is a constant that depends on the details of the system. Thus, in the topological regime, odd-frequency pairing is divergent near zero frequency, while in the trivial regime, odd-frequency pairing is strictly linear in frequency with a slope χ . Note that χ can be arbitrarily large in the trivial regime, particularly near a gap closing point. Thus, trivial zero-energy Andreev bound states can have large odd-frequency pairing amplitudes which can be confused with Majorana zero modes. However, since χ is not a topological invariant, it can be tuned by changing the parameters of the system. In contrast, the topological index I is a topological invariant and cannot be changed by tuning the parameters of the system. Thus, we can use the persistence of the divergent odd-frequency pairing amplitude under parameter changes as a

diagnostic tool to distinguish between Majorana zero modes and trivial Andreev bound states.

We note that SBBC is only shown for time-independent chiral symmetric superconductors. As we will see in Chapter 5, a weak version of SBBC can be generalized to time-periodic Floquet chiral symmetric superconductors. A full proof of the Floquet SBBC is still an open problem which we will not address in this thesis. We will, however, use the weak version of SBBC to study the topological properties of Floquet chiral symmetric superconductors in Chapter 5.

2.6 anomalous proximity effect

In the previous section, we saw that odd-frequency pairing is a strong signature of Majorana zero modes. However, it is not always possible to directly probe the odd-frequency pairing amplitude in experiments. Instead, we can only indirectly probe it. Due to the exotic nature of odd-frequency pairing, it can lead to a plethora of exotic phenomena in superconducting heterostructures. One such phenomenon is the anomalous proximity effect. The anomalous proximity effect is a deep subject that has been studied extensively in the literature. Due to the vastness of the subject, we will only review the basics of the anomalous proximity effect in the context of chiral symmetric superconductors and Majorana zero modes.

2.6.1 Proximity Effect in Dirty Metal/Superconductor Junctions

Before we discuss the anomalous proximity effect, let us first review the conventional proximity effect. Generally speaking, the proximity effect is the phenomenon where a superconductor attached to a normal metal can induce superconducting correlations in the normal metal. Effectively, a small section of the normal metal adjacent to the superconductor will behave like a superconductor. However, since these proximity-induced superconducting correlations are not sustained by a superconducting gap, they decay exponentially away from the Normal metal/Superconductor (NS) interface. Interestingly, if we consider a superconductor/normal metal/superconductor (SNS) junction, the proximity effect can lead to a supercurrent across the junction even if the normal metal is not superconducting provided that the normal metal is not too long. It was later clarified that the proximity effect can be explained in terms of the Andreev reflection process [29, 75]. An electron in the normal metal with energy E , momentum k and spin σ incident on the NS interface can be reflected as a hole with energy $-E$, momentum $-k$, and spin $-\sigma$ back into the normal metal. This process can create an Andreev bound state at the NS interface. The proximity effect is understood as the penetration

of interfacial Andreev bound states into the normal metal. Interestingly, the total resistance of the junction is reduced due to the proximity effect. If the normal metal becomes dirty, impurities can scatter the electrons and holes, thus, reducing the Andreev reflection probability. Thus, Andreev bound states can be destroyed by impurities and the proximity effect is suppressed. We note that the fate of the proximity effect and Andreev bound states depends on the pairing symmetry of the superconductor. Generally speaking, Andreev bound states don't generally form at the interface leading to no proximity effect. In other cases, the Andreev bound states are formed but are weak to disorder leading to a conventional proximity effect. Finally, in some cases, the Andreev bound states can be robust against disorder leading to quantized conductance independent of the impurity strength. This is the anomalous proximity effect. To understand these scenarios, Let us

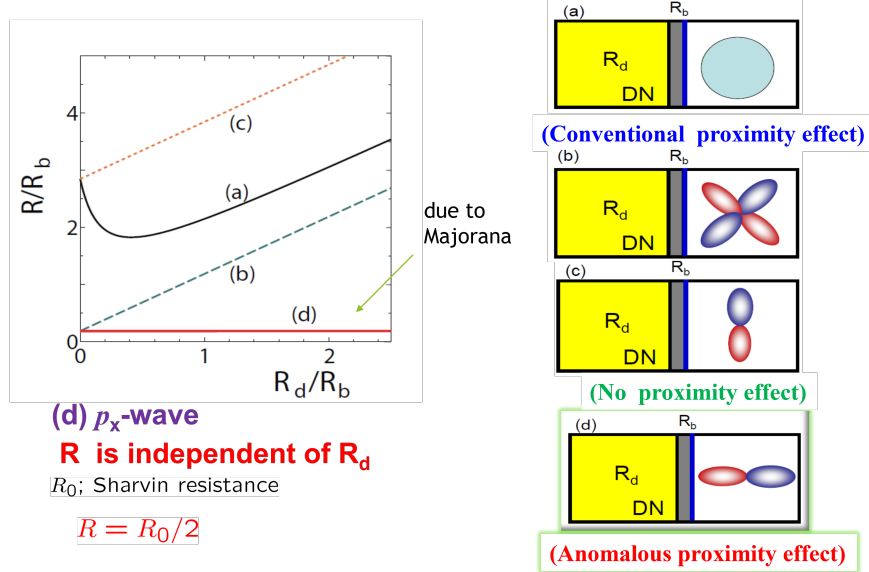


Figure 2.5: Resistance of a dirty metal/superconductor junction as a function of the resistance of the dirty metal for different pairing symmetries of the superconductor. (a) s -wave superconductor, (b) d_{xy} -wave superconductor, (c) p_y -wave superconductor, (d) p_x -wave superconductor.

consider a dirty metal/superconductor junction. Let the resistance of the dirty metal be R_d . We assume that the junction isn't fully transparent and we model this by a barrier with resistance R_b . Classically, the resistance of the NS junction at zero bias voltage is given by:

$$R_{NS}^{\text{classical}} = R_d + R_b \quad (2.108)$$

However, quantum mechanically, the superconductor renormalizes both the normal metal resistance and the barrier resistance to \tilde{R}_d and \tilde{R}_b respectively. Thus, the resistance of the NS junction is given by:

$$R_{NS} = \tilde{R}_d + \tilde{R}_b \quad (2.109)$$

\tilde{R}_d and \tilde{R}_b can be obtained from quasiclassical Green's function theory via the Usadel equation or using recursive Green's function method and Lee-Fisher formula [36, 38–41, 45, 69, 70, 76], however, this is beyond the scope of this thesis. Instead, we will focus on the qualitative behavior of the resistance as a function of the resistance of the dirty metal R_d for different pairing symmetries of the superconductor. The results are summarized in Fig. 2.5.

For an s -wave superconductor, the resistance of the junction initially decreases as the resistance of the dirty metal increases. However, after a certain point, the resistance of the junction increases linearly with the resistance of the dirty metal in agreement with the classical expectation. This is the conventional proximity effect. We can understand this behavior as follows: For small R_d , zero-energy surface Andreev bound states (SABS) are formed at the NS interface. These SABS are initially robust against disorder and thus, the resistance of the junction initially decreases. However, for strong disorder, the SABS are destroyed and we restore the classical limit.

For both d_{xy} -wave and p_y -wave superconductors, no SABS are formed at the NS interface. Thus, the resistance of the junction is linear in R_d and we don't observe any proximity effect.

Finally, for a p_x -wave superconductor, the resistance of the junction is quantized at half of Sharvin resistance and is independent of the resistance of the dirty metal. This is the anomalous proximity effect. Here, Sharvin resistance is defined as follows:

$$R_0 = \frac{\hbar}{2e^2} N_c \quad (2.110)$$

where N_c is the number of propagating channels on the Fermi surface (zero energy). The reason behind this quantization is that the SABS forming at the NS interface are actually Majorana zero modes which are topologically protected against disorder. As we will see next, the anomalous proximity effect is a direct result of chiral symmetry.

2.6.2 Anomalous Proximity Effect from Chiral Symmetry

Anomalous proximity effect can be easily explained in terms of chiral symmetry. Previously, we have only explained 1d chiral symmetric superconductors. However, to fully understand the anomalous proximity effect, we need to work in two

dimensions. Thankfully, since we can always reduce a two-dimensional system to a one-dimensional system by assuming translational invariance in one direction and fixing the momentum in that direction, we can still use the machinery we developed in Sec.2.2.2 to study the anomalous proximity effect.

Let us consider a two-dimensional chiral symmetric superconductor with a BdG Hamiltonian H satisfying the chiral symmetry condition $\Gamma H \Gamma^{-1} = -H$. We assume that the system is translationally invariant in the y direction and semi-infinite in the x direction with boundary located at $x = 0$. Thus, k_y is a good quantum number and we can define a one-dimensional BdG Hamiltonian $H(k_y)$ in the x direction for each fixed k_y . The Hamiltonian $H(k_y)$ still satisfies the chiral symmetry condition $\Gamma H(k_y) \Gamma^{-1} = -H(k_y)$. Thus, we can define a winding number $W(k_y)$ for each fixed k_y as follows:

$$W(k_y) = \frac{i}{4\pi} \int_{-\pi}^{\pi} dk_x \text{Tr}\{\Gamma H^{-1}(k_x, k_y) \partial_{k_x} H(k_x, k_y)\} \quad (2.111)$$

where $H(k_x, k_y)$ is the bulk Hamiltonian of H . The absolute value of the momentum-dependent winding number $|W(k_y)|$ counts the number of zero-energy edge states for each k_y . It is straightforward to see that the total number of zero-energy edge states is given summing over all k_y :

$$N_0 = \sum_{k_y} |W(k_y)| \quad (2.112)$$

where N_0 is the total number of zero-energy edge states.

Now, let us attach a clean normal metal to the edge of the superconductor at $x = 0$. Since the normal metal is clean, it does not break spatial translation symmetry in the y direction. Thus, we can still use the momentum k_y as a good quantum number. We saw that the resistance of the junction is proportional to the number of the propagating channels at zero energy. Thus, we have

$$R_{NS} \propto N_0 = \sum_{k_y} |W(k_y)| \quad (2.113)$$

If we now consider the case where the normal metal is dirty, the momentum k_y is no longer a good quantum number and $\sum_{k_y} |W(k_y)|$ is no longer topologically invariant. However, using chiral symmetry, we can still find out the number of propagating channels at zero energy.

As disorder is introduced, impurities can make the zero-energy edge states couple to each other. This leads to hybridization of the zero-energy states into finite energy states, reducing the number of propagating channels at zero energy. However, chiral symmetry introduces a strong constraint on the hybridization of

the zero-energy states. In particular, chiral symmetry prohibits the hybridization of zero-energy states with the same chirality. Since finite energy states cannot be eigenstates of the chiral operator, see Eq. (2.38). On the other hand, zero-energy states with opposite chirality can hybridize with each other. Thus, the number of propagating channels at zero energy is given by the difference between the number of zero-energy states with positive chirality and the number of zero-energy states with negative chirality. In 2d, this is given by the following topological invariant:

$$I = N_+ - N_- = \sum_{k_y} W(k_y) \quad (2.114)$$

where N_+ and N_- are the number of zero-energy states with positive and negative chirality respectively. Thus, we see that the resistance of dirty metal/superconductor junctions is given by:

$$R_{NS} \propto |I| = \left| \sum_{k_y} W(k_y) \right| \quad (2.115)$$

In one dimension, this is simply the absolute value of the winding number. Thus, we see that the resistance of dirty metal/superconductor junctions is quantized and is independent of the resistance of the dirty metal.

Thus, the anomalous proximity effect can directly probe the topological properties of the superconductor. In fact, this means that unlike popular belief, disorder is beneficial for characterizing and probing the topological properties of chiral symmetric superconductors. However, note that in our analysis, we considered a semi-infinite superconductor. In practice, superconductors in the lab are finite and finite-size effects can affect the resistance of the junction. In particular, we show in Chapter 4 that disorder destroys the anomalous proximity effect in junctions with short superconductors. Furthermore, we explore the length dependence of the anomalous proximity effect in finite length superconductors. Finally, we establish the anomalous proximity effect as a diagnostic tool for Majorana zero modes in finite length systems.

2.7 Floquet Theory

In the theory of linear differential equations, Floquet theorem is a theorem that describes the solutions of a time periodic linear differential equation[77].

Let us consider a very general linear system of differential equations. Assume that we have a linear system of n differential equations of the following form:

$$\partial_t \vec{X}(t) = A(t) \vec{X}(t) \quad \vec{X}(0) = \vec{X}_0 \quad (2.116)$$

where $\vec{X}(t)$ is a vector field and $A(t)$ is a linear $n \times n$ coefficient matrix that depends on time.

The general solution is given in terms of the following time-ordered product

$$\vec{X}(t) = \mathcal{T} \exp\left(\int_0^t A(s)ds\right) \vec{X}_0 \quad (2.117)$$

Generally speaking, there is no closed-form solution to the differential equation; however, Floquet theorem indicates that a closed-form solution can be found provided that the coefficient matrix $A(t)$ is time-periodic.

Theorem

Consider a linear differential equation of the form

$$\partial_t \vec{X}(t) = A(t) \vec{X}(t) \quad (2.118a)$$

and let $A(t+T) = A(t)$ for some non-zero positive T , then, there exist a solution to the differential equation of the following form

$$\vec{X}_\alpha(t) = e^{\epsilon_\alpha t} \vec{Y}_\alpha(t) \quad (2.118b)$$

such that ϵ_α is defined modulo $\frac{2\pi}{T}$ and $\vec{Y}(t)$ satisfies $\vec{Y}(t+T) = \vec{Y}(t)$

2.7.1 Floquet theory in quantum mechanics

Central equation of quantum mechanics is the Schrodinger equation. Since Schrodinger equation is a linear equation in time, we can apply Floquet theorem to quantum systems with time-periodic Hamiltonians. For a reference on Floquet theorem in the context of quantum mechanics, we recommend the following article [78].

Let $H(t)$ be a given Hamiltonian satisfying the following condition.

$$H(t+T) = H(t) \quad (2.119)$$

Consider the associated time-dependent Schrodinger equation

$$i\partial_t |\psi(t)\rangle = H(t) |\psi(t)\rangle \quad |\psi(t_0)\rangle = |\psi_0\rangle \quad (2.120)$$

We can integrate the Schrodinger equation to obtain the general solution

$$|\psi(t)\rangle = \mathcal{T} \exp\left(-i \int_{t_0}^t H(s) ds\right) |\psi(t_0)\rangle = U(t, t_0) |\psi(t_0)\rangle \quad (2.121)$$

However, we need to deal with time-ordering in the above equation. The conventional method to deal with the above expression is by writing the propagator $U(t, t_0)$ in terms of Dyson series and applying Wick theorems to express the time ordered quantities in terms of normal-ordered quantities which are easier to evaluate(cf. chapter 4 in [79]).

The problem with the conventional approach is that it only works for small perturbations and cannot capture topological effects. Floquet theorem provide an alternative formulation for time-periodic Hamiltonians that captures topological properties.

Floquet theorem states that the general solutions to Schrodinger's equation for the time-periodic Hamiltonian are given by

$$|\psi_j(t)\rangle = e^{-i\epsilon_j(t-t_0)} |u_j(t)\rangle \quad (2.122)$$

with $|u_j(t+T)\rangle = |u_j(t)\rangle$, $\epsilon_j \in \left\{ -\frac{\Omega}{2}, \frac{\Omega}{2} \right\}$

where $\Omega = \frac{2\pi}{T}$, the states $|u_j(t)\rangle$ are called Floquet modes, and ϵ_j is called quasienergy. The quasienergy plays the role of crystal momentum in Bloch theorem and it is conserved modulo Ω

Given any initial state $|\psi_0\rangle$, one can expand it in terms of the states $\{|u_j(t_0)\rangle$ since they form a complete orthogonal basis. Let $|\psi_0\rangle$ be given by

$$|\psi_0\rangle = \sum_j C_j |u_j(t_0)\rangle \quad (2.123)$$

It follows that the solution to Schrodinger equation with the boundary condition $|\psi(t)\rangle = |\psi_0\rangle$ is

$$|\psi(t)\rangle = \sum_j C_j e^{-i\epsilon_j(t-t_0)} |u_j(t)\rangle \quad (2.124)$$

Proof of Floquet Theorem:

We now show the proof of Floquet theorem.

Let $H(t+T) = H(t)$. The propagator is given by

$$U(t, t_0) = \mathcal{T} \exp\left\{ -i \int_{t_0}^t H(t') dt' \right\} \quad (2.125)$$

In the language of group theory, the propagator is the time-translation operator and it is an element of $U(1)$ Lie group. Thus, it satisfies the following two properties:

$$U(t_0, t_0) = \mathbb{I} \quad (2.126a)$$

$$U(t', t)U(t, t_0) = U(t', t_0) \quad (2.126b)$$

It also obeys Schrodinger equation

$$i\partial_t U(t, t_0) = H(t)U(t, t_0) \quad (2.126c)$$

From Schrodinger equation, we can show that the following.

$$i\partial_t U(t + nT, t_0 + nT) = H(t + nT)U(t + nT, t_0 + nT) = H(t)U(t + nT, t_0 + nT) \quad (2.127)$$

Where $n \in \mathbb{Z}$. Since the operators $U(t + nT, t_0 + nT)$ and $U(t, t_0)$ satisfy the same equation with the same initial condition, it follows that they are the same operator

$$U(t + nT, t_0 + nT) = U(t, t_0) \quad (2.128)$$

Next, we use the $U(1)$ group properties. We see that for $t \in [t_0, t_0 + T]$, the following property is satisfied

$$U(t + nT, t_0) = U(t + nT, t_0 + nT)U(t_0 + nT, t_0) \quad (2.129)$$

It is easy to show that $U(t_0 + nT, t_0) = [U(t_0 + T, t_0)]^n$. We define the one-period propagator $U_T[t_0]$ as follows that

$$U_T[t_0] = U(t_0 + T, t_0) \quad (2.130)$$

Since $U_T[t_0]$ is unitary, we can diagonalize it. Let $|u_j(t_0)\rangle$ be the eigenvector associated with the eigenvalue $\exp(-iT\epsilon_j)$

$$U_T[t_0] |u_j(t_0)\rangle = \exp(-iT\epsilon_j) |u_j(t_0)\rangle \quad (2.131)$$

Since all eigenvalues of a unitary operators have modulus = 1, it follows that ϵ_j is only defined modulo $\frac{2\pi}{T}$

From the one-period propagator $U_T[t_0]$, it is possible to define a hermitian operator $H_f[t_0]$ by taking the logarithm of $U_T[t_0]$. we define

$$H_f[t_0] = \frac{i}{T} \log(U_T[t_0]) \quad (2.132)$$

$H_f[t_0]$ is known as the Floquet Hamiltonian

Now, let us restrict t to the region $[t_0, t_0 + T]$. In this region, we define the following unitary operator

$$P(t, t_0) = U(t, t_0) \exp(iH_f[t_0](t - t_0)) \quad (2.133)$$

It is easy to show that the above operator satisfies the following properties

$$P(t_0, t_0) = \mathbb{I} \quad (2.134a)$$

$$P(t + T, t_0) = P(t, t_0) \quad (2.134b)$$

This implies that $P(t, t_0)$ is periodic in the first argument.

The propagator can be rewritten in terms of $H_f[t_0]$ and $P(t, t_0)$ as

$$U(t, t_0) = U(t, t_0) \exp(iH_f[t_0](t - t_0)) \exp(-iH_f[t_0](t - t_0)) = P(t, t_0) \exp(-iH_f[t_0](t - t_0)) \quad (2.135)$$

It follows that the solution to Schrodinger equation is

$$|\psi_j(t)\rangle = e^{-i\epsilon_j(t-t_0)} |u_j(t)\rangle$$

with $|u_j(t)\rangle = P(t, t_0) |u_j(t_0)\rangle$, $\epsilon_j \in \left\{ -\frac{\Omega}{2}, \frac{\Omega}{2} \right\}$

where $\Omega = \frac{2\pi}{T}$

2.7.2 Rotating Frame Method

Floquet theory provides two equivalent frameworks to deal with time-periodic quantum systems. These two systems are known as: (1)Rotating Frame Formalism, and (2)Extended Hilbert space formalism. In the next two sections, we will briefly introduce the two formalisms.

In quantum mechanics, it is often convenient to change the frame of reference in order to simplify the calculations. For example, the interaction picture is often employed when dealing with perturbation theory. Now, one can ask the following question: can we find a rotating frame of reference where the time-periodic hamiltonian is static? The answer is yes.

Assume that we know the unitary operator $P(t, t_0)$. It is possible to define a rotating frame using the unitary operator $P(t, t_0)$. First, let us define the solution to Schrodinger equation as $|\psi(t)\rangle = P(t, t_0) |\tilde{\psi}(t)\rangle$. We substitute into Schrodinger equation:

$$i\partial_t \left(P(t, t_0) |\tilde{\psi}\rangle \right) = iP(t, t_0) \left| \partial_t \tilde{\psi}(t) \right\rangle + \left(i\partial_t P(t, t_0) \right) \left| \tilde{\psi}(t) \right\rangle = H(t)P(t, t_0) \left| \tilde{\psi}(t) \right\rangle \quad (2.136)$$

The Schrodinger equation implies that:

$$i\partial_t \left| \tilde{\psi}(t) \right\rangle = \left[P^\dagger(t, t_0)H(t)P(t, t_0) - iP^\dagger(t, t_0)\partial_t P(t, t_0) \right] \left| \tilde{\psi}(t) \right\rangle \quad (2.137)$$

In other words, the state $|\tilde{\psi}(t)\rangle$ satisfies Schrodinger equation For the following hamiltonian:

$$\tilde{H}(t) = P^\dagger(t, t_0)H(t)P(t, t_0) - iP^\dagger(t, t_0)\partial_t P(t, t_0) \quad (2.138)$$

We notice that the hamiltonian $\tilde{H}(t)$ is not related to the original hamiltonian $H(t)$ by a simple unitary transformation. Rather, it contains an additional term. We note that the additional term can be thought of as a gauge transformation. This gauge term is necessary since the unitary transformation $P(t, t_0)$ is local in time.

Now, recall the definition of $P(t, t_0)$

$$P(t, t_0) = U(t, t_0) \exp(iH_f[t_0](t - t_0))$$

By differentiating the above equation, we find that:

$$\begin{aligned} \partial_t P(t, t_0) &= \left(\partial_t U(t, t_0) \right) e^{iH_f[t_0](t-t_0)} + iU(t, t_0) e^{iH_f[t_0](t-t_0)} H_f[t_0] \\ &= -iH(t)P(t, t_0) + iP(t, t_0)H_f[t_0] \end{aligned}$$

Substituting into equation (2.138), we find that

$$\tilde{H}(t) = H_f[t_0] \quad (2.139)$$

This implies that the hamiltonian in the rotating frame is nothing but the Floquet Hamiltonian.

2.7.3 Extended Hilbert Space Formalism

The extended Hilbert space formalism is a different approach to deal with time-periodic systems. The basic idea of the extended Hilbert space formalism stems from a simple observation.

Consider the following operator

$$K(t') = H(t') - i\partial_{t'} \quad (2.140)$$

Let us apply the operator $K(t')$ to the Floquet mode $|u_j(t')\rangle$

$$\begin{aligned} K(t')|u_j(t')\rangle &= \left(H(t') - i\partial_{t'}\right)e^{+i\epsilon_j(t'-t_0)}e^{-i\epsilon_j(t'-t_0)}|u_j(t')\rangle \\ &= e^{+i\epsilon_j(t'-t_0)}\left(H(t') - i\partial_{t'} + \epsilon_j\right)e^{-i\epsilon_j(t'-t_0)}|u_j(t')\rangle \\ &= \epsilon_j|u_j(t')\rangle \end{aligned} \quad (2.141)$$

In the last step, we used the fact that $e^{-i\epsilon_j(t'-t_0)}|u_j(t')\rangle$ satisfy the time-dependent Schrodinger equation for the hamiltonian $H(t')$

From the above equation, we see that the Floquet modes $|u_j(t')\rangle$ are eigenstates of the operator $K(t')$ with eigenvalues ϵ_j

Furthermore, we notice that multiplying by $\varphi_n(t') = e^{-i\Omega nt'}$ gives us the following result:

$$K(t')|u_{jn}(t')\rangle = K(t')\varphi_n(t')|u_j(t')\rangle = (\epsilon_j - \Omega n)\varphi_n(t')|u_j(t')\rangle = \epsilon_{jn}|u_{jn}(t')\rangle \quad (2.142)$$

where we defined $\epsilon_{jn} = \epsilon_j - \Omega n$

Since we can define the eigenvalue equation (2.141) at any $t' \in [t_0, T + t_0]$, it is possible to construct an extended Hilbert space where the operator $K(t')$ is treated as the Hamiltonian. This construction was developed by J. Howland in 1974. We give a summary below.

Let \mathcal{H} be the Hilbert space for the quantum system of interest. We extend the Hilbert space \mathcal{H} to the extended Hilbert space $\mathcal{H}_{ext} = L^2[0, T] \otimes \mathcal{H}$ where $L^2[0, T]$ is the set of all T-periodic normalizable functions. In this extended Hilbert space, we treat the operator $K(t')$ as the Hamiltonian operator.

In the extended Hilbert space, the temporal part is spanned by Fourier vectors $\{\varphi_m(t') = e^{-im\Omega t'}\}_{m \in \mathbb{Z}}$

The inner product is defined as:

$$\langle\langle u(t')|v(t')\rangle\rangle_T = \frac{1}{T} \int_0^T dt' \int_{-\infty}^{\infty} dx u^*(x, t)v(x, t) \quad (2.143)$$

Let $\{\phi_\alpha\}_{\alpha \in \mathbb{Z}}$ be a complete orthonormal basis of the original Hilbert space \mathcal{H} .

Then, any state in the external Hilbert space \mathcal{H}_{ext} is given by

$$\begin{aligned} |u(t')\rangle &= \sum_{\alpha} \sum_{m=-\infty}^{\infty} u_{m,\alpha} \varphi_m(t') |\phi_{\alpha}\rangle \\ &= \sum_{\alpha} C_{\alpha}(t') |\phi_{\alpha}\rangle \quad \text{with} \quad C_{\alpha} = \sum_{m=-\infty}^{\infty} u_{m,\alpha} \varphi_m(t') \\ &= \sum_m \varphi_m(t') |\Phi_m\rangle \quad \text{with} \quad |\Phi_m\rangle = \sum_{\alpha} u_{m,\alpha} |\phi_{\alpha}\rangle \end{aligned}$$

We see that the operator $K(t')$ is naturally defined as a linear operator acting on the extended Hilbert space \mathcal{H}_{ext} .

Let the operator $K(t')$ be the hamiltonian operator in the extended Hilbert space \mathcal{H}_{ext} . The solutions to Schrodinger equation in the extended space \mathcal{H}_{ext} can be easily obtained. They are given by:

$$|\psi_{jn}(t, t')\rangle = e^{-i\epsilon_{jn}t} |u_{jn}(t')\rangle \quad (2.144)$$

We notice that the solutions to the Schrodinger equation in the extended Hilbert space reduce to the solutions for Schrodinger equation in the original Hilbert space \mathcal{H} when $t = t'$

$$|\psi_{jn}(t, t' = t)\rangle = |\psi_j(t)\rangle \quad (2.145)$$

It is often convenient to express the extended Hilbert space Hamiltonian $K(t')$ in terms of its Fourier modes. Consider the eigenvalue problem in the extended Hilbert space:

$$K(t') |u_j(t')\rangle = [H(t') - i\partial_{t'}] |u_j(t')\rangle = \epsilon_j |u_j(t')\rangle \quad (2.146)$$

We can expand the above equation in the Fourier basis $\{\varphi_m(t') = e^{-im\Omega t'}\}_{m \in \mathbb{Z}}$

The eigenstate is given by

$$|u_j(t')\rangle = \sum_m \varphi_m(t') |u_j^m\rangle \quad (2.147)$$

Meanwhile, the extended Hilbert space Hamiltonian becomes

$$K_{mn} = \frac{1}{T} \int_0^T \varphi_m^*(s) K(s) \varphi_n(s) ds = H_{mn} - n\Omega\delta_{mn} \quad (2.148)$$

The eigenvalue equation becomes

$$\sum_n K_{mn} |u_j^n\rangle = \sum_n H_{mn} |u_j^n\rangle - m\Omega |u_j^m\rangle = \epsilon_j |u_j^m\rangle \quad (2.149)$$

To end this chapter, we note that the Hamiltonians $H(t), H_f[t_0], K(t')$ are related to each other non-trivially. We emphasize that $H(t)$ is NOT unitarily equivalent to the effective Hamiltonians $H_f[t_0]$ and $K(t')$. Meanwhile, $H_f[t_0]$ and $K(t')$ are unitarily equivalent.

Proof:

$$\begin{aligned} K(t') &= H(t) \Big|_{t=t'} - i\partial_{t'} \\ &= \sum_j \epsilon_j |u_j(t')\rangle \langle u_j(t')| \\ &= \sum_j \epsilon_j P(t', t_0) |u_j\rangle \langle u_j| P^\dagger(t', t_0) \\ &= P(t', t_0) H_f[t_0] P^\dagger(t', t_0) \end{aligned}$$

2.7.4 Topological Floquet superconductors

Since the discovery of the quantum hall effect, topology has played a central role in condensed matter physics. However, materials that realize non-trivial topological characteristics are scarce in nature. In particular, topological p-wave superconductors are yet to be confirmed in experiment.

Several proposals to engineer topological superconductors were published. Of particular interest to us is the Floquet engineering of topological phases. Kitagawa et. al. proposed that Majorana fermions can be engineered in cold atom experiments using optical traps[80]. In this section, we present a summary

of this proposal, highlighting the elusive Floquet Majorana π modes.

Let us consider a one dimensional chain of fermionic atoms trapped inside a 3D Bose-Einstein condensate(BEC) of molecules. We assume that the atoms have two internal degrees of freedom that we denote by $\sigma = \uparrow$ and $\sigma = \downarrow$. The Hamiltonian is given by

$$H = \sum_{p,\sigma} a_\sigma^\dagger(p)(\epsilon(p) + V)a_\sigma(p) + \sum_p (\Delta a_\uparrow^\dagger(p)a_\downarrow^\dagger(-p) + h.c.) \quad (2.150)$$

Here, $a_\sigma(p)$ is the annihilation operator of an atom with internal degree of freedom σ . The kinetic energy is given by $\epsilon(p) = \frac{p^2}{2m}$. V is the optical trap potential. The atoms can move between the BEC and the optical trap. This movement creates a fictitious s-wave superconducting order characterized by Δ .

Let us shine two laser beams on the trapped atoms with recoil momentum k in the direction of the chain. This will induce a coupling between atoms. Let the coupling strength be B . The Hamiltonian now becomes

$$H \rightarrow H = \sum_{p,\sigma} a_\sigma^\dagger(p)(\epsilon(p) + V)a_\sigma(p) + \sum_p (\Delta a_\uparrow^\dagger(p)a_\downarrow^\dagger(-p) + Ba_\uparrow^\dagger(p+k)a_\downarrow^\dagger(p-k) + h.c.) \quad (2.151)$$

After applying a unitary transformation to the above Hamiltonian, we can show that this system is unitarily equivalent to the Rashba nanowire Hamiltonian[17, 18]. The Rashba nanowire Hamiltonian is given by

$$H = \sum_p \psi^\dagger(p) \left((\epsilon(p) - \mu) \tau_z + \lambda p \sigma_z + B \tau_z \sigma_x + \Delta \tau_y \sigma_y \right) \psi(p) \quad (2.152)$$

where $\psi(p) = (a_\uparrow(p), a_\downarrow(p), a_\uparrow^\dagger(p), a_\downarrow^\dagger(p))^T$ is the Nambu spinor. τ_i, σ_i is the i-th Pauli matrix in the particle-hole and spin space respectively. The chemical potential is given by $\mu = -(V + \frac{k^2}{2m})$ and the Rashba spin-orbit coupling strength is given by $\lambda = k/m$.

By adjusting the optical trap potential or the incident laser beams frequency, it is possible to engineer a time-periodic chemical potential. For example, let us consider the Rashba nanowire Hamiltonian with a time-periodic chemical potential given by

$$\mu(t) = \begin{cases} \mu_1 & nT < t < (n + \frac{1}{2})T \\ \mu_2 & (n + \frac{1}{2})T < t < (n + 1)T \end{cases} \quad n \in \mathbb{Z} \quad (2.153)$$

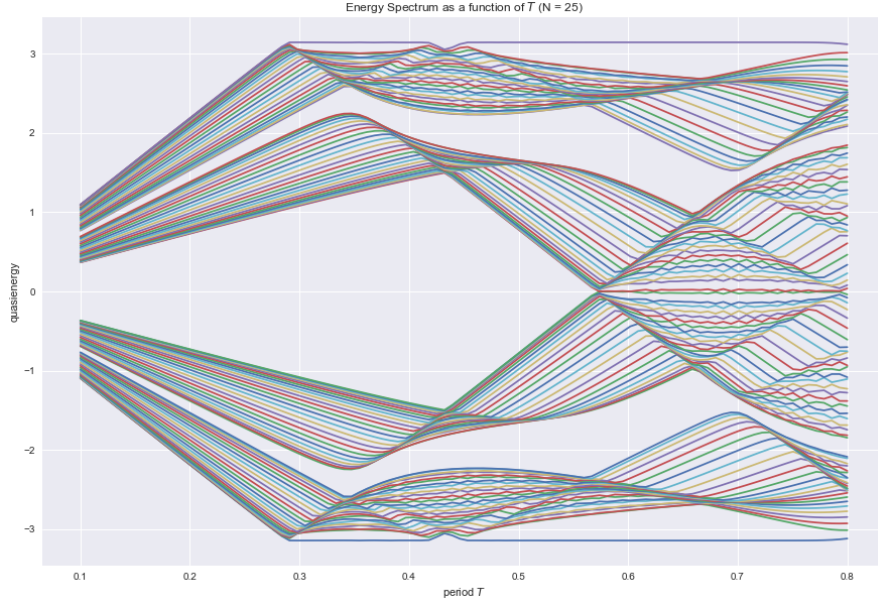


Figure 2.6: Quasienergy spectrum of Rashba nanowire with 25 sites. The parameters are given in terms of the hoping integral w as follows: $B = 2w, \Delta = 4w, \lambda = 2w, \mu_1 = -2w, \mu_2 = -6w$

Kitagawa et. al. studied this system within the Floquet theory. They found that in addition to Majorana zero modes, the system also possesses unique Majorana edge modes at π energy even in the static trivial regime(see figure). By altering the period, the system's topology and the number of Majorana π and zero modes can be tuned.

We emphasize that the Floquet Majorana edge modes are unique to time-periodic systems and are drastically different from the conventional Majorana edge modes in the static case. One obvious difference is that Floquet Majorana edge modes are not restricted to lie at zero energy. This is because time-periodicity of the Hamiltonian implies that the quasienergy spectrum is $\frac{2\pi}{T}$ -periodic. Thus, quasiparticle excitations at energy E and $E + \frac{2\pi}{T}$ correspond to the same state. Meanwhile, particle-hole symmetry implies that for a quasiparticle excitation at energy E , there exist a quasi-hole excitation at energy $-E$. The periodicity of the spectrum and particle-hole symmetry imply that excitations at energy $E = \frac{\pi}{2}$ are their own antiparticles. Thus, Majorana states can be found at energy $E = \frac{\pi}{2}$.

In chapter 5, we will study the Floquet Majorana edge modes in detail. In particular, we investigate the relationship between the Floquet Majorana edge modes and odd-frequency pairing. We also extend the spectral bulk-boundary correspondence to Floquet systems in the presence of both Majorana zero modes

and Floquet Majorana π modes. Finally, we study the robustness of our results against disorder and finite-size effects.

2.8 Conclusion

In this chapter, we introduced the essential theoretical background for understanding the rest of the thesis. We started by introducing the basics of superconductivity and the Bogoliubov-de Gennes formalism. We then introduced the concept of chiral symmetry and its implications for superconductors. In particular, we showed that chiral symmetry leads to the existence of zero-energy edge states in superconductors. We then introduced the central star of this thesis, the Majorana bound states. We explored the properties of Majorana bound states and how to engineer heterostructures that host them. We then introduced mainstream experimental signatures to detect Majorana bound states and the challenges associated with these signatures, mainly Andreev bound states. We then introduced our main topological probe of Majorana bound states, odd-frequency pairing. We showed that odd-frequency pairing induced by Majorana bound states are fundamentally different from the odd-frequency pairing induced by Andreev bound states. We showed that accumulated odd-frequency pairing is directly related to the number of Majorana bound states in the system. We then introduced the anomalous proximity effect and showed that it can be used to probe the topological properties of chiral symmetric superconductors. Finally, we introduced Floquet theory and its applications in engineering topological superconductors. In particular, we introduced the elusive Floquet Majorana π modes.

Chapter 3

Odd-Frequency Pairing in Static Superconductor-Semiconductor Junctions

As we have outlined in the previous chapter, the hunt for Majorana bound states (MBSs) in condensed matter platforms has become a central theme in the field with immense efforts across the globe. Yet, MBS remains elusive. The main obstacle facing scientists today is that the main experimental signature (the zero bias conductance peak) is perfectly replicated by trivial Andreev bound states (ABSs). In this chapter, we introduce odd-frequency pairing as a powerful probe of MBSs in semiconductor-superconductor junctions. Here, we consider two Normal metal/Superconductor (NS) junctions. First, we consider an NS junction with trivial superconductor. In this situation, the junction can only host trivial ABSs. By analyzing the difference between the trivial phases without ABSs and with ABSs, we build an qualitative and quantitative understanding of the ABSs in isolation. Next, we consider an NS junction with topological superconductor. In this situation, the system can host both ABSs and MBSs depending on the value of external Zeeman field. By systematically analyzing the emergent pairing correlations, their symmetry and frequency and spatial dependence, we establish odd-frequency pairing amplitude as an unambiguous probe of MBSs. Mainly, we show that while both ABSs and MBSs share similar characteristics, the odd-frequency pairing generated by them has distinct low frequency profiles with MBSs having divergent ($\sim 1/\omega$) in junctions with long superconducting region. This is in contrast to the trivial helical phase whose odd-frequency pair amplitude has linear dependence albeit with large values near zero frequency and is independent of the superconducting segment length. This chapter is based on the work published in [1].

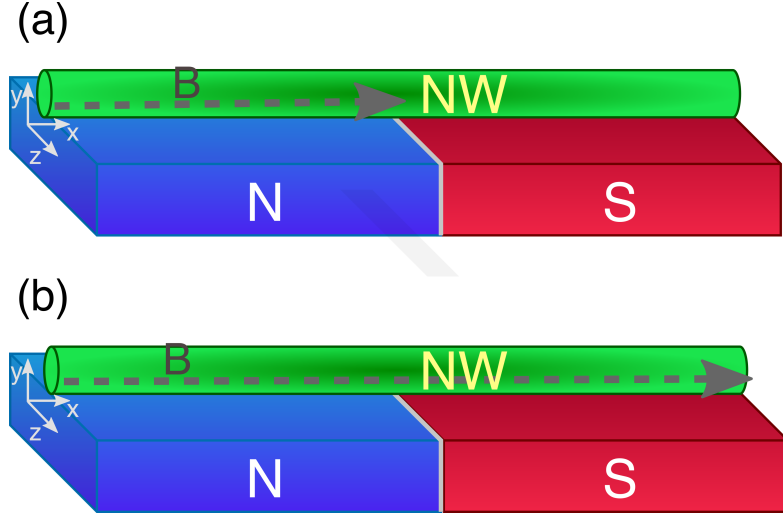


Figure 3.1: Schematics of the NS junctions considered in this chapter. (a) A semiconductor nanowire (NW, green) is placed in contact with a superconductor (S, red) and a normal metal (N, blue). The N region has a finite Zeeman field B , indicated by a dashed horizontal arrow. (b) The same junction as in (a) but with a Zeeman field applied over the entire NW. In both cases, a very thin insulating layer (I, grey) is placed in the middle of the junction to avoid the leakage of Cooper pairs into the normal region and to ensure a homogeneous order parameter inside the superconducting region.

3.1 Model and methods

In this chapter, we consider an NS junction based on the Rashba nanowire model we introduced in Sec. 2.3.3. The junction is realized by placing a semiconductor Rashba nanowire (NW) in partial proximity to a superconductor (S) such that a superconducting pairing potential is induced in right half of the NW. The left half is considered metallic (N). We assume that gate voltages can be applied to the NW such that the chemical potential in N and S can be controlled independently. We also assume that a Zeeman field can be applied to the NW, either in N only or in both N and S. This Zeeman field can be induced either by proximity to a ferromagnet or by an external magnetic field. The physical realization of the Zeeman is not detrimental to the results we present in this chapter. Furthermore, we assume that both the superconducting gap and chemical potential are not smoothly varying in space, i.e., they are piecewise constant in N and S regions. We model this by placing a very thin insulating layer in the middle of the junction. The schematic of the junction is shown in Fig. 3.1.

3.1.1 System Hamiltonian

We model the NS junction with a tight-binding version of the Hamiltonian in Eq. (2.75) extending along the x direction. The Hamiltonian reads:

$$H = H_{\text{NW}} + H_{\text{B}} + H_{\Delta}, \quad (3.1)$$

where

$$\begin{aligned} H_{\text{NW}} &= \sum_{j=1}^N \psi_j^\dagger ((2w - \mu(j)) \tau_z \sigma_0) \psi_j \\ &\quad + \sum_{j=1}^{N-1} \psi_j^\dagger \left(-w \tau_z \sigma_0 - i \frac{\alpha}{2a} \tau_0 \sigma_z \right) \psi_{j+1} + h.c., \\ H_{\text{B}} &= \sum_{j=1}^N \psi_j^\dagger (-B(j) \tau_z \sigma_x) \psi_j, \\ H_{\Delta} &= \sum_{j=L_{\text{N}}/a+1}^N \psi_j^\dagger (\Delta \tau_y \sigma_y) \psi_j. \end{aligned} \quad (3.2)$$

Here, $\psi_j = (c_{j\uparrow}, c_{j\downarrow}, c_{j\uparrow}^\dagger, c_{j\downarrow}^\dagger)^T$ is the Nambu spinor at site j , and $c_{j\sigma}$ ($c_{j\sigma}^\dagger$) are electron ladder operators that destroy (create) a fermionic state at site j with spin σ . The Pauli matrices in Nambu and spin spaces are denoted by τ_i and σ_i , respectively, with $i = 0, x, y, z$. The first term in Eq. (3.1) describes the NW with a site-dependent chemical potential $\mu(j)$ measured from the bottom of the band ($2w$), where w is the nearest-neighbor hopping amplitude. The Rashba spin-orbit coupling strength is given by α along the z direction, and a is the lattice spacing. The second term is the Zeeman term which is taken along the x direction with $B(j)$ being the Zeeman field at site j . The third term is the induced superconducting pairing potential Δ that is restricted to the right half of the NW for $j > L_{\text{N}}/a$, where L_{N} is the length of the N region. The length of the system is given by $L = Na$, with N being the number of sites. The length of the S region is given by $L_{\text{S}} = (L - L_{\text{N}})$.

Our setup matches with the standard experimental setup used in conductance experiments to search for MBSs in semiconductor NWs [16, 67, 81, 82], see Fig. 2.1. In these conductance experiments, a main source of uncertainty is the presence of trivial zero-energy ABSs that can mimic MBSs. There are many possible sources that can generate trivial zero-energy ABSs. In this chapter, we consider Andreev bound states emerging from confinement and helicity in the N region, which can be induced by a Zeeman field. In order to allow for a large helical phase in the N region, we assume that the chemical potential in N can be tuned independently

from the S region and is generally smaller than that in S. This is a reasonable assumption since the voltage gates used in experiments are more effective in the N region than in the S region. Thus, we have:

$$\mu(j) = \begin{cases} \mu_N, & 1 \leq ja \leq L_N, \\ \mu_S, & L_N < ja \leq L. \end{cases} \quad (3.3)$$

For correct identification of MBSs, it is crucial to understand the physics of trivial zero-energy ABSs in isolation. To this end, we consider two different spatial profiles of the Zeeman field $B(j)$. First, we consider a Zeeman field restricted to the N region only, as seen in Fig. 3.1(a). In this case, the Zeeman field is given by $B(j) = B\theta(L_N - ja)\theta(ja)$ where $\theta(x)$ is the Heaviside step function. This scenario can be realized by placing a ferromagnet in contact with the N region. In this scenario, no Zeeman field enters the superconductor, thus, disallowing the formation of spin-polarized bands which is necessary for the formation of MBSs as we discussed in Sec. 2.3.3. We will see that this scenario hosts trivial zero-energy ABSs over a long range of Zeeman fields. The second scenario we consider is an NS junction with a Zeeman field constant all over the N and S regions, as seen in Fig. 3.1(b). This can be realized by placing a ferromagnet in contact with the entire NW or by applying an external Zeeman field. In this case, the Zeeman field is given by $B(j) = B$. This scenario is capable of hosting both trivial zero-energy ABSs and MBSs, which appear in distinct phases driven by the Zeeman field. By analyzing the two scenarios from a superconducting correlation perspective, we can understand the physics of trivial zero-energy ABSs and MBSs in realistic NS junctions.

In our numerical simulations, we fix the parameters used in this chapter to realistic values based on the experimental values reported for InSb and InAs NWs proximated by Al or NbTiN superconductors [16]. In particular, we set the lattice spacing $a = 10$ nm, the hopping integral $t = 25$ meV, the Rashba spin-orbit coupling strength $\alpha = 20$ meVnm, and the superconducting gap $\Delta = 0.25$ meV. The chemical potential in the S region is set to $\mu_S = 0.5$ meV, while in the N region we consider two values. In Sec. 3.3, we set $\mu_N = 0.5$ meV, while in Sec. 3.4, we set $\mu_N = 0.1$ meV.

3.1.2 Calculation of Superconducting Pair Amplitudes

To analyze the emergent superconducting correlations in the NS junctions discussed above, we employ the machinery of the Nambu Green's function method [58, 83] as we outlined in Sec. 2.5.2. The Nambu Green's function is defined as:

$$\mathcal{G}_{jj',\sigma\sigma'}(z) = [z - H]_{jj',\sigma\sigma'}^{-1}, \quad (3.4)$$

where H is given by Eq. (3.1) and describes the respective NS junctions under consideration. Here, we have used complex-valued frequency z to unify the description

of the retarded, advanced, and Matsubara Green's functions. For retarded and advanced Green's functions, we have $z = \omega \pm i\delta$, where δ is an infinitesimally small positive number. For the Matsubara Green's function, we have $z = i\omega_n$, where $\omega_n = (2n + 1)\pi k_B T$ are the Matsubara frequencies with $n = 0, \pm 1, \pm 2, \dots$ and k_B being the Boltzmann constant. Since we are dealing with a zero temperature regime, we will treat the Matsubara Green's function as a continuous parameter.

We can exploit the structure of the Nambu Green's function in Nambu space to express the Nambu Green's function as a 2×2 block matrix in particle-hole space as follows:

$$\mathcal{G}_{jj',\sigma\sigma'}(z) = \begin{pmatrix} G_{jj',\sigma\sigma'}(z) & F_{jj',\sigma\sigma'}(z) \\ \bar{F}_{jj',\sigma\sigma'}(z) & \bar{G}_{jj',\sigma\sigma'}(z) \end{pmatrix}, \quad (3.5)$$

where $G_{jj',\sigma\sigma'}(z)$ and $\bar{G}_{jj',\sigma\sigma'}(z)$ are the normal electron-electron and hole-hole Green's functions, respectively, while $F_{jj',\sigma\sigma'}(z)$ and $\bar{F}_{jj',\sigma\sigma'}(z)$ are the anomalous electron-hole and hole-electron Green's functions, respectively. We are mainly interested in the anomalous Green's functions, which describe the superconducting correlations in the system. Particularly, we are interested mainly in local superconducting correlations at $j = j'$. We don't consider the non-local correlations since both the MBSs and ABSs are localized at the junction interface, thus, the non-local correlations are not expected to be relevant. Using the antisymmetry condition discussed in Sec. 2.5.2, we can symmetrize the anomalous Green's functions over frequency and spin to obtain the even-frequency spin-singlet (ESE) and odd-frequency spin-triplet (OTE) pair amplitudes. First, we symmetrize over frequency as follows:

$$F_{\sigma\sigma',j}^E(z) = \frac{1}{2} (F_{jj,\sigma\sigma'}(z) + F_{jj,\sigma\sigma'}(-z)), \quad (3.6)$$

for the local even-frequency component, and

$$F_{\sigma\sigma',j}^O(z) = \frac{1}{2} (F_{jj,\sigma\sigma'}(z) - F_{jj,\sigma\sigma'}(-z)). \quad (3.7)$$

for the local odd-frequency component.

It is convenient to express the pair amplitudes in the d-vector notation from Eq. (2.86). In this notation, the ESE pair amplitude is given according to Eq. (2.91) as:

$$d_s(z, j) = F_{\uparrow\downarrow,j}^E(z) \quad (3.8)$$

Similarly, from Eqs. (2.96)-(2.98), we obtain the local OTE pair amplitudes in the d-vector notation as:

$$d_x(z, j) = \frac{1}{2} (F_{\downarrow\downarrow,j}^O(z) - F_{\uparrow\uparrow,j}^O(z)) \quad (3.9)$$

$$d_y(z, j) = \frac{i}{2} (F_{\downarrow\downarrow,j}^O(z) + F_{\uparrow\uparrow,j}^O(z)) \quad (3.10)$$

$$d_z(z, j) = F_{\uparrow\downarrow,j}^O(z) \quad (3.11)$$

In what follows, we will explore pairing correlations under retarded and Matsubara Green's functions. For the retarded Green's function, we will use $z = \omega + i\delta$ with $\delta = 10^{-5}$ meV, while for the Matsubara Green's function we will use $z = i\omega_n$ with ω_n is Matsubara frequency.

3.2 Different phases of the NS junction

Before we analyze the two different scenarios we outlined in Sec. 3.1, we first need to understand the different Zeeman field driven phases appearing in the NS junction. Since the junction is made of two parts, it is natural to assume that the overall phase of the junction is determined by the different phases in the N and S regions. We have discussed the S region in Sec. 2.3.3 and we know that the S region is in a topologically nontrivial phase when the Zeeman field is larger than a critical value $B_c = \sqrt{\Delta^2 + \mu_S^2}$ [17, 18, 66, 84], where Δ is the superconducting gap and μ_S is the chemical potential in S. In this case, the S region hosts MBSs at the ends of the NW. We now discuss the different phases in the N region. Let us consider the N region in the continuum limit. In this case, the energy spectrum of the N region is given by:

$$E_{\pm}(k) = \frac{\hbar^2 k^2}{2m} - \mu_N \pm \sqrt{\alpha^2 k^2 + B^2}, \quad (3.12)$$

where k is the wave vector and m is the effective mass of electrons in the NW. We show the continuum spectrum in Fig. 3.2. When both the Zeeman field and Rashba SOC are absent, the spectrum degenerate with two parabolic bands on top of each other. SOC shifts the bands apart in momentum space. The spin for all states is locked to the momentum except for the states at $k = 0$ due to the spin degeneracy at $k = 0$. An applied Zeeman field B will open a gap in the spectrum at $k = 0$ whose size is given by $2B$. This gap is called the helical gap and is highlighted in grey in Fig. 3.2. If the chemical potential μ_N lies inside the helical gap (i.e., $\mu_N < B$), half of the spin is absent from the spectrum, and the system hosts two counter-propagating states with opposite spins similar to the helical edge states in quantum spin Hall insulators. This is the helical phase of the N region. If the chemical potential is larger than the Zeeman field, we lie outside the helical gap and all spin degrees of freedom are present in the spectrum. In this case, the N region is in a trivial phase. We emphasize that the helical phase is not topological.

The formation of bound states in our NS junction is similar to what occurs when having a particle in a box or in a potential barrier, which is why confinement plays a role as well in the helical nanowire coupled to a superconductor. Due to finite

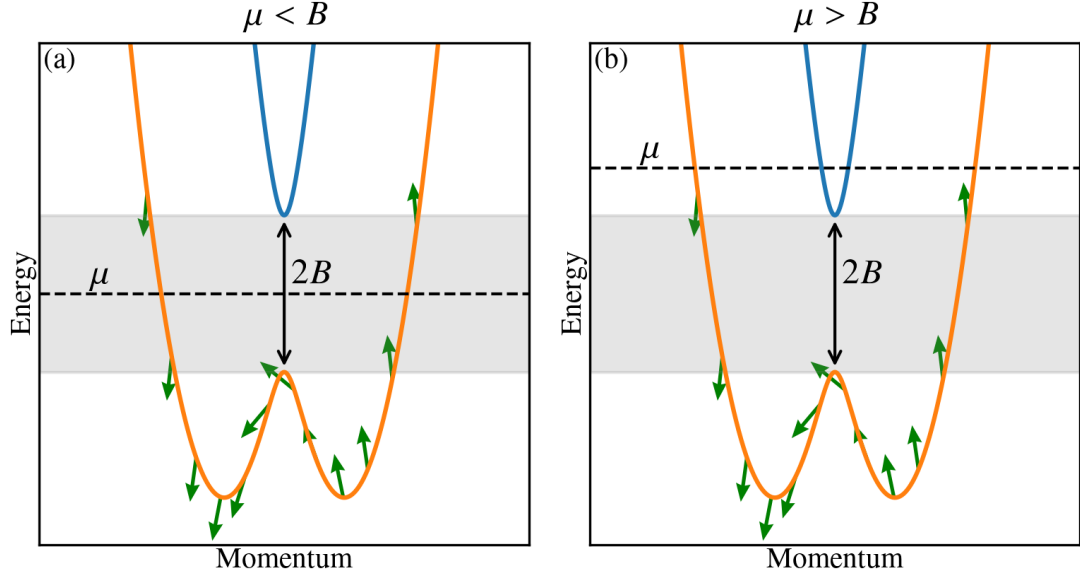


Figure 3.2: Spectrum of the N region in the continuum limit as a function of the wavevector k with the chemical potential $\mu < B$ (a) and $\mu > B$ (b). The helical gap is highlighted in grey.

length, the energy levels of the N region are discrete and depending on the length of the N region, there can be many levels. When having an NS junction with N being helical, the discrete levels of N are lower in energy than the superconducting gap Δ and can even happen around zero energy.

Apart from that, confinement makes them localize at the boundaries, which then leak into the S region as well giving rise to an inverse proximity effect; similarly we have the regular proximity effect. In this way, a helical metal can accommodate bound states simply due to confinement and helicity. Thus, we see that the NS junction can be in one of the following three phases:

- **Trivial phase:** The N region is in a trivial phase with $\mu_N > B$ with both spin degrees of freedom active. The S region is also in a trivial phase with $B < B_c$. In this case, the NS junction does not host any ABSs or MBSs.
- **Trivial Helical Phase:** The N region is in a helical phase with $\mu_N < B$ with only one spin degree of freedom active. The S region is also in a trivial phase with $B < B_c$. In this case, the NS junction hosts trivial zero-energy ABSs bound to the NS interface. [28]
- **Topological phase:** The S region is in a topological phase with $B > B_c$ and hosts MBSs at the ends of the NW. The N region can be either in a

trivial phase or in a helical phase. In this case, the NS junction hosts only MBSs at the ends of the NW. [17, 18, 66, 84]

3.3 Junctions Hosting Only Trivial Zero-Energy ABSs

In this section, we consider the NS junction with a Zeeman field only in N, as seen in Fig. 3.1(a). This setup prevents the superconductor from becoming topologically nontrivial, which allows us to focus solely on characterizing the trivial ABSs. We assume that the chemical potential is uniform in both N and S regions and is set to $\mu_{N,S} \equiv \mu = 0.5$ meV. Thus, the N region becomes helical at $B > B_h \equiv \mu_N$ [28]. To fully understand the physics of trivial ABSs, we first analyze their formation in the low-energy spectrum and then we their influence on the emergent superconducting correlations.

3.3.1 Low-energy Spectrum and the Nature of Trivial Zero-Energy Andreev Bound States

We diagonalize the BdG Hamiltonian given by Eq. (3.1) with $B(j) = B\theta(L_N - ja)\theta(ja)$ and constant chemical potential $\mu_{N,S} = \mu$ to obtain the low-energy spectrum of the NS junction. The results are shown in Fig. 3.3(a,b,d,e) as a function of the Zeeman field B under different lengths of the N region L_N and S region L_S . We also show the spatial profile of the summation of wavefunction probability density of the states closest to zero energy $|\psi(x)|^2 = |\psi_E(x)|^2 + |\psi_{-E}(x)|^2$ at distinct values of the Zeeman field in Fig. 3.3(c,f). Here, we have defined the wavefunction $\psi_{\pm E}(x)$ as the eigenstates of Eq. (3.1) at the position $x = ja$ and energy $\pm E$. $\psi_{\pm E}(x)$ has the following Nambu structure $\psi_{\pm E}(x = ja) = (u_j^\uparrow, u_j^\downarrow, v_j^\uparrow, v_j^\downarrow)^T$, where u_j^σ and v_j^σ are the electron and hole components, respectively. Let us first focus on the low-energy spectrum of the NS junction with short N regions [Fig. 3.3(a,d)]. Since the N region is short, the spacing between the energy levels is large. In fact, only a pair of energy levels exist within the superconducting gap, each being doubly degenerate at $B = 0$. As we turn on the Zeeman field, the degeneracy is lifted with one level with given spin merging with the quasicontinuum while the other level with opposite spin move downward and oscillates around zero energy. As a result, only two non-degenerate energy levels exist within the superconducting gap for finite Zeeman fields. These two levels cross each other at $B = \Delta$ (green dashed line) and then continue to oscillate around zero energy without any further crossings. We note that changing the length of the superconductor from $L_S = 200a$ in Fig. 3.3(a) to $L_S = 400a$ in Fig. 3.3(d) does not change the in-gap states at all. Another

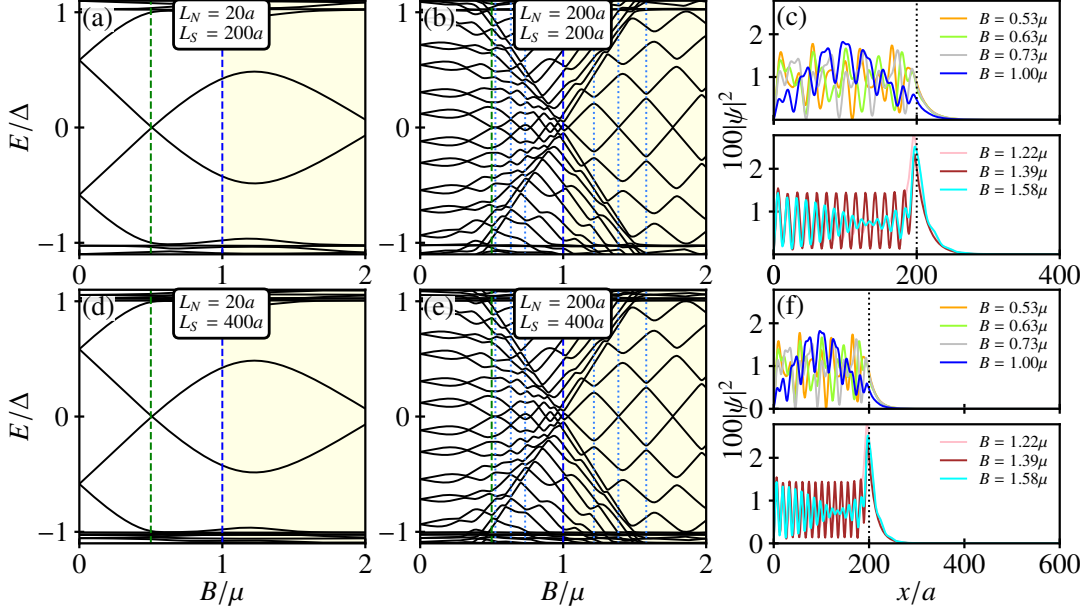


Figure 3.3: (a,b) Low energy spectrum for an NS junction with the Zeeman field B in N as a function of B for $L_N = 20a$ and $L_N = 200a$, both at $L_S = 200a$. (c) Wavefunction probability density of the state closest to zero energy as a function of the spatial coordinate at distinct values of the Zeeman field for $L_{N,S} = 200a$; curves in the top panel correspond to $B \leq \mu$, whereas those in the bottom panel correspond to $B > \mu$, with $\mu = \mu_{N,S}$. (d,e), and (f) Same as in (a,b) and (c), respectively, but for $L_S = 400a$. The green and blue dashed vertical lines in (a,b,d,e) mark $B = \Delta$ and $B = \mu$, respectively, with $B \geq \mu$ in yellow color; the dotted cyan curves in (b,e) indicate the values of B at which the wavefunction probability densities are plotted in (c,f). Parameters: $a = 10\text{ nm}$, $\mu_{N,S} \equiv \mu = 0.5\text{ meV}$, $\Delta = 0.25\text{ meV}$, $w = 25\text{ meV}$, $\alpha = 20\text{ meV nm}$.

interesting observation is that the helical transition at $B = \mu$ (blue dashed line) does not affect the in-gap states. This is because the N region is very short and the helical phase is not well developed.

The situation becomes more interesting when we consider long N regions [Fig. 3.3(b,e)]. Here, the energy levels are much closer to each other and several particle-hole pairs of energy levels appear within the superconducting gap. Below the helical transition $B < \mu$, the lowest energy levels oscillate around zero energy in an irregular fashion since the two spin sectors are active. Similar to the short N region, the lowest energy levels cross each other at $B = \Delta$ and continue to oscillate around zero energy irregularly. Meanwhile, after $B = \Delta$, a set of higher

energy levels appears and disperses towards zero energy linearly with B . This set of levels is formed by the higher energy states in the N region that are pushed down by the Zeeman field. This leads to a gap closing and reopening feature at the helical transition $B = \mu$. This gap closing and reopening feature mimics the one observed at the topological phase transition; however, here it is not related to topology [28]. Above the helical transition $B > \mu$, one spin sector is removed and the low-energy sector represents a spin-polarized spectrum with zero-energy crossings. Since only one spin sector is active in the helical phase, the spectrum disperses linearly with B . In particular, the lowest energy levels oscillate around zero energy with zero-energy crossings in a regular fashion with a periodicity determined by the Zeeman field. The behavior of the low-energy spectrum in Fig. 3.3 reveals that trivial zero-energy ABSs indeed form without any relation to topology or Majorana physics in NS junctions. We note that the oscillations in the N region is independent of L_S , signaling that its origin stems from the N region and it is most likely localized at the NS interface.

To confirm this localization, we analyze the wavefunction probability density of the states closest to zero energy for long N region in Fig. 3.3(c,f). Below the helical transition $B < \mu$ (top panels of Fig. 3.3(c,f)), the wavefunction probability density is characterized by an irregular oscillations in the N region resulting from the interplay of four different Fermi momenta defined by the SOC, Zeeman field, and chemical potential. The oscillations decay exponentially in the S region due to the superconducting gap. Above the helical transition $B > \mu$ (bottom panels of Fig. 3.3(c,f)), the N region become spin-polarized and thus we only have two Fermi momenta defining the oscillations in the N region. As a result, the oscillations in the N region become regular sinusoidal oscillations with a periodicity determined by the Zeeman field. The wavefunction probability density becomes bounded to the interface, acquiring a large value at the NS interface. On the other hand, in the S region, the wavefunction probability density decays exponentially with very small oscillations. We note that these general features of the wavefunction probability density are independent of the length of the S region L_S , which is consistent with the low-energy spectrum in Fig. 3.3(b,e).

3.3.2 Emergent Superconducting Correlations from Trivial ABSs

Now that we have established the conditions for the formation of trivial zero-energy ABSs, we shift our attention to the impact of these ABSs on the emergent superconducting correlations in the NS junction. To this end, we consider NS junctions with $L_N = 200a$ and $L_S = 200a$, which is a realistic length for the N region in experiments [16, 67, 81, 82]. We then calculate the retarded pair

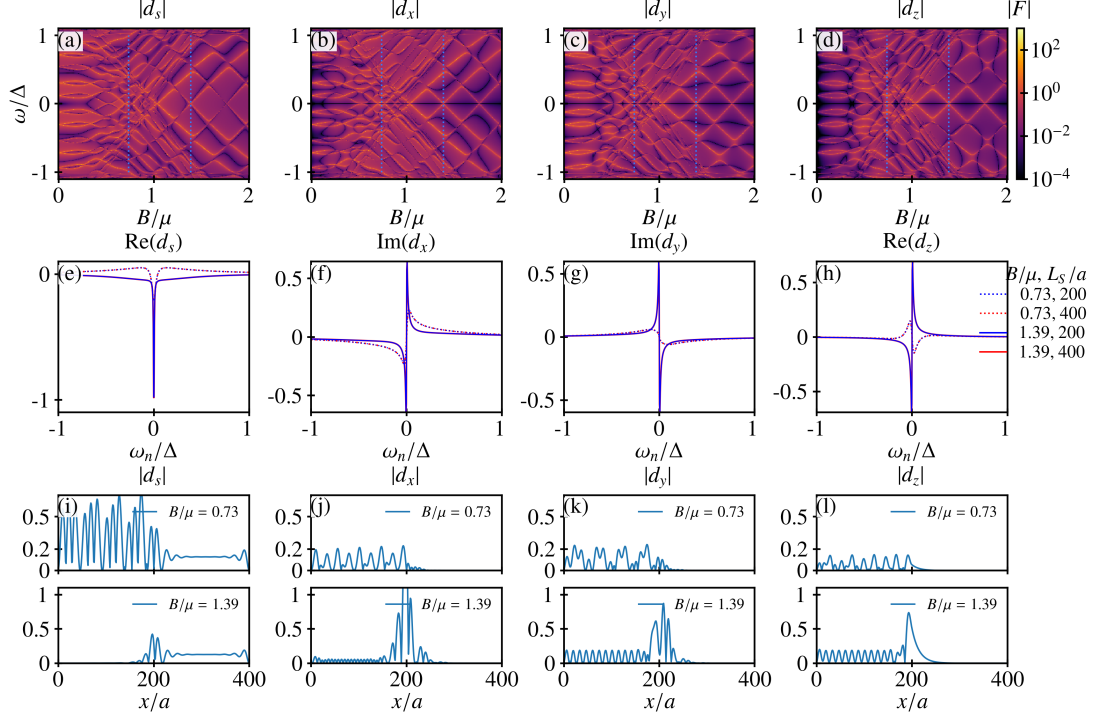


Figure 3.4: (a-d) Absolute value of the retarded pair amplitudes for an NS junction with the Zeeman field B in N as a function of frequency ω and B near the junction interface in N. (e-h) Pair amplitudes from (a-d) as a function of Matsubara frequency ω_n at $x = 192a$ for two distinct values of B and L_S ; the curves below (above) the helical transition are depicted in dashed (solid), while for a short (long) S region the curves are shown in blue (red). (i-l) Spatial profile of the pair amplitudes in (a-d) at $\omega \approx 0$ and for B below and above the helical transition. The Zeeman field B in the top panel of (i-l) is fixed at $B = 0.73\mu$ which is below the helical transition, while the Zeeman field in the bottom panel is chosen above the helical transition $B = 1.39\mu$. Parameters: $x = 192a$, $L_N = 200a$, while $L_S = 200a$ unless otherwise specified. The rest of the parameters are the same as in Fig. 3.3.

amplitudes using the Nambu Green's function method outlined in Sec. 3.1.2. The results are shown in Fig. 5.3(a-d) as a function of frequency ω and Zeeman field B near the NS interface in N at $x = 192a$. We also show the pair amplitudes as a function of Matsubara frequency ω_n at the same fixed position $x = 192a$ in Fig. 5.3(e-h) for two distinct values of B and L_S . Finally, we show the spatial profile of the retarded pair amplitudes at $\omega \approx 0$ in Fig. 3.4(i-l) for the same values of B as in (e-h).

As seen in Fig. 5.3(a-d), the retarded pair amplitudes exhibit a rich structure as

a function of frequency and Zeeman field. Interestingly, both the even-frequency spin-singlet (ESE) and odd-frequency spin-triplet (OTE) pair amplitudes emerge at the NS interface, coexisting with each other over a wide range of Zeeman fields. Although the superconducting gap Δ is s-wave meaning that only the ESE pair amplitude is expected to be present, the OTE pair amplitudes emerge due to the interplay of SOC and Zeeman field. Perhaps unsurprisingly, both the ESE and OTE pair amplitudes exhibit large values whenever the frequency ω matches the energy levels in the low-energy spectrum shown in Fig. 5.2.

Now, let's look at each pair amplitude in detail. The ESE pair amplitude defined in Eq. (3.8) is shown in Fig. 3.4(a) as a function of frequency ω and Zeeman field B . ESE pair amplitude consistently have large values for frequencies within the superconducting gap regardless of the Zeeman field. This is in contrast to the OTE pair amplitudes which are generically weak for very small magnetic fields. In fact, we can see that the OTE pair amplitudes vanish for $B = 0$ in Fig. 3.4(b-d). As we increase the Zeeman field, the OTE pair amplitudes start to have non-zero values at the NS interface, as seen in Fig. 3.4(b-d). It is interesting to note that the equal spin-triplet OTE pair amplitudes d_x and d_y are larger than the mixed spin-triplet OTE pair amplitude d_z for small Zeeman fields, while having comparable values for large Zeeman fields, particularly in the helical phase. Perhaps the most interesting feature of the OTE pair amplitudes is that they vanish at zero frequency $\omega = 0$ for all values of the Zeeman field B . This is a signature of the OTE pair amplitudes being odd in frequency, as expected. Furthermore, the OTE pair amplitudes exhibit a linear dependence on frequency ω near zero frequency, which is a common feature of OTE pair amplitudes in topologically trivial systems [33, 46, 85–93]. We further confirm this linear frequency dependence in Fig. 3.4(e-h) where we show the Matsubara OTE pair amplitudes as a function of Matsubara frequency ω_n at two distinct values of B and L_S . Note that we show the pair amplitudes as a function of Matsubara frequency since the frequency dependence is simpler to identify. We choose the two values of B such that they correspond to near zero-energy in the trivial phase at $B = 0.73\mu$ and a zero-energy crossing in the helical phase at $B = 1.39\mu$. We see that for small frequencies near zero, the OTE pair amplitudes exhibit a linear dependence on Matsubara frequency ω_n despite having very large slopes especially in the helical phase. This is in fact a manifestation of the spectral bulk-edge correspondence [46–48] which we have discussed in Sec. 2.5.4. As we explained in that section, OTE pair amplitudes in the trivial phase can be expressed as $F^{\text{OTE}} \sim \xi \omega_n + \mathcal{O}(\omega_n^3)$, where ξ is the slope of the linear dependence. Back then we argued that the slope ξ diverges at the zero-energy crossing of the ABSs, which is exactly what we observe in Fig. 3.4(e-h). However, away from the zero-energy crossing, the slope is smaller and the linear frequency dependence of the OTE pair amplitudes is more visible. More

interestingly, we see that the OTE pair amplitudes do not change as we increase the length of the S region L_S , which is a signature of their spatial locality at the NS interface. Thus, we can see that the pairing amplitudes can reveal the topologically trivial nature of the zero-energy ABSs in the NS junction.

We now examine the spatial profile of the retarded pair amplitudes at $\omega \approx 0$ in Fig. 3.4(i-l). We plot the pair amplitudes for two distinct values of the Zeeman field B below and above the helical transition with $B = 0.73\mu$ and $B = 1.39\mu$, respectively. The top panels in Fig. 3.4(i-l) show the pair amplitudes below the helical transition, while the bottom panels show the pair amplitudes above the helical transition. A common feature of the pair amplitudes in both the trivial and helical phases is that the OTE pair amplitudes d_x, d_y, d_z resemble the wavefunction probability density of the states closest to zero energy shown in Fig. 3.3(c,f). Meanwhile, the ESE pair amplitude d_s doesn't resemble the wavefunction probability density. In both the helical and trivial phases, the ESE pair amplitude d_s is almost constant in the S region. This is because no Zeeman field is present in the S region, and thus the ESE pair amplitude is determined by the superconducting gap Δ which is constant in S. In the N region, the ESE pair amplitude displays different behaviors in the trivial and helical phases. Below the helical transition $B < \mu$, the Zeeman field is not strong enough to destroy the proximity effect. Moreover, both spin sectors are active in the N region, and thus the ESE pair amplitude is finite in the N region and displays random oscillations somewhat reminiscent of the wavefunction probability density in Fig. 3.3(c,f). In the helical phase $B > \mu$, only one spin sector is active in the N region due to spin-momentum locking. Thus, the only possible pairing in N has to be of polarized spin-triplet nature. Since the ESE pair amplitude cannot abruptly vanish, it has to decay very quickly from the interface into the bulk of N. This is indeed what we observe in the bottom panels of Fig. 3.4(i). Let us now focus on the OTE pair amplitudes. Interestingly, in both the trivial and helical phases, the OTE pair amplitudes have finite values across the entire N region, including far away from the NS interface. This is in contrast to the ESE pair amplitude which decays quickly in N. On the other hand, the OTE pair amplitudes decay exponentially in the S region. This is because the superconducting gap Δ favors singlet pairing in S. In order to form OTE pair amplitudes in S, one needs to first break a singlet Cooper pair and then form a triplet pair, which is energetically unfavorable. As a result, the OTE pair amplitudes decay exponentially in S in both the trivial and helical phases. The OTE pair amplitudes in the N region also exhibit oscillations that are similar to the wavefunction probability density in Fig. 3.3(c,f). However, the oscillations in the OTE pair amplitudes are regular and periodic in the helical phase, while they are irregular and beating in the trivial phase. This is because the OTE pair amplitudes are formed by the interference of two Fermi momenta in the helical phase,

while they are formed by four Fermi momenta in the trivial phase. Another key difference between the OTE pair amplitudes in the trivial and helical phases is that the OTE pair amplitudes in the helical phase have huge enhancement at the NS interface and is generally larger than the ESE pair amplitude across the entire N region. Interestingly, for large Zeeman fields in the helical phase, we notice that the x component of the OTE pair amplitude d_x has smaller magnitude than the y and z components inside the N region, see Fig. 3.4(j-l). We interpret this as a signature of Zeeman depairing effect in the N region. In particular, since the Zeeman field points in the x -direction, it has a tendency to break triplet pairs with zero angular momentum in the x -direction. This corresponds to pairs of the form $| \rightarrow \leftarrow \rangle + | \leftarrow \rightarrow \rangle$. This is precisely the spin configuration of the x component of the OTE pair amplitude d_x . Meanwhile, the y and z components of the OTE pair amplitudes are spin-polarized triplet pairs along the x -direction, which are not affected by the Zeeman field. Thus, d_x is considered to be a short-range triplet pair amplitude, while d_y and d_z are long-range triplet pair amplitudes. This is consistent with previous studies on magnetic superconducting heterostructures [94–96]. It is worth noting that because of SOC, d_x remains all over the N region, albeit with a very small amplitude. We note that the finite values of ESE and OTE in N signal the proximity effect, while the finite values of OTE pairing in S can be interpreted as the inverse proximity effect. At this point, we would like to highlight that the large values of the pair amplitudes at the interface correspond to the same regime where we found trivial ABSs, see Fig. 3.3(b,c,e,f). As a result, the presence of trivial ABSs can indeed enhance the OTE pair amplitudes in the helical regime $B > \mu$, even in the absence of topology or MBSs. However, exactly at zero frequency, the OTE pairing vanishes, thus revealing the topologically trivial origin of ABSs.

3.4 Junctions Hosting Both Trivial ABSs and MBSs

We now shift our attention to the second scenario we outlined in Sec. 3.1 and in Fig. 3.1(b). In this scenario, we consider an NS junction with a uniform Zeeman field across the entire junction. Since the Zeeman field exists inside the S region, it can drive the S region into a topological phase at $B > B_c \equiv \sqrt{\Delta^2 + \mu_S^2}$ with MBSs at the ends of the S region [17, 18]. Meanwhile, the N region can be either in a trivial non-helical phase with $\mu_N > B$ or in a helical phase with $\mu_N < B$. Since the helical phase transition in N and the topological phase transition in S can happen independently of each other at distinct values of the Zeeman field, we can have a situation where the N region is in a helical phase while the S region is

in a trivial phase. In this case, the NS junction hosts trivial ABSs at the interface. On the other hand, if the S region is in a topological phase, the NS junction hosts MBSs at the ends of the S region. In order to have a sizable trivial helical phase in the N region, we consider a depleted N region with $\mu_N < \mu_S$, which is a realistic assumption in experiments [16, 67, 81, 82]. This way, the trivial helical phase can be achieved at a Zeeman field smaller than the topological phase transition in S. Similarly to the previous section, we first analyze the low-energy spectrum of the NS junction and then we study the emergent superconducting correlations now in the presence of both trivial ABSs and MBSs. For the numerical calculations, we consider $m\mu_N = 0.1$ meV and $\mu_S = 0.5$ meV. The other parameters are the same as in Sec. 3.3.

3.4.1 Low-energy Spectrum: from helical ABSs to MBSs

Similarly to the previous section, we diagonalize the BdG Hamiltonian given by Eq. (3.1) with uniform Zeeman field $B(j) = B$ and a piecewise constant chemical potential $\mu(j) = \mu_N \theta(L-j)a + (\mu_S - \mu_N) \theta(ja-L_N) \theta(L-j)a$ to obtain the low-energy spectrum of the NS junction. The results are depicted in Fig. 3.5(a,b,d,e) as a function of the Zeeman field B under different lengths of the N region L_N and S region L_S . Just as in fig. 3.3, we fix the length of the N region to $L_N = 20a$ in the top panels (a,b) and $L_N = 200a$ in the bottom panels (d,e). The length of the S region is fixed to $L_S = 200a$ in the left panels (a,d) and $L_S = 400a$ in the right panels (b,e). In Fig. 3.5(c,f), we also show the spatial profile of the summation of wavefunction probability density of the states closest to zero energy at distinct values of the Zeeman field indicated by dotted vertical lines in Fig. 5.4(b,e). As we explained in Sec. 3.2, the NS junction can be in one of the following three phases: trivial non-helical phase, trivial helical phase, and topological phase. The trivial non-helical phase extends for $0 \leq B < \mu_N$, while the trivial helical phase extends for

$m\mu_N < B < B_c$. The topological phase extends for $B > B_c$. In Fig. 3.5(a,b,d,e), we highlight the trivial helical phase with yellow shaded region. The helical transition at $B = \mu_N$ and the topological phase transition at $B = B_c$ are marked with blue and red dashed vertical lines, respectively.

We first consider the low-energy spectrum of the NS junction with short N regions [Fig. 3.5(a,d)]. Similar to the previous section, the energy levels of the N region are well separated from each other, and only a pair of energy levels exist within the superconducting gap. As the Zeeman field is turned on, the two energy levels are pushed downwards, crossing each other once and then oscillating around zero energy. Unlike before, however, the amplitude of the oscillations is suppressed due to level repulsion between the two energy levels and the quasi-continuum of states in the S region. As a result, the two energy levels in the N region cross each

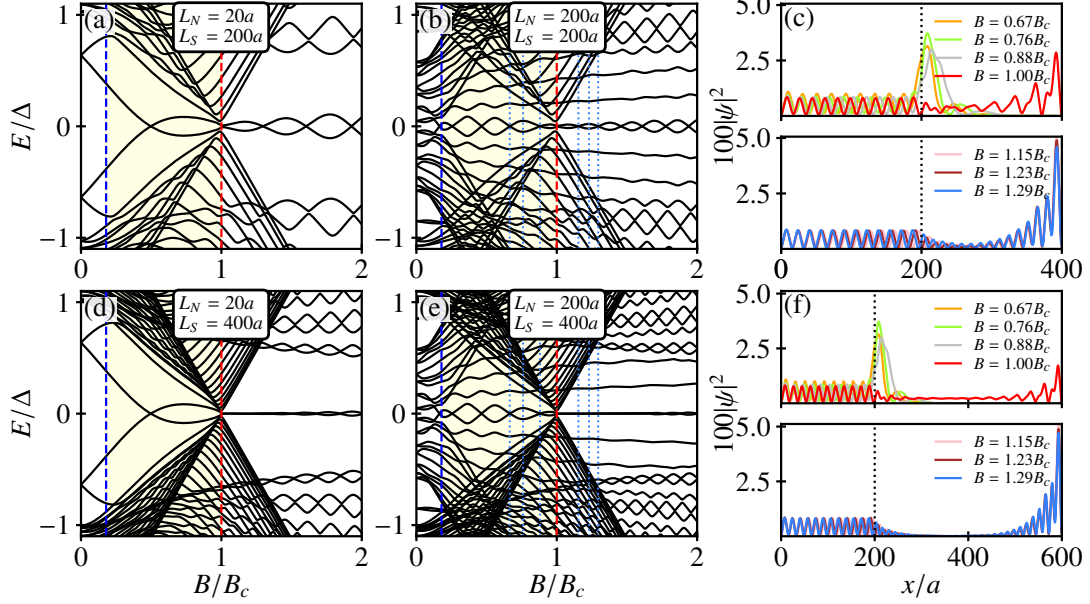


Figure 3.5: (a,b) Low energy spectrum for an NS junction with the Zeeman field B in N and S as a function of B for $L_N = 20a$ and $L_N = 200a$, both at $L_S = 200a$. (c) Wavefunction probability density of the state closest to zero energy as a function of the spatial coordinate at distinct values of the Zeeman field; curves in the top panel correspond to $\mu_N < B \leq B_c$, whereas those in the bottom panel correspond to $B > B_c$, with $B_c = \sqrt{\mu_S^2 + \Delta^2}$. (d,e), and (f) Same as in (a,b) and (c), respectively, but for $L_S = 400a$. The blue and red curves in (a,b,d,e) mark $B = \mu_N$ and $B = B_c$, respectively, with $\mu_N < B < B_c$ in yellow color; the cyan dotted curves in (b,e) indicate the values of B at which the wavefunction probability densities are plotted in (c,f). Parameters: $a = 10$ nm, $\mu_N = 0.1$ meV, $\mu_S = 0.5$ meV, $\Delta = 0.25$ meV, $w = 25$ meV, $\alpha = 20$ meV nm.

other again at the topological phase transition $B = B_c$, which is marked with a red dashed vertical line in Fig. 3.5(a,d). In fact, bulk states in the S region are also pushed down by the Zeeman field, which leads to a gap closing and reopening feature at $B = B_c$. After the topological phase transition, the superconducting bulk gap opens and the two energy levels coming from the N region smoothly evolve into MBSs at the ends of the S region. In the topological phase, the MBSs oscillate around zero energy with a few zero-energy crossings. These Majorana oscillations increase in amplitude as the Zeeman field increases. Increasing the length of the S region from $L_S = 200a$ in Fig. 3.5(a) to $L_S = 400a$ in Fig. 3.5(d) does not change the low-energy spectrum in the helical phase. In the topological phase, however, the Majorana oscillations amplitude is suppressed by increasing

the length of the S region. This is because the length of the S region in that case is larger than twice the Majorana localization length ℓ_M , which is defined as the distance over which the MBSs are localized. As a result, the MBSs become more spatially nonlocal and well-separated from each other, which reduces the overlap between them and thus suppresses the Majorana oscillations.

We now consider the case of long N regions [Fig. 3.5(b,e)]. Here, the discrete energy levels of N become densely packed and several pairs of energy levels appear within the superconducting gap. Another key observation is that there exists a gap closing at $B = \mu_N$, which marks a transition into the helical phase. The lowest positive and highest negative energy levels oscillate around zero energy with multiple zero-energy crossings in the helical phase. The helical phases trivial ABS oscillations in this is different from the trivial ABSs in the previous section. In fact, the oscillations in the helical phase are reminiscent of the Majorana oscillations in the topological phase, but with amplitudes that are inversely proportional with the Zeeman field B . If we check the topological phase in Fig. 3.5(b,e), we see that the number of zero-energy crossings of Majorana oscillations increased as the length of the N region increases. Furthermore, we now have in-gap non-zero energy levels that are almost flat as a function of the Zeeman field. Perhaps the most interesting feature of the low-energy spectrum in Fig. 3.5(b,e) is that the helical ABSs and MBSs are separated from the first excited energy level by an energy gap of roughly the same size and display similar oscillatory behavior. This can be easily confused with the topological phase and MBSs. However, by increasing the length of the superconducting regions S, we find that the helical ABSs do not change while the amplitude of the Majorana oscillations reduces, see Fig. 3.5(d,e). This effect is a direct indicator that MBSs are indeed spatially nonlocal while helical ABSs are local in space.

Further insights can be obtained from the wavefunction probability density of the states closest to zero energy in Fig. 3.5(c,f). Deep in the N region, both the trivial helical ABSs and topological MBSs exhibit homogeneous oscillatory behavior with a constant amplitude. The critical difference between the two is that the helical ABSs are localized at the NS interface, while the MBSs are localized at the ends of the S region. In fact, the wavefunction probability density of the helical ABSs has a gaussian-like profile with a large value at the NS interface with a decaying tail towards the bulk of S and oscillatory behavior in the N region. On the other hand, the wavefunction probability density of the right MBSs has a strong peak at the rightmost edge of S. While the left MBSs are absent at the interface and leak inside the N region, becoming delocalized in N, while decaying exponentially in S. Increasing the length of the S region from $L_S = 200a$ in Fig. 3.5(c) to $L_S = 400a$ in Fig. 3.5(f) does not change the wavefunction probability density of the helical ABSs. However, long S regions reduces the overlap between the MBSs at both

ends of S. Nevertheless, MBS at both edges of the S region are linked in space which is at the core of their spatial nonlocality [29, 97–101]

3.4.2 Emergent Superconducting Correlations from Trivial ABSSs and MBSSs

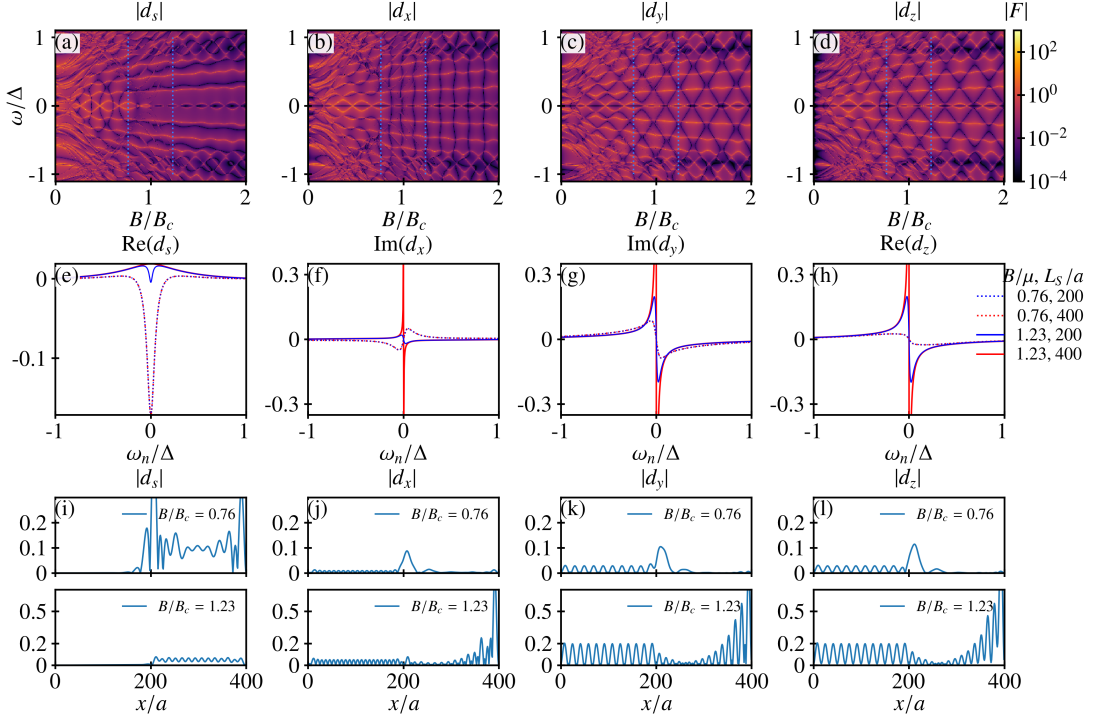


Figure 3.6: (a-d) Absolute value of the retarded pair amplitudes for an NS junction with the Zeeman field B in N and S as a function of frequency ω and B near the junction interface in N. (e-h) Pair amplitudes from (a-d) as a function of Matsubara frequency ω_n at $x = 192a$ for two distinct values of B and L_S ; the curves below (above) the topological transition are depicted in dashed (solid), while for a short (long) S region the curves are shown in blue (red). (i-l) Spatial profile of the pair amplitudes in (a-d) at $\omega \approx 0$ and for B below and above the topological transition. The Zeeman field B in the top panel of (i-l) is fixed at $B = 0.76B_c$ which is below the helical transition, while the Zeeman field in the bottom panel is chosen above the helical transition $B = 1.23B_c$. Parameters: $x = 192a$, $L_N = 200a$, while $L_S = 200a$ unless otherwise specified. The rest of the parameters are the same as in Fig. 3.5.

Following the same approach as in Sec. 3.3, we now calculate the retarded pair

amplitudes for the NS junction with both trivial ABSs and MBSs. The results are shown in Fig. 3.6(a-d) as a function of frequency ω and Zeeman field B near the NS interface in N at $x = 192a$. We also show the pair amplitudes as a function of Matsubara frequency ω_n at the same fixed position $x = 192a$ in Fig. 3.6(e-h) for two distinct values of B and L_S . Finally, we show the spatial profile of the retarded pair amplitudes at $\omega \approx 0$ in Fig. 3.6(i-l) for the same values of B as in (e-h). We choose the two values of B such that both correspond to the maximum of the helical oscillations in the trivial phase at $B = 0.76B_c$ and the maximum of the Majorana oscillations in the topological phase at $B = 1.23B_c$.

We can see that the retarded pair amplitudes in Fig. 3.6(a-d) reflects the low-energy spectrum in Fig. 3.5 including the helical gap closing and formation of helical ABSs, as well as the topological phase transition and formation of MBSs. If we look at the ESE pair amplitude in Fig. 3.6(a), we see that it has large values in the topologically trivial phases $B < B_c$. In contrast, ESE pairing is significantly smaller in the topological phase $B > B_c$. In fact, ESE in the topological phase is almost homogeneous inside the superconducting gap. Nevertheless, the ESE pair amplitude still show Majorana oscillations in the topological phase albeit very weakly. This is in contrast to the OTE pair amplitudes in Fig. 3.6(b-d) which are very large in the topological phase and exhibit strong enhancement at the Majorana oscillations. OTE is also very large in the helical phase and is comparable to ESE pairing. The coexistence of the ESE and OTE pair correlations is due to the combined effect of Zeeman field, SOC, and spatial translational invariance breaking at the NS interface [31, 33, 70, 71]. While different components of the OTE pair amplitudes d_x , d_y , and d_z have similar behavior in the helical phase, they exhibit different behaviors in the topological phase. In particular, the d_x component is larger than the d_y and d_z components in the helical phase. In contrast, d_x is smaller than d_y and d_z in the topological phase. Interestingly, all OTE pair amplitudes vanish at zero frequency $\omega = 0$ in both the trivial and topological phases, which is a signature of their odd-frequency nature. Moreover, they display lines with vanishing values which are different for different components of the OTE pair amplitudes. The d_x component has vanishing values along vertical lines at almost constant Zeeman fields, while the d_y and d_z components have vanishing values with checkerboard patterns. We note that the vanishing values of the OTE pair amplitudes at zero frequency is a signature of the topologically trivial nature. hence, it is surprising that the OTE pair amplitudes vanishes at zero frequency in the topological phase where MBSs are expected to induce an odd-frequency pairing that diverges at zero frequency [33, 46], see also Sec. 2.5.4.

To explain this surprising result, we need to analyze the Matsubara pair amplitudes in Fig. 3.6(e-h). Let us first focus on the OTE pair amplitudes in the helical phase $B = 0.76B_c$, which are shown in dashed blue(red) curves for

$L_S = 200a(400a)$ in Fig. 3.6(f-h). We observe that OTE pairing is odd in frequency ω_n , as expected, and has a linear dependence on Matsubara frequency ω_n near zero frequency. unsurprisingly, the OTE pair amplitudes are independent of the length of S in the helical phase, which is consistent with the results in Sec. 3.3. In fact, the OTE pair amplitudes in the helical phase are similar to those in Fig. 5.3(f-h) for the system with B only in N. The fact that the OTE pair amplitudes are independent of the length of S in the helical phase is a direct result of the trivial nature of the ABSs in the helical phase. Meanwhile, the OTE pair amplitudes in the topological phase $B = 1.23B_c$ have strong dependence on the length of S, as shown in solid blue(red) curves in Fig. 3.6(f-h). We observe that when the length of S is $L_S = 200a$, the OTE pair amplitudes are linear in Matsubara frequency ω_n close to zero frequency and they don't diverge at zero frequency. However, when the length of S is increased to $L_S = 400a$, the OTE pair amplitudes become divergent at zero frequency $\omega_n \approx 0$. We explain this behavior by analyzing the low-energy spectrum in Fig. 3.5(b,e) and the wavefunction probability density in Fig. 3.5(c,f). For $L_S = 200a$, the MBSs are not truly zero modes, as they oscillate around zero energy with a finite energy splitting, see Fig. 3.5(b). In this case, the wavefunction probability density of the MBSs has a finite overlap in space, see Fig. 3.5(c). As a result, the OTE pair amplitudes are not divergent at zero frequency. However, when we increase the length of S to $L_S = 400a$, the MBSs become truly zero modes with vanishing energy splitting and their wavefunction probability density has no spatial overlap, see Fig. 3.5(e,f). In this case, the OTE pair amplitudes diverge at zero frequency $\omega_n \approx 0$ and have a linear dependence on Matsubara frequency ω_n , which is consistent with the results in Sec. 2.5.4 and with previous studies [33, 45, 74, 102, 103]. As we explained in Sec. 2.5.4, the divergence of the OTE pair amplitudes at zero frequency is a signature of the self-conjugation of MBSs, which occurs when the MBSs are truly zero modes with vanishing energy splitting. This can be seen by writing down the normal (g) and anomalous (f) Green's function associated with the Majorana operator of a truly zero-energy MBS occurring in very long S regions: $\gamma = \gamma^\dagger$ as $g(\omega_n) = \langle \gamma^\dagger \gamma \rangle = \langle \gamma \gamma \rangle = f(\omega_n) = 1/i\omega_n$, where in the second equality, we have used the self-conjugation of the Majorana operator. Thus, the divergent odd-frequency profile reveals the self-conjugation of truly MBSs. In summary, we can write the OTE pairing in the topological phase as,

$$F_{\text{MBS}}^{\text{O}}(B > B_c) \approx \frac{i\omega_n}{\omega_n^2 + E_{\text{MBS}}^2} \quad (3.13)$$

where

$$E_{\text{MBS}} = \begin{cases} \text{finite}, & L_S \leq 2\ell_M, \\ 0, & L_S \gg 2\ell_M, \end{cases} \quad (3.14)$$

where ℓ_M is the Majorana localization length, which is defined as the distance over which the MBSs are localized. The energy splitting E_{MBS} is finite for short S

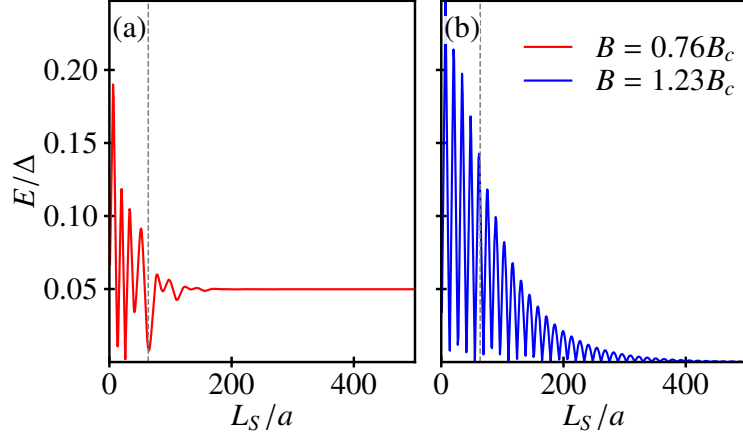


Figure 3.7: Energy of the lowest positive state as a function of the length of the S region L_S for distinct values of the Zeeman field B in the helical ($B = 0.76B_c$) and topological ($B = 1.23B_c$) phases. The dashed vertical grey line marks the coherence length of the superconductor. Parameters: $L_N = 200a$. The rest of the parameters are the same as in Fig. 3.5.

regions $L_S \leq 2\ell_M$, while it vanishes for long S regions $L_S \gg 2\ell_M$. The dependence of the energy splitting on the length of S is shown in Fig. 3.7 for two distinct values of the Zeeman field in the helical and topological phases. We see that in the topological phase, the energy of MBSs oscillates as a function of the length of S with zero energy crossings. However, the amplitude of the oscillations is exponentially suppressed as the length of S increases. Interestingly, in the helical phase, the energy of ABSs also initially oscillates as a function of the length of S with zero energy crossings; however, with crucial distinctions. First, the amplitude and periodicity of the oscillations are irregular and generally random. Second, the oscillations are completely suppressed for $L_S \geq \xi$ where $\xi = 1/\tanh^{-1}(\Delta/2w)$ is the coherence length of the superconductor, which is marked with a dashed vertical line in Fig. 3.7. Above the coherence length, the energy of the ABSs is constant and is entirely determined by the N region. This is in contrast to the topological phase where the energy of MBSs oscillates as a function of the length of S even above the coherence length and above the Majorana localization length ℓ_M . Therefore, we can conclude that the OTE pairing in the topological phase is divergent near $\omega_n \sim 0$ only in the presence of truly zero-energy MBSs, which occurs in very long superconductors when the length of the superconducting region is much longer than twice the Majorana localization length. In our case, this occurs for $L_S \geq 300a$, see Fig. 3.7(b). The strong response of the OTE pairing to an increase in the length of S can also be interpreted as a signature of spatial Majorana nonlocality since

MBSs appear located at the edges of the superconducting region. It is worth mentioning that this sensitivity to changes in L_S has been recently discussed in the context of zero bias conductance in similar nanowire junctions[104].

We now turn our attention to the spatial profile of the pair amplitudes in Fig. 3.6(i-l). Since the helical phase is mostly dependent on the N region, the spatial profile of the pair amplitudes in the helical phase is similar to what we obtained in Sec. 3.3 for the system with B only in N, see Fig. 3.4(i-l). The ESE pair amplitude decays into the bulk of N, while the OTE pair amplitudes exhibit homogeneous oscillations in N. At the interface, all pair amplitudes are enhanced, with the OTE pair amplitudes developing larger values that then decay in an exponentially oscillatory fashion into the bulk of S. We interpret the finite values of OTE pairing in S as the inverse proximity effect which is a result of the interplay between SOC, Zeeman field, and conventional spin-singlet s -wave superconductivity. In the topological phase, we see that ESE pairing is generally smaller than the OTE pair amplitudes, see bottom panels in Fig. 3.6(i-l). In S, we see that ESE pair amplitude oscillates around a finite value, form almost a plateau with bumps on it. OTE pairing is largely enhanced at the edges where MBSs are located. OTE displays similar oscillatory behavior as in the helical phase in the N region. Unlike the helical phase, however, the OTE pair amplitude is not enhanced at the interface due to the Majorana leakage into N. Moreover, the OTE pair amplitude can survive in the bulk of S wherever MBSs are present. This is in contrast to the helical phase where OTE pair amplitudes are vanishingly small deep in the superconducting region. Thus, we conclude that the proximity (inverse proximity) effect in the topological phase, characterized by superconducting correlations in N (S), is dominated by OTE pair amplitudes.

3.4.3 Accumulated Pair Amplitudes and their Zeeman Dependence

In Sec. 2.5.4, we discussed the spectral bulk-boundary correspondence of MBSs and the divergence of a generalized odd-frequency function defined in semi-infinite systems. We have seen that the accumulated OTE pair amplitudes at the boundary of a topological superconductor diverges at zero frequency as $\sum_j F_{\text{OTE}}(j, \omega_n \approx 0) \sim W/\omega_n$, where W is the winding number of the topological superconductor, see Eqs. (2.103) and (2.106). In that section, we assumed that the system is semi-infinite and didn't consider finite size effect as well as junction systems. Unfortunately, the situation is more complicated in junction systems and we cannot have a nice precise analytical expression for the accumulated OTE pair amplitudes. However, we still would like to analyze the accumulated pair amplitudes in the NS junction with both trivial ABSs and MBSs. In particular, we would like

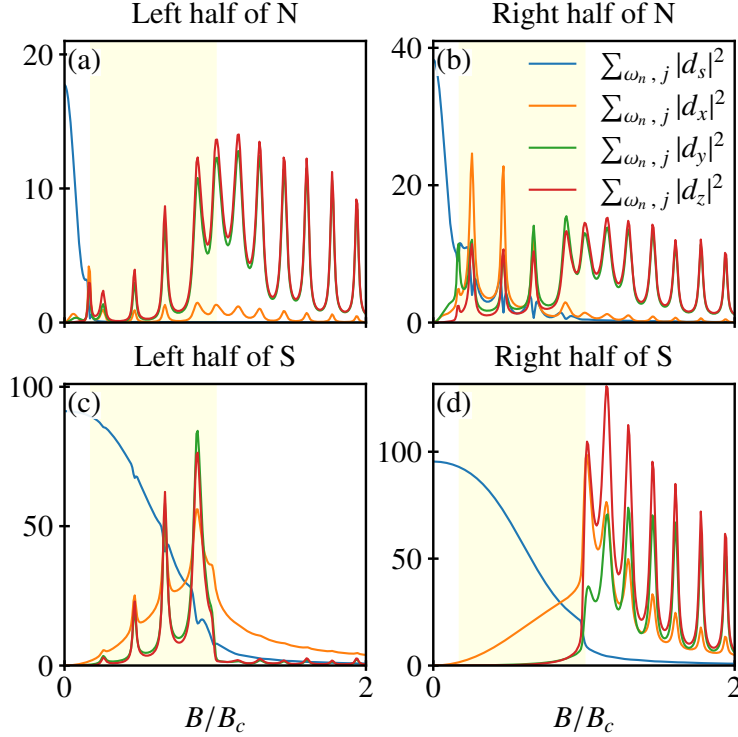


Figure 3.8: Squared magnitude of the spin-singlet and spin-triplet pair amplitudes $\sum_{\omega_n, j} |d_\beta(j)|^2$, with $\beta = s, x, y, z$, as a function of the Zeeman field B summed over (a) the left half of N, (b) the right half of N, (c) the left half of S, and (d) the right half of S. Parameters: $L_N = 200a$, $L_S = 200a$. The rest of the parameters are the same as in Fig. 3.5.

to understand how the accumulated pair amplitudes depend on the Zeeman field B and how they can be used to detect the helical phase transition and the topological phase transition. To this end, we define a modified version of Eq. (2.103). In particular, we consider the accumulated squared pair amplitudes summed over Matsubara frequencies and half the space in N (S), namely, $\sum_{\omega_n, j} |d_\beta(j)|^2$, with $\beta = s, x, y, z$ and j denoting the lattice index. We perform this summation over different quarters of the NS junction, namely, the left half of N, the right half of N, the left half of S, and the right half of S. We present the results in Fig. 3.8 as a function of the Zeeman field B . We observe that the accumulated squared pair amplitudes in Fig. 3.8 exhibit different interesting features contingent on the region where they are summed. Additionally, we also find universal features that are independent of the region where they are summed. In particular, we find that accumulated squared OTE pair amplitudes exhibit oscillatory behavior with

chainsaw-like teeth at the zero-energy crossings of both helical ABSs and MBSs. On the other hand, the accumulated squared singlet pair amplitudes are ubiquitously present at $B = 0$ and decay as the Zeeman field B increases with decay rates that depend on both the region where they are summed and the type of phase. In the left half of N, the spin-singlet part decays rapidly and completely dies off at the helical phase transition $B = \mu_N$, see Fig. 3.8(a). In the right half of N, the spin-singlet part can survive in the helical phase but eventually dies out in the topological phase, see Fig. 3.8(b). In the left half of S, the spin-singlet part decays slower with sizable values in the helical phase and smaller values in the topological phase, see Fig. 3.8(c). In the right half of S, the spin-singlet part still have sizeable values in the helical phase but it suddenly drops at the topological phase transition and dies out in the topological phase, see Fig. 3.8(d).

Looking at the spin-triplet parts, we find that they are absent at $B = 0$ and emerge as B increases. In the left half of N, the spin-triplet parts is very small in the helical phase except at the zero-energy crossings of the helical ABSs, where it develops large values (chainsaw-like teeth), see Fig. 3.8(a). In the topological phase, the spin-triplet parts become large but show an over all small linear decrease as B increases. We observe similar behavior in the right half of N, see Fig. 3.8(b). Interestingly, the x component of the spin-triplet part is significantly smaller than the y and z components in both halves of N regardless of the phase. The situation inside the S regions is remarkable. In the left half of S, the spin-triplet parts grow linearly with B in the helical phase with chainsaw-like teeth at the zero-energy crossings. Triplet parts reach their maximum values near the topological phase transition before they dramatically drop at the topological phase transition with the y and z components exactly vanish to almost zero in the topological phase, see Fig. 3.8(c). We note that the x component is still finite in the topological phase, albeit with a small decaying value. In the right half of S, both the y and z components of the spin-triplet parts are almost zero in the helical phase, while the x component is finite and grows linearly with B without the teeth structure at the zero-energy crossings, see Fig. 3.8(d). Exactly at the topological phase transition, all triplet components grow dramatically, developing the chainsaw-like teeth structure in the topological phase.

3.4.4 Experimental Signatures of Odd-Frequency Pairing

We now discuss how one can experimentally detect the OTE pairing in the NS junction with both trivial ABSs and MBSs and confirm the nature of the underlying phase. We note that current improvements in experimental techniques have made it possible to fabricate very clean semiconductor nanowires with high-quality superconducting contacts. Thus, disorder is not a major issue in these systems, which allows us to focus on the clean limit. We will reserve the discussion of the

effect of disorder to Chapter 4. In this section, we will focus on the experimental signatures of OTE pairing in clean NS junctions. Our results suggest that true Majorana signatures can be observed by varying the length of the superconducting region. In experiment, it is not possible to change the length of the superconducting region after the fabrication of the device. While it is possible to fabricate devices with different lengths of the superconducting region, it is not feasible to perfectly replicate the same device with different lengths and each device will have its own imperfections. Nevertheless, it is still possible to control the length of the superconducting region by applying a gate voltage to the superconducting region, which can change the effective length of the superconducting region. Alternatively, one can fix the length of the entire junction and change the lengths of the N and S regions by sliding the superconductor along the semiconductor nanowire. The specifics of the experimental setup, while interesting, are beyond the scope of this work. Instead, we will focus on the experimental signatures of OTE pairing.

An important caveat to keep in mind is that there is no direct way to measure the OTE pairing in experiments. This is due to the fact that the pair amplitude F is not directly measurable, see Refs. [31, 33, 88, 94, 105]. Nevertheless, it is possible to indirectly reveal the presence of OTE pairing in superconductor-semiconductor hybrid systems by measuring several experimental signatures, as we discuss below.

In Sec. 3.4.3, we discussed the accumulated squared pair amplitudes summed over Matsubara frequencies and spatial coordinates. We speculate that the interesting behavior of the accumulated squared pair amplitudes in Fig. 3.8 can be detected by means of Andreev spectroscopy. This is because Andreev reflection probability is directly related to the squared magnitude of the anomalous Green's function, $|F|^2$. Thus, the accumulated squared pair amplitudes can be accessed through Andreev spectroscopy. In particular, we expect that Andreev spectroscopy would be able to detect the chainsaw-like teeth structure at the zero-energy crossings of the helical ABSs and MBSs. We believe that performing Andreev spectroscopy would be most effective if we perform it at the right side of S. As we saw in Fig. 3.8(d), the accumulated squared OTE pair amplitudes in the right half of S vanishes in the helical phase and develops large values at the topological phase. Directly measuring Andreev transport associated with the OTE pairing would give away to distinguish between the helical and topological phases. However, we note that, under generic circumstances, both even- and odd-frequency pairings contribute to the Andreev transport [106], making it difficult to isolate the OTE pairing signal. Nevertheless, there already exist ways to identify the contribution from odd-frequency pairing via Andreev transport, e.g. in multiterminal junctions [85, 107]. Thus, albeit challenging, the OTE pairing can be detected by means of Andreev spectroscopy in superconductor-semiconductor hybrid systems.

In addition to Andreev spectroscopy, OTE pairing can be detected by means

of Josephson effect [69, 108]. The Josephson effect is extremely sensitive to the pairing symmetry and can reveal the presence of OTE components. In particular, a scanning tunneling microscope experiment with a superconducting tip can be used to probe the current-phase relation at specific points in the junction. The current-phase relation is expected to differ significantly when OTE correlations are present.

Another experimental signature of OTE pairing is the zero-energy LDOS in the normal region of a diffusive normal-superconductor junction [36, 41, 43, 45, 109–112]. This leads to quantized zero-bias conductance peaks in the normal region regardless of the the normal metal resistance [36, 41, 43, 45, 109–112]. This phenomenon is known as the anomalous proximity effect which we discuss in more detail in the next chapter.

3.5 Effect of Zeeman Field Orientation on the Helical and Topological Regimes

Up to this point, our analysis has been confined to a specific configuration where the applied Zeeman field is perfectly perpendicular to the direction of Rashba spin-orbit coupling. While this is a common and instructive theoretical starting point, experimental setups may involve unavoidable misalignments, and a full understanding of the system’s response to a generic field orientation is crucial for robustly interpreting experimental data. In this section, we therefore extend our model to investigate how tilting the Zeeman field with respect to the spin-orbit axis affects the stability and characteristics of both the helical and topological phases. To this end, we modify the Zeeman term in the Hamiltonian as follows:

$$H_B = -B \sum_{j=1}^N \psi_j^\dagger \left(\sin(\theta) \cos(\phi) \tau_z \sigma_x + \cos(\theta) \tau_z \sigma_z + \sin(\theta) \sin(\phi) \tau_0 \sigma_y \right) \psi_j, \quad (3.15)$$

where θ and ϕ are the polar and azimuthal angles defining the orientation of the Zeeman field. A rotation by the azimuthal angle ϕ merely rotates the field around the spin-orbit axis (z -axis), which does not alter the relative magnitudes of the field components parallel and perpendicular to the spin-orbit direction. Consequently, the fundamental phase boundaries are unaffected by ϕ . The polar angle θ , however, directly tunes these components and thus has a profound impact on the system’s phase diagram.

The stability of both the helical and topological phases is profoundly affected by the field orientation, as it can lead to a closure of the bulk superconducting

gap. Specifically, the gap of the proximitized superconductor closes whenever the component of the Zeeman field parallel to the spin-orbit axis, $B_z = B \cos(\theta)$, becomes equal in magnitude to the pairing potential, i.e., $|B_z| = \Delta$ [113–116]. It is crucial to note that this gap-closing condition depends only on the parallel field component and is independent of the perpendicular components that drive the system towards the helical or topological regimes. Consequently, when this condition is met, the superconductor itself becomes gapless. This obliterates any confinement of low-energy states, meaning that both the gaped helical and gaped topological phases cease to exist. For a given total field strength B , this gap closure occurs at a critical polar angle $\theta_c = \arccos(\Delta/B)$.

This strong angular dependence is detailed in Fig. 3.9, which shows the evolution of the low-energy spectrum as a function of B for several tilt angles θ . A critical observation is that the helical phase is entirely absent when the Zeeman field is aligned parallel to the spin-orbit axis ($\theta = 0$), as seen in Fig. 3.9(a). In this configuration, the Zeeman and spin-orbit terms no longer compete in a way that creates the spin-polarized, counter-propagating bands necessary for helicity [117]. As θ is increased from zero, a helical region (shaded yellow) emerges and expands, reaching its maximum extent when the field is fully perpendicular at $\theta = \pi/2$, before shrinking and vanishing again at $\theta = \pi$.

The topological phase also exhibits a critical dependence on θ . While the onset of the topological phase remains at $B = B_c$, its stability is compromised by the component of the Zeeman field parallel to the spin-orbit axis, $B_z = B \cos(\theta)$. This parallel component acts to close the superconducting gap. When it becomes equal in magnitude to the pairing potential, i.e., $|B \cos(\theta)| = \Delta$, the bulk gap of the system closes, which destroys the topological protection. This condition defines a critical angle $\theta_c = \arccos(\Delta/B)$. As a result, a gaped and topologically non-trivial phase can only exist within the angular window $\theta \in (\theta_c, \pi - \theta_c)$, in consistence with previous results [113–116]. This behavior is evident in Fig. 3.9, where the topological region shows a finite gap only for intermediate angles.

The nature of the low-energy wavefunctions, shown in Fig. 3.9(c,f), directly reflects the state of the bulk superconducting gap. In the gapless regimes where $|B_z| \geq \Delta$ (e.g., panel c), the absence of a gap in the S region prevents the formation of any bound states. The wavefunctions correspond to delocalized, continuum states that extend across the entire junction. In contrast, once the system enters the gapped regime where $|B_z| < \Delta$ (panel f), the superconductor can again confine states, allowing the familiar localized bound states to re-emerge: trivial ABSs pinned to the N/S interface in the helical phase, and topological MBSs localized at the system's extremities in the topological phase.

The emergent pair amplitudes serve as an even more sensitive probe of these angular-dependent phase transitions, as detailed in Fig. 3.10. Panel (a) shows

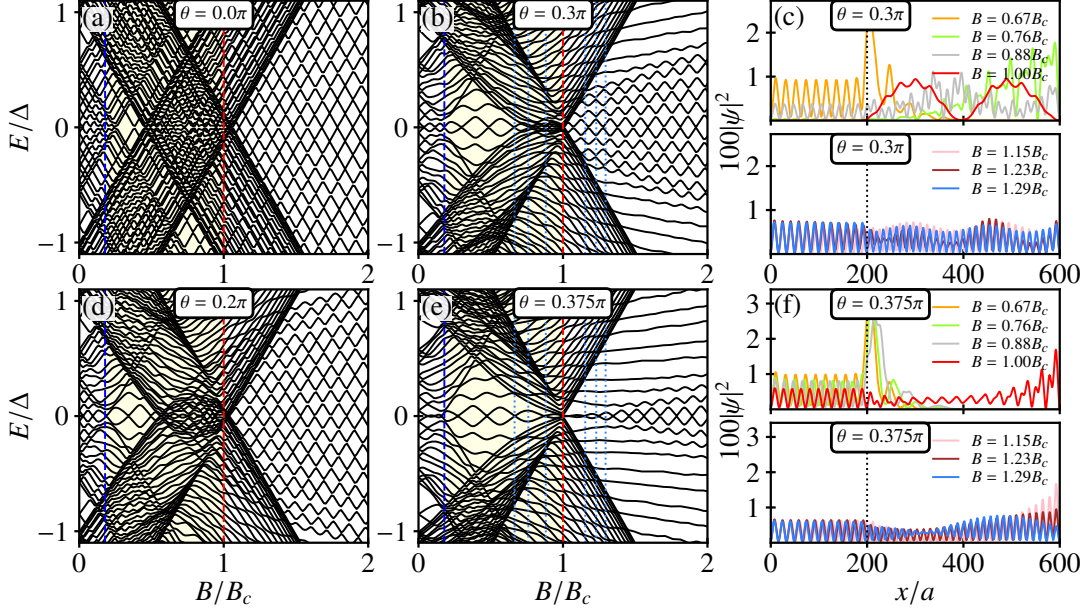


Figure 3.9: Low-energy spectrum for an NS junction with the Zeeman field B in N and S as a function of B at distinct values of the polar angle θ of the Zeeman field: (a) $\theta = 0$, (b) $\theta = 0.3\pi$, (c) $\theta = 0.2\pi$, and (d) $\theta = 0.375\pi$. Wavefunction probability densities of the state closest to zero energy as a function of the spatial coordinate at $\theta = 0.3\pi$ (c) and $\theta = 0.375\pi$ (f). The blue and red curves mark $B = \mu_N$ and $B = B_c$, respectively. The dotted curves in (b,e) indicate the values of B at which the wavefunction probability densities are plotted in (c,f). Parameters: $L_N = 200a$, $L_S = 400a$, and $\phi = 0$. The rest of the parameters are the same as in Fig. 3.5.

that the magnitudes of all pair amplitudes are strongly suppressed in the gapless regimes, consistent with the absence of well-defined bound states. Sharp resonant peaks appear precisely at the critical angles θ_c and $\pi - \theta_c$, marking the points of bulk gap closure. Within the gapped topological window, the OTE components d_y and d_z are dominant and maximized near $\theta = \pi/2$, reaffirming that a perpendicular field configuration is optimal for generating these unconventional pairs.

The dependence on the azimuthal angle ϕ , shown in panel (b) for the optimal $\theta = \pi/2$ case, reveals the anisotropic nature of the spin-triplet pairing. This behavior is a direct manifestation of the distinction between short-range and long-range triplet pairs. When the field is along x ($\phi = 0$), it breaks pairs with spin projection zero along the x -axis, which corresponds to the d_x component. This component is thus suppressed in the normal region, as seen in the spatial profile of Fig. 3.10(c).

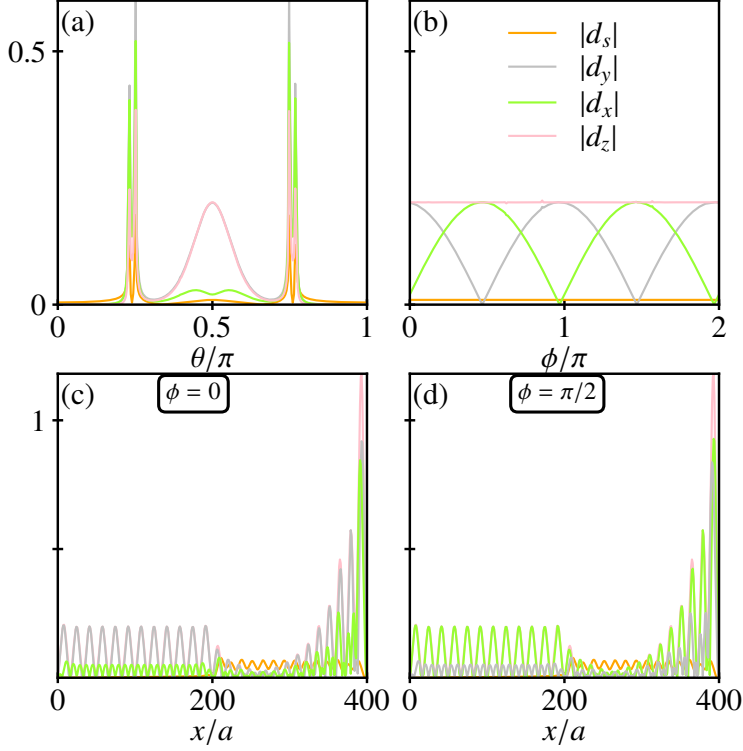


Figure 3.10: Absolute value of the pair amplitudes $|d_\beta|$ in the topological phase at $\omega \approx 0$ near the NS interface in N ($x = 192a$) as a function of θ at $\phi = 0$ (a) and as a function of ϕ at $\theta = 0.5\pi$ (b). (c) Spatial profile of the pair amplitudes at $\omega \approx 0$ and for $\theta = \pi/2$ and $\phi = 0$. (d) Same as in (c) for $\phi = \pi/2$. Parameters: $x = 192a$, $B = 1.23B_c$, $L_N = 200a$, and $L_S = 200a$. The rest of the parameters are the same as in Fig. 3.5.

Similarly, when the field is along y ($\phi = \pi/2$), the d_y component is suppressed (Fig. 3.10(d)). The d_z component, whose constituent spins are polarized along the field direction, represents a long-range, spin-polarized supercurrent that is robust against this dephasing. This is a manifestation of short- and long-range spin-polarized supercurrents, discussed before in the context of FS junctions [94–96]. The strong dependencies of the phase boundaries and the anisotropic nature of the OTE pairing on the field orientation provide a rich set of additional experimental knobs. A systematic study of these angular dependencies could provide a multi-faceted approach to confirming the presence of either helical or topological states.

3.6 Conclusions

In this chapter, we have performed an in-depth theoretical investigation into the nature of emergent superconducting correlations in semiconductor-superconductor junctions, with the primary goal of establishing a robust method for distinguishing between topologically trivial Andreev bound states and genuine Majorana bound states. We addressed the critical issue that both types of states can manifest as zero-energy features in transport experiments, creating significant ambiguity. By systematically analyzing two distinct junction configurations—one engineered to host only trivial ABSs and another capable of hosting both ABSs and MBSs—we have mapped out the unique fingerprints associated with each, focusing on their spatial properties, frequency dependence, and response to geometric and external parameters.

A key physical distinction that we have highlighted is the difference in spatial locality between the two types of in-gap states. Trivial ABSs, which in our model arise from the combination of helicity and confinement in the normal region, are fundamentally interface phenomena. We have shown that their properties, including their low-energy spectrum and associated pairing correlations, are largely determined by the normal metal and are insensitive to the length of the adjacent superconductor. In stark contrast, Majorana bound states are intrinsically non-local quantum objects, existing as a pair of states localized at the opposite ends of the topological superconducting segment. We have demonstrated that this inherent nonlocality has a direct and measurable consequence: the energy splitting of the MBS pair, and consequently their associated zero-frequency signatures, are strongly and controllably dependent on the superconducting length L_S . This geometric dependence serves as a powerful, albeit experimentally challenging, tool for differentiation.

Our central analysis focused on the symmetry of the proximity-induced Cooper pairs, which provides a deeper understanding of the physics at play. We have demonstrated that in these systems with broken spin-rotation and time-reversal symmetries, both conventional even-frequency spin-singlet (ESE) and unconventional odd-frequency spin-triplet (OTE) correlations coexist and determine the system's properties. However, their roles are starkly different. In the helical phase, while the presence of trivial ABSs can significantly enhance the OTE pairing amplitude, this pairing always exhibits a strictly linear dependence on frequency, causing it to vanish exactly at $\omega = 0$. This behavior, which is independent of the superconducting length L_S , robustly signals the topologically trivial nature of the underlying state. The situation is profoundly different in the topological phase, where the nature of the OTE pairing becomes a sensitive probe of Majorana physics.

The definitive signature of a true, well-isolated Majorana bound state, as we

have shown, is the emergence of a divergent, $\sim 1/\omega$ profile in the odd-frequency pairing amplitude. This unique feature is a direct consequence of the Majorana's defining self-conjugate property ($\gamma = \gamma^\dagger$), which imprints a singular pole structure onto the anomalous Green's function. Crucially, we demonstrated that this divergent signature is only fully realized when the MBSs are true zero-energy modes, a condition that is only met in the limit of long superconductors where L_S is much greater than the Majorana localization length, effectively suppressing their hybridization. For shorter topological segments, the residual hybridization splits the MBSs into a finite-energy Andreev-like pair, which regularizes the OTE pairing back to a linear frequency dependence near $\omega = 0$, making it superficially resemble the trivial case. Therefore, the divergent OTE profile is not just a sign of topology, but a signature of Majorana nonlocality and quantum coherence extending over the length of the superconductor.

Finally, we extended our analysis to consider the effect of a generic Zeeman field orientation, finding that it provides additional knobs for experimental control and characterization. The stability windows of both the helical and topological phases, as well as the anisotropic structure of the OTE d-vector, show strong and distinct dependencies on the polar and azimuthal angles of the field. In summary, this chapter provides a comprehensive theoretical framework for using the rich physics of odd-frequency pairing to navigate the complex landscape of zero-energy states in superconductor-semiconductor hybrids, establishing the divergent, geometrically-sensitive OTE pairing as a robust and definitive signature of non-local Majorana physics.

Chapter 4

Anomalous Proximity Effect in Semiconductor-Superconductor Junctions

In the previous chapter, we have established odd-frequency pairing as a powerful probe of topological superconductivity. Unfortunately, to our knowledge, it is not possible to directly observe odd-frequency pairing in experiment and we are limited to indirect measurement. Nonetheless, it is still possible to observe its indirect effects. One promising indirect signature of odd-frequency pairing and topology is the anomalous proximity effect characterized by a zero-energy peak (ZEP) in the local density of states and quantized conductance observed in disordered normal metal/superconductor junctions. We note that the anomalous proximity effect has been explored previously as a signature of non-trivial superconductivity in [36–45], however, previous theoretical investigations have relied on semiclassical approximations such as Usadal equation or have assumed infinite system sizes. This has left largely unexplored how the anomalous proximity effect precisely manifests in realistic, finite-length systems and, critically, whether trivial ABSs common in such setups can also generate a ZEP obscuring true Majorana signatures.

In this chapter, we theoretically investigate the anomalous proximity effect in finite-length clean normal metal/disordered normal metal/superconductor (CN/DN/S) junctions based on a Rashba semiconductor nanowire model. We systematically analyze the LDOS and the induced spin-singlet and odd-frequency spin-triplet pair correlations at the edge of the normal metal. We find that while both the trivial ABSs and topological MBSs can induce a ZEP in the LDOS in the clean limit, which is predominantly generated by odd-frequency spin-triplet pair correlations, their behavior under disorder reveals crucial distinctions. The ZEP associated with trivial ABSs is shown to be universally fragile, rapidly splitting with increasing disorder. In contrast, the ZEP originating from MBSs in the

topological phase exhibits a stability that is critically contingent on the length of the S region. For short S segments, this topological ZEP also shows fragility similar to the trivial case. However, when the S region is sufficiently long, the ZEP remains robustly pinned at zero energy even in the presence of significant disorder. Throughout these scenarios, conventional spin-singlet correlations are found to be consistently suppressed near zero energy in the normal metal. This pronounced difference in the disorder resilience of the ZEP therefore serves as a key distinguishing feature between topological MBSs and trivial ABSs.

Our results pave the way to better understand the conditions under which the anomalous proximity effect can serve as a reliable diagnostic for MBSs in realistic, unconventional geometries, and highlight the pivotal role of spin-triplet pairing. This chapter is primarily based on our publication, Ahmed et al. [2].

4.1 Model and Methods

To study the anomalous proximity effect, we extend the model we introduced in chapter 3. Particularly, we consider a Rashba nanowire partially proximated in the right segment to a conventional s-wave superconductor, thus realizing a superconducting (S) segment. The unproximated segment is a normal metallic (N) segment. This segment is divided into two regions; the normal metallic region adjacent to the S region is considered dirty (DN) with onsite scalar disorder, meanwhile, the left region is considered clean (CN). Thus, we realize a clean normal metal/disordered normal metal/superconductor (CN/DN/S) junction geometry. We assume that the normal metallic region -including the clean and dirty regions- is depleted, thus having a lower chemical potential than that of the superconducting region. Furthermore, a uniform external Zeeman field is applied along the entire junction. A schematic of this setup is presented in Fig. 4.1.

As we see in Fig. 4.1, we set the length of each segment as follows: L_{CN} is the length of the CN segment, L_{DN} is the length of the DN segment, and L_S is the length of the S segment. We also take the length of the entire normal region contained both the CN and DN region to be L_N . We assume that a probe is attached at the left end of the junction where we do our measurements.

4.1.1 System Hamiltonian

Having outlined the system geometry, we now explain the theoretical model. We model the system by employing a tight-binding Bogoliubov-de Gennes (BdG) Hamiltonian on a one dimensional lattice with lattice constant a . The Hamiltonian is similar to the one we introduced in Chapter 3 with the exception that now we include an additional dirty metallic region in the middle of the junction.

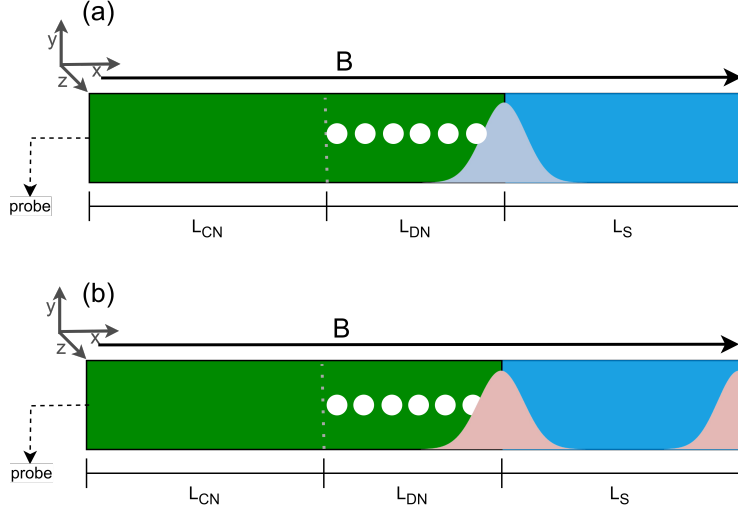


Figure 4.1: Schematic of the CN/DN/S junction.

We express the Hamiltonian in the following way:

$$H = \sum_i \Psi_i^\dagger \mathcal{H}_{ii} \Psi_i + \sum_{\langle i,j \rangle} \left(\Psi_i^\dagger \mathcal{H}_{ij} \Psi_j + \text{H.c.} \right), \quad (4.1)$$

where $\Psi_i = (c_{i\uparrow}, c_{i\downarrow}, c_{i\uparrow}^\dagger, c_{i\downarrow}^\dagger)^T$ is the Nambu spinor at site i , and $c_{i\sigma}^\dagger$ ($c_{i\sigma}$) is the creation (annihilation) operator for an electron with spin σ at site i . In the above equation, the summation $\langle i, j \rangle$ is taken over nearest neighbors only.

Similarly to Chapter 3, we write the local Hamiltonian matrix \mathcal{H}_{ii} as follows:

$$\mathcal{H}_{ii} = (2w - \mu_i - v_i)\tau_z \sigma_0 + B\tau_z \sigma_x + \Delta \Theta(i - L_N/a)\tau_y \sigma_y, \quad (4.2)$$

while the nonlocal Hamiltonian \mathcal{H}_{ij} between nearest-neighbor sites i and $j = i + 1$ is:

$$\mathcal{H}_{ij} = -w\tau_z \sigma_0 - i \frac{\alpha}{2a} \tau_0 \sigma_z. \quad (4.3)$$

Here, we adopt the same notation as in the previous chapter. Mainly, we take τ_j and σ_j to be the Pauli matrices in particle-hole space and spin respectively, with $j = 0, x, y, z$. Here, τ_0 and σ_0 denote the 2×2 identity matrix. The hopping amplitude is t_{hop} , spin-orbit coupling is α , Zeeman field is B , and the proximity-induced s-wave superconducting gap is Δ . The local Hamiltonian contains a Heaviside step function $\Theta(x)$ ensuring that the superconducting term is nonzero only inside the S region, i.e., $x = ja > L_N$. We allow the chemical potential to take different values in each region such that we have:

$$\mu_i = \begin{cases} \mu_N & i \leq L_N/a, \\ \mu_S & i > L_N/a, \end{cases} \quad (4.4)$$

As explained in Chapter 3, in order to realize a system where both trivial and topological bound states can exist, we assume that the chemical potential in the N region to be depleted, taking a smaller value compared to that in the S region ($\mu_N < \mu_S$). Here, we remind the reader that a helical phase transition occur in N at $B = B_h \equiv \mu_N$, while a topological phase transition occur in S at $B = B_c \equiv \sqrt{\mu_S^2 + \Delta^2}$

Disorder enters our Hamiltonian as an on-site scalar term v_i for $L_{CN}/a < i \leq L_N/a$. Scalar disorder is drawn from a uniform normal distributions $v_i \in [-W, W]$ where W represents the strength of the applied scalar disorder. Throughout this chapter, we gauge the strength of disorder relative to the chemical potential in the S region. We consider the regime $W \lesssim \mu_S$ to be the weak disorder regime, $W \approx (1 \sim 3)\mu_S$ is moderate disorder regime where disorder is comparable to the chemical potential, while strong disorder regime corresponds to disorder much larger than the chemical potential $W \gg \mu_S$.

Having introduced the model, we now discuss the parameters used in the numerical simulations for this chapter. We use parameters consistent with Chapter 3 which are representative of InAs and InSb nanowires [16] with the only caveat that we adopt a longer lattice constant in this chapter to speed up numerical computation. This leads to smaller hopping amplitude and smaller lattices. The parameters used are as follows: lattice constant $a = 50\text{nm}$, hopping amplitude $t = 1\text{ meV}$, the chemical potential in the superconductor $\mu_S = 0.5\text{ meV}$, the chemical potential in the normal region $\mu_N = 0.1\text{ meV}$, the superconducting gap $\Delta = 0.25\text{ meV}$, and the spin-orbit coupling strength $\alpha = 20\text{ meV nm}$. This leads to a critical Zeeman field $B_c = \sqrt{\Delta^2 + \mu_S^2} \approx 0.56\text{ meV}$. In the numerical simulations, we consider disorder strengths W varying between 0 and $5\mu_S$ to simulate weak, moderate, and strong disorder regimes. We allow the DN and CN regions lengths to vary while keeping the length of the entire normal region fixed to $L_N = 40a$ throughout the entire chapter. Importantly, we allow the length of the S region to vary between $L_S = 20a$ and $L_S = 100a$ which allow us to understand the behavior of the system under disorder for short and long S regions. Finally, we use an ensemble averaging over 200 independent disorder realizations to smooth out our results.

4.1.2 Calculation of LDOS and Pair Correlations

We now discuss the relevant quantities we calculate in this chapter. We note that while the anomalous proximity effect is an effect regarding quantized conductance, we do not calculate the conductance in this chapter. Instead, we focus on the local density of states (LDOS) and pair correlations. Our motivation is that it is well-known fact in linear response theory that conductance is proportional to the LDOS at the Fermi energy [58, 83, 118]. Therefore, we can use the LDOS as a proxy for conductance. Furthermore, the LDOS provide us with further insight into the

system, such as the nature of the zero-energy states and their robustness against disorder. In addition to the LDOS, we also calculate the pair correlations. For that purpose, we use the Nambu Green's function method defined in Section 2.5 as:

$$\mathcal{G}_{j\sigma,j'\sigma'}^{r(a)}(E) = (E \pm i\eta - H)^{-1}_{j\sigma,j'\sigma'}, \quad (4.5)$$

where $r(a)$ denotes the retarded (advanced) Green's function, E is the energy, η is a small positive number, and H is the Hamiltonian of the system. We then utilize the Nambu particle-hole structure and write the Nambu Green's function in the following matrix form:

$$\mathcal{G}_{j\sigma,j'\sigma'}^{r(a)}(E) = \begin{pmatrix} G_{j\sigma,j'\sigma'}^{r(a)} & F_{j\sigma,j'\sigma'}^{r(a)} \\ \tilde{F}_{j\sigma,j'\sigma'}^{r(a)} & \tilde{G}_{j\sigma,j'\sigma'}^{r(a)} \end{pmatrix}, \quad (4.6)$$

where $G_{j\sigma,j'\sigma'}^{r(a)}$ is the normal Green's function, $F_{j\sigma,j'\sigma'}^{r(a)}$ is the anomalous Green's function, and $\tilde{F}_{j\sigma,j'\sigma'}^{r(a)}$ and $\tilde{G}_{j\sigma,j'\sigma'}^{r(a)}$ are their corresponding particle-hole conjugates. Now, let us define the projection operators into the particle space and hole space as follows:

$$P_p = 0.5(\tau_z + \tau_0)\sigma_0, \quad P_h = 0.5(\tau_z - \tau_0)\sigma_0. \quad (4.7)$$

Using these projection operators, we can extract the electron and hole local density of states at site i and energy E as follows: n

$$\rho_p(E, i) = -\frac{1}{\pi}\text{Im}[Tr(P_p \mathcal{G}_{ii}^r(E))], \quad (4.8)$$

$$\rho_h(E, i) = -\frac{1}{\pi}\text{Im}[Tr(P_h \mathcal{G}_{ii}^r(E))]. \quad (4.9)$$

Here, the trace is taken over the spin and particle-hole indices. $\rho_p(E, i)$ and $\rho_h(E, i)$ are the electron and hole local density of states at site i and energy E , respectively. The local density of states (LDOS) is then defined as the sum of the electron and hole parts:

$$\rho(E, i) = \rho_p(E, i) + \rho_h(E, i) = -\frac{1}{\pi}\text{Im}[Tr(\mathcal{G}_{ii}^r(E))]. \quad (4.10)$$

We also study the pair correlations in the system. Since we consider a disordered system, we focus only on the local pair correlations due to their robustness against disorder [76]. Similarly to the previous chapter, we use the d-vector representation of the anomalous Green's function to extract the local pair correlations. The anomalous Green's function at site i and energy E is defined as:

$$\hat{F}(i, E) = (d_s(i, E) + \vec{d}(i, E) \cdot \vec{\sigma})(i\sigma_y), \quad (4.11)$$

with d_s being the spin-singlet component and $\vec{d} = (d_x, d_y, d_z)^T$ being the spin-triplet components of the pair correlations. The local pair correlations can be calculated as:

$$d_s(i, E) = \frac{F_{i\uparrow,i\downarrow}(E) - F_{i\downarrow,i\uparrow}(E)}{2}, \quad (4.12)$$

$$d_x(i, E) = \frac{F_{i\downarrow,i\downarrow}(E) - F_{i\uparrow,i\uparrow}(E)}{2}, \quad (4.13)$$

$$d_y(i, E) = i \frac{F_{i\downarrow,i\uparrow}(E) + F_{i\uparrow,i\downarrow}(E)}{2}, \quad (4.14)$$

$$d_z(i, E) = \frac{F_{i\uparrow,i\downarrow}(E) + F_{i\downarrow,i\uparrow}(E)}{2}. \quad (4.15)$$

The antisymmetric nature of the pair amplitudes ensures that the local spin-singlet component d_s is even in frequency, while the local spin-triplet components d_x , d_y , and d_z are odd in frequency as we have discussed in Chapter 3 and Section 2.5. See also [31–34, 88, 94]. We note that in this chapter, we focus on the magnitude of the d-vector only, i.e., $|d_s|$, and $|\vec{d}| = \sqrt{d_x^2 + d_y^2 + d_z^2}$. We don't consider different components of the d-vector separately as they are not relevant to the anomalous proximity effect.

We end this section by noting that the LDOS and pair correlations are calculated at the leftmost site of the N region ($i = 1$) where the probe is attached. This is done to simulate a realistic experimental setup where the probe is attached to the left end of the junction. The parameters used in the numerical simulations are the same as those used in the previous chapter, with the exception that we scale the lattice constant to $a = 50$ nm to speed up numerical computation. This leads to smaller hopping amplitude and smaller lattices overall. The parameters used are: the hopping amplitude $w = 1$ meV, the chemical potential in the superconductor $\mu_S = 0.5$ meV, the chemical potential in the normal region $\mu_N = 0.1$ meV, the superconducting gap $\Delta = 0.25$ meV, and the spin-orbit coupling strength $\alpha = 20$ meV nm. We consider a range of disorder strengths W varying between 0 and $5\mu_S$ to simulate weak, moderate, and strong disorder regimes. To study the effect of the S region length, we consider $L_S = 20a, 40a, 60a, 80a, 100a$. We also consider different lengths of the DN region $L_{DN} = 2a, 20a, 40a$ while keeping the length of the entire normal region always fixed to $L_N = 40a$. The critical Zeeman field for the topological transition is $B_c = \sqrt{\Delta^2 + \mu_S^2} \approx 0.56$ meV. The broadening parameter is set to $\eta = 10^{-3}$. Results involving disorder are averaged over 200 independent of disorder realizations, unless otherwise specified. We emphasize that since we scaled the lattice constant to $a = 50$ nm, the number of lattice sites in the system is significantly reduced compared to the previous chapter. Thus, one needs to be careful when comparing the results of this chapter with those of the previous chapter.

4.2 Low-Energy Spectrum and Zero-Energy States in CN/DN/S Junctions

As we explained in Section 2.6, the anomalous proximity effect is characterized by quantized conductance at zero bias voltage. This can be explained by multiple Andreev reflections (MARs) at the DN/S interface independent of disorder. In Section 2.6.2, we have shown that this robust quantized conductance is due to the presence of zero-energy states in the junction which facilitate the MARs. We have shown that in the limit of very strong disorder and assuming semi-infinite S, robust conductance quantization is only possible if the zero-energy states are protected by chiral symmetry. However, in the presence of finite-length S regions, the zero-energy states can hybridize and acquire finite energy. Such finite energy states can still lead to almost quantized conductance, but they are not robust against disorder. Therefore, to understand the anomalous proximity effect in finite-length CN/DN/S junctions, we need to study the low-energy spectrum of the junction and the nature of the zero-energy states. Of particular interest is the behavior of the zero-energy states under disorder and how they depend on the length of the S region.

4.2.1 Low-Energy Spectrum in CN/DN/S Junctions with Short S Regions

We consider a CN/DN/S junction with a short S region ($L_S = 20a$) under the influence of disorder in the DN region. We consider different lengths of the DN region $L_{DN} = 2a, 20a, 40a$ while keeping the length of the entire normal region fixed to $L_N = 40a$. We calculate the low-energy spectrum as a function of the Zeeman field B for both single disorder realizations and ensemble averages. The results are shown in Fig. 4.2. Before we discuss the effect of disorder on the low-energy spectrum, we first examine the clean limit (light gray curves in Fig. 4.2). In the clean limit, the low-energy spectrum of the CN/DN/S junction is exactly the same as that of the clean NS junction we discussed in Chapter 3. In other words, the junction undergoes two phases transitions: a helical phase transition in the N region at $B = B_h \equiv \mu_N$ and a topological phase transition in the S region at $B = B_c \equiv \sqrt{\Delta^2 + \mu_S^2}$. In the helical phase ($\mu_N < B < B_c$), we observe trivial Andreev bound states (ABSs) localized at the interface and oscillating around zero energy as a function of increasing Zeeman field B . In the topological phase ($B > B_c$), we observe zero-energy MBSs localized at the ends of the S region. Due to the short length of the S region, these MBSs hybridize, leading to energy eigenvalues that oscillate around zero energy as a function of increasing Zeeman field B .

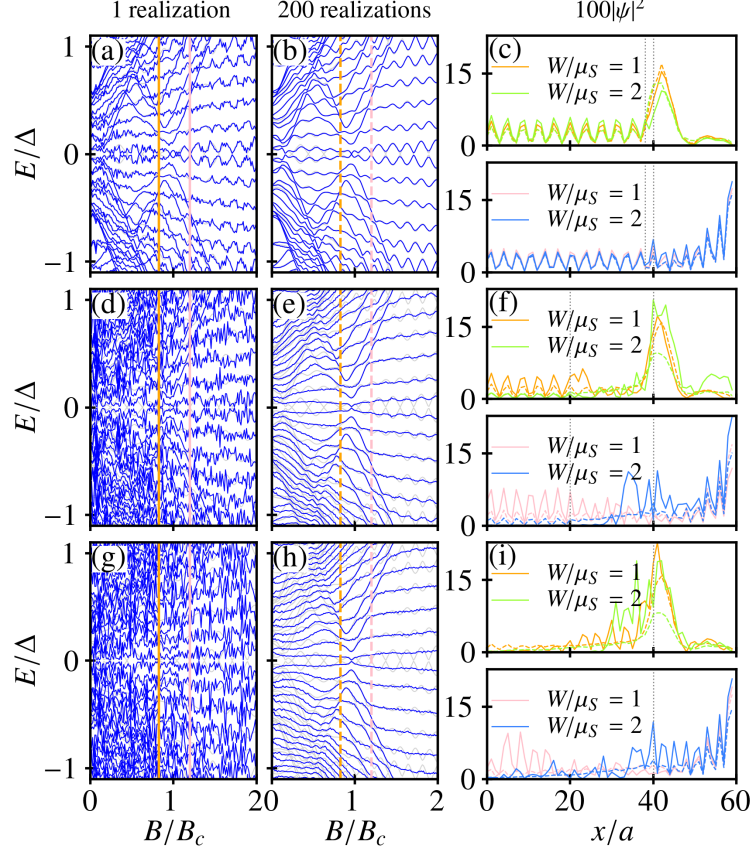


Figure 4.2: Low energy spectrum for CN/DN/S junction with short S region as a function of the Zeeman field B at $W = \mu_S$ for $L_{DN} = 2a$ (a,b), $L_{DN} = 20a$ (d,e), and $L_{DN} = 40a$ (g,h). Panels (a,d,g) show the spectrum for one disorder realization, whereas panels (b,e,h) show the average spectrum over 200 disorder realizations. The light gray curves in (a,b,d,e,g,h) show the spectrum for the clean case ($W = 0$). Panels (c,f,i) show the wavefunction probability density of the zero-energy states with one disorder realization (solid) and for ensemble average (dashed) with $L_{DN} = 2a$ (c), $L_{DN} = 20a$ (f), and $L_{DN} = 40a$ (i). The top panels in (c,f,i) show the wavefunction probability density for the trivial zero-energy ABSs at $B = 0.825B_c$, whereas the bottom row shows the wavefunction probability density for the MBSs at $B = 1.2B_c$. The orange and pink curves in (a,b,d,e,g,h) show the values of B for which the wavefunction probability density is shown in (c,f,i). The parameters used are: $L_S = 20a$, $L_N = 40a$, $a = 50$ nm, $\mu_S = 0.5$ meV, $\mu_N = 0.1$ meV, $\Delta = 0.25$ meV, $\alpha = 20$ meV nm, $w = 1$ meV, and $W = \mu_S$ unless otherwise stated.

Next, we turn on disorder in the DN region. We set the disorder strength to $W = \mu_S$ which is a moderate disorder strength comparable to the chemical potential in the S region. Naively, we expect that disorder will lead to a smearing of the low-energy spectrum and a splitting of the zero-energy states in the trivial phase. Meanwhile, in the topological phase, naively, we expect that the MBSs will remain at zero energy and disorder will not affect them. However, as we see in Fig. 4.2, this is not the case. In fact, we see that contingent on the length of the DN region, disorder can significantly affect the low-energy spectrum in both the trivial and topological phases.

If we consider a single disorder configuration as in Fig. 4.2(a,d,g), the spectrum has frequent violent fluctuations with B . The energy levels oscillate rapidly and frequently hit zero energy, even in the trivial phase ($B < B_c$). The fluctuations become more rapid as the length of the DN region increases, compare Fig. 4.2(a) with Fig. 4.2(d,g). This rapid oscillatory behavior is observed for all values of B regardless of whether the system is in the trivial or topological phase.

Let us now consider the ensemble averaged spectrum in Fig. 4.2(b,e,h). Ensemble averaging reduces the rapid fluctuations in the spectrum, leading to a smoother behavior. This allows us to see the effect of disorder on the low-energy spectrum more clearly. Our first observation is that disorder opens a gap in the low-energy spectrum in both the trivial and topological phases which grows with increasing DN region length. This is evident in Fig. 4.2(b,e,h) where we see that zero-energy states in the trivial phase ($B < B_c$) and the topological phase ($B > B_c$) acquire finite energy. On the other hand, we notice that when the bound states are not exactly at zero energy, disorder can, in fact, decrease the energy of the bound state (compare the gray and blue curves near oscillation maxima in Fig. 4.2(e,h)). Our second observation is that the oscillations around zero energy in the clean limit are significantly suppressed in the presence of disorder in both the trivial and topological phases. We also observe that the longer the DN region, the more pronounced the suppression of oscillations becomes. If the DN region is very short (Fig. 4.2(b)), the suppression is minimal, and the spectrum retains its shape. We also see that the topological phase is more robust against disorder than the trivial phase. As we increase the length of the DN region; however, both the trivial and topological phases show a similar fragility against disorder. Particularly, when the entire N region is dirty (Fig. 4.2(h)), the oscillations in the spectrum are completely suppressed, and the energy levels become almost flat. In this case, the lowest positive energy level in both the trivial and topological phases disperse linearly with the Zeeman field B with a negative slope in the helical phase and a positive slope in the topological phase. Interestingly, we also observe that the gap closing in the topological phase ($B = B_c$) is a robust feature of the low-energy spectrum, even in the presence of disorder. This is in contrast to the trivial phase where the gap

closing is not robust against disorder and the gap can remain open for long DN regions.

We now turn our attention to the zero-energy states probability density shown in Fig. 4.2(c,f,i). We focus on the zero-energy states at $B = 0.825B_c$ in the trivial phase (top panels) and $B = 1.2B_c$ in the topological phase (bottom panels), which correspond to the values of B for which the lowest positive energy level is at the zero energy crossing in the clean limit for $L_S = 20a$. we show the wavefunction probability density for a single disorder realization (solid lines) and for the ensemble average (dashed lines) with $W = \mu_S$ and $W = 2\mu_S$. For $L_{DN} = 2a$, we see that the wavefunction probability density in both the trivial and topological phases is robust against disorder. The wavefunction is localized at the DN/S interface in the trivial phase and at the ends of the S region in the topological phase. The oscillatory profile of the wavefunction in the N region is also preserved, similar to the clean limit. This is expected since the DN region is very short and disorder cannot significantly affect the wavefunction profile. As we increase the length of the DN region to $L_{DN} = 20a$ and $L_{DN} = 40a$, the effect of disorder on the wavefunction profile becomes more noticeable. In both the trivial and topological phases, the wavefunction become more localized at the DN/S interface and decays exponentially into the N region. As a result, the oscillatory behavior in the N region is lost. Particularly, in the topological phase, MBSs cannot leak into the N region as they do in the clean limit. Instead, they behave similarly to the trivial ABSs, being localized at the DN/S interface with decaying profile into the N region. We note that the decay length of the wavefunction into the N region increases with increasing disorder strength W . We note that due to the increased localization of the MBS at the DN/S interface, the overlap between the MBSs at the ends of the S region is enhanced, leading to a larger energy splitting between the MBSs.

4.2.2 Dependence on S Region Length

In the previous section, we saw that disorder can significantly affect the low-energy spectrum in CN/DN/S junctions with short S regions. Particularly, disorder can lead to an increase of the overlap between the MBSs wavefunctions, leading to energy hybridization and finite energy gap opening. It stands to reason that by increasing the length of the S region, we can reduce the overlap between the MBSs wavefunctions and thus reduce the effect of disorder on the low-energy spectrum. In this section, we investigate the effect of disorder in CN/DN/S junctions with different lengths of the S region. In particular, we consider the case of $L_S = 20a, 40a, 60a, 80a, 100a$ and study the stability of the lowest positive energy level in the trivial and topological phases against increasing disorder strength W . We also consider different lengths of the DN region $L_{DN} = 2a, 20a, 40a$ while keeping the length of the entire normal region fixed to $L_N = 40a$. Let us first consider

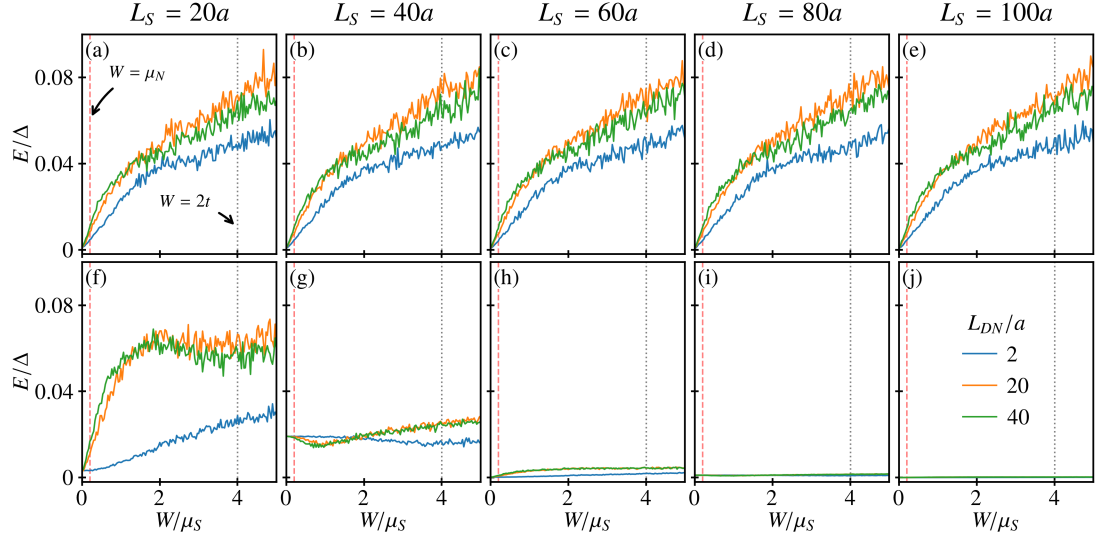


Figure 4.3: Lowest positive energy level E as a function of scalar disorder strength W in the trivial $B = 0.825B_c$ (a,b,c,d,e) and topological $B = 1.2B_c$ (f,g,h,i,j) phases for $L_S = 20a$ (a,f), $L_S = 40a$ (b,g), $L_S = 60a$ (c,h), $L_S = 80a$ (d,i), and $L_S = 100a$ (e,j). The parameters used are: $L_N = 40a$, $a = 50$ nm, $\mu_S = 0.5$ meV, $\mu_N = 0.1$ meV, $\Delta = 0.25$ meV, $\alpha = 20$ meV nm, $t = 1$ meV, $B = 0.825B_c$ for the trivial phase and $B = 1.2B_c$ for the topological phase.

the case of the trivial phase at $B = 0.825B_c$ in Fig. 4.3(a-e). We see that the zero-energy or near-zero energy states in the trivial states are highly sensitive to disorder regardless of the length of the S or DN regions. In particular, we observe that the ABS energy grows linearly with disorder strength W for weak-to-moderate disorder ($W \lesssim 2\mu_S$). For moderate to strong disorder ($W \gtrsim 2\mu_S$), we see that the energy splitting of the ABSs is slowed down slightly with a smaller slope. This behavior is independent of the length of the S region. Surprisingly, we also see that the length of the DN region has a negligible effect on the lowest positive energy level in the trivial phase with different lengths of the DN region leading to almost identical results. This is in contrast to the topological phase, where the length of the DN region affect the energy of the lowest positive energy level in short S regions significantly, as we will see below.

We now shift our focus to the topological phase at $B = 1.2B_c$ in Fig. 4.3(f-j). In that case, we observe a general trend that the energy splitting of MBSs is suppressed with increasing L_S . For short S region (Fig. 4.3(f)), we see a clear difference between short and long DN regions in the topological phase. For short DN regions ($L_{DN} = 2a$), the energy splitting of MBSs is significantly smaller than that of longer DN regions ($L_{DN} = 20a$ and $L_{DN} = 40a$). On the other hand, for

longer DN regions, the energy splitting of MBSs is almost identical to that of the trivial ABSs, see Fig. 4.3(a,f). This indicates that MBSs in short S regions show some robustness against disorder especially for short DN regions. However, it is not robust enough to survive longer DN regions, making it difficult to distinguish between the trivial and topological phases in junctions with short S regions. On the other hand, for long S regions ($L_S = 80a$ and $L_S = 100a$), we see that the energy splitting is completely suppressed regardless of the length of the DN region or the disorder strength W . Thus, MBSs in long S regions are robustly pinned to zero energy regardless of the disorder strength.

We note that for $L_S = 40a$ and for our choice of parameters, the lowest positive energy level in the topological phase is not exactly at zero energy in the clean limit (see Fig. 4.3(g)). We have encountered this situation in the previous chapter, see Fig. 3.7. In that figure, we have shown that the lowest positive energy level in the topological phase oscillates at zero energy with exponentially decaying amplitudes as a function of increasing superconductor length L_S . Thus, the lowest positive energy level in the topological phase is not exactly at zero energy in the clean limit for $L_S = 40a$ even though it was at zero energy for $L_S = 20a$. Let's now discuss the effect of disorder on the lowest positive energy level in the topological phase for $L_S = 40a$ where the energy is not exactly at zero energy in the clean limit. In this case, we see that the energy of the lowest positive energy level initially decreases with increasing disorder strength W in the weak-to-moderate disorder regime ($W \lesssim 2\mu_S$). In the moderate-to-strong disorder regime ($W \gtrsim 2\mu_S$), the energy continues to decrease if DN region is short ($L_{DN} = 2a$), while it starts to increase for longer DN regions ($L_{DN} = 20a$ and $L_{DN} = 40a$).

Given that trivial ABSs mimic topological MBSs in junctions with short S segment, we are interested in understanding the associated LDOS in both phases. Since current experiments rely

4.3 LDOS and Pair Correlations in CN/DN/S Junctions

Given that the MBSs in the topological phase behave similarly to the trivial ABSs in junctions with short S regions, we are interested in understanding whether the LDOS and pair correlations can distinguish between the trivial and topological phases in the presence of disorder. We note that many experimental setups rely on the zero-bias peak (ZEP) in the LDOS to identify MBSs in the topological phase. However, as we have seen in the previous section, MBSs in short superconductors are lifted from zero energy and behave similarly to trivial ABSs. We expect that the LDOS and pair correlations should reflect this behavior. Nevertheless, we will

see that the LDOS and pair correlations can still provide us with useful information about the nature of the zero-energy states in CN/DN/S junctions. In this section, we will first discuss the proximity effect for short S regions and then discuss the LDOS and pair correlations for long S regions.

4.3.1 No Anomalous Proximity Effect in CN/DN/S Junctions with Short S Regions

In this section, we investigate the LDOS and pair correlations in CN/DN/S junctions with short S regions ($L_S = 20a$) under the influence of disorder in the DN region. We consider different lengths of the DN region $L_{DN} = 2a, 20a, 40a$ while keeping the length of the entire normal region fixed to $L_N = 40a$. We calculate the LDOS at the leftmost site of the N region ($i = 1$) as a function of energy E and disorder strength W . We also calculate the pair correlations at the same site and energy. The results are shown in Figs. 4.4, 4.5, and 4.6 for the LDOS, spin-singlet pair correlations, and spin-triplet pair correlations, respectively. We consider both the trivial phase at $B = 0.825B_c$ and the topological phase at $B = 1.2B_c$.

Fig. 4.4 shows the LDOS at $i = 1$ as a function of energy E and disorder strength W for different lengths of the DN region. The top row (a,b,c,d,e) shows the LDOS for the trivial phase, while the bottom row (f,g,h,i,j) shows the LDOS for the topological phase. First, let us focus on the LDOS in the trivial phase (top row of Fig. 4.4). When disorder is switched off ($W = 0$), a sharp zero-energy peak (ZEP) appears in the LDOS, see Fig. 4.4(a-c) as well as the grey curve in Fig. 4.4(d). Switching on disorder leads to a splitting of the ZEP into a fan-shaped structure in the LDOS, see Fig. 4.4(a,b,c). Thus even for very small disorder strength and even for very short DN regions, the ZEP in the trivial phase is very sensitive to disorder. Indeed, we see that in Fig. 4.4(d), the ZEP in the trivial phase is completely smeared out for $W/\mu_S = 1$ and $W/\mu_S = 2$. In fact, the ZEP in the trivial phase is completely flattened out into an almost constant value in the energy range inside the fan-shaped structure independent of the DN region's length, see the colored curves in Fig. 4.4(d).

Interestingly, if we fix the energy $E \approx 0$ and look at the spatial profile of the LDOS in Fig. 4.4(e), we see that the effect of disorder is not limited to the DN region, but it also affects the entire junction including the the clean normal metal CN and superconducting S regions. When disorder is absent, the LDOS is sharply peaked at the N/S interface and has oscillatory profile in the entire N region. As disorder is introduced, the LDOS is suppressed across the entire junction. The peak at the N/S interface becomes significantly smaller and the oscillatory profile in the N region is replaced by a decaying profile. Note that some oscillations are still present in the LDOS profile, but they are significantly suppressed compared

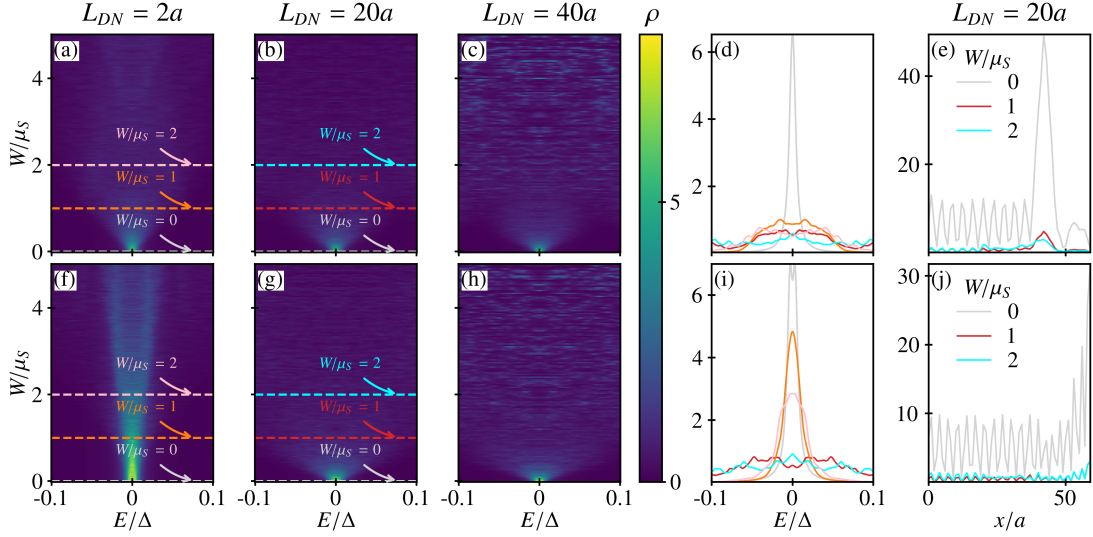


Figure 4.4: LDOS for short S region ($L_S = 20a$) junctions evaluated at the leftmost site of the N region ($i = 1$) as a function of energy E and scalar disorder strength W with $L_{DN} = 2a$ (a,f), $L_{DN} = 20a$ (b,g), and $L_{DN} = 40a$ (c,h). Panels (d,i) show line cuts of the LDOS in (a,f,b,g) for $W/\mu_S = 0, 1, 2$. Panels (e,j) show the spatial profile of the LDOS at $E \approx 0$ for $W/\mu_S = 0, 1, 2$ with $L_{DN} = 20a$. Top row (a,b,c,d,e): trivial phase ($B = 0.825B_c$). Bottom row (f,g,h,i,j): topological phase ($B = 1.2B_c$). Other parameters used are: $L_S = 20a$, $L_N = 40a$, $a = 50$ nm, $\mu_S = 0.5$ meV, $\mu_N = 0.1$ meV, $\Delta = 0.25$ meV, $\alpha = 20$ meV nm, $w = 1$ meV, and $\eta = 0.001$ meV.

to the clean limit. Interestingly, the LDOS in the S region is completely absent in the presence of disorder, indicating that the inverse proximity effect is completely suppressed. This is in contrast to the clean limit where the LDOS in the S region is finite.

Having discussed the LDOS in the trivial phase, we now turn our attention to the topological phase (bottom row of Fig. 4.4). Similar to the trivial phase, when disorder is switched off ($W = 0$), a sharp ZEP appears in the LDOS, see Fig. 4.4(f-g) as well as the grey curve in Fig. 4.4(i). Switching on disorder also leads to a splitting of the ZEP into a fan-shaped structure in the LDOS, see Fig. 4.4(f,g,h). However, the width of this fan-shaped structure is controlled by the length of the DN region. For short DN regions ($L_{DN} = 2a$), the fan-shaped structure is very narrow, see Fig. 4.4(f). Thus, the ZEP in the topological phase is more robust against disorder than in the trivial phase for short DN regions. As we increase the length of the DN region, the fan-shaped structure becomes wider, see Fig. 4.4(g,h). Interestingly, we see that it is impossible to distinguish between the trivial and

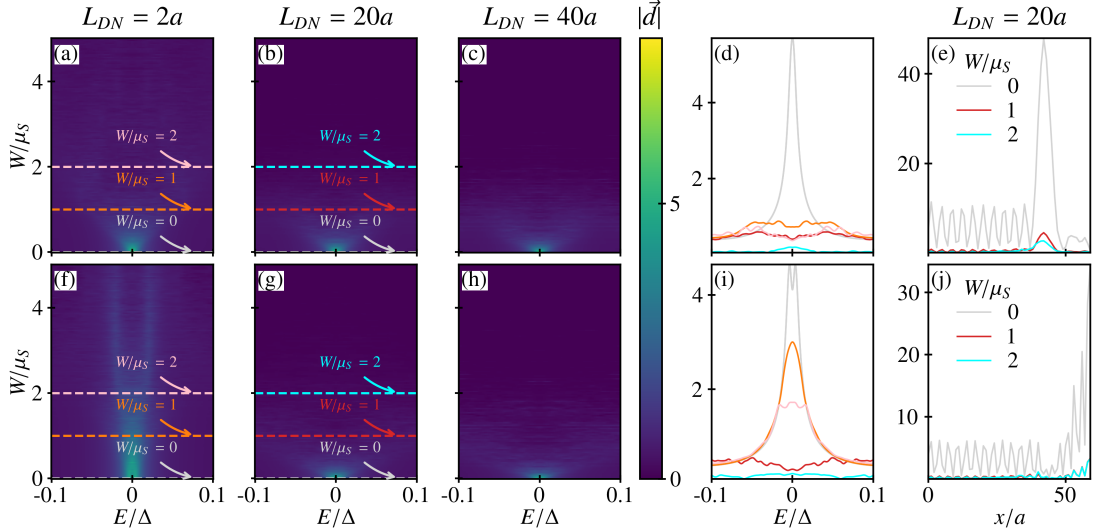


Figure 4.5: Absolute value of the spin-triplet pair correlations $|\vec{d}|$ for short S region ($L_S = 20a$) junctions evaluated at the leftmost site of the N region ($i = 1$) as a function of energy E and scalar disorder strength W with $L_{DN} = 2a$ (a,f), $L_{DN} = 20a$ (b,g), and $L_{DN} = 40a$ (c,h). Panels (d,i) show line cuts of the spin-triplet pair correlations in (a,f,b,g) for $W/\mu_S = 0, 1, 2$. Panels (e,j) show the spatial profile of the spin-triplet pair correlations at $E \approx 0$ for $W/\mu_S = 0, 1, 2$ with $L_{DN} = 20a$. Top row (a,b,c,d,e): trivial phase ($B = 0.825B_c$). Bottom row (f,g,h,i,j): topological phase ($B = 1.2B_c$). Other parameters used are: $L_S = 20a$, $L_N = 40a$, $a = 50$ nm, $\mu_S = 0.5$ meV, $\mu_N = 0.1$ meV, $\Delta = 0.25$ meV, $\alpha = 20$ meV nm, $w = 1$ meV, and $\eta = 0.001$ meV.

topological phases in the presence of disorder for long DN regions. In fact, the LDOS in the topological phase for longer DN regions (see Fig. 4.4(g,h)) is almost identical to that in the trivial phase (see Fig. 4.4(b,c)). This means that we don't have proximity effect for short S regions even in the topological phase. In other words, the ZEP in the topological phase is not a reliable probe for distinguishing between the trivial and topological phases in the presence of disorder with long DN regions. We can gain further insight into the robustness of the ZEP in the topological phase by looking at the spatial profile of the LDOS at $E \approx 0$ in Fig. 4.4(j). We see that the LDOS in the topological phase is also suppressed across the entire junction, similar to the trivial phase. Moreover, even the LDOS at the rightmost site of the S region is also significantly suppressed in the presence of disorder. This is a signature that disorder led to a significant hybridization of the MBSs wavefunctions at the ends of the S region, leading to a finite energy splitting and a total suppression of the anomalous proximity effect.

To understand the origin of the zero-energy peak (ZEP) and the features observed in the LDOS for the short superconducting segment, we now examine the proximity-induced spin-triplet and spin-singlet pair correlations.

Figure 4.5 demonstrates that the magnitude of the spin-triplet correlations, $|\vec{d}|$, closely follows the behavior of the LDOS. In both the trivial (top row) and topological (bottom row) phases, a ZEP in the triplet pairing is present in the clean limit. Upon introducing disorder, this peak rapidly splits and broadens into a fan-shaped structure, mirroring the fragility seen in the LDOS. This is further clarified by the line cuts, which show the sharp peak flattening into a broad, suppressed plateau as disorder strength increases. The spatial profiles [Fig. 4.5(e,j)] reveal that the triplet correlations, while significant at the DN/S interface in the clean limit, are heavily damped by disorder throughout the entire normal region. The key observation is the pronounced similarity in the response of both phases, especially for longer DN regions, confirming that for short S segments, spin-triplet pairing does not offer a clear distinction between trivial and topological states.

In stark contrast, the spin-singlet component, shown in Fig. 4.6, exhibits entirely different characteristics. A universal feature in both the trivial and topological phases is the profound suppression of spin-singlet pairing near zero energy, which manifests as a distinct dip rather than a peak. This dip persists regardless of disorder strength. Moreover, the spatial profiles [Fig. 4.6(e,j)] consistently show that the spin-singlet pairing is negligible within the normal metal (both CN and DN regions) and is effectively confined to the S region. This unambiguous suppression of conventional pairing in the normal wire confirms that the ZEP in the LDOS is not of spin-singlet origin. Instead, the low-energy proximity effect is clearly dominated by unconventional odd-frequency spin-triplet correlations whose fragility in short junctions is the root cause of the suppressed LDOS peak.

4.3.2 Anomalous Proximity Effect for Long S Regions

Having established the inherent fragility of zero-energy features in short superconducting segments, we now turn to the central hypothesis of this chapter: that sufficient topological protection, which can be achieved by physically separating the Majorana bound states, should stabilize their experimental signatures against disorder. We investigate this by increasing the length of the superconducting region to $L_S = 100a$. Theoretically, this increase in length should exponentially suppress the wavefunction overlap between the MBSs at opposite ends of the S segment, quenching their hybridization energy ($E_{hyb} \propto e^{-L_S/\xi}$) and allowing the true, protected nature of the state at the N/S interface to be revealed [66, 84, 115, 119].

The LDOS analysis for this long junction, presented in Fig. 4.7, provides com-

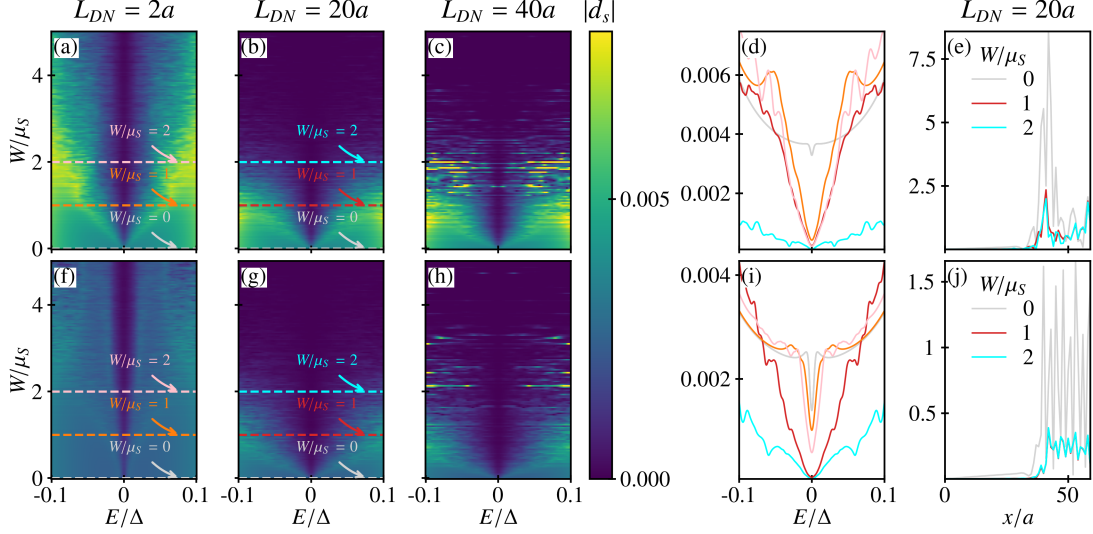


Figure 4.6: Absolute value of the spin-singlet pair correlation for short S region ($L_S = 20a$) junctions evaluated at the leftmost site of the N region ($i = 1$) as a function of energy E and scalar disorder strength W with $L_{DN} = 2a$ (a,f), $L_{DN} = 20a$ (b,g), and $L_{DN} = 40a$ (c,h). Panels (d,i) show line cuts of the spin-singlet pair correlations in (a,f,b,g) for $W/\mu_S = 0, 1, 2$. Panels (e,j) show the spatial profile of the spin-singlet pair correlations at $E \approx 0$ for $W/\mu_S = 0, 1, 2$ with $L_{DN} = 20a$. Top row (a,b,c,d,e): trivial phase ($B = 0.825B_c$). Bottom row (f,g,h,i,j): topological phase ($B = 1.2B_c$). Other parameters used are: $L_S = 20a$, $L_N = 40a$, $a = 50$ nm, $\mu_S = 0.5$ meV, $\mu_N = 0.1$ meV, $\Delta = 0.25$ meV, $\alpha = 20$ meV nm, $w = 1$ meV, and $\eta = 0.001$ meV.

pling evidence supporting this hypothesis by revealing a dramatic divergence in the behavior of the trivial and topological phases. The results for the trivial phase, shown in the top row of Fig. 4.7, unequivocally demonstrate that the length of the S-region has no bearing on the stability of trivial ABSs. The behavior is qualitatively and quantitatively identical to the short-wire case: the ZEP remains highly susceptible to disorder and rapidly devolves into a broad, fan-like continuum. This confirms that the fragility of the trivial ZEP is an intrinsic property of the state itself, not a finite-size effect related to L_S .

In stark and compelling contrast, the topological phase, depicted in the bottom row of Fig. 4.7, undergoes a fundamental change in its character. The ZEP, which was fragile for short L_S , now exhibits profound robustness against disorder. As seen in the 2D plots of panels (f), (g), and (h), the ZEP persists as a sharp, bright line at precisely $E = 0$ across the entire range of disorder strengths studied, up to $W = 5\mu_S$. The fan-like splitting that characterized the trivial state is completely absent.

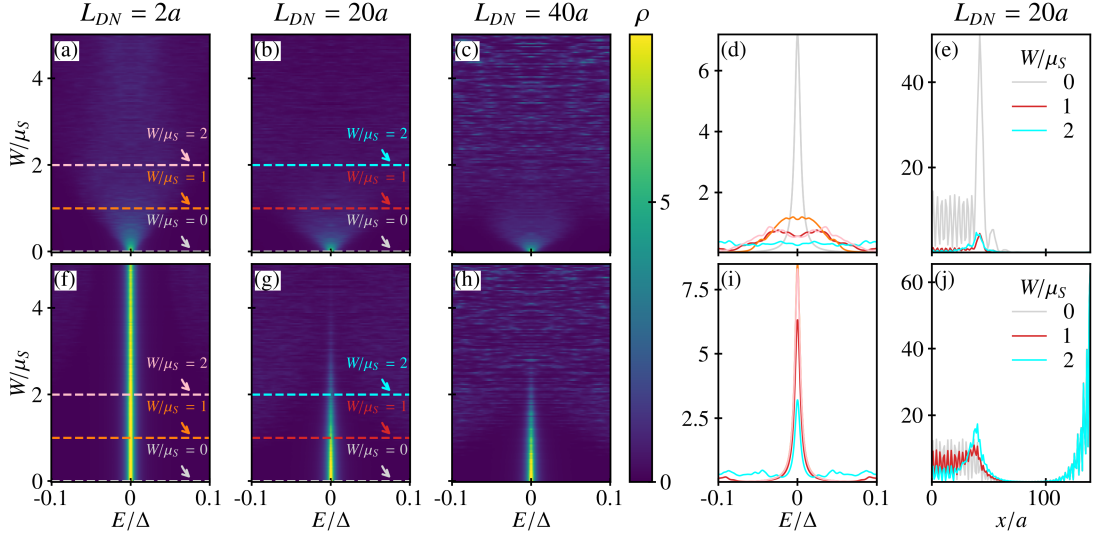


Figure 4.7: LDOS for long S region ($L_S = 100a$) junctions evaluated at the leftmost site of the N region ($i = 1$) as a function of energy E and scalar disorder strength W with $L_{DN} = 2a$ (a,f), $L_{DN} = 20a$ (b,g), and $L_{DN} = 40a$ (c,h). Panels (d,i) show line cuts of the LDOS in (a,f,b,g) for $W/\mu_S = 0, 1, 2$. Panels (e,j) show the spatial profile of the LDOS at $E \approx 0$ for $W/\mu_S = 0, 1, 2$ with $L_{DN} = 20a$. Top row (a,b,c,d,e): trivial phase ($B = 0.825B_c$). Bottom row (f,g,h,i,j): topological phase ($B = 1.2B_c$). Other parameters used are: $L_S = 100a$, $L_N = 40a$, $a = 50$ nm, $\mu_S = 0.5$ meV, $\mu_N = 0.1$ meV, $\Delta = 0.25$ meV, $\alpha = 20$ meV nm, $w = 1$ meV, and $\eta = 0.001$ meV.

The line cuts in panel (i) offer a striking visual confirmation of this resilience. While the clean-limit peak (grey curve) is sharp, the disordered peaks ($W/\mu_S = 1, 2$) remain almost perfectly centered at zero energy, retaining significant height and a sharp profile, in direct opposition to the flattened plateaus seen in the trivial case. The spatial profile in panel (j) reveals a subtle but important detail about the nature of this protection. While the MBS remains pinned at zero energy, disorder does affect its spatial form by enhancing its localization at the DN/S interface. This "squeezing" of the wavefunction away from the disordered region can be interpreted as the system's mechanism for preserving the zero-energy state by minimizing its exposure to potential fluctuations.

To confirm that this newfound robustness in the LDOS is underpinned by a corresponding stabilization of the unconventional pairing, we again analyze the induced pair correlations. The results for the spin-triplet pairing, shown in Fig. 4.8, now serve as a faithful reporter of the system's topological nature. In the trivial phase (top row), the triplet ZEP remains fragile, mirroring the LDOS behavior.

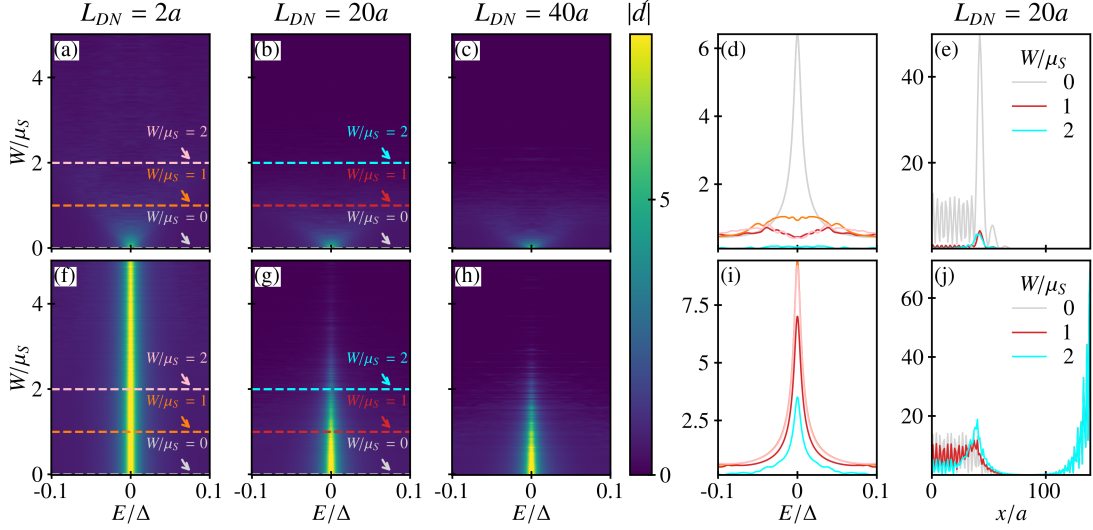


Figure 4.8: Absolute value of the spin-triplet pair correlations $|\vec{d}|$ for long S region ($L_S = 100a$) junctions evaluated at the leftmost site of the N region ($i = 1$) as a function of energy E and scalar disorder strength W with $L_{DN} = 2a$ (a,f), $L_{DN} = 20a$ (b,g), and $L_{DN} = 40a$ (c,h). Panels (d,i) show line cuts of the spin-triplet pair correlations in (a,f,b,g) for $W/\mu_S = 0, 1, 2$. Panels (e,j) show the spatial profile of the spin-triplet pair correlations at $E \approx 0$ for $W/\mu_S = 0, 1, 2$ with $L_{DN} = 20a$. Top row (a,b,c,d,e): trivial phase ($B = 0.825B_c$). Bottom row (f,g,h,i,j): topological phase ($B = 1.2B_c$). Other parameters used are: $L_S = 100a$, $L_N = 40a$, $a = 50$ nm, $\mu_S = 0.5$ meV, $\mu_N = 0.1$ meV, $\Delta = 0.25$ meV, $\alpha = 20$ meV nm, $w = 1$ meV, and $\eta = 0.001$ meV.

However, in the topological phase (bottom row), the triplet ZEP is spectacularly robust, remaining large and sharply peaked at zero energy despite the presence of strong disorder. This provides direct evidence that the protected Majorana state continues to mediate a strong, persistent odd-frequency proximity effect that is immune to disorder.

Finally, the spin-singlet correlations, shown in Figure 4.9, continue their passive role. The characteristic dip at zero energy and the strict confinement to the S-region persist, confirming that conventional pairing is not involved. Therefore, the combined analysis of the long-junction case successfully resolves the ambiguity present in the short-junction scenario. The disorder resilience of the zero-energy peak, observable in both the LDOS and the spin-triplet correlations, emerges as a definitive and reliable litmus test for topological superconductivity, but only when the system geometry is chosen to ensure robust topological protection.

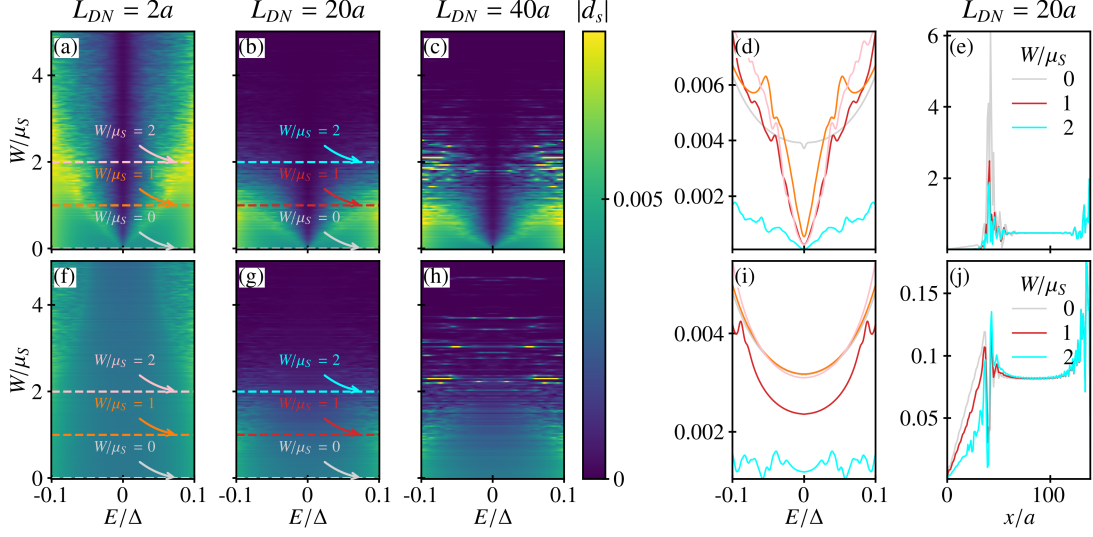


Figure 4.9: Absolute value of the spin-singlet pair correlation for long S region ($L_S = 100a$) junctions evaluated at the leftmost site of the N region ($i = 1$) as a function of energy E and scalar disorder strength W with $L_{DN} = 2a$ (a,f), $L_{DN} = 20a$ (b,g), and $L_{DN} = 40a$ (c,h). Panels (d,i) show line cuts of the spin-singlet pair correlations in (a,f,b,g) for $W/\mu_S = 0, 1, 2$. Panels (e,j) show the spatial profile of the spin-singlet pair correlations at $E \approx 0$ for $W/\mu_S = 0, 1, 2$ with $L_{DN} = 20a$. Top row (a,b,c,d,e): trivial phase ($B = 0.825B_c$). Bottom row (f,g,h,i,j): topological phase ($B = 1.2B_c$). Other parameters used are: $L_S = 100a$, $L_N = 40a$, $a = 50$ nm, $\mu_S = 0.5$ meV, $\mu_N = 0.1$ meV, $\Delta = 0.25$ meV, $\alpha = 20$ meV nm, $w = 1$ meV, and $\eta = 0.001$ meV.

4.4 Conclusion

The reliable identification of Majorana bound states in experimental systems represents a critical milestone towards the realization of topological quantum computing. A significant obstacle on this path is the existence of trivial, non-topological states that can generate similar experimental signatures, such as zero-bias conductance peaks, thereby creating profound ambiguity in the interpretation of experimental data. This chapter has been dedicated to addressing this challenge by performing a systematic theoretical analysis of the anomalous proximity effect in a realistic and experimentally relevant model of a semiconductor-superconductor junction with an extended, disordered normal metal region. We have meticulously investigated the influence of key system parameters, namely the strength of scalar disorder and the lengths of the different junction segments, on the low-energy electronic structure and the nature of the induced superconductivity.

Our primary finding establishes a crucial dichotomy in the stability of zero-energy states, a dichotomy that is fundamentally governed by the system's geometry. We have demonstrated that while both trivial Andreev bound states and topological Majorana bound states give rise to a zero-energy peak in the local density of states in the absence of disorder, their response to potential fluctuations is starkly different. The ZEP originating from trivial ABSs exhibits a universal fragility; it invariably splits and is suppressed by disorder, regardless of other system parameters. In contrast, the stability of the MBS-induced ZEP is a conditional property, critically dependent on the length of the superconducting segment. We found that for short superconducting segments, where the Majorana wavefunctions at opposite ends of the wire can hybridize through the superconductor, the topological ZEP is also fragile and therefore effectively indistinguishable from its trivial counterpart in the presence of disorder. It is only in the regime of a long superconducting segment, where this hybridization is exponentially suppressed, that the ZEP becomes truly robust, remaining resolutely pinned to zero energy and thus serving as a faithful indicator of the underlying non-trivial bulk topology.

A cornerstone of this work, providing deeper insight into the physics at play, is our detailed analysis of the superconducting pair correlations that mediate the proximity effect. We have shown unequivocally that the anomalous proximity effect, and the associated ZEP in the normal metal, is sustained by unconventional odd-frequency, spin-triplet Cooper pairs. This was confirmed by the direct observation that the magnitude of these triplet correlations mirrors the behavior of the LDOS—being fragile for trivial states and short topological wires, but robust for long topological wires. Simultaneously, we have demonstrated that conventional, even-frequency spin-singlet pairing is consistently suppressed at zero energy and is spatially confined to the superconductor itself, playing no role in the zero-bias anomaly observed at the remote probe. This result not only clarifies the microscopic origin of the observed phenomena but also strengthens the established theoretical link between Majorana fermions and the emergence of odd-frequency pairing states as a key component of their phenomenology.

In summary, our findings provide a clear and actionable set of guidelines for the experimental search for Majorana bound states using tunneling spectroscopy. We conclude that the anomalous proximity effect, when properly interpreted, can indeed be a reliable diagnostic tool. However, the mere observation of a zero-bias peak is insufficient proof of topology; its resilience against the introduction of disorder emerges as the key litmus test. Our work highlights that this test is only meaningful in devices engineered with sufficiently long superconducting segments, which are necessary to leverage the full extent of topological protection. This study therefore informs the design of future experiments, emphasizing the need to control not just material properties but also the device geometry, in order to

successfully navigate the complex landscape of trivial and topological states and unambiguously identify the elusive Majorana fermion.

Chapter 5

Odd frequency pairing in Floquet Topological Superconductors

So far, the preceding chapters have established odd-frequency pairing as a powerful probe of Majorana fermions and topological superconductivity in static systems. However, we note that real experimental setups are prone to external perturbations. In the previous chapter, we have discussed the effect of on-site disorder on Majorana fermions and odd-frequency pairing. However, this is only one possible type of potential experimental implications. Another example of possible perturbations is time-dependent fluctuations in the applied gate-voltages or external magnetic fields, etc. Such time-dependent perturbations can potentially have significant effects on Majorana fermions and odd-frequency pairing. Furthermore, understanding dynamical situations is very important for two main reasons. On one hand, odd-frequency pairing is inherently a dynamical phenomenon and it is natural to expect that it can be generated and controlled in systems with time-dependent modulations. On the other hand, topological quantum computation relies on braiding and manipulating Majorana zero modes (MZMs), which is also a dynamical process. Therefore, it is crucial to understand how time-dependent modulations can affect the properties of MZMs and odd-frequency pairing. While a complete characterization of the impact of dynamic perturbation is of utmost importance, in this chapter we focus our attention exclusively to time-periodic modulations, which are known to induce new dynamical phases and exotic phenomena with no static counterparts [120, 121]. In particular, time-periodic modulations can induce Floquet topological superconducting phases, which are characterized by the presence of a new type of Majorana modes known as Majorana π modes (MPMs) [80]. In this chapter, we focus on these so-called Floquet topological superconductors and explore the emergence of Majorana π modes (MPMs) in driven topological superconductors and their relationship with odd-frequency pairing.

As a concrete model, we extend the Kitaev chain model we introduced in

[2.3.2](#) to include time-periodic modulations in the chemical potential. The time-periodic Kitaev chain is described by a time-dependent Hamiltonian, which we treat within Floquet theory. As we saw in Sec. [2.7.4](#) and as we will see later in this chapter, time-periodic modulation leads to the generation of Majorana modes not only at zero energy but also at energies equal to $\pm\pi\hbar/T$. We show that multiple Majorana modes belonging to both species can emerge with up to three Majorana zero modes (MZMs) and three Majorana π modes (MPMs) at the same edge simultaneously, consistent with previously shown results [14, 122–125]. Our main results in this chapter is that the presence of MZMs and MPMs leads to the emergence of extremely large odd-frequency spin-polarized s -wave pairing amplitudes. We show that the odd-frequency pairing exhibit a divergent profile near the energies of the edge modes with MZMs leading to a $\sim 1/\omega$ behavior and MPMs leading to a $\sim 1/(\omega - \pi\hbar/T)$ behavior. We explain this divergent behavior by generalizing the spectral bulk-boundary correspondence (SBBC, see [2.5.4](#)) to the dynamical regime. Furthermore, we show that the odd-frequency pairing is protected by chiral symmetry and is robust against chiral symmetry-preserving disorder, such as scalar disorder. This stability against disorder indicates that odd-frequency pairing can be used as a robust probe of MZMs and MPMs in driven topological superconductors. This chapter is based on our work published in Ref. [3].

5.1 Model

unlike the previous chapters, we don't consider the Rashba nanowire model here. Instead, for the sake of simplicity, we consider a 1d spin-polarized p-wave superconductor which we describe by the Kitaev chain Hamiltonian. We note that the Kitaev chain is in fact equivalent to the Rashba nanowire model in the limit of strong Zeeman field [32, 115]. Thus, the Kitaev chain can be considered as a low-energy effective model for semiconductor-superconductor hybrid systems. We subject the Kitaev chain to time-periodic modulations in the chemical potential, which we model by a piece-wise constant function of time. The time-periodic Kitaev chain Hamiltonian in Nambu space is given by:

$$H(t) = \sum_{j=1}^N \psi_j^\dagger(-\mu(t)\tau_z)\psi_j + \sum_{j=1}^{N-1} \psi_j^\dagger(-w\tau_z + i\Delta\tau_y)\psi_{j+1} + \text{h.c.}, \quad (5.1)$$

where we used the Nambu spinor representation of the fermionic operators, $\psi_j^\dagger = (c_j^\dagger, c_j)^T$, with c_j (c_j^\dagger) being the annihilation (creation) operator at site j for spin-polarized electrons, and $\tau_{z,y}$ are the Pauli matrices in the particle-hole space. The second line of Eq. (5.1) describes nearest-neighbor interaction between the Nambu spinors, where w is the nearest-neighbor hopping amplitude and Δ is the p -wave superconducting order parameter. The first line describes the chemical potential $\mu(t)$, which we take to be the following:

$$\mu(t) = \begin{cases} \mu_1, & nT < t \leq (n + \frac{1}{2})T, \\ \mu_2, & (n + \frac{1}{2})T < t \leq (n + 1)T, \end{cases} \quad n \in \mathbb{Z}, \quad (5.2)$$

with T being the driving period. The system is considered to be of finite length $L = Na$, where N is the number of sites and a is the lattice spacing. For the sake of simplicity, we take the lattice spacing to be $a = 1$.

We note that Eqs. (5.1) and (5.2) implies that we can write the time-dependent Hamiltonian as a piece-wise constant Kitaev chain Hamiltonian given as follows:

$$H(t) = \begin{cases} H_1, & nT < t \leq (\frac{1}{2} + n)T, \\ H_2, & (\frac{1}{2} + n)T < t \leq (n + 1)T. \end{cases} \quad (5.3)$$

Here, H_1 and H_2 are Kitaev chain Hamiltonians given by Eq. 2.61 with chemical potential equal to μ_1 and μ_2 , respectively. In Sec. 2.3.2, we have discussed the case of static Kitaev chain ($\mu_1 = \mu_2 \equiv \mu$).

While understanding the short time dynamics of the Kitaev chain is important to fully characterize our system, we only consider on the long time dynamics. By that, we mean that we concentrate on the time-evolution of the system at time $t = t_0 + nT$ for $n \in \mathbb{Z}$, where t_0 is an arbitrary initial time. This is known as the stroboscopic evolution of the system. Then, the stroboscopic evolution of the system after n periods is given by the time evolution operator as follows:

$$U(t_0 + nT, t_0) = \mathcal{T} \exp \left\{ \left(-\frac{i}{\hbar} \int_{t_0}^{t_0 + nT} H(s) ds \right) \right\} = U(t_0 + T, t_0)^n \equiv U_T[t_0]^n, \quad (5.4)$$

where \mathcal{T} is the time-ordering operator. In the last step, we used the Lie group property of the time evolution operator and the fact that the Hamiltonian is time-periodic, i.e., $H(t + T) = H(t)$ to write the stroboscopic evolution operator as the n -th power of the time evolution operator over one period, $U_T[t_0]$. From Eq. (5.4), we see that the stroboscopic evolution is completely determined by the time evolution operator over one period. This allows us to define an effective Hamiltonian for the stroboscopic evolution, known as the Floquet Hamiltonian, which is given by

$$H_F[t_0] = \frac{i\hbar}{T} \log(U_T[t_0]), \quad (5.5)$$

where \log is the natural logarithm. In our case, the one-period time evolution operator is given by

$$\begin{aligned} U_T[t_0] &= \mathcal{T} \exp \left\{ \left(-\frac{i}{\hbar} \int_{t_0}^{t_0+T} H(s) ds \right) \right\} \\ &= \begin{cases} e^{-\frac{i}{\hbar} H_1 t_0} e^{-\frac{i}{\hbar} H_2 T/2} e^{-\frac{i}{\hbar} H_1 (T/2-t_0)} & 0 < t_0 < \frac{T}{2} \\ e^{-\frac{i}{\hbar} H_2 t_0} e^{-\frac{i}{\hbar} H_1 T/2} e^{-\frac{i}{\hbar} H_2 (T-t_0)} & \frac{T}{2} < t_0 < T \end{cases} \end{aligned} \quad (5.6)$$

We see that the explicit form of the one-period propagator depends heavily on the initial time t_0 . However, we note that the choice of initial time t_0 is equivalent to choosing a frame of reference for the time coordinate, and thus, it corresponds to a unitary transformation. In other words, t_0 constitutes a gauge choice, and it does not affect the physical properties of the system. In particular, it does not affect the eigenvalues of the Floquet Hamiltonian $H_F[t_0]$. Thus, we use this freedom to choose t_0 to simplify the calculations. In this chapter, we choose $t_0 = 0$ unless otherwise stated. In this case, the one-period time evolution operator is given by

$$U_T[0] = e^{-\frac{i}{\hbar} H_2 T/2} e^{-\frac{i}{\hbar} H_1 T/2}. \quad (5.7)$$

The Floquet Hamiltonian can then be obtained by using Baker-Campbell-Hausdorff (BCH) expansion of the logarithm in Eq. (5.5). Due to the complexity of the BCH expansion, we assume periodic boundary conditions and consider the case of small period T to obtain an effective Floquet Hamiltonian. In this case, we can expand the logarithm in Eq. (5.5) as follows:

$$H_F(k) = \frac{i\hbar}{T} \log \left(\mathcal{T} e^{-i\frac{1}{\hbar} \int_{t_0}^{t_0+T} H(t, k) dt} \right), = \sum_{j=1}^{\infty} h_j \left(\frac{T}{\hbar} \right)^{j-1} \text{mod} \left(\frac{2\pi}{T} \right), \quad (5.8)$$

where the first few BCH coefficients h_j are given by

$$\begin{aligned}
h_1 &= \frac{1}{2}(H_1 + H_2) \\
&= -[(\mu_1 + \mu_2)/2 + 2w \cos(k)]\tau_z - 2\Delta \sin(k)\tau_y, \\
h_2 &= \frac{1}{2} \frac{1}{2^2} [H_1, H_2] \\
&= \frac{i}{2} \Delta(-\mu_1 + \mu_2) \sin(k)\tau_x, \\
h_3 &= \frac{1}{12} \frac{1}{2^3} ([H_1, [H_1, H_2]] + [H_2, [H_2, H_1]]) \\
&= \frac{-1}{12} \Delta(\mu_1 - \mu_2)^2 \sin(k)\tau_y, \\
h_4 &= -\frac{1}{24} \frac{1}{2^4} [H_2, [H_1, [H_1, H_2]]] \\
&= \frac{i}{24} \Delta(\mu_1 - \mu_2) \sin(k) [-2\Delta^2 - \mu_1\mu_2 - 2w^2 - 2(\mu_1 + \mu_2)w \cos k + 2(\Delta^2 - w^2) \cos(2k)]\tau_x,
\end{aligned} \tag{5.9}$$

We note that the effective Hamiltonian (5.5) is in fact defined modulo $2\pi/T$ since the complex logarithm is not unique and has a branch cut. To avoid this ambiguity, we consider the logarithm branch cut in a way that the eigenvalues of H_F , also known as *quasienergies*, belong to the region $[-\pi\hbar/T, \pi\hbar/T]$. This guarantees that the quasienergies are well-defined and that the effective Hamiltonian is unique and satisfies the condition $|\langle \psi | H_F | \psi \rangle| \leq \pi\hbar/T$ for any arbitrary stationary state $|\psi\rangle$ [121].

From Eq. (5.9), we can already see that the Floquet Hamiltonian depends non-trivially on T . As the periodic time increases, higher order terms in the BCH formula become more dominant. Furthermore, while the original Hamiltonian has short-range interaction, we can already see that higher terms in the expansion can produce long range hopping and pairing between electrons. This behavior can lead to higher number of Majorana fermions under certain conditions. This is indeed what we observe in the spectrum which we will discuss in the next section.

We note that for the sake of simplicity, we set the lattice spacing to $a = 1$ and the chemical potential of the first half of the cycle to $\mu_1 = 0$. We measure all quantities in units of the hopping amplitude w and Planck's constant \hbar . We assume that the superconducting order parameter is finite and equal to $\Delta = w$.

5.2 Floquet Majorana edge modes: Topological invariants and quasienergy spectrum

Having established the effective Floquet Hamiltonian in Eq. (5.5), we now proceed to investigate the emergence of Majorana edge modes in our driven system. Before we do so, however, let us first understand the bulk energies of the Floquet Hamiltonian and how they depend on the period T and the chemical potential $\mu_{1,2}$. This will allow us to understand the emergence of Majorana edge modes.

5.2.1 Bulk dispersion relation and multiple Fermi points

In the previous section, we showed that the effective Floquet Hamiltonian can be obtained by performing a BCH expansion of the one-period time evolution operator. This is a powerful method that allows us to obtain the effective Hamiltonian in a systematic way. However, it is important to note that the BCH expansion is only valid for small periods T . Thankfully, the simple drive we consider here allows us to obtain the effective Hamiltonian in a closed form even for finite periods. For that, we set the initial time to $t_0 = 0$ and use Eq. (5.6) to obtain the one-period time evolution operator as a product of two exponentials, one for each half of the cycle. Then, we can use the properties of Pauli matrices to obtain the effective Floquet Hamiltonian and the bulk quasienergies. The details of this procedure are given in Appendix 5.5.1. Here, we only present the final result for the bulk quasienergies. We find that the bulk Floquet quasienergies are given by

$$E_F(k) = \pm \frac{\hbar}{T} \arccos \left[\cos(E_1 T/2\hbar) \cos(E_2 T/2\hbar) - \frac{\mathbf{E}_1 \cdot \mathbf{E}_2}{E_1 E_2} \sin(E_1 T/2\hbar) \sin(E_2 T/2\hbar) \right], \quad (5.10)$$

where $E_j = |\mathbf{E}_j|$, with $\mathbf{E}_j = (0, -2\Delta \sin k, -\mu_j - 2w \cos k)^T$ is the vector representation of the Hamiltonians at each half cycle $H_j(k) = \mathbf{E}_j \cdot \boldsymbol{\tau}$, with $\boldsymbol{\tau} = (\tau_x, \tau_y, \tau_z)^T$ being the vector of Pauli matrices in the particle-hole space. We note that the dispersion relation in Eq. (5.10) is defined modulo $2\pi/T$. We see this is embedded in the definition of the quasienergies in Eq. (5.10), which are given by the inverse cosine function. We choose the branch cut of the inverse cosine function such that the quasienergies are defined in the region $[-\pi\hbar/T, \pi\hbar/T]$. Thus, the energy bands are symmetric with respect $E_F(k) = \pm \hbar\pi/T$. Particle-hole symmetry is also preserved in the quasienergies, which is a consequence of the particle-hole symmetry of the original Hamiltonian $H(t)$ in Eq. (5.1). This means that the quasienergies are symmetric with respect to zero energy. We show the bulk quasienergies in Fig. 5.1 for different values of the period T and chemical potentials $\mu_{1,2}$. We choose $\mu_1 = 0$

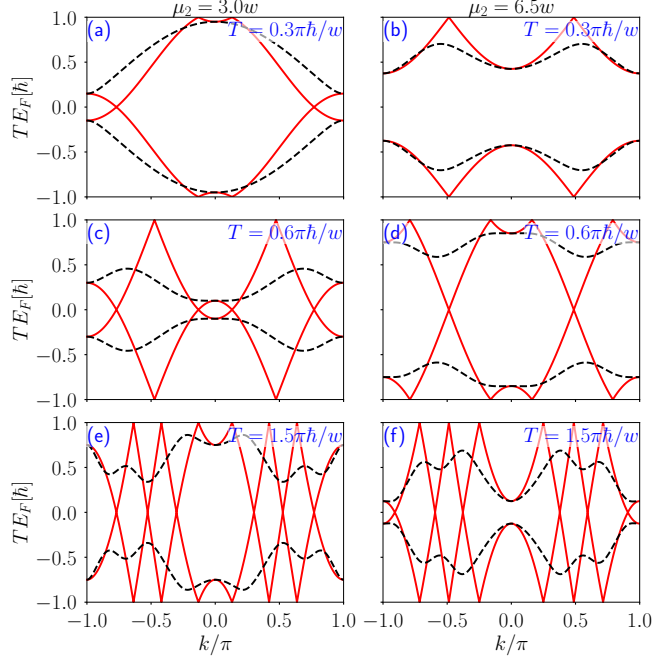


Figure 5.1: Bulk energy bands as a function of momentum k for $\mu_2/w = 3$ (left column) and $\mu_2/w = 6.5$ (right column) at $\mu_1 = 0$ and distinct values of the period T . Solid red and black dashed curves depict the energies at $\Delta = 0$ and $\Delta = w$. Top (a,b), middle (c,d), and bottom panels (e,f) correspond to $T = 0.3\pi\hbar/w$, $0.6\pi\hbar/w$, and $1.5\pi\hbar/w$, respectively.

and pick two values for μ_2 , namely $\mu_2 = 3w$ and $\mu_2 = 6.5w$. The choice of these values is motivated by the fact that they correspond to a topologically nontrivial and a trivial phase, respectively, in the static limit $T \rightarrow 0$. For the sake of completeness, we also show the bulk energies at zero and finite pair potential, depicted by solid red and dashed black curves, respectively. We know that for the static Kitaev chain, the zero pair potential limit in the topological phase corresponds to a normal metal, while in the trivial phase it corresponds to a trivial insulator. This is exactly what we observe in the solid red curves in Fig. 5.1(a,b). In Fig. 5.1(a,b), we see that for $\mu_2 = 3w$, the bulk quasienergies at zero pair potential have a Fermi surface (two Fermi points) at zero energy, while for $\mu_2 = 6.5w$, there is no Fermi surface at zero energy. This is consistent with the fact that the period T is small, and thus, the system is described by the static Kitaev chain Hamiltonian with chemical potential given by the average of the two chemical potentials, i.e., $\mu = (\mu_1 + \mu_2)/2$. In this case, the system with finite pair potential is in the topological phase in panel (a) and in the trivial phase in panel (b). We note that in both cases, we also have Fermi surfaces at finite energies, which are given by

$E_F = \pm\pi\hbar/T$. This is a direct consequence of the time-periodic modulation of the chemical potential, which leads to the appearance of new anomalous Majorana modes (MPMs) at finite energies.

As we increase the period T , we see that the bulk quasienergies change dramatically, as shown in Fig. 5.1(c-f). In particular, we start to observe multiple Fermi surfaces at both zero and finite energies. This is very interesting since it suggests that the system can host multiple Majorana modes at the edges of the system [14, 32, 123–125]. We note that the multiple Fermi surfaces are very intriguing since they originate purely from the logarithm operation in the effective Floquet Hamiltonian. This is because the two Hamiltonians H_1 and H_2 commute with each other for $\Delta = 0$ and nested commutators vanish. The logarithm operation then leads to the folding of the energy bands, which results in multiple Fermi surfaces [120, 121]. This is a very interesting effect of the drive, which can be used to engineer multiple Majorana modes at the edges of the system. To understand the emergence of Majorana modes, we need to go beyond the bulk quasienergies and explore the topological invariants of the system, which we do in the next subsection.

5.2.2 Topological Invariants

To further understand the topological phases of the driven system described by Eq. (5.5) and the response of the system to the time-periodic modulation, we need to identify the symmetries of the effective Floquet Hamiltonian. The original Hamiltonian $H(t)$ has chiral symmetry with chiral operator $\Gamma = \tau_x$, which anti-commutes with the Hamiltonian for all times t . Note that however, it is not obvious that the Floquet Hamiltonian H_F also has chiral symmetry. To see this, we note that chiral symmetry of the effective Floquet Hamiltonian is preserved if the one-period time evolution operator $U_T[t_0]$ satisfies the condition $\Gamma U_T[t_0]\Gamma = U_T^\dagger[t_0]$. This condition is satisfied for a specific choice of the initial time t_0 . In our case, we find that chiral symmetry is preserved at $t_0 = \pm T/4$, which give symmetric time evolution. At these two special initial times, the one-period time evolution operator can be expressed as

$$\begin{aligned} U_T^+ &\equiv U_T[T/4] = e^{-\frac{iT}{4\hbar}H_1}e^{-\frac{iT}{2\hbar}H_2}e^{-\frac{iT}{4\hbar}H_1}, \\ U_T^- &\equiv U_T[-T/4] = e^{-\frac{iT}{4\hbar}H_2}e^{-\frac{iT}{2\hbar}H_1}e^{-\frac{iT}{4\hbar}H_2}, \end{aligned} \quad (5.11)$$

where H_1 and H_2 are the Kitaev chain Hamiltonians with chemical potentials μ_1 and μ_2 , respectively. This allows us to define two chiral symmetric Floquet Hamiltonians as follows:

$$H_F^\pm = \frac{i\hbar}{T} \log(U_T^\pm). \quad (5.12)$$

Note that while the two Floquet Hamiltonians H_F^\pm are related to each other by a unitary transformation and thus have the same eigenvalues, they don't have

the same eigenstates. Thus, the eigenstates of H_F^+ and H_F^- can have different properties, such as localization and chirality [11]. This is an important feature of the Floquet Hamiltonian, which allows us to define the winding numbers of MZMs and MPMs using the winding numbers of the two Floquet Hamiltonians H_F^\pm . Using these Hamiltonians, we can define two winding numbers as follows:

$$W^\pm = \frac{1}{4\pi i} \int_{-\pi}^{\pi} dk \text{Tr} \left\{ \Gamma [H_F^\pm(k)]^{-1} \partial_k [H_F^\pm(k)] \right\}, \quad (5.13)$$

where $H_F^\pm(k)$ is the momentum-space Hamiltonians. These winding numbers are agnostic towards the energy of the edge modes and only depend on the difference of the chirality of the edge modes at zero and $\pi\hbar/T$ energies [11]. In order to separate the information about the MZMs and MPMs, we can use the fact that the MPMs wavefunctions of H_F^+ and H_F^- have opposite chirality, while the MZMs wavefunctions of H_F^+ and H_F^- have the same chirality. This allows us to define two extra winding numbers as follows [10, 11, 126]:

$$W_0 = \frac{W^+ + W^-}{2} \quad \text{and} \quad W_\pi = \frac{W^+ - W^-}{2}, \quad (5.14)$$

where W_0 and W_π are the winding numbers of MZMs and MPMs, respectively. By the index theorem, we know that the winding numbers W_0 and W_π take integer values and the absolute value of the winding numbers gives the number of MZMs and MPMs at the edges of the system, respectively. Having established the topological invariants of the driven system, we can now explore their behavior as a function of the period T and the chemical potential μ_2 . We do this in Fig. 5.2(a,b), where we show the winding numbers $W_{0,\pi}$ as functions of the period T and the chemical potential μ_2 . We set the chemical potential of the first half of the cycle to $\mu_1 = 0$ and consider a finite pair potential $\Delta = w$. We also show line cuts of the winding numbers at $\mu_2 = 3w$ and $\mu_2 = 6.5w$ in Fig. 5.2(c,d). These values of μ_2 correspond to a topologically nontrivial and a trivial phase, respectively, in the static limit $T \rightarrow 0$. The topological invariants are computed by discretizing the integrals in Eq. (5.13) over the momentum Brillouin zone.

First, let us look at the behavior close to $T = 0$. As we can see in Fig. 5.2(a,b), the winding numbers close to $T = 0$ behave like static Kitaev chain. Mainly, we see that the winding number W_π that counts MPMs is zero for all values of μ_2 , while the winding number W_0 that counts MZMs takes two values, $W_0 = 0$ and $W_0 = 1$ with the phase transition point occurring at $\mu_2 = 4w$. This is consistent with the fact that the static limit of our driven system is described by the Kitaev chain with chemical potential $\mu = (\mu_1 + \mu_2)/2 = \mu_2/2$, which displays a topological phase transition at $\mu = 2w$.

Interestingly, while the phase transition in W_0 at $\mu_2 = 4w$ is a robust feature of the static limit, it persists throughout the entire range of T in our system. We

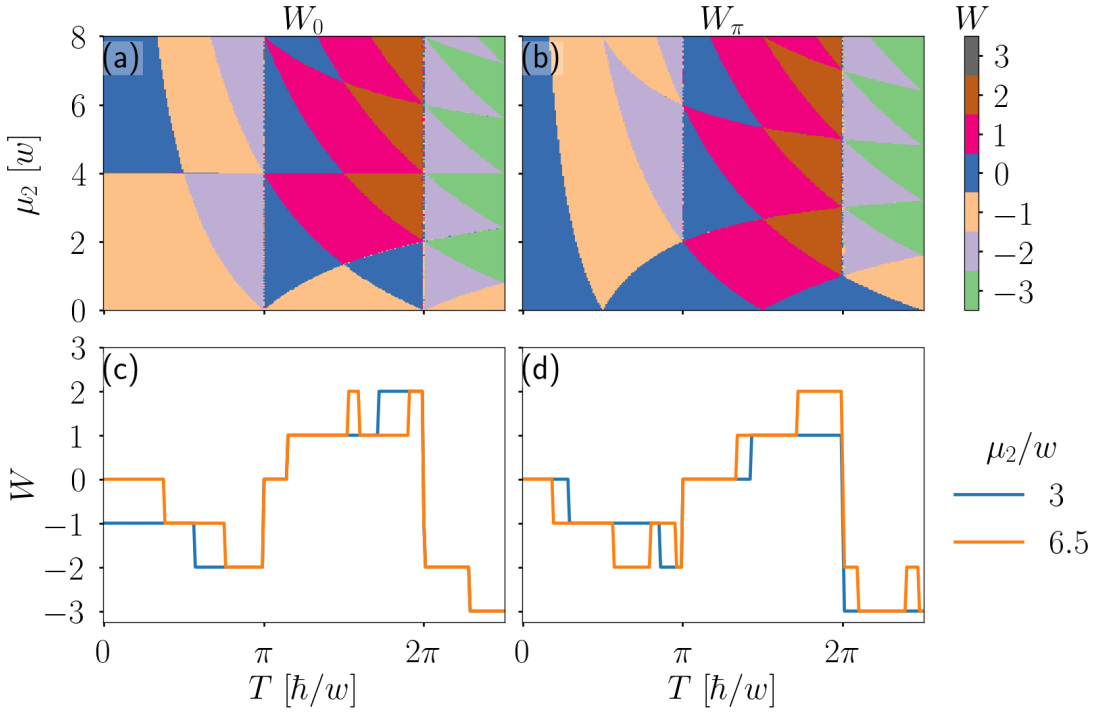


Figure 5.2: Topological invariants W_0 (a) and W_π (b) as a function of the chemical potential μ_2 and period T . Panels (c,d) show line cuts of (a,b) as a function of T at fixed μ_2 . Parameters: $\Delta = w, \mu_1 = 0$.

note that this result is not a mere coincidence of our choice of parameter. Rather, it is a robust feature of our model. Moreover, we also observe topological phase transition lines at $T = n\pi$ for both W_0 and W_π . However, we note that these vertical phase transition lines are sensitive to the choice of the chemical potential μ_1 . In fact, for a nonzero μ_1 , the vertical lines become curved.

Perhaps the most important feature of the topological invariants is that they can take arbitrarily large integer values as T increases, with multiple phase transition points. In fact, we observe up to $W_0 = \pm 3$ and $W_\pi = \pm 3$ in Fig. 5.2(a,b). This is a very interesting result since it means that we can have 6 or more Majorana modes at the edges of the system including both MZMs and MPMs even when the static limit is topological trivial.

5.2.3 Open-boundary quasienergy spectrum

Now that we explored the bulk properties of the driven Kitaev chain, we shift our attention to systems with open boundaries. In this case, we can expect the emergence of Majorana edge modes at the boundaries of the system. We explore this

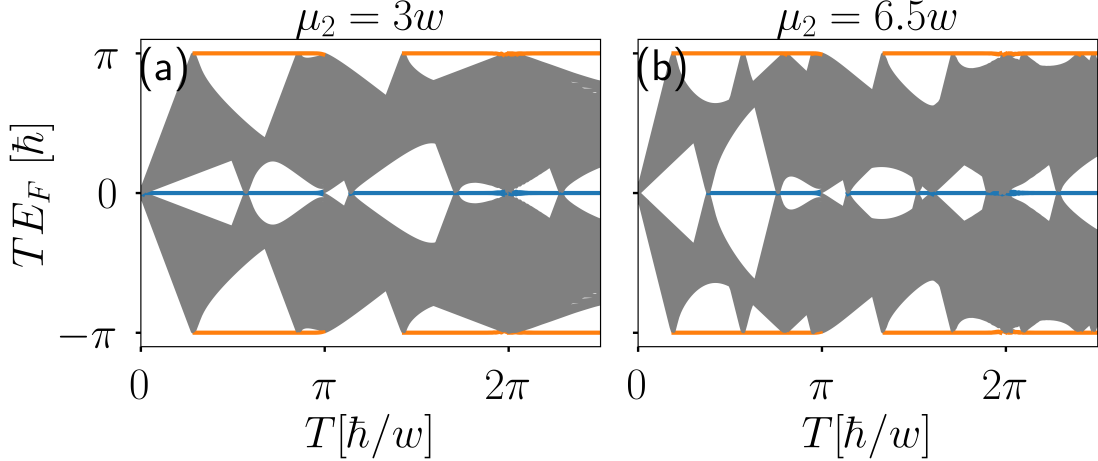


Figure 5.3: (a,b) Quasienergy spectrum as a function of the period T for $\mu_2 = 3w$ and $\mu_2 = 6.5w$. Here, MZMs and MPMs are depicted by blue and orange lines, respectively. Parameters: $\Delta = w, \mu_1 = 0, N = 100$.

by fixing the system length to $L = 100a$ and numerically diagonalize the effective Floquet Hamiltonian in Eq. (5.5) with open-boundary conditions. We consider the same parameters as in the previous subsection, namely $\mu_1 = 0$, $\Delta = w$, and consider two values for $m\mu_2$, namely $\mu_2 = 3w$ and $\mu_2 = 6.5w$. As we discussed earlier, these two values correspond to the topological and trivial phase in the static limit, respectively. For the sake of visualization, the quasienergies are rescaled by the factor T/\hbar so that they are defined in the region $[-\pi, \pi]$ in Fig. 5.3(a,b). In Fig. 5.3(a,b), we see that the quasienergy spectrum is characterized by a quasicontinuum of quasienergies which has non-trivial dependence on the period T . This quasicontinuum of states contains all bulk quasienergies, which we discussed in Sec. 5.2.1. In addition, we also observe dispersionless energy levels at zero ($\pm\pi\hbar/T$) quasienergies, shown in blue(orange) lines in Fig. 5.3(a,b). These are our edge modes which are well localized at the edges of the system. We refer to these modes as Majorana zero modes (MZMs) and Majorana π modes (MPMs) since they are located at zero and $\pi\hbar/T$ quasienergies, respectively. We observe that the MZMs and MPMs are well separated from the bulk quasienergies by a bulk gap which is also highly dependent on the period T .

Interestingly, we see that the appearance of MZMs and MPMs is inevitable as long as the period T is finite. In fact, we observe that the MZMs and MPMs appear at finite T even when the static limit is topologically trivial, i.e., $\mu_2 = 6.5w$ in Fig. 5.3(b). Furthermore, we observe multiple gap closings and reopenings in the quasienergy spectrum as a function of T . These gap closings and reopenings allow the number of MZMs and MPMs to change, which is consistent with the

topological invariants we discussed in Sec. 5.2.2. In fact, we observe that the number of MZMs and MPMs can change by two at each gap closing and reopening. This is a very interesting result since it means that we can control the number of Majorana modes at the edges of the system by simply tuning the period T . We attribute the appearance of multiple MZMs and MPMs to the fact that the effective Floquet Hamiltonian has multiple Fermi surfaces, as we discussed in Sec. 5.2.1. This is a direct consequence of the logarithm operation in the effective Floquet Hamiltonian, which leads to the folding of the energy bands and the appearance of multiple Fermi surfaces [120, 121]. This can also be explained by the emergence of long-range pairing and hopping terms in the effective Floquet Hamiltonian, see Eq. (5.9). In fact, we can see that the fourth order BCH expansion in Eq. (5.9) already contains long-range pairing terms, with higher order terms expected to contain even longer-range hopping terms. Long range pairing and hopping terms are known to lead to multiple Majorana edge modes in static systems and also in driven systems, see e.g., Refs. [10, 14, 122–125, 127–129].

5.3 Odd-frequency superconducting pairing at stroboscopic times

After establishing the effective Floquet Hamiltonian and the emergence of Majorana edge modes, we are now ready to study the nature of the emergent superconducting correlations in the system, which is the main focus and motivation of this chapter. For that purpose, we will analyze the superconducting pair amplitudes at stroboscopic times using the effective Hamiltonian in Eq. (5.5) and the Green’s function method defined in Sec. 2.5. An important aspect of our system is that the drive explicitly breaks time translational invariance, which implies that pair amplitudes should depend on the time coordinates of the two electrons forming a Cooper pair. This is in contrast to static systems, where the pair amplitudes only depends on the relative time coordinate of the two electrons. Instead of fully analyzing the pair amplitudes as a function of the two time coordinates, we will focus on the pair amplitudes at stroboscopic times, which is sufficient to capture the essential features of the superconducting correlations in our system. In Appendix 5.5.3, we show that the retarded (advanced) Green’s function of electrons at stroboscopic times can be obtained from the effective Floquet Hamiltonian in Eq. (5.5) as follows:

$$\mathcal{G}_F^{r(a)}(\omega) = (\omega \pm i\delta - H_F)^{-1}, \quad (5.15)$$

where we have added an infinitesimally small positive number δ to ensure the retarded (advanced) nature of the Green’s function. We choose $\delta = 10^{-5}$ for the purpose of numerical calculations. Note that this stroboscopic Green’s function

depends on the choice of the initial time t_0 . For the sake of clarity, we drop the t_0 dependence in the notation but we should keep in mind that the Green's function is defined as a function of the initial time t_0 . Using this stroboscopic Green's function, we can use the machinery we developed in Sec. 2.5 to compute the pair amplitudes at stroboscopic times from the off-diagonal components of the Green's function in Nambu space as follows:

$$\mathcal{G}_F^{r(a)}(\omega) = \begin{pmatrix} G^{r(a)}(\omega) & F^{r(a)}(\omega) \\ \bar{F}^{r(a)}(\omega) & \bar{G}^{r(a)}(\omega) \end{pmatrix}, \quad (5.16)$$

where $G^{r(a)}(\omega)$ and $F^{r(a)}(\omega)$ are the normal and anomalous components of the Green's function, respectively. Having established the stroboscopic pair amplitudes, we can now analyze their symmetries and the nature of the superconducting correlations in our system. In our case, since the system is spin-polarized, the pair amplitudes are automatically spin-polarized triplet. Since Fermi-Dirac statistics enforces the pair amplitudes to be antisymmetric under the exchange of all quantum numbers [30, 31, 33, 34, 88, 130–132], and since we have already established that the pair amplitudes are spin-polarized triplet, we can conclude that the pair amplitudes are either Even-frequency spin-triplet odd-parity (ETO) or odd-frequency spin-triplet even-parity (OTE). In this chapter, we focus on the OTE pair amplitudes due to their robustness against disorder [31, 37, 45, 76]. In particular, we focus on the local on-site pair amplitudes F_{ii}^r , where i is the site index in the lattice. F_{ii}^r is automatically OTE since it is a local quantity and thus does not depend on the relative position of the two electrons forming a Cooper pair and thus, it is an OTE pair amplitude. We write the induced local OTE pair amplitudes as follows:

$$F_{ii}^{\text{odd}}(\omega) = F_{ii}^r(\omega). \quad (5.17)$$

We recall that in Sec. 2.5.4, we have shown that the accumulated OTE pair amplitudes at the edges of the system are related to the Majorana edge modes and an extended winding number in the static limit [31, 33, 46–48, 73, 88].

5.3.1 Accumulated odd-frequency pairing at the edges

To investigate the relationship between the OTE pair amplitudes and Majorana edge modes in our driven system, we consider the accumulated OTE pair amplitudes at the edges of the system, which is defined as the sum of the local OTE pair amplitudes over the leftmost sites of the system. This is given by

$$F_{\text{odd}}(\omega) = \sum_{i=1}^{N/2} F_{ii}^{\text{odd}}(\omega), \quad (5.18)$$

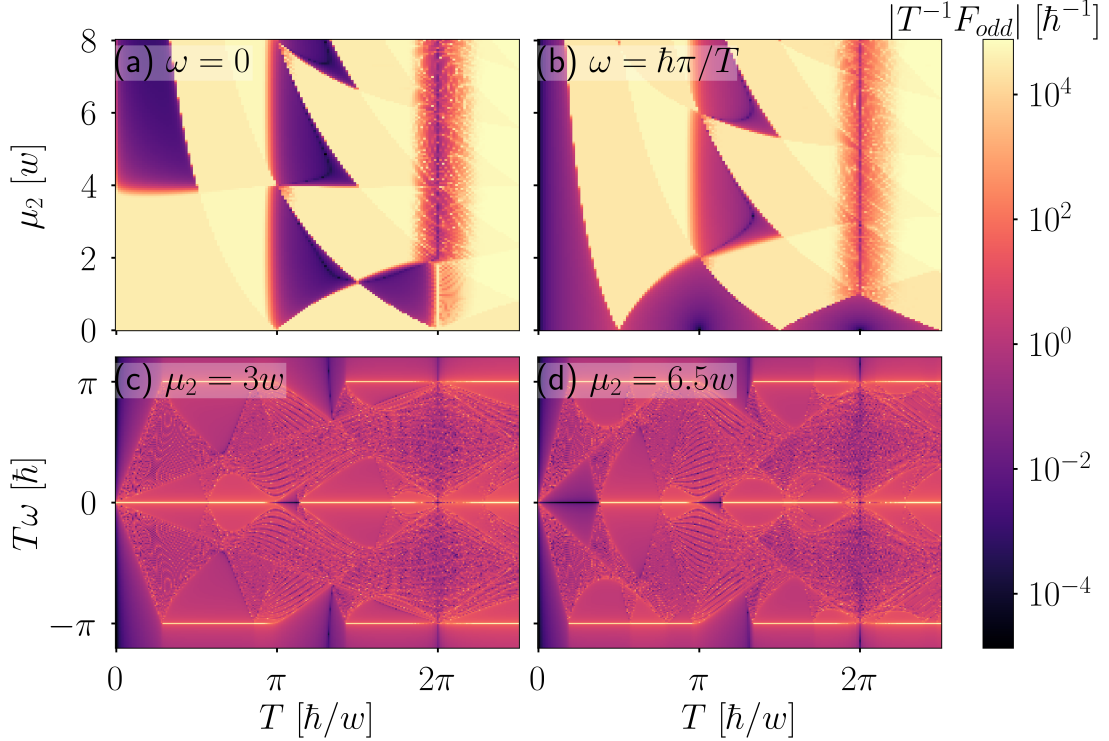


Figure 5.4: (a,b) Absolute value of the accumulated odd-frequency pair amplitude F_{odd} as a function of μ_2 and T for $\omega = 0$ and $\omega = \pi\hbar/T$. (c,d) Same as in (a,b) but now as a function of ω and T for $\mu_2 = 3w$ and $\mu_2 = 6.5w$. Parameters: $\Delta = w$, $\mu_1 = 0$, $N = 100$, $\delta/w = 10^{-5}$.

where we have terminated the summation at the midpoint of the lattice to approximate the accumulated OTE pair amplitudes in a semi-infinite system. More importantly, we choose to set the initial time $t_0 = T/4$. The reason for this choice will become clear in the next subsection. Let us now analyze the accumulated OTE pair amplitudes F_{odd} as a function of the period T and the chemical potential μ_2 . We note that the accumulated OTE pair amplitudes F_{odd} is a complex quantity. In what follows, we will focus on the absolute value of the accumulated OTE pair amplitudes, which we denote by $|F_{\text{odd}}|$. This is sufficient to capture the essential features of the superconducting correlations in our system.

First, we analyze $|F_{\text{odd}}|$ for two fixed frequencies, namely $\omega = 0$ and $\omega = \pi\hbar/T$. The former corresponds to the MZMs, while the latter corresponds to the MPMs. We show the results in Fig. 5.4(a,b) as a function of the chemical potential μ_2 and the period T . Our main observation is that $|F_{\text{odd}}|$ at $\omega = 0$ and $\omega = \pi\hbar/T$ acquires very large values in the parameter space where the topological invariants W_0 and W_π are nonzero, respectively. More importantly, the values of $|F_{\text{odd}}|$ at $\omega = 0$ and

$\omega = \pi\hbar/T$ becomes larger as the number of MZMs and MPMs increases. This shows the strong connection between the OTE pair amplitudes and the Majorana edge modes in our driven system.

To further understand this intriguing relationship, we take line cuts of $|F_{\text{odd}}|$ at fixed chemical potentials $\mu_2 = 3w$ and $\mu_2 = 6.5w$, which are shown in Fig. 5.4(c,d). Here, we observe that $|F_{\text{odd}}|$ is peaked whenever the frequency ω is equal to the energy of an eigenvalue of the effective Floquet Hamiltonian H_F . This is an unsurprising result since the OTE pair amplitudes are obtained from the stroboscopic Green's function, which has poles at the eigenvalues of the effective Floquet Hamiltonian. Nevertheless, we note that the peaks of $|F_{\text{odd}}|$ are not very large for bulk quasienergies, i.e., $\omega \neq 0$ and $\omega \neq \pi\hbar/T$. In contrast, the peaks at $\omega = 0$ and $\omega = \pi\hbar/T$ are orders of magnitude larger than the peaks at bulk quasienergies. This is a very interesting result since it shows that the OTE pair amplitudes are strongly enhanced as a direct consequence of the Majorana edge modes. In fact, we observe that the size of the peaks at $\omega = 0$ and $\omega = \pi\hbar/T$ has the same order of magnitude as $\delta^{-1} \sim 10^5$, which is the expected divergent behavior of the OTE pair amplitudes at the edges of the system in the static limit [31, 33, 46–48, 73, 88]. This is a very important result since it suggests that a nontrivial relationship exists between the accumulated OTE pair amplitudes, the Majorana edge modes, and the topological invariants in our driven system. Unfortunately, at $T \gtrsim 2\pi\hbar/w$, the finite-size effects start to play a significant role, which spoils the relationship between the OTE pair amplitudes and the Majorana edge modes. This is because around this value of T , we have a very small energy gap in the quasienergy spectrum, see Fig. 5.3(a,b). This small energy gap leads to a large localization length of the Majorana edge modes, which is comparable to the system size. As a result, Majorana edge modes have a huge overlap with each other, which affects the OTE pair amplitudes. Nevertheless, we have verified that for a large enough system size, the relationship between the OTE pair amplitudes and the Majorana edge modes is preserved. In fact, as we will see in Sec. 5.3.2, the relationship between the OTE pair amplitudes and the Majorana edge modes is protected by chiral symmetry and is in fact a robust topological feature of the system. Before we show this, however, let us first analyze the frequency and space dependence of the OTE pair amplitudes in our driven system. We now turn our attention to the frequency and space dependence of the OTE pair amplitudes in our driven system. Previously in Fig. 5.4(c,d), we have already seen that the OTE pair amplitudes $|F_{\text{odd}}|$ are peaked at $\omega = 0$ and $\omega = \pi\hbar/T$. We now take a closer look at these peaks and analyze their dependence on the period T for two fixed chemical potentials $\mu_2 = 3w$ and $\mu_2 = 6.5w$. We show the results in Fig. 5.5(a,b). In these two panels, we can clearly see that the OTE pair amplitudes $|F_{\text{odd}}|$ at $\omega = 0$ and $\omega = \pi\hbar/T$ develop plateaus as a function of T . These plateaus are peaked at the values of T where

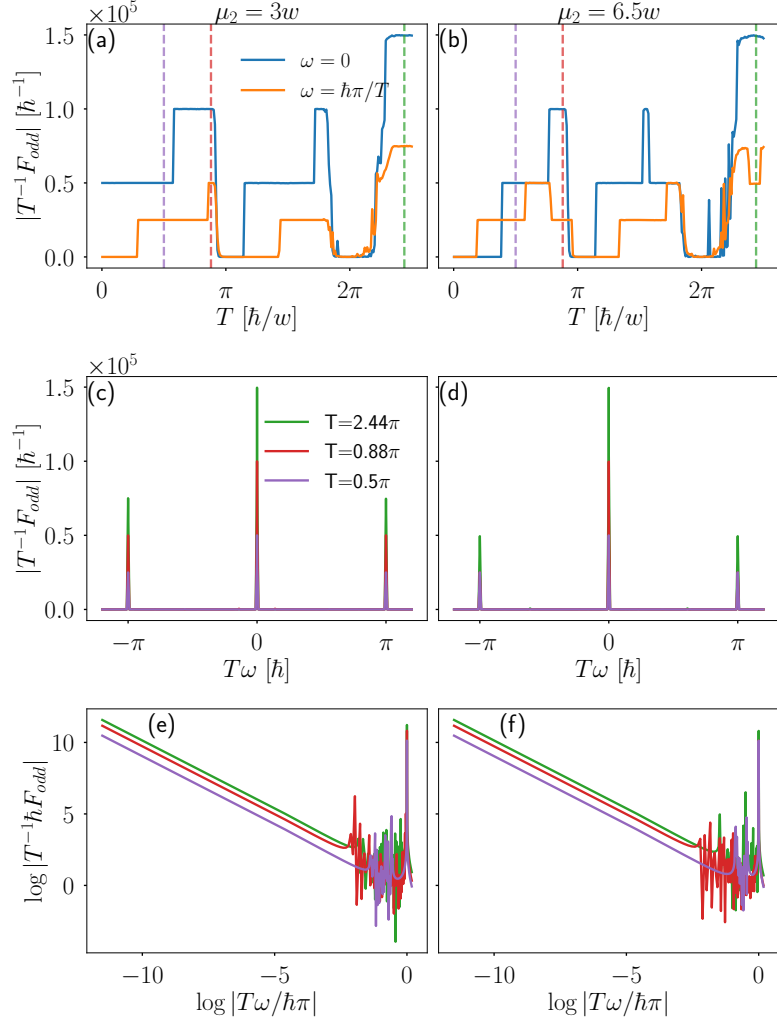


Figure 5.5: Absolute value of the accumulated odd-frequency pair amplitude F_{odd} as a function of T (a,b), and ω (c,d,e,f). The left and right columns correspond to $\mu_2 = 3w$ and $\mu_2 = 6.5w$, respectively. Parameters: $\Delta = w$, $\mu_1 = 0$, $N = 100$.

the topological invariants W_0 and W_π are nonzero, respectively. Moreover, the heights of the plateaus are proportional to the absolute values of the topological invariants $|W_0|$ and $|W_\pi|$. This shows that the OTE pair amplitudes at $\omega = 0$ and $\omega = \pi\hbar/T$ disperse as a function of T in a very similar way as the topological invariants W_0 and W_π . In fact, we can see one-to-one correspondence between the plateaus of the OTE pair amplitudes and the topological invariants, compare Fig. 5.5(a,b) with Fig. 5.2(a,b).

Looking at the frequency dependence of the OTE pair amplitudes at fixed T s, we see that the OTE pair amplitudes $|F_{\text{odd}}|$ are strongly peaked at $\omega = 0$

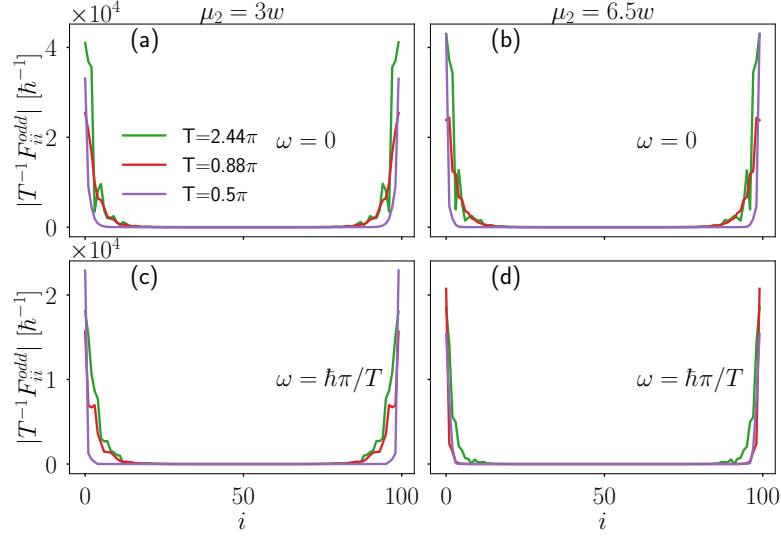


Figure 5.6: Onsite odd-frequency pair amplitude F_{ii}^{odd} as a function of space i . The left and right columns correspond to $\mu_2 = 3w$ and $\mu_2 = 6.5w$, respectively. Parameters: $\Delta = w$, $\mu_1 = 0$, $N = 100$.

and $\omega = \pm\pi\hbar/T$, as shown in Fig. 5.5(c,d). Furthermore, we note that the OTE amplitude develops larger values when the number of MZMs or MPMs is larger, as seen by noting the green, red, and magenta colors in e.g., Fig. 5.5(c,d). Meanwhile, the OTE pair amplitudes at bulk quasienergies are much smaller and in fact, they are almost negligible compared to the peaks at $\omega = 0$ and $\omega = \pi\hbar/T$. This is confirmed in Fig. 5.5(e,f), where we look at the log-log plot of the OTE pair amplitudes $|F_{\text{odd}}|$ as a function of ω . Here, we can clearly identify the divergent behavior of the OTE pair amplitudes at $\omega = 0$ and $\omega = \pi\hbar/T$. In fact, we see that the OTE pair amplitudes have linear dependence in the log-log scale near $\omega = 0$ ¹ and a divergent peak at $\omega = \pi\hbar/T$. For the bulk quasienergies, we see peaks in the log-log scale; however, they are much smaller and thus, they do not affect the overall behavior of the OTE pair amplitudes. As a matter of fact, we note that these peaks at the bulk quasienergies disappears in the semi-infinite limit and thus they are a finite-size effect.

Having established the frequency dependence of the OTE pair amplitudes, we now turn our attention to the spatial profile of OTE pair amplitudes. Here, we focus only on OTE pair amplitudes at frequencies $\omega = 0$ and $\omega = \pi\hbar/T$, which correspond to the quasienergies of MZMs and MPMs, respectively. Since we are

¹For $\log|T\omega/\hbar\pi| = -12$, which is roughly the leftmost value of the x axis in Fig. 5.5(e,f), we obtain $\omega \approx 10^{-6}(\hbar\pi/T)$ and $F_{\text{odd}} \approx 10^5(T/\hbar)$, thus revealing the enhancement of the OTE amplitude at zero energy.

interested in the spatial profile, we focus our attention on the local on-site s-wave OTE pairing $F_{ii}^{\text{odd}}(\omega)$, rather than the accumulated OTE pair amplitudes $F_{\text{odd}}(\omega)$. The results are summarized in Fig. 5.6, where we have plotted the absolute value of the local OTE pair amplitudes $|F_{ii}^{\text{odd}}|$ as a function of the site index i for various values of μ_2 and ω . In particular, we have considered two values of μ_2 , namely $\mu_2 = 3w$ in the left column [Fig. 5.6(a,c)] and $\mu_2 = 6.5w$ in the right column [Fig. 5.6(b,d)]. The top row [Fig. 5.6(a,b)] corresponds to $\omega = 0$ while the bottom row [Fig. 5.6(c,d)] corresponds to $\omega = \pi\hbar/T$. We note that in each panel of Fig. 5.6, we have plotted $|F_{ii}^{\text{odd}}|$ for different values of T , which are shown in the legends.

Our main observation is that the local OTE pair amplitudes $|F_{ii}^{\text{odd}}|$ are strongly peaked at the edges of the system, i.e., at $i \approx 1$ and $i \approx N$. This is a very interesting result since it shows that the OTE pair amplitudes are strongly localized at the edges of the system, which is a characteristic feature of Majorana edge modes. In fact, we can see that the local OTE pair amplitudes $|F_{ii}^{\text{odd}}|$ vanishes in the bulk of the system. This strong connection between the OTE pair amplitudes and the Majorana edge modes is a direct consequence of the chiral symmetry of the system, which was shown to protect the OTE pair amplitudes at the edges of the system in static topological superconductors [31, 33, 46–48, 73, 88]. Thus, our finding indicates that similar relationship hold in periodically driven superconductors. In the next section, we will prove that this relationship between OTE pairing and Majorana modes is indeed a topological feature of the system and is protected by the chiral symmetry of the effective Floquet Hamiltonian.

5.3.2 Characterization of topology by the odd-frequency pairing amplitude

Up to this point, we have seen multiple evidences that a strong relationship exists between the OTE pair amplitudes and the Majorana edge modes in our driven system. In particular, we have seen that the OTE pair amplitudes are localized at the edges of the system and that they are strongly peaked at the quasienergies of MZMs and MPMs. Moreover, we have also seen that the OTE pair amplitudes are strongly enhanced in the parameter space where the topological invariants W_0 and W_π are nonzero. In this section, we analytically establish this relationship between the OTE pair amplitudes and the Majorana edge modes as a topological feature of the system. We dub this relationship as the Floquet Spectral Bulk Boundary Correspondence (FSBBC). This FSBBC generalizes the spectral bulk boundary correspondence (SBBC) in static systems [46–48] to periodically driven systems.

Since FSBBC is a topological feature of the system, it is independent of the details of the Hamiltonian. In fact, the only ingredient we need to establish FSBBC is the chiral symmetry of the effective Floquet Hamiltonian. Thus, in this

section, we deviate from the specific model we have studied so far and consider a generic chiral symmetric Floquet Hamiltonian. We define a generic chiral symmetric Floquet Hamiltonian to be a Floquet Hamiltonian that satisfies the chiral symmetry condition for a given initial time t_0 as follows:

$$H_F[t_0] = -\Gamma H_F[t_0]\Gamma, \quad (5.19)$$

where $H_F[t_0]$ is the effective Floquet Hamiltonian at the initial time t_0 , and Γ is the chiral operator. The effective Floquet Hamiltonian $H_F[t_0]$ is a $dN \times dN$ matrix, where d is the number of degrees of freedom per site and N is the number of sites in the system. In terms of $H_F[t_0]$ and the chiral operator Γ , we can define an accumulated odd-frequency function $F_N(z)$ as a function of the complex frequency z as follows:

$$F_N(z) = \sum_{i=1}^{N/2} \frac{1}{4} \text{Tr}\{\Gamma \mathcal{G}_{ii}(z) + \mathcal{G}_{ii}(z)\Gamma\} = \frac{1}{4} \text{Tr}_{\text{Edge}}\{\Gamma \mathcal{G}(z) + \mathcal{G}(z)\Gamma\} \quad (5.20)$$

where $\mathcal{G}(z) = (z - H_F[t_0])^{-1}$ is the Green's function of the effective Floquet Hamiltonian at the initial time t_0 , and Tr_{Edge} is a trace operation defined on the left half of the system, i.e., it sums over the leftmost $N/2$ sites only. This accumulated odd-frequency function $F_N(z)$ is the finite-size version of the odd-frequency function $F(z)$ that appears in the static SBBC formulation [46–48], see also Eq. (2.101).

Following similar steps as in Eq. (2.102), we can show that the accumulated odd-frequency function $F_N(z)$ is an odd function of z , i.e., $F_N(-z) = -F_N(z)$. This is a direct consequence of the chiral symmetry of the effective Floquet Hamiltonian, which ensures that the Green's function $\mathcal{G}(z)$ satisfies $\mathcal{G}(-z) = -\Gamma \mathcal{G}(z)\Gamma$. We note that this odd function can be expressed in terms of the accumulated OTE pair amplitudes at the edges of the system following the same steps as in Eq. (2.103).

Having established the accumulated odd-frequency function $F_N(z)$, we can now relate it to the Majorana edge modes and the topological invariants of the system. In fact, we can show that in the semi-infinite limit ($N \rightarrow \infty$), the accumulated odd-frequency function $F_N(z)$ is a meromorphic function of z which is analytic in the complex plane except at the poles corresponding to the quasienergies of the Majorana edge modes. Furthermore, we can show that the residues of these poles are given exactly by the topological invariants of the system. In particular, we show that the residues of the poles at $z = E_0 = 0$ and $z = E_\pi = \pi\hbar/T$ are given by the winding numbers W_0 and W_π , respectively. Thus, we arrive at the central result of this section, which is the Floquet Spectral Bulk Boundary Correspondence (FSBBC). In terms of $H_F[t_0]$ and the chiral operator Γ , we define

the Floquet Spectral Bulk Boundary Correspondence (FSBBC) as follows:

$$\begin{aligned} \lim_{N \rightarrow \infty} F_N(z) &= F_\infty(z) \\ &= \frac{1}{2} \left(\frac{W_0}{z - E_0} + \frac{W_\pi}{2(z - E_\pi)} + \frac{W_\pi}{2(z + E_\pi)} + \mathcal{O}(z) \right), \end{aligned} \quad (5.21)$$

where $F_\infty(z)$ is the accumulated odd-frequency function in the semi-infinite limit, and W_0 and W_π are the winding numbers defined in Eq. (5.14). The energies $E_0 = 0$ and $E_\pi = \pi\hbar/T$ correspond to the quasienergies of the Majorana zero modes (MZMs) and Majorana π modes (MPMs), respectively. The $\mathcal{O}(z)$ term represents higher order corrections that vanish in the limit $z \rightarrow 0$ or $z \rightarrow \pi\hbar/T$. To prove the FSBBC in Eq. (5.21), we can follow similar steps as in the proof of the SBBC in static systems, see Eq. (2.104) and Appendix 5.5.2.

We note that the residues of the poles at the MPMs are halved compared to the MZMs. This is because in the above definition of the FSBBC, we have considered the MPMs as two separate poles at $z = \pm E_\pi$, while in reality, they are the same pole due to the periodicity of the quasienergies. In numerical calculations, we can only see half of the actual value of the residues at the MPMs. This is consistent with our numerical results in Fig. 5.5, where we see that the height of the peak at $\omega = \pi\hbar/T$ is half of what it is expected to be according to Eq. (5.21).

Having established the FSBBC in Eq. (5.21), we can now analyze its implications for the OTE pair amplitudes in our driven system. In our system, we have already found two initial times $t_0 = \pm T/4$ whose effective Floquet Hamiltonian H_F^\pm satisfies the chiral symmetry condition with $\Gamma = \tau_x$. Setting $t_0 = T/4$ and plugging the effective Floquet Hamiltonian H_F^+ into Eq. (5.20), we find that the accumulated odd-frequency function $F_N(z)$ is given by:

$$\begin{aligned} F_N(z) &= \frac{1}{4} \sum_{i=1}^{N/2} \text{Tr} \{ \tau_x \mathcal{G}_{ii}(z) + \mathcal{G}_{ii}(z) \tau_x \} = \frac{1}{2} \sum_{i=1}^{N/2} (F_{ii}(z) + \bar{F}_{ii}(z)) \\ &= \frac{1}{2} \sum_{i=1}^{N/2} (F_{ii}(z) - F_{ii}(-z)) = \sum_{i=1}^{N/2} F_{ii}^{\text{odd}}(z) \\ &= F_{\text{odd}}(z), \end{aligned} \quad (5.22)$$

The last equality follows from the definition of the accumulated odd-frequency pair amplitudes in Eq. (5.18). Thus, we identify the accumulated odd-frequency pair amplitudes $F_{\text{odd}}(z)$ in our model as the odd-frequency function $F_N(z)$ appearing in the FSBBC in Eq. (5.21). This means that the accumulated odd-frequency pair amplitudes $F_{\text{odd}}(z)$ in our model is indeed a topological feature of the system and is protected by the chiral symmetry of the effective Floquet Hamiltonian. In particular, we find that in the semi-infinite limit, the accumulated odd-frequency

pair amplitudes $F_{\text{odd}}(z)$ diverges at the quasienergies of MZMs and MPMs, which is consistent with our numerical results in Fig. 5.5. Moreover, we find that the heights of the peaks at $\omega = 0$ and $\omega = \pi\hbar/T$ are proportional to the winding numbers W_0 and W_π , respectively. This is a very important result since it shows that the OTE pair amplitudes are a direct measure of the topology of the system.

A key insight from our analysis, presented in Eq. (5.21), is that the accumulated odd-frequency pair amplitude functions as a real-space representation of the topological winding number. This connection is remarkably general, as its derivation relies solely on the chiral symmetry of the one-period evolution operator, not on the specific details of the Hamiltonian. Consequently, the relationship is topologically protected and remains stable against any perturbations that preserve this symmetry. This principle is expected to hold for all 1D systems with chiral or sub-lattice symmetry (e.g., classes AIII, BDI, CII, DIII [6]), such as in Rashba systems [32] or helical Shiba chains [133], and under various time-periodic drives, provided chiral symmetry is maintained. This interpretation is consistent with other known real-space formulations of the winding number [48, 134, 135].

5.3.3 Robustness Against Scalar Disorder

A defining characteristic of any topological phenomenon is its resilience to local perturbations that preserve the underlying protective symmetries. To test the robustness of the Floquet Spectral Bulk-Boundary Correspondence (FSBBC) established in Eq. (5.21), we now investigate the impact of chiral symmetry-preserving disorder.

To this end, we introduce quenched scalar disorder into our model by adding a random on-site potential term to the time-periodic Hamiltonian:

$$H_{\text{dis}}(t) = H(t) + \sum_{i=1}^N v_i \psi_i^\dagger \tau_z \psi_i, \quad (5.23)$$

where $H(t)$ is the clean Hamiltonian from Eq. (5.1). The random potentials v_i are drawn from a uniform distribution within the interval $[-\frac{V_0}{2}, \frac{V_0}{2}]$, where V_0 represents the disorder strength.

In our numerical analysis, we examine the behavior of the accumulated odd- ω pairing amplitude, F_{odd} , in the presence of this disorder. We present results for an intermediate disorder strength of $V_0 = w$, with F_{odd} averaged over 10 disorder realizations, which we found sufficient for convergence. Figure (5.7) illustrates the disorder-averaged F_{odd} as a function of the driving period T for several system lengths. For a relatively small system of $N = 100$ sites [Fig. (5.7)(a,e)], which matches the size used in the clean-limit calculations of Fig. (5.5), the correspondence between the odd- ω pairing and the topological winding numbers remains

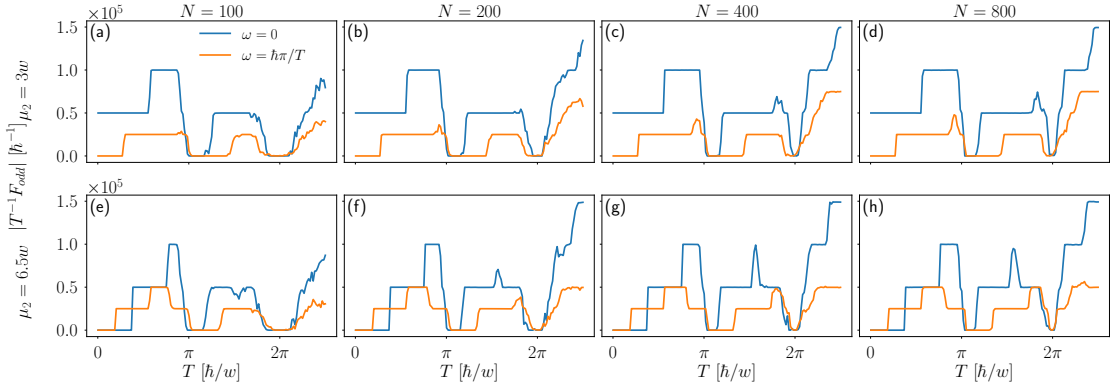


Figure 5.7: Same as in Fig. 5.5(a,b) but in the presence of on site disorder and for chain length of 100 sites(a,e), 200 sites(b,f), 400 sites(c,g), 800 sites(d,h). Parameters: $V_0 = w$, $\Delta = w$, $\mu_1 = 0$

apparent, especially for shorter periods. However, for larger T , this one-to-one mapping is obscured by pronounced finite-size effects, which are exacerbated by disorder.

Crucially, as the system size increases [Fig. (5.7)(b-d, f-h)], the correspondence is progressively restored. In the largest system shown ($N = 800$), the plateaus in F_{odd} that signify distinct topological phases become well-defined, and the transition points are clearly identifiable, mirroring the behavior of the topological invariants.

In general, the FSBBC relationship is expected to hold as long as the Majorana edge modes remain protected by a bulk energy gap. The correspondence would only break down for disorder strong enough to close this gap, which would render the winding number ill-defined. Our findings therefore confirm that the connection detailed in Eq. (5.21) is a topologically-protected feature, robust against scalar disorder. We anticipate this principle applies broadly to all one-dimensional systems within the chiral symmetry classes (AIII, BDI, CII, and DIII) [6].

5.4 Concluding Remarks

In this chapter, we have explored the intimate connection between Majorana modes and odd-frequency superconductivity within the framework of Floquet topological systems. By analyzing a one-dimensional p -wave superconductor subject to a time-periodic chemical potential, we have demonstrated how dynamical driving can be used to generate and control rich topological phases.

Our primary finding is the generalization of the spectral bulk-boundary correspondence to the Floquet domain. This **Floquet Spectral Bulk-Boundary Correspondence (FSBBC)** reveals that the accumulated odd-frequency pair-

ing at the system's edge serves as a real-space topological invariant. We showed that this pairing exhibits a divergent profile at the quasienergies of the emergent Majorana modes: a $\sim 1/\omega$ dependency for Majorana zero modes (MZMs) and a $\sim 1/(\omega - \pi\hbar/T)$ dependency for Majorana π modes (MPMs). This relationship holds even when multiple edge modes of both types coexist and, as demonstrated, is robust against chiral-symmetry-preserving disorder.

These results have several important implications. From a fundamental perspective, they establish odd-frequency pairing as a powerful tool for characterizing Floquet topological phases, even in disordered systems. From a practical viewpoint, the ability to control odd-frequency pairing dynamically may be relevant for applications in superconducting spintronics, which leverages spin-polarized Cooper pairs [136]. The experimental realization of these phenomena is tied to the ongoing progress in fabricating semiconductor-superconductor hybrid devices [16, 81], where the necessary ingredients for realizing and driving topological superconductivity are being actively developed.

This work also opens several avenues for future research. A natural extension would be to verify these principles in more complex and realistic models, such as Rashba nanowires [32] or helical Shiba chains [133]. Another promising direction is to investigate the interplay of driving, topology, and odd-frequency pairing in non-ideal scenarios, for instance, by incorporating dissipation, which connects to the rich field of non-Hermitian physics [13], or by including many-body interactions. Finally, exploring more complex driving protocols, such as those involving multiple frequencies, could potentially lead to the discovery of novel dynamical phases of matter, including odd-frequency time-crystalline states.

5.5 Appendices of Chapter 5

5.5.1 Derivation of Bulk Quasienergy

In this appendix, we provide a detailed derivation of the bulk quasienergy expression presented in Eq. (5.10). We begin with the one-period time-evolution operator U_T in momentum space. For convenience, we set the initial time frame to $t_0 = 0$, which gives

$$U_T(k) = e^{-i\frac{T}{2\hbar}H_2(k)}e^{-i\frac{T}{2\hbar}H_1(k)} = e^{-i\frac{T}{2\hbar}\mathbf{E}_2\cdot\boldsymbol{\tau}}e^{-i\frac{T}{2\hbar}\mathbf{E}_1\cdot\boldsymbol{\tau}}, \quad (5.24)$$

where the Hamiltonians for each half-period are represented by vectors $\mathbf{E}_j = (0, -2\Delta \sin k, -\mu_j - 2w \cos k)^T$ in the basis of Pauli matrices $\boldsymbol{\tau} = (\tau_x, \tau_y, \tau_z)$.

Since this expression is a product of elements from the SU(2) group, the product has to be an element of SU(2) and thus it can be expressed as a single exponential. We use Euler formula for Pauli matrix exponentials to find a single exponential

form. Expanding each term in Eq. (5.24) yields

$$\begin{aligned} U_T &= \left(\cos \frac{E_2 T}{2\hbar} \mathbb{1} - i \hat{\mathbf{E}}_2 \cdot \boldsymbol{\tau} \sin \frac{E_2 T}{2\hbar} \right) \left(\cos \frac{E_1 T}{2\hbar} \mathbb{1} - i \hat{\mathbf{E}}_1 \cdot \boldsymbol{\tau} \sin \frac{E_1 T}{2\hbar} \right) \\ &= \mathbb{1} \left[\cos \frac{E_1 T}{2\hbar} \cos \frac{E_2 T}{2\hbar} - \hat{\mathbf{E}}_1 \cdot \hat{\mathbf{E}}_2 \sin \frac{E_1 T}{2\hbar} \sin \frac{E_2 T}{2\hbar} \right] \\ &\quad - i \left[\hat{\mathbf{E}}_1 \sin \frac{E_1 T}{2\hbar} \cos \frac{E_2 T}{2\hbar} + \hat{\mathbf{E}}_2 \sin \frac{E_2 T}{2\hbar} \cos \frac{E_1 T}{2\hbar} + \hat{\mathbf{E}}_1 \times \hat{\mathbf{E}}_2 \sin \frac{E_1 T}{2\hbar} \sin \frac{E_2 T}{2\hbar} \right] \cdot \boldsymbol{\tau}, \end{aligned} \quad (5.25)$$

where $E_j = |\mathbf{E}_j|$ and $\hat{\mathbf{E}}_j = \mathbf{E}_j/E_j$. The bulk quasienergies $E_F(k)$ are the eigenvalues of the effective Floquet Hamiltonian $H_F(k)$, which defines the one-period evolution operator as $U_T(k) = e^{-i\frac{T}{\hbar}H_F(k)}$. Applying Euler's formula to this definition gives

$$e^{-i\frac{T}{\hbar}H_F(k)} = \mathbb{1} \cos \frac{E_F T}{\hbar} - i \hat{\mathbf{E}}_F \cdot \boldsymbol{\tau} \sin \frac{E_F T}{\hbar}. \quad (5.26)$$

The bulk quasienergies can be found by equating the trace (the term proportional to the identity matrix $\mathbb{1}$) of Eq. (5.25) and Eq. (5.26). This directly leads to

$$\cos \frac{E_F T}{\hbar} = \cos \frac{E_1 T}{2\hbar} \cos \frac{E_2 T}{2\hbar} - \frac{\mathbf{E}_1 \cdot \mathbf{E}_2}{E_1 E_2} \sin \frac{E_1 T}{2\hbar} \sin \frac{E_2 T}{2\hbar}. \quad (5.27)$$

Solving for $E_F(k)$ gives the expression in Eq. (5.10) in the main text. This result is general for any two-step drive acting on a two-band system.

As a specific point of interest, consider the momentum $k = \pi$. Here, $\sin(k) = 0$ and $\cos(k) = -1$, so \mathbf{E}_j is purely in the τ_z direction. The expression simplifies to $\cos(T E_F / \hbar) = \cos[T(E_1 + E_2)/(2\hbar)] = \cos[T(|-\mu_1 + 2w| + |-\mu_2 + 2w|)/(2\hbar)]$. If we impose the condition $\mu_1 + \mu_2 = 4w$, which corresponds to the topological phase transition point of the time-averaged static Hamiltonian, we find $\cos(T E_F / \hbar) = 1$. This implies that the quasienergy gap closes, with $E_F = 2\pi n \hbar / T$ for $n \in \mathbb{Z}$, demonstrating a drive-induced gap closing inherited from the static system's topology.

5.5.2 Floquet Bulk-Boundary Correspondence and Odd-Frequency Pairing

In this appendix, we formalize the proof of the Floquet Spectral Bulk-Boundary Correspondence (FSBBC) given in Eq. (5.21). This derivation applies to a general class of 1D Hamiltonians and driving protocols, with the sole requirement being the existence of a chiral symmetry. Specifically, we require a unitary operator

$\Gamma[t_0]$ with $\Gamma[t_0]^2 = 1$ that, for a specific initial time frame t_0 , makes the one-period evolution operator $U_T[t_0]$ satisfy

$$\Gamma[t_0]U_T[t_0]\Gamma[t_0] = U_T^\dagger[t_0]. \quad (5.28)$$

This condition ensures that the corresponding Floquet Hamiltonian $H_F[t_0]$ is also chiral symmetric, $\{H_F[t_0], \Gamma[t_0]\} = 0$.

We begin by defining a complex function $F_N(z)$ that quantifies the accumulated odd-frequency response on the left edge of a finite system of N sites:

$$F_N(z) = \frac{1}{4}\text{Tr}_{\text{Edge}}\{\Gamma[t_0]\mathcal{G}(z) + \mathcal{G}(z)\Gamma[t_0]\}, \quad (5.29)$$

where $\mathcal{G}(z) = (z - H_F[t_0])^{-1}$ is the Green's function, and Tr_{Edge} denotes a trace over the internal degrees of freedom summed over the left half of the chain ($j = 1, \dots, N/2$). Due to the chiral symmetry of $H_F[t_0]$, $F_N(z)$ is an odd function of z , i.e., $F_N(-z) = -F_N(z)$. In our specific model, this function corresponds to the accumulated odd-frequency pair amplitude.

Our central claim is that in the thermodynamic limit ($N \rightarrow \infty$), the residues of the poles of $F_\infty(z)$ at $z = 0$ and $z = \pi\hbar/T$ are determined by the topological winding numbers W_0 and W_π . Let's prove this for the pole at $z = 0$. The residue is given by

$$\lim_{z \rightarrow 0} zF_N(z) = \lim_{z \rightarrow 0} \frac{1}{4} \sum_{j=1,\sigma}^{N/2} \langle j, \sigma | \Gamma[t_0] \frac{z}{z - H_F[t_0]} + \frac{z}{z - H_F[t_0]} \Gamma[t_0] | j, \sigma \rangle. \quad (5.30)$$

Inserting a complete set of eigenstates $|E\rangle$ of $H_F[t_0]$ and using the fact that $\langle E | \Gamma[t_0] | E' \rangle \neq 0$ only if $E' = -E$, the expression becomes

$$\lim_{z \rightarrow 0} \sum_{j,\sigma,E} \frac{1}{2} \langle j, \sigma | E \rangle \langle E | \frac{z^2}{z^2 - E^2} \Gamma[t_0] | -E \rangle \langle -E | j, \sigma \rangle. \quad (5.31)$$

In the limit $z \rightarrow 0$, the factor $z^2/(z^2 - E^2)$ approaches 1 for states with $E = 0$ and 0 for any gapped state with finite energy $E \neq 0$. Therefore, only the zero-energy modes contribute to the sum. For a sufficiently large system, these zero modes are topologically protected edge states localized at the boundaries. The partial trace over the left half of the system will thus select only the zero modes localized at

the left edge. In the thermodynamic limit, this gives

$$\begin{aligned} \lim_{z \rightarrow 0} z F_\infty(z) &= \sum_{\substack{E=0, \\ \text{left edge}}} \frac{1}{2} \langle E | \Gamma[t_0] | E \rangle \sum_{j=1,\sigma}^{\infty} | \langle j, \sigma | E \rangle |^2 \\ &= \frac{1}{2} \sum_{E=0, \text{left}} \langle E | \Gamma[t_0] | E \rangle \\ &= \frac{N_0^+ - N_0^-}{2} = \frac{W_0}{2}, \end{aligned} \quad (5.32)$$

where N_0^\pm is the number of zero-energy modes at the left edge with positive/negative chirality. The final step uses the index theorem relating this difference in chirality to the winding number W_0 [11].

An analogous derivation holds for the residue at $z = E_\pi = \pi\hbar/T$, where the sum is dominated by the Majorana π modes. This leads to

$$\lim_{z \rightarrow E_\pi} (z - E_\pi) F_\infty(z) = \frac{N_\pi^+ - N_\pi^-}{4} = \frac{W_\pi}{4}. \quad (5.33)$$

The factor of 1/4 arises because there are two poles related to MPMs at $\pm E_\pi$, which share the winding number W_π . Combining these results proves the FSBBC relation in Eq. (5.21). Since the proof relies only on chiral symmetry, the result is topologically protected.

5.5.3 Relation Between Effective and True Green's Functions

This appendix establishes the formal connection between the stroboscopic Green's function \mathcal{G}_F , derived from the effective Floquet Hamiltonian H_F , and the "true" two-time Green's function $\mathcal{G}(t, t')$, derived from the full time-periodic Hamiltonian $H(t)$. This dictionary justifies using \mathcal{G}_F to analyze the system's stroboscopic dynamics.

Time Domain

The true retarded Green's function is defined via the time-evolution operator $U(t, t')$ [118] as:

$$\mathcal{G}(t, t') = -i\Theta(t - t') U(t, t') = -i\Theta(t - t') \mathcal{T} e^{-\frac{i}{\hbar} \int_{t'}^t H(s) ds}, \quad (5.34)$$

where $\Theta(t - t')$ is the Heaviside step function. The effective Green's function for a given time frame t_0 is, similarly, $\mathcal{G}_F[t_0](t, t') = -i\Theta(t - t') e^{-i(t-t')H_F[t_0]/\hbar}$.

The link between these two is the so-called "kick" operator, a unitary and T -periodic operator defined as

$$P(t, t_0) = U(t, t_0) e^{i(t-t_0)H_F[t_0]/\hbar}. \quad (5.35)$$

Using this operator, we can show that the true and effective Green's functions are related by a unitary transformation:

$$\mathcal{G}(t, t') = P(t, t_0) \mathcal{G}_F[t_0](t, t') P^\dagger(t', t_0). \quad (5.36)$$

This key relation can be verified by substituting it into the equation of motion for $\mathcal{G}(t, t')$, $(i\hbar\partial_t - H(t))\mathcal{G}(t, t') = \delta(t - t')$, and using the identity $H_F[t_0] = P^\dagger(t, t_0)H(t)P(t, t_0) - i\hbar P^\dagger(t, t_0)\dot{P}(t, t_0)$.

A crucial property of the kick operator is that it becomes the identity at all stroboscopic times, i.e., $P(t_0 + nT, t_0) = \mathbb{1}$ for any integer n . If we evaluate Eq. (5.36) at stroboscopic times $t = t_0 + nT$ and $t' = t_0 + n'T$, it simplifies to

$$\mathcal{G}(t_0 + nT, t_0 + n'T) = \mathcal{G}_F[t_0](nT, n'T). \quad (5.37)$$

This proves that the stroboscopic Green's function \mathcal{G}_F is identical to the true Green's function \mathcal{G} when both time arguments are sampled at integer multiples of the driving period T .

Frequency Domain

The connection in the frequency domain is more involved because $\mathcal{G}(t, t')$ is not fully time-translation invariant. Its Fourier transform is a matrix in the basis of Floquet modes, labeled by integers n, m . This so-called extended-space Green's function, $\mathcal{G}_{nm}(\omega)$, is related to the Fourier transform of the effective Green's function, $\mathcal{G}_F(\omega)$, by

$$\mathcal{G}_{nm}(\omega) = P_n(t_0) \mathcal{G}_F[t_0](\omega) P_m^\dagger(t_0), \quad (5.38)$$

where $P_n(t_0)$ are the Fourier coefficients of the periodic kick operator $P(t, t_0)$. This relation provides a complete dictionary between the full quantum dynamics and the effective stroboscopic description, validating the approach used in Section 5.3.

Chapter 6

Conclusion and Outlook

In this thesis, we have performed a comprehensive theoretical and numerical investigation into the emergent superconducting pairing correlations in systems capable of hosting Majorana bound states (MBSs) and trivial Andreev bound states (ABSs). The central motivation of our work has been to address the critical challenge of unambiguously identifying topological superconductivity and Majorana fermions, whose experimental detection has been confounded by the ability of trivial states to mimic their zero-energy signatures. To this end, we have systematically demonstrated that odd-frequency pairing serves as a powerful probe of topological superconductivity, revealing fundamental distinctions that are inaccessible to conventional transport measurements alone.

6.1 Conclusion

The main findings of this thesis, presented across Chapters 3, 4, and 5, establish a cohesive framework for utilizing odd-frequency pairing as a definitive topological probe. Our main contributions can be summarized as follows:

In Chapter 3, we have analyzed the emergent pairing correlations in finite-length static superconductor-semiconductor (NS) junctions. We established that while both trivial ABSs and topological MBSs generate significant odd-frequency spin-triplet even-parity (OTE) pair amplitudes, their low-frequency dependence provides a crucial distinguishing feature. The OTE pairing induced by trivial ABSs was found to exhibit a strictly *linear* frequency dependence, vanishing precisely at zero frequency. In stark contrast, we have demonstrated that true zero-energy MBSs, which are realized in sufficiently long superconducting segments where their spatial nonlocality is manifest, induce an OTE pairing profile that is uniquely *divergent* ($\sim 1/\omega_n$) close to zero frequency. This divergence, a direct consequence of the inherent self-conjugation of Majorana fermions, serves as a definitive hallmark

of the topological phase.

In Chapter 4, we extended our study to investigate the influence of disorder by analyzing the anomalous proximity effect in finite-length clean normal/disordered normal/superconductor (CN/DN/S) junctions. Our results reveal that the zero-energy peak (ZEP) in the local density of states (LDOS) against disorder is critically contingent on the nature of the underlying zero-energy state and the system's geometry. We found that the ZEP associated with trivial ABSs is universally *fragile*, rapidly splitting and decaying with the introduction of scalar disorder. The ZEP originating from MBSs in short superconducting segments exhibits a similar fragility. However, for long superconducting segments that suppress Majorana hybridization, the topological ZEP remains remarkably *robust* and pinned at zero energy, even under significant disorder. We have conclusively shown that this robust ZEP, the key signature of the anomalous proximity effect, is sustained by odd-frequency spin-triplet correlations, whereas conventional even-frequency spin-singlet pairing is consistently suppressed at zero energy in the normal region.

Finally, in Chapter 5, we have explored the rich physics of periodically driven (Floquet) topological superconductors. We have shown that a time-periodic drive can be utilized to engineer a complex phase diagram featuring not only multiple zero-energy Majorana modes (MZMs) but also Majorana π -modes (MPMs). Crucially, we discovered that these distinct Majorana modes are characterized by unique odd-frequency pairing signatures, exhibiting a $\sim 1/\omega$ divergence for MZMs and a $\sim 1/(\omega - \pi\hbar/T)$ divergence for MPMs. This investigation culminated in the establishment of a generalized spectral bulk-boundary correspondence for driven chiral symmetric systems. This correspondence reveals that the accumulated boundary odd-frequency pairing is a real-space topological invariant, directly proportional to the bulk winding number, thereby providing a powerful tool to characterize topology in time-periodic systems even in the presence of disorder.

In summary, our work has established odd-frequency pairing as a robust and unambiguous signature of topological superconductivity, providing a powerful framework for distinguishing Majorana bound states from trivial Andreev bound states. The insights gained from our investigations pave the way for future experimental efforts to identify and manipulate Majorana fermions in solid-state systems.

6.2 Outlook

The findings of this thesis open several promising avenues for future research, spanning from immediate experimental proposals to more foundational theoretical explorations.

Experimental Probes of Odd-Frequency Pairing. A crucial next step is the experimental verification of our theoretical predictions. The distinct frequency dependence and disorder resilience of the odd-frequency pairing signatures can be indirectly probed through several existing experimental techniques. Spatially-resolved Andreev spectroscopy, for instance, could be employed to detect the predicted behavior of the accumulated pair amplitudes, whose "chainsaw-like" features, as shown in Chapter 3, mark the helical and topological phase transitions. Furthermore, the anomalous current-phase relation in Josephson junctions, which is highly sensitive to the underlying pairing symmetry, could be probed with a superconducting scanning tunneling microscope (STM) tip to confirm the presence of the dominant OTE components we predict in the topological phase.

Theoretical Exploration of Complex Systems. While our work provides a robust foundation in one-dimensional models, a natural and important progression is the extension of this framework to more complex systems. This includes two-dimensional platforms, where Majorana modes can be hosted in vortex cores or at the edges of planar junctions, and higher-order topological superconductors, which support Majorana corner modes. Investigating the manifestation of odd-frequency pairing signatures in these higher-dimensional systems is an exciting frontier. Moreover, exploring the interplay between odd-frequency pairing and many-body interactions beyond the mean-field approximations used in this thesis could reveal novel, interaction-driven topological phases with unique pairing characteristics. This is especially relevant in the context of strongly correlated systems with non-abelian anyons such as fractional quantum Hall insulator/superconductor junctions, where the interplay of fractional statistics, odd-frequency pairing, and disorder could lead to new emergent phenomena.

Floquet Engineering and Non-Hermitian Physics. Our investigation into driven systems in Chapter 5 suggests a powerful methodology for the dynamical control of topological phases and their associated pairing symmetries. Further exploration of more complex drive protocols could lead to the engineering of novel Floquet topological states that are not accessible in static systems. Another intriguing direction is to study the interplay between odd-frequency pairing and non-Hermitian physics. Real experimental systems are inherently open and dissipative, and understanding how these non-Hermitian effects modify the spectral bulk-boundary correspondence and the stability of odd-frequency pairing is essential for real-world applications and may unveil new phenomena, such as a non-Hermitian skin effect for Cooper pairs.

Applications in Superconducting Spintronics. The ability to generate and manipulate spin-polarized triplet Cooper pairs is a central goal of superconducting spintronics. Our finding that OTE pairing is the dominant correlation in the topological regime and can be dynamically controlled via a Floquet drive suggests a new paradigm for spintronic devices. Future work could focus on designing specific device geometries that leverage these emergent odd-frequency correlations to create, filter, and manipulate pure spin supercurrents with high efficiency and control, paving the way for a new generation of topological superconducting spintronic technologies.

Bibliography

- [1] E. Ahmed, S. Tamura, Y. Tanaka, and J. Cayao, *Physical Review B* **111**, 224508 (2025).
- [2] E. Ahmed, Y. Tanaka, and J. Cayao, arXiv preprint arXiv:2505.03726 (2025).
- [3] E. Ahmed, S. Tamura, Y. Tanaka, and J. Cayao, *Physical Review B* **111**, 024507 (2025).
- [4] K. v. Klitzing, G. Dorda, and M. Pepper, *Phys. Rev. Lett.* **45**, 494 (1980).
- [5] F. D. M. Haldane, *Rev. Mod. Phys.* **89**, 040502 (2017).
- [6] C.-K. Chiu, J. C. Y. Teo, A. P. Schnyder, and S. Ryu, *Rev. Mod. Phys.* **88**, 035005 (2016).
- [7] S. M. Bhattacharjee, M. Mj, and A. Bandyopadhyay, *Topology and condensed matter physics*, Vol. 19 (Springer, 2017).
- [8] T. D. Stanescu, *Introduction to topological quantum matter & quantum computation* (CRC Press, 2024).
- [9] M. Sato and Y. Ando, *Rep. Prog. Phys.* **80**, 076501 (2017).
- [10] H. Wu, S. Wu, and L. Zhou, *New J. Phys.* **25**, 083042 (2023).
- [11] J. K. Asbóth, B. Tarasinski, and P. Delplace, *Phys. Rev. B* **90**, 125143 (2014).
- [12] C. Nayak, S. H. Simon, A. Stern, M. Freedman, and S. Das Sarma, *Reviews of Modern Physics* **80**, 1083 (2008).
- [13] K. Kawabata, K. Shiozaki, M. Ueda, and M. Sato, *Phys. Rev. X* **9**, 041015 (2019).
- [14] L. Zhou, *Phys. Rev. B* **101**, 014306 (2020).
- [15] A. Y. Kitaev, *Physics-усpekhi* **44**, 131 (2001).
- [16] R. M. Lutchyn, E. P. Bakkers, L. P. Kouwenhoven, P. Krogstrup, C. M. Marcus, and Y. Oreg, *Nat. Rev. Mater.* **3**, 52 (2018).

- [17] Y. Oreg, G. Refael, and F. von Oppen, *Phys. Rev. Lett.* **105**, 177002 (2010).
- [18] R. M. Lutchyn, J. D. Sau, and S. Das Sarma, *Phys. Rev. Lett.* **105**, 077001 (2010).
- [19] V. Mourik, K. Zuo, S. M. Frolov, S. R. Plissard, E. P. A. M. Bakkers, and L. P. Kouwenhoven, *Science* **336**, 1003 (2012).
- [20] A. Das, Y. Ronen, Y. Most, Y. Oreg, M. Heiblum, and H. Shtrikman, *Nature Physics* **8**, 887 (2012).
- [21] G. Kells, D. Meidan, and P. W. Brouwer, *Phys. Rev. B* **86**, 100503 (2012).
- [22] O. Dmytruk, D. Loss, and J. Klinovaja, *Phys. Rev. B* **102**, 245431 (2020).
- [23] S. Das Sarma and H. Pan, *Phys. Rev. B* **103**, 195158 (2021).
- [24] J. Cayao and P. Burset, *Phys. Rev. B* **104**, 134507 (2021).
- [25] J. Cayao, *Phys. Rev. B* **110**, 085414 (2024).
- [26] C. Reeg, O. Dmytruk, D. Chevallier, D. Loss, and J. Klinovaja, *Phys. Rev. B* **98**, 245407 (2018).
- [27] B. S. de Mendonça, A. L. R. Manesco, N. Sandler, and L. G. G. V. Dias da Silva, *Phys. Rev. B* **107**, 184509 (2023).
- [28] J. Cayao, E. Prada, P. San-Jose, and R. Aguado, *Phys. Rev. B* **91**, 024514 (2015).
- [29] J. Cayao, A. M. Black-Schaffer, E. Prada, and R. Aguado, *Beilstein J. Nanotechnol.* **9**, 1339 (2018).
- [30] V. L. Berezinskii, *JETP Lett.* **20**, 287 (1974).
- [31] Y. Tanaka, M. Sato, and N. Nagaosa, *J. Phys. Soc. Jpn.* **81**, 011013 (2012).
- [32] Y. Tanaka, S. Tamura, and J. Cayao, *Prog. Theor. Exp. Phys.* **2024**, 08C105 (2024).
- [33] J. Cayao, C. Triola, and A. M. Black-Schaffer, *Eur. Phys. J. Spec. Top.* **229**, 545 (2020).
- [34] J. Linder and A. V. Balatsky, *Rev. Mod. Phys.* **91**, 045005 (2019).
- [35] A. Di Bernardo, Z. Salman, X. L. Wang, M. Amado, M. Egilmez, M. G. Flokstra, A. Suter, S. L. Lee, J. H. Zhao, T. Prokscha, E. Morenzoni, M. G. Blamire, J. Linder, and J. W. A. Robinson, *Phys. Rev. X* **5**, 041021 (2015).
- [36] Y. Tanaka and S. Kashiwaya, *Phys. Rev. B* **70**, 012507 (2004).
- [37] D. Takagi, S. Tamura, and Y. Tanaka, *Phys. Rev. B* **101**, 024509 (2020).
- [38] Y. Nagae, L. Katayama, and S. Ikegaya, arxiv preprint arxiv:2502.02053 (2025).

- [39] Y. Asano, Y. Tanaka, and S. Kashiwaya, *Phys. Rev. Lett.* **96**, 097007 (2006).
- [40] S. Ikegaya, Y. Asano, and Y. Tanaka, *Phys. Rev. B* **91**, 174511 (2015).
- [41] S. Ikegaya, S.-I. Suzuki, Y. Tanaka, and Y. Asano, *Phys. Rev. B* **94**, 054512 (2016).
- [42] S. Ikegaya and Y. Asano, *Phys. Rev. B* **95**, 214503 (2017).
- [43] Y. Tanaka, S. Kashiwaya, and T. Yokoyama, *Phys. Rev. B* **71**, 094513 (2005).
- [44] Y. Asano, Y. Tanaka, T. Yokoyama, and S. Kashiwaya, *Phys. Rev. B* **74**, 064507 (2006).
- [45] Y. Asano and Y. Tanaka, *Phys. Rev. B* **87**, 104513 (2013).
- [46] S. Tamura, S. Hoshino, and Y. Tanaka, *Phys. Rev. B* **99**, 184512 (2019).
- [47] S. Tamura, S. Hoshino, and Y. Tanaka, *Phys. Rev. B* **104**, 165125 (2021).
- [48] A. Daido and Y. Yanase, *Phys. Rev. B* **100**, 174512 (2019).
- [49] H. K. Onnes, in *Through measurement to knowledge: the selected papers of heike kamerlingh onnes 1853–1926* (Springer, 1991), pp. 261–263.
- [50] M. G. Alford, A. Schmitt, K. Rajagopal, and T. Schäfer, *Reviews of Modern Physics* **80**, 1455 (2008).
- [51] A. Abokhalil, arXiv preprint arXiv:2306.01019 (2023).
- [52] G. R. Stewart, *Advances in Physics* **66**, 75 (2017).
- [53] J. Bardeen, L. N. Cooper, and J. R. Schrieffer, *Physical review* **108**, 1175 (1957).
- [54] D. A. Cardwell, D. C. Larbalestier, and A. Braginski, *Handbook of superconductivity: fundamentals and materials, volume one*, Vol. 1 (CRC Press, 2022).
- [55] M. Tinkham, *Introduction to superconductivity* (Courier Corporation, 2004).
- [56] N. N. Bogoljubov, V. V. Tolmachov, and D. Širkov, *Fortschritte der physik* **6**, 605 (1958).
- [57] P.-G. De Gennes, *Superconductivity of metals and alloys* (CRC press, 2018).
- [58] A. Zagoskin, *Quantum theory of many-body systems: techniques and applications* (Springer, 2014).
- [59] D. J. Thouless, M. Kohmoto, M. P. Nightingale, and M. den Nijs, *Phys. Rev. Lett.* **49**, 405 (1982).
- [60] C. L. Kane and E. J. Mele, *Phys. Rev. Lett.* **95**, 226801 (2005).

- [61] B. A. Bernevig and S.-C. Zhang, *Phys. Rev. Lett.* **96**, 106802 (2006).
- [62] E. Majorana, *Soryushiron Kenkyu Electronics* **63**, 149 (1981).
- [63] A. Y. Kitaev, *Annals of physics* **303**, 2 (2003).
- [64] R. Aguado and L. Kouwenhoven, *Phys. Today* **73**, 44 (2020).
- [65] P. Marra and A. Nigro, *J. Phys.: Condens. Matter* **34**, 124001 (2022).
- [66] K. Laubscher and J. Klinovaja, *Journal of Applied Physics* **130** (2021).
- [67] K. Flensberg, F. von Oppen, and A. Stern, *Nat. Rev. Mater.* **6**, 944 (2021).
- [68] E. J. Lee, X. Jiang, M. Houzet, R. Aguado, C. M. Lieber, and S. De Franceschi, *Nature nanotechnology* **9**, 79 (2014).
- [69] Y. Tanaka, A. A. Golubov, S. Kashiwaya, and M. Ueda, *Phys. Rev. Lett.* **99**, 037005 (2007).
- [70] Y. Tanaka, Y. Tanuma, and A. A. Golubov, *Phys. Rev. B* **76**, 054522 (2007).
- [71] M. Eschrig, T. Löfwander, T. Champel, J. C. Cuevas, J. Kopu, and G. Schön, *J. Low Temp. Phys.* **147**, 457 (2007).
- [72] T. Yokoyama, Y. Tanaka, and A. A. Golubov, *Phys. Rev. B* **75**, 134510 (2007).
- [73] Y. Tanaka and S. Tamura, *J. Supercond. Nov. Magn.* **34**, 1677 (2021).
- [74] Z. Huang, P. Wölfle, and A. V. Balatsky, *Phys. Rev. B* **92**, 121404 (2015).
- [75] A. Golubov and M. Y. Kupriyanov, *Journal of low temperature physics* **70**, 83 (1988).
- [76] Y. Tanaka and A. A. Golubov, *Phys. Rev. Lett.* **98**, 037003 (2007).
- [77] G. Floquet, fr, *Annales scientifiques de l'École Normale Supérieure 2e série*, **12**, 47 (1883).
- [78] M. Holthaus, *Journal of Physics B: Atomic, Molecular and Optical Physics* **49**, 013001 (2015).
- [79] M. E. Peskin and D. V. Schroeder, *Quantum field theory. the advanced book program*, 1995.
- [80] L. Jiang, T. Kitagawa, J. Alicea, A. R. Akhmerov, D. Pekker, G. Refael, J. I. Cirac, E. Demler, M. D. Lukin, and P. Zoller, *Phys. Rev. Lett.* **106**, 220402 (2011).
- [81] E. Prada, P. San-Jose, M. W. de Moor, A. Geresdi, E. J. Lee, J. Klinovaja, D. Loss, J. Nygård, R. Aguado, and L. P. Kouwenhoven, *Nat. Rev. Phys.* **2**, 575 (2020).
- [82] S. M. Frolov, M. J. Manfra, and J. D. Sau, *Nat. Phys.* **16**, 718 (2020).

- [83] G. D. Mahan, *Many-particle physics* (Springer Science & Business Media, 2013).
- [84] P. Marra, *J. Appl. Phys.* **132**, 231101 (2022).
- [85] P. Burset, B. Lu, H. Ebisu, Y. Asano, and Y. Tanaka, *Phys. Rev. B* **93**, 201402 (2016).
- [86] J. Cayao and A. M. Black-Schaffer, *Phys. Rev. B* **98**, 075425 (2018).
- [87] S.-Y. Hwang, P. Burset, and B. Sothmann, *Phys. Rev. B* **98**, 161408 (2018).
- [88] C. Triola, J. Cayao, and A. M. Black-Schaffer, *Ann. Phys.* **532**, 1900298 (2020).
- [89] M. A. Silaev, I. V. Bobkova, and A. M. Bobkov, *Phys. Rev. B* **102**, 100507 (2020).
- [90] J. Cayao, C. Triola, and A. M. Black-Schaffer, *Phys. Rev. B* **103**, 104505 (2021).
- [91] S. Pal and C. Benjamin, *Phys. Rev. B* **104**, 054519 (2021).
- [92] D. Chakraborty and A. M. Black-Schaffer, *Phys. Rev. Lett.* **129**, 247001 (2022).
- [93] K. S. Heinrich, H. G. Hugdal, M. Amundsen, and S. H. Jacobsen, *arXiv:2412.07529* (2024).
- [94] F. S. Bergeret, A. F. Volkov, and K. B. Efetov, *Rev. Mod. Phys.* **77**, 1321 (2005).
- [95] A. I. Buzdin, A. S. Mel'nikov, and N. G. Pugach, *Phys. Rev. B* **83**, 144515 (2011).
- [96] A. V. Samokhvalov, J. W. A. Robinson, and A. I. Buzdin, *Phys. Rev. B* **100**, 014509 (2019).
- [97] E. Prada, P. San-Jose, and R. Aguado, *Phys. Rev. B* **86**, 180503 (2012).
- [98] S. Das Sarma, J. D. Sau, and T. D. Stanescu, *Phys. Rev. B* **86**, 220506 (2012).
- [99] J. Cayao, P. San-Jose, A. M. Black-Schaffer, R. Aguado, and E. Prada, *Phys. Rev. B* **96**, 205425 (2017).
- [100] D. Kuiria and M. P. Nowak, *Phys. Rev. B* **108** (2023).
- [101] V. K. Vimal and J. Cayao, *Phys. Rev. B* **110**, 224510 (2024).
- [102] D. Kuzmanovski, A. M. Black-Schaffer, and J. Cayao, *Phys. Rev. B* **101**, 094506 (2020).
- [103] J. Cayao, *Phys. Rev. B* **110**, 125408 (2024).

- [104] D. Sahu, V. Khade, and S. Gangadharaiah, *Phys. Rev. B* **108**, 205426 (2023).
- [105] J. Linder and A. V. Balatsky, *Rev. Mod. Phys.* **91**, 045005 (2019).
- [106] S. Tamura, V. Kornich, and B. Trauzettel, *Phys. Rev. B* **109**, L100505 (2024).
- [107] J. Cayao, P. Burset, and Y. Tanaka, *Phys. Rev. B* **109**, 205406 (2024).
- [108] T. Yokoyama, Y. Tanaka, and A. A. Golubov, *Phys. Rev. B* **78**, 012508 (2008).
- [109] S.-P. Chiu, V. Mishra, Y. Li, F.-C. Zhang, S. Kirchner, and J.-J. Lin, *Nanoscale* **15**, 9179 (2023).
- [110] Y. Tanaka, Y. Asano, A. A. Golubov, and S. Kashiwaya, *Phys. Rev. B* **72**, 140503 (2005).
- [111] Y. Asano, Y. Tanaka, A. A. Golubov, and S. Kashiwaya, *Phys. Rev. Lett.* **99**, 067005 (2007).
- [112] S. Ikegaya, S. Tamura, D. Manske, and Y. Tanaka, *Phys. Rev. B* **102**, 140505 (2020).
- [113] J. Osca, D. Ruiz, and L. ç. Serra, *Phys. Rev. B* **89**, 245405 (2014).
- [114] S. Rex and A. Sudbø, *Phys. Rev. B* **90**, 115429 (2014).
- [115] J. Cayao, “Hybrid superconductor-semiconductor nanowire junctions as useful platforms to study Majorana bound states”, [arXiv:1703.07630], PhD thesis (Autonomous University of Madrid (UAM), Madrid, Spain, May 2016).
- [116] S. Mondal, P.-H. Fu, and J. Cayao, [arXiv: 2503.08318](https://arxiv.org/abs/2503.08318) (2025).
- [117] J. Cayao, N. Nagaosa, and Y. Tanaka, *Phys. Rev. B* **109**, L081405 (2024).
- [118] H. Bruus and K. Flensberg, *Many-body quantum theory in condensed matter physics* (Oxford University Press, 2004).
- [119] R. Aguado, *Riv. Nuovo Cimento* **40**, 523 (2017).
- [120] N. Goldman and J. Dalibard, *Phys. Rev. X* **4**, 031027 (2014).
- [121] M. Bukov, L. D’Alessio, and A. Polkovnikov, *Advances in Physics* **64**, 139 (2015).
- [122] L. Zhou, [Symmetry](https://doi.org/10.3390/sym14122546) **14**, 10.3390/sym14122546 (2022).
- [123] D. Mondal, A. K. Ghosh, T. Nag, and A. Saha, *Phys. Rev. B* **107**, 035427 (2023).

- [124] D. Mondal, A. K. Ghosh, T. Nag, and A. Saha, *Phys. Rev. B* **108**, L081403 (2023).
- [125] M. Thakurathi, A. A. Patel, D. Sen, and A. Dutta, *Phys. Rev. B* **88**, 155133 (2013).
- [126] J. K. Asbóth and H. Obuse, *Phys. Rev. B* **88**, 121406 (2013).
- [127] W. DeGottardi, M. Thakurathi, S. Vishveshwara, and D. Sen, *Phys. Rev. B* **88**, 165111 (2013).
- [128] Q.-J. Tong, J.-H. An, J. Gong, H.-G. Luo, and C. H. Oh, *Phys. Rev. B* **87**, 201109 (2013).
- [129] A. Soori, *Phys. E* **146**, 115545 (2023).
- [130] A. Balatsky and E. Abrahams, *Phys. Rev. B* **45**, 13125 (1992).
- [131] E. Abrahams, A. Balatsky, D. J. Scalapino, and J. R. Schrieffer, *Phys. Rev. B* **52**, 1271 (1995).
- [132] P. Coleman, A. Georges, and A. M. Tsvelik, *Journal of Physics: Condensed Matter* **9**, 345 (1997).
- [133] C.-H. Hsu, P. Stano, J. Klinovaja, and D. Loss, *Semiconductor Science and Technology* **36**, 123003 (2021).
- [134] L. Lin, Y. Ke, and C. Lee, *Phys. Rev. B* **103**, 224208 (2021).
- [135] I. Mondragon-Shem, T. L. Hughes, J. Song, and E. Prodan, *Phys. Rev. Lett.* **113**, 046802 (2014).
- [136] J. Linder and J. W. Robinson, *Nature Physics* **11**, 307 (2015).